

Dynamic Behaviour in Metal-Organic Frameworks as a Response to Guest Removal and Uptake, and Temperature

The University of Sheffield

Department of Chemistry



A thesis submitted to the Faculty of Science for the Requirement of a PhD

Daniel Watkins

dwatkins1@sheffield.ac.uk

Table of Contents

Acknowledgements	4
List of Abbreviations	5
Abstract	7
1. Introduction	8
1.1. Abstract	8
1.2. The Importance of MOFs	8
1.3. Flexible Metal-Organic Frameworks	12
1.3.1. MIL-53: The Discovery of Flexibility	12
1.3.2. Flexibility in Three Dimensions	16
1.3.3. Flexibility in Two Dimensions – Wine-racks	19
1.3.4. Flexibility in One Dimension – Pillared/Layered MOFs	24
1.4. Rational Design	29
1.4.1. The Synthetic Challenge	29
1.4.2. Choice of Metal	29
1.4.3. Ligand Functionalisation	32
1.5. SHF-61	34
1.6. Conclusions	43
1.7. References	44
2. Gas Uptake in SHF-61: <i>in situ</i> Diffraction Studies	50
2.1. Abstract	50
2.2. Introduction	50
2.3. Experimental	52
2.3.1. Synthesis & General Procedures	52
2.3.2. Single-Crystal Diffraction Experiments	52
2.3.3. Powder Diffraction Experiments	66
2.3.4. Infra-red Spectroscopy Studies	74
2.3.5. Volumetric Gas Adsorption	79
2.4. Results & Discussion	80
2.4.1. CO ₂ Uptake at 298 K	80
2.4.2. CO ₂ Uptake at 195 K	85
2.4.3. SO ₂ Uptake at 273 K	90
2.5. Conclusion	92
2.6. References	92
3. Solvent-Uptake in SHF-61: <i>in situ</i> Spectroscopy Studies	95
3.1. Abstract	95

3.2.	Introduction	95
3.3.	Experimental	97
3.3.1.	Synthesis & General Procedures	97
3.3.2.	General Information on Uptake Experiments	97
3.3.3.	DMF Uptake on Activated SHF-61-DMF (closed framework)	98
3.3.4.	Experiments on Open-Pore SHF-61	99
3.4.	Results & Discussion	100
3.4.1.	DMF Uptake in Closed-Pore SHF-61	100
3.4.2.	DMF Uptake in Open-Pore SHF-61	104
3.4.3.	Chloroform Uptake in Open-Pore SHF-61	108
3.4.4.	Cyclopentanone Uptake in Open-Pore SHF-61	112
3.4.5.	Cyclopentanone Uptake in Open-Pore SHF-61 (DMF Contaminated)	116
3.4.6.	Isopropanol Uptake in Open-Pore SHF-61 (DMF Contaminated)	121
3.4.7.	Water Uptake in Open-Pore SHF-61	123
3.4.8.	Discussion of SHF-61 Solvent Dependence	126
3.5.	Conclusion	127
3.6.	References	128
4.	The Dynamic Behaviour of a Trigonal Metal-Organic Framework: Response to Solvent Removal, Gas Uptake and Temperature	130
4.1.	Abstract	130
4.2.	Introduction	130
4.3.	Experimental	134
4.3.1.	General Techniques	134
4.3.2.	Synthesis and Characterisation	136
4.3.3.	Solvent Removal	139
4.3.4.	Gas Uptake with <i>in situ</i> X-ray Diffraction	143
4.3.5.	Variable Temperature Studies	149
4.4.	Results & Discussion	154
4.4.1.	Synthesis & Characterisation	154
4.4.2.	Solvent Removal	161
4.4.3.	Gas Uptake	169
4.4.4.	Temperature-Dependent Flexibility	180
4.5.	Conclusion	185
4.5.1.	Summary	185
4.5.2.	Next Steps	185
4.6.	References	186
5.	Conclusions	190

Acknowledgements

First, I'd like to thank Lee, for his supervision over the last four years. I have often been struck by his kindness, warmth and generosity. Even when I messed things up (and there are a few such occasions), Lee was always patient, approachable, and focused his attention to fixing the problem and

bettering the situation. Particularly towards the end of the project, as the submission deadline approached ever faster, Lee's support and patience was unwavering. From him I have learned a great deal, and I'm sure I will continue to learn while we publish the results of this project.

I'd also like to thank the other members (and ex-members) of the Brammer Group – Tom, Elliot, Jamie, Rebecca, Feifan, Stephen, Dave, Julia, Millie, Jen, Freya, Imogen, Emmy, Alberto and Andrea – for being a genuine pleasure to work with. That list includes patient teachers, diligent students and good friends. I haven't found this project easy, or even very enjoyable, and without these people I'm not sure I would have seen it through to the end. This statement can be extended also to Andy, Phil, Alex, Jon, Sam and Craig, who have helped me out more than I think they realise. Between the two of them, Tom and Elliot in particular taught me most of the technical and analytical skills needed for this project; without them, I really wouldn't have been able to do the project.

I'm very grateful to the hardworking technical staff in the department, who provide an endless stream of favours to postgraduate students on a daily basis. A large amount of the data in this thesis was collected at Diamond Light Source, and I gratefully acknowledge the staff at Beamlines I19, I11 and B22, for going above and beyond the call of duty to help us out on numerous occasions.

Finally, I'd like to acknowledge Tim Easun and Alex Tansell of Cardiff University Chemistry Department, for their help collecting and processing the *in situ* infra-red spectroscopy data that makes up the entirety of chapter 3 (and then some).

I feel immensely privileged to have known and worked with such great people.

“Any of your, uh, scientists working on anything new?”

“All of them. That's their job.”

Rick and Morty; Series 2, Episode 6

List of Abbreviations

MOF	metal-organic framework
SBU	secondary Building Unit
bipy	bipyridine

im	imidazole
BTC²⁻	trimesate
BDC²⁻	terephthalate
NO₂BDC²⁻	nitroterephthalate
NH₂BDC²⁻	aminoterephthalate
BrBDC²⁻	bromoterephthalate
DABCO	1,4-diazabicyclo-[2.2.2]octane
H₄TCPBDA²⁻	<i>N,N,N',N'</i> -tetrakis(4-carboxyphenyl)-biphenyl-4,4'-diamine
TCPBDA⁴⁻	deprotonated <i>N,N,N',N'</i> -tetrakis(4-carboxyphenyl)-biphenyl-4,4'-diamine
DMF	<i>N,N</i> -dimethylformamide
CyP	cyclopentanone
dia	diamondoid (network topology)
qtz	quartz (network topology)
NTE	negative thermal expansion
PTE	positive thermal expansion
NAE	negative area expansion
PAE	positive area expansion
NLE	negative linear expansion
PLE	positive linear expansion
VT	variable temperature
PXRD	powder X-ray diffraction
SCXRD	single-crystal X-ray diffraction
IR	infra-red (spectroscopy/spectrum)
NMR	nuclear magnetic resonance (spectroscopy/spectrum)
EA	elemental analysis
TGA	thermogravimetric analysis
VOC	volatile organic compound
Abs	absorption (infra-red)

Abstract

Metal-Organic Frameworks (MOFs) are a porous class of coordination polymer, in which dynamic behaviour as a response to various stimuli has been increasingly reported over the past two decades. Chapter 1 of this thesis provides a brief, non-comprehensive introduction to some of the reported flexible MOF materials and their dynamic response under various conditions, such as change of pressure or temperature, or the presence of small molecule guests in their pores. Building upon previous work in the group, chapters 2 and 3 describe gas- and solvent-uptake experiments respectively on the **SHF-61** MOF, $[\text{NMe}_2\text{H}_2][\text{In}(\text{NH}_2\text{BDC})_2]$, which is unique in its ability to undergo both continuous flexibility and solvent-dependent activation behaviour. Comparisons are made both to the published work on this material, and analogous studies on other metal-organic frameworks in the literature. Chapter 4 describes a different, but related material $[\text{NMe}_2\text{H}_2][\text{Cd}(\text{NO}_2\text{BDC})_2]$, which although previously reported, had not previously been recognised as exhibiting dynamic behaviour. The MOF is found to have temperature-dependent carbon dioxide uptake behaviour, and exhibits uniaxial negative linear expansion as a response to solvent removal, gas uptake and temperature change. The mechanism of flexibility in this cadmium-based MOF is fundamentally different to that which governs the behaviour of the **SHF-61** system. Chapter 5 concludes the thesis, and provides suggestions for future work relating to these two MOF systems.

1. Introduction

1.1. Abstract

This chapter provides the reader with a brief overview of flexible metal-organic frameworks (MOFs) and the different forms they can take, as well as some of the mechanisms by which solid-state flexibility can occur. A few key concepts are introduced with illustrative examples, and the foundation work, on which a large portion of this thesis is based, is described in detail.

1.2. The Importance of MOFs

A metal-organic framework, is (generally) a crystalline, microporous material composed of an infinite array of metal nodes interconnected by organic linkers.^{1,2} These metal nodes can either be single ions or clusters, which are termed ‘Secondary Building Units’ (SBUs), and are often based on transition metals such as zirconium, copper, zinc and cadmium.^{1,3} Two common SBU motifs are shown in Figure 1.1, but it should be noted that over 130 have been reported.⁴ The vast majority of organic linkers are rigid aromatic ligands, which are coordinated to the metal-containing SBUs *via* nitrogen atoms or carboxylate groups;^{1,3} some examples can be seen in Figure 1.2.

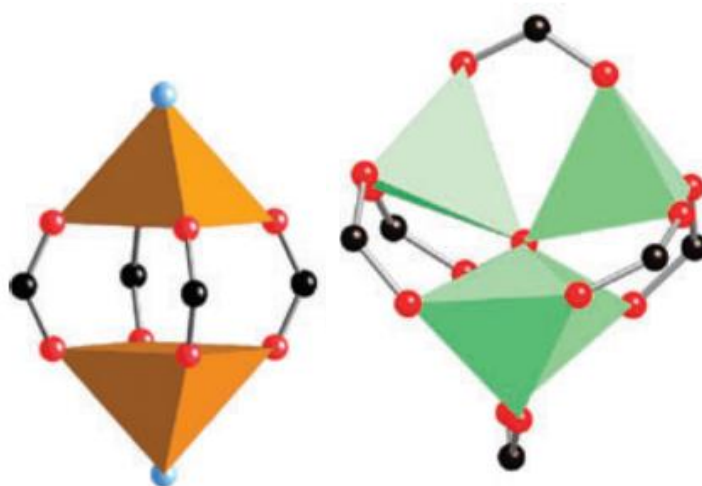


Figure 1.1. Two examples of SBUs: left) a common square paddle-wheel SBU, with four points of extension in a square arrangement (see HKUST-1 later); right) a well-known SBU, consisting of four tetrahedral metal ions which share a central oxide and are coordinated by six carboxylates in an octahedral arrangement (see MOF-5 later). Black = carbon; red = oxygen; blue = capping ligand. Image adapted from reference 4 with permission of the Royal Society of Chemistry.

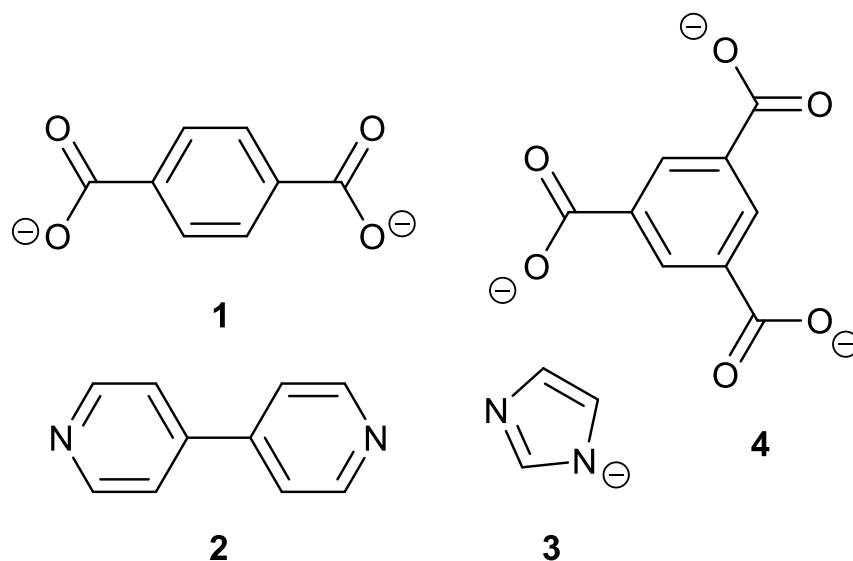


Figure 1.2. Some common linkers used in the synthesis of MOFs. 1) terephthalate (BDC); 2) bipyridine (bipy); 3) imidazolate (im); 4) trimesate (BTC).

Commonly prepared by solvothermal or mechanochemical methods,³ MOFs are of interest primarily because of their broad range of potential applications,⁵ which include: catalysis⁶⁻⁸; energy storage and conversion⁹; light harvesting¹⁰; inkless printing;¹¹ drug delivery;¹²⁻¹⁴ antibacterial activity;¹⁵ and the capture and detection of metal-ions¹⁶ and small molecules such as water,¹⁷ cellular oxygen,¹⁸ pollutants,¹⁹ VOCs²⁰ and toxic nerve agents.²¹ The most promising (and arguably important) application, however, is gas storage and separation; particularly hydrogen²²⁻²⁴ and carbon dioxide^{25,26}. **HKUST-1**²⁷ and **MOF-5**²⁸ – discovered by Williams *et. al.* and Yaghi *et. al.* respectively – are two metal-organic frameworks widely known for their hydrogen adsorption properties. **HKUST-1**, [Cu₃(BTC)₂(H₂O)₃], is comprised of copper-paddlewheel SBUs (*c.f.* fig. 1) connected *via* trimesate ligands in a face-centred cubic arrangement (Figure 1.3) and has been reported by Lin *et. al.* to have hydrogen uptake values of up to 1.95 wt.% at low temperature (77 K), although raising the temperature does reduce hydrogen uptake.²⁹ An important point to note is that other research groups have reported different values for hydrogen uptake by **HKUST-1**, which highlights the sensitivity of MOFs to experimental procedures and conditions.³⁰⁻³²

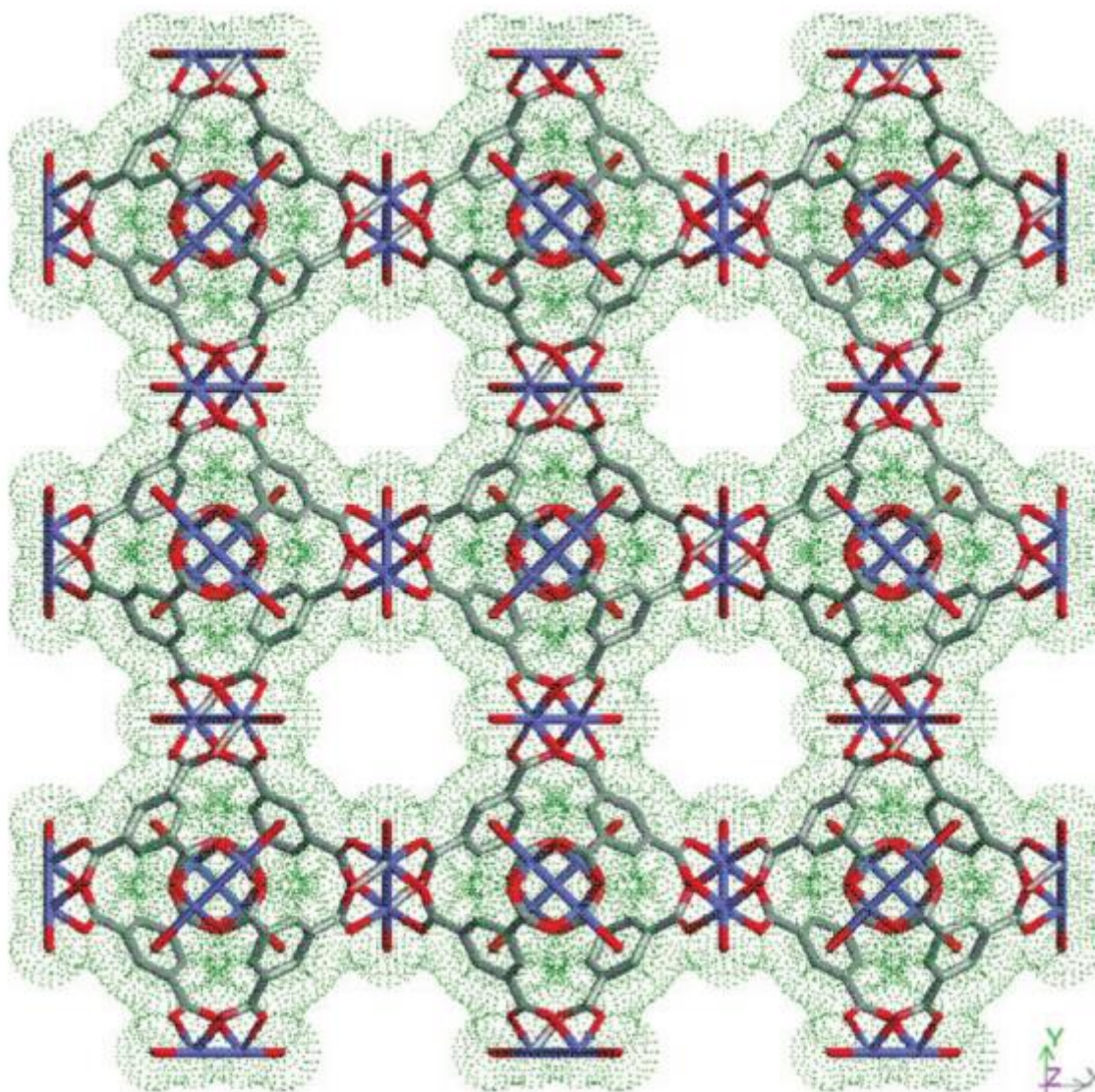


Figure 1.3. The face-centred-cubic structure of HKUST-1; note the square-paddlewheel SBUs (which are capped by water molecules in this case). . Image reproduced from reference 27 with permission of the Science Publishing Group.

MOF-5 ($Zn_4(O)(BDC)_3$) has a primitive cubic structure in which octahedral SBUs consisting of a Zn_4O cluster are connected by terephthalate linkers (Figure 1.4).²⁸ Low temperature hydrogen uptake values as high as 4.5 wt.% have been reported for this material,³³ and whilst it should not be ignored that the initial work performed on **MOF-5** has proved difficult to reproduce,³⁴ the remarkable potential shown by MOFs such as these has created a huge surge of interest within the chemical community, causing the field to grow at an ever-accelerating rate.

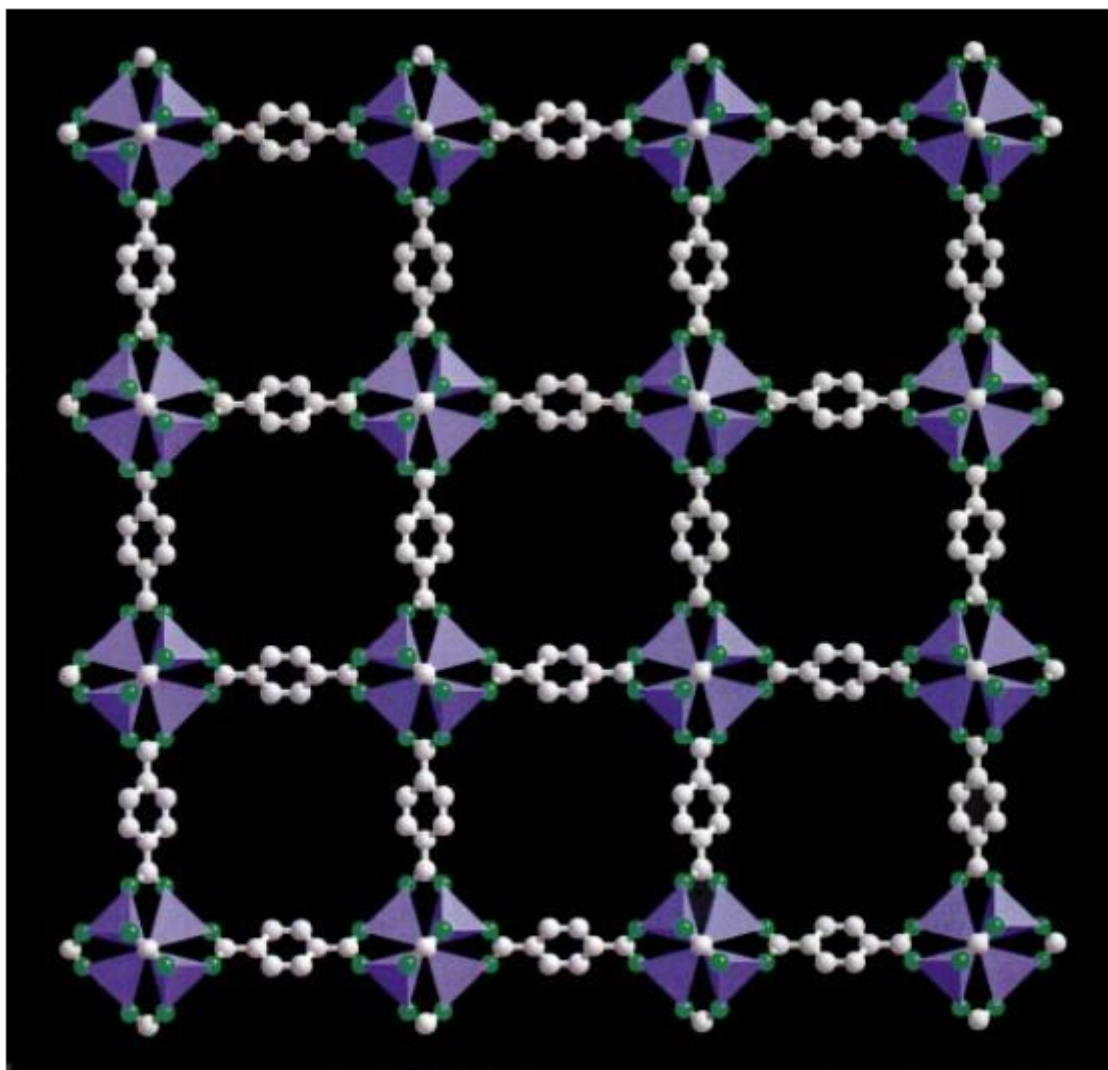


Figure 1.4. The network structure of MOF-5, showing the ZnO₄ tetrahedra (purple) that comprise the SBUs. Image reproduced from reference 28 with permission of Nature Publishing Group.

Regarding applications, a number of MOFs have been made available commercially by the company BASF (Badische Anilin und Soda Fabrik): Basolite[®] C300 (**HKUST-1**); Basolite[®] F300 (**Fe-HKUST-1**); Basolite[®] Z377 (**MOF-177**); Basolite[®] Z1200 (**ZIF-8**); and Basolite[®] A100 (**Al-MIL-53**).^{5,35,36} Currently, the most developed MOF in terms of commercial application is Basolite[®] A520,³⁶ which is an aluminium-based MOF constructed of one-dimensional parallel aluminium-hydroxide chains, interlinked by fumarate ligands (Figure 1.5).^{36,37} Utilizing its considerable methane adsorption properties, BASF have been able to develop a methane storage and transport system for heavy duty vehicles.

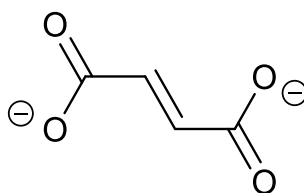
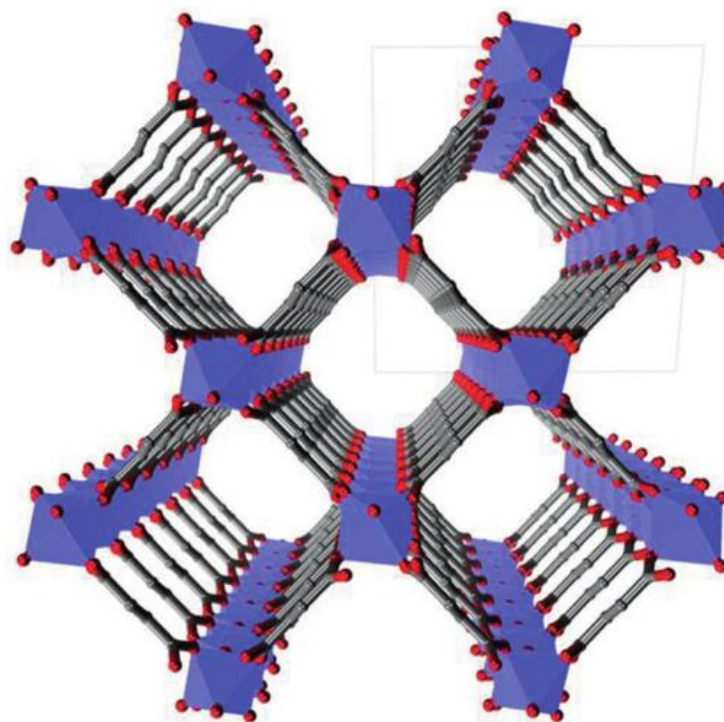


Figure 1.5. Top: The structure of the Basolite[®] A520. Image reproduced from reference 37 with permission of Wiley-VCH. Bottom: The structure of the fumarate dianion; the linker component of Basolite[®] A520.

1.3. Flexible Metal-Organic Frameworks

1.3.1. MIL-53: The Discovery of Flexibility

The concept of structurally dynamic porous materials was first introduced by Kitagawa *et al.* in the late 1990s,^{35,38} and in 2002, Férey *et al.* discovered the first metal-organic framework capable of undergoing large, reversible transitions between structures with varying pore-size, upon exposure to certain conditions.³⁹ Formally named **MIL-53** (MIL = Materials Institut Lavoisier), the framework, Cr(OH)(BDC), consists of repeating Cr^{III}-OH chains running parallel to the *c*-axis, which are interconnected by terephthalate ligands to form a grid which lies in the *ab*-plane (Figure 1.6).

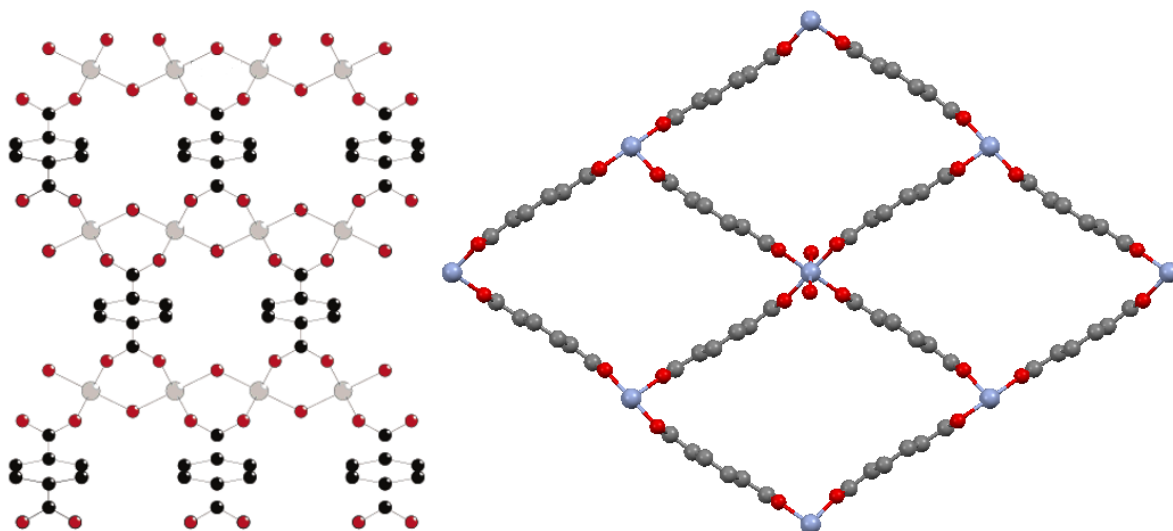


Figure 1.6. Left: view of MIL-53 along the *a*-axis, showing the Cr-OH chains (horizontal). Image adapted from reference 39 with permission Chemical Society. Right: the grid-structure of MIL-53, viewed along the *c*-axis. Blue = Cr; Red = O; Grey = C. Notice that each Cr^{III} centre has pseudo-octahedral geometry with hydroxides coordinated to the axial sites and terephthalate ligands to the equatorial sites.

MIL-53 is prepared hydrothermally from chromium(III) nitrate and terephthalic acid, in the presence of hydrofluoric acid. As synthesised (**MIL-53as**), it resides in the orthorhombic space group *Pnam*, with its pores occupied by free terephthalic acid molecules. Upon heating to 300 °C, the guest molecules are lost, and the pores open slightly. This is accompanied by a change of space group to *Imcm* and a cell volume increase of around 46 Å³ (**MIL-53ht**). When cooled to 30 °C, the structure takes up water (one molecule per formula unit), and the pores close. This is associated with a large volume decrease of almost 500 Å³ and a change of crystal system to monoclinic; space group *C2/c* (**MIL-53lt**). **MIL-53lt** can be converted to **MIL-53ht** by heating at 100 °C. A schematic of the pores opening/closing is shown in Figure 1.7.

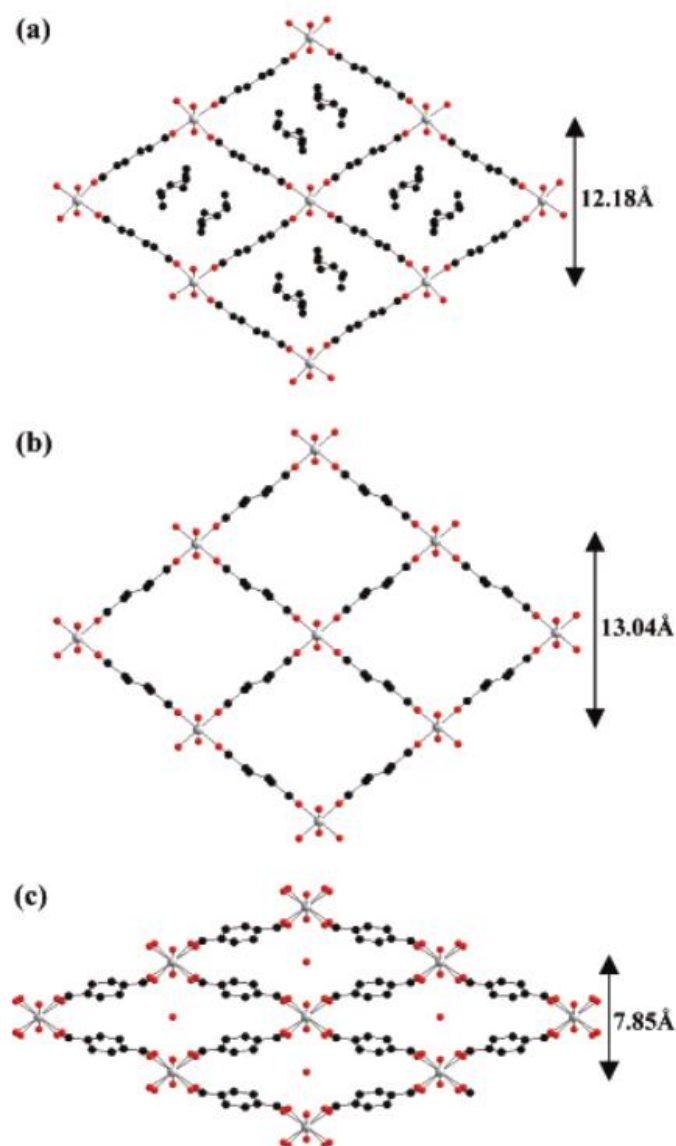


Figure 1.7. The pore systems of MIL-53as (a), MIL-53ht (b) and MIL-53lt (c), with the pore width shown on the right. Note the presence of disordered terephthalic acid in (a) and water in (c). Also note the twisting of the ligands in (c), described by Férey as a knee-cap mechanism. Image reproduced from reference 39 with permission of the American Chemical Society.

The closing of the pores upon incorporation of guest molecules may seem somewhat counter-intuitive, but it has since been shown to occur due to the formation of favourable hydrogen-bonding interactions between the guest water molecules and the hydroxyl and carboxylate groups of the framework.⁴⁰ Immersion of **MIL-53lt** in ethanol and acetone did not produce any structural change, and when **MIL-53ht** was immersed in ethanol and acetone, the trace water in the solvent was quickly adsorbed, forming exclusively **MIL-53lt**. This indicates that **MIL-53** preferentially adsorbs water over either solvent. *N,N*-Dimethylformamide (DMF), however, was found to replace the water in

MIL-53lt to form the “solvated” structure **MIL-53solv**, which can be thought of as an intermediate state between **MIL-53lt** and **MIL-53as**, in the space group *Pnam*. Conversion of **MIL-53solv** into **MIL-53ht** occurs upon heating at 150 °C. Table 1.1 summarizes the unit cell dimensions of the different structures.

Table 1.1. The unit cell parameters and space groups of the different phases of MIL-53, clearly indicating a trend in the series. It can be seen that the volume decreases as the *a*-axis lengthens and the *b*-axis shortens, and the variation in the *c*-axis is minimal.

Phase	<i>a</i> / Å	<i>b</i> / Å	<i>c</i> / Å	β / deg	<i>V</i> / Å ³	Space Group	Guest
MIL-53ht	16.733(1)	13.038(1)	6.812(1)	90	1486.1	Imcm	
MIL-53as	17.340(1)	12.178(1)	6.822(1)	90	1440.6	Pnam	BDC
MIL-53solv	17.905(1)	11.218(1)	6.825(1)	90	1370.9	Pnam	DMF
MIL-53lt	19.685(4)	7.849(1)	6.782(1)	104.90(1)	1012.6	<i>C2/c</i>	H ₂ O

These results show a guest-dependent breathing effect; in a more extensive follow-up study it was shown that the pore size of MIL-53 depends on the strength of the host-guest interactions and not the size of the guest species.^{40,41}

Gas-adsorption studies on **MIL-53** by Ferey *et al.* indicate that its flexibility is influenced significantly by the identity of the guest molecule.⁴² The adsorption isotherms for methane and carbon dioxide at 304 K are shown in Figure 1.8. The structure starts in the open-pore phase **MIL-53ht**, and the CH₄ isotherm shows behaviour expected for any porous material capable of gas adsorption; that is, a decreasing rate of adsorption as more gas is adsorbed. The CO₂ isotherm, however, shows a clear step at around 6 bar. By analysing the adsorption enthalpies, it was deduced that CO₂ adsorption in the initial stages of the experiment causes the framework pores to narrow, due to hydrogen-bonding interactions between the CO₂ molecules and framework hydroxyl groups. However, when the pressure reaches 6 bar, it is sufficient to force gas molecules into the pores of the framework, thus re-

opening the MOF and allowing gas adsorption to continue as normal. It should be noted that **MIL-53** exhibits CO₂ adsorption properties that are better than those typical for zeolites, and better even than most MOFs.⁴²

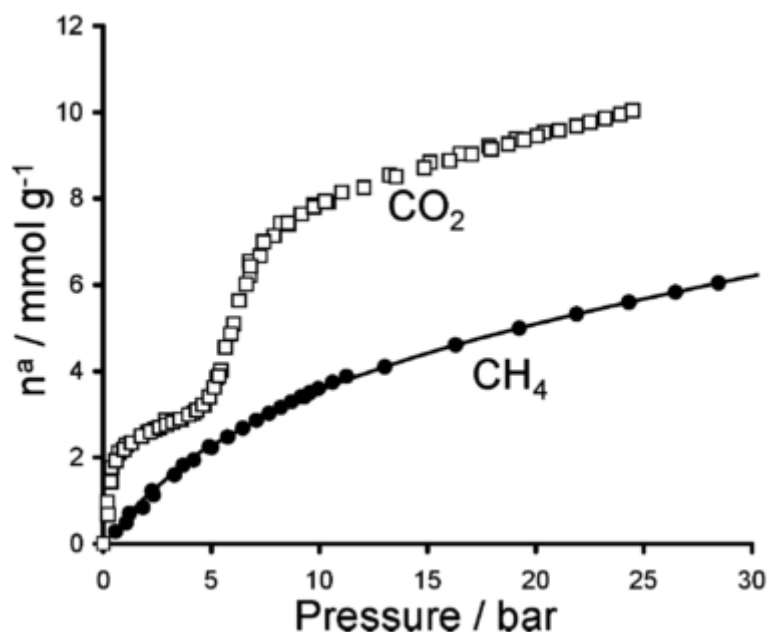


Figure 1.8. The CO₂ and CH₄ adsorption isotherms for MIL-53. The step in the CO₂ isotherm, which is absent in the CH₄ isotherm, indicates that CO₂ is interacting with the framework, whereas CH₄ is not. Image reproduced from reference 42 with permission of the American Chemical Society.

Since the discovery of **MIL-53**, there has been an increasing number of flexible MOFs reported, and several key reviews have been published focussing primarily on their structural characterisation, breathing mechanisms and applications.^{35,36,41,43-45} The following three sections of this chapter (1.3.2 – 1.3.4) will outline some of the more common mechanisms of flexibility which can occur in MOFs, with some illustrative examples.

1.3.2. Flexibility in Three Dimensions

Given the necessary mechanical requirements, relatively few MOFs are capable of flexibility in three dimensions.⁴⁵ A useful example is **ZIF-8**, or [Zn(MeIm)₂], a zeolitic 2-methylimidazole-based MOF, which, although rigid under ambient conditions, has been shown by Moggach *et al.* to exhibit pressure-dependent flexibility.⁴⁶ As synthesised, the ZIF holds 12 molecules of methanol in its large pores. Upon applying pressure up to 0.18 GPa to a single crystal in a diamond anvil cell (DAC)

containing a hydrostatic medium (4:1 methanol:ethanol), they found that the cell volume and pore volume of the material both increased, as species of the hydrostatic medium were forced into the framework. Increasing the pressure further to 0.96 GPa, the cell and pore volume decreased, with the volume at 0.96 GPa being just below that at ambient conditions. Upon increasing the pressure further to 1.47 GPa, a single crystal to single crystal (sc-sc) transition occurred to a state in which the volume of the pores is decreased, but the cell volume, and number of molecules adsorbed is increased. This is possible due to a twisting of the 2-methylimidazolate ligands, which allows the pores to be interconnected *via* small channels, thus causing an increase in the overall pore volume within the framework (Figure 1.9). This illustrates an important point: the interactions between the medium species and the framework must be more favourable than the interactions between medium species in high pressure environments. Upon lowering the pressure, the structure reverted to the original phase at 0.82 GPa, accompanied by a loss of almost 60 % of the adsorbed methanol, and as the pressure was lowered further the volume and number of adsorbed species also lowered until only 2 methanol species were adsorbed at atmospheric pressure (*c.f.* 12 before experiment).

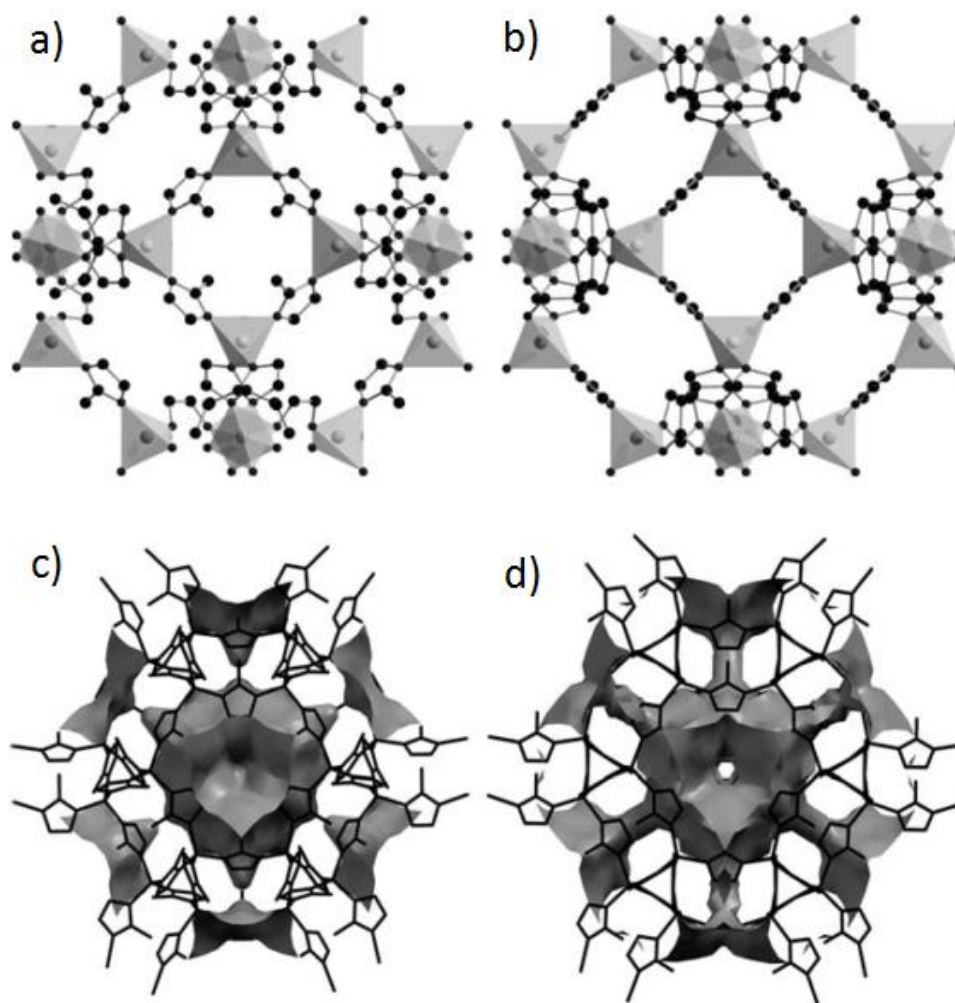


Figure 1.9. a) the structure of ZIF-8 under ambient conditions, showing the ZnN₄ tetrahedra; b) ZIF-8 at 1.47 GPa, with the new orientation of the ligands clearly visible; c) A view of the pore space in ZIF-8 under ambient conditions; d) Pore space at 1.47 GPa, showing the small channels connecting adjacent nanopores. Image reproduced from reference 46 with permission of Wiley-VCH.

Whilst three-dimensional flexibility can be forced using high pressure, it can also occur under fairly mild conditions. **MIL-88A(Fe)**, a MOF consisting of iron(III) centres linked by fumarate dianions was studied in 2005 by a combination of powder diffraction and computational simulations and found to exhibit a volume increase of almost 86 % when its evacuated form adsorbed water.⁴⁷ Although **MIL-88A(Fe)** is often referred to as a swelling MOF (including by the original authors), its volume expansion occurs *via* an expansion of the *a*- and *b*-axes and a contraction of the *c*-axis (with retention of its hexagonal space group) (Figure 1.10). This type of dynamic behaviour will be discussed in more detail in chapter 4.

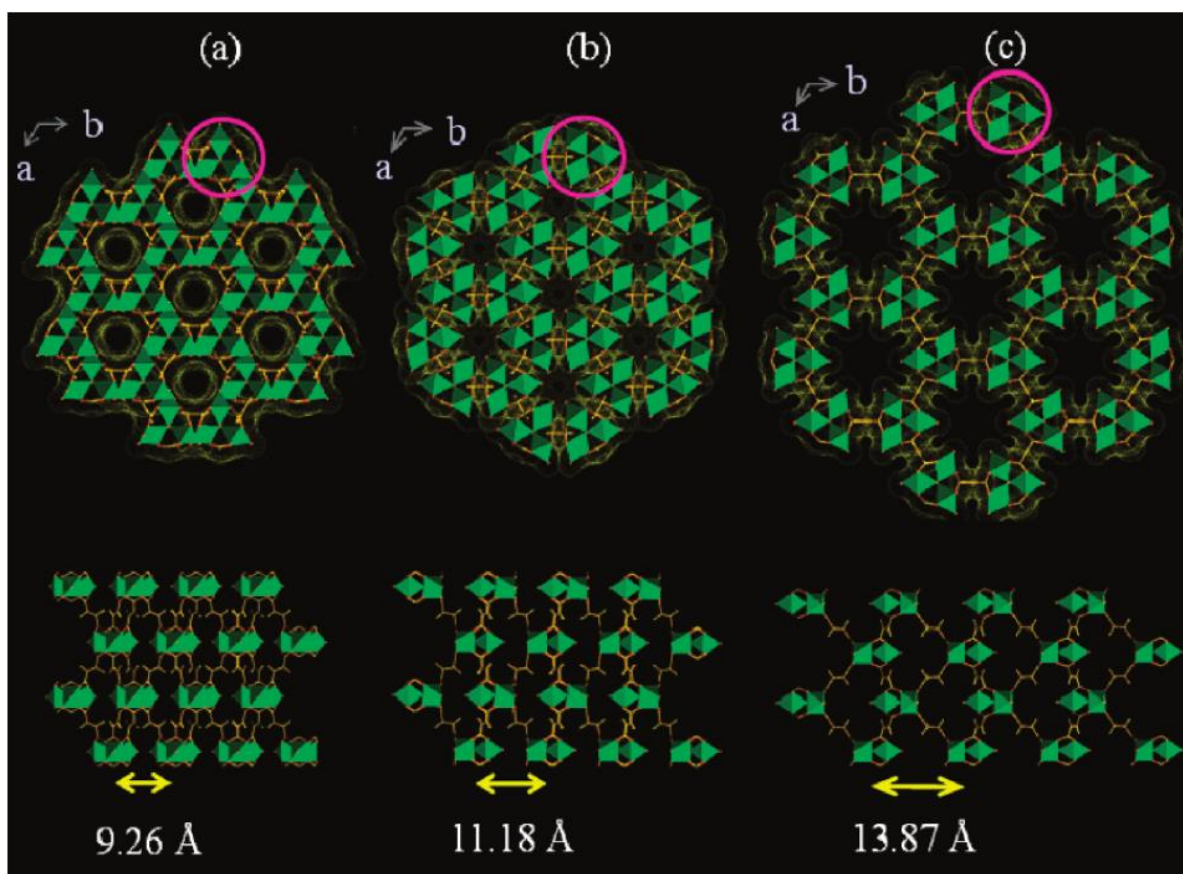


Figure 1.10. Views of MIL-88A(Fe) structures along the c -axis: a) evacuated form (after heating at 423 K); b) as-synthesised form, containing residual solvent; c) hydrated form, which contains over 6 water molecules per iron(III) centre. The measurements at the bottom correspond to the length of the a -axis. Careful examination reveals that the flexibility arises from ligand twisting. Image reproduced from reference 47 with permission of the American Chemical Society.

1.3.3. Flexibility in Two Dimensions – Wine-racks

Two-dimensional flexibility refers to when a MOF exhibits dynamic motion in two dimensions but remains rigid in the third. **MIL-53** is a typical example, as its b - and c -axis changes are so large compared to that of the a -axis. Like **ZIF-8**, the expansion/contraction of **MIL-53** arises from movement of the ligands (*c.f.* Figure 1.7, section 1.3.1), but the flexibility is limited to two dimensions due to a rigid chain of chromium and hydroxide ions, causing **MIL-53** to exhibit a so-called wine-rack topology.³⁹ In **MIL-53**, the ligands display a so-called “knee-cap” type motion, which is essentially a rotation about the O...O vector of the carboxylate oxygens. Another example of a wine-rack-type structure is [Co(BDP)]·2DEF·H₂O (BDP = 1,4-benzenedipyrazolate (Figure 1.11); DEF = *N,N*-Diethylformamide). Reported by Long *et al.* in 2008,⁴⁸ this material displays five distinct steps in

its low-temperature nitrogen adsorption isotherms (Figure 1.12), which were shown in a subsequent paper to correspond to different phases; dry, filled and three intermediates (int.1, int.2 and int.3).⁴⁹



Figure 1.11. The structure of 1,4-benzenedipyrazolate (BDP).

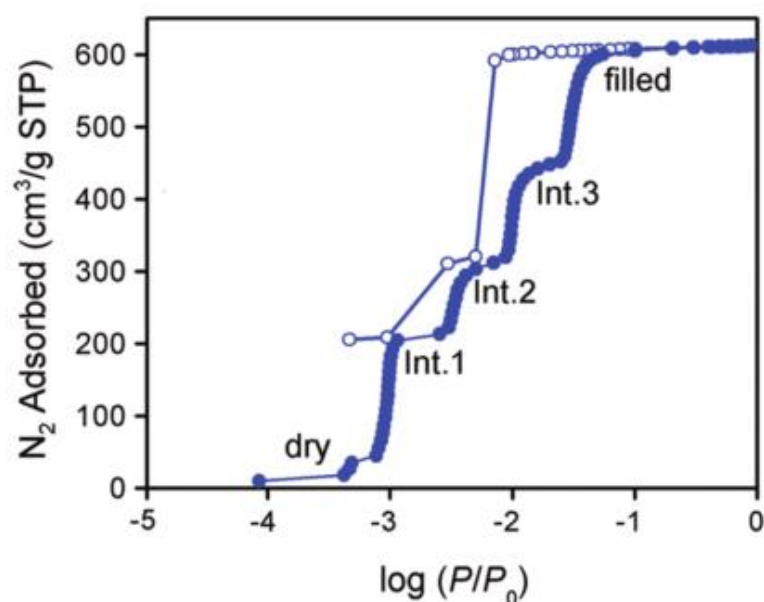


Figure 1.12. N₂ isotherm of Co(BDP) measured at 77 K, showing the five distinct steps. Filled circles are adsorption measurements, and hollow circles are desorption. Image reproduced from reference 49 with permission of the American Chemical Society.

Molecular simulations were used to provide structures for each of the phases, which are shown in Figure 1.13. In the dry (evacuated) phase, the cobalt centres have square-planar geometry, and the ligands are twisted significantly, to minimise empty space in the structure. As the nitrogen pressure is increased, the ligands straighten in steps, opening the structure to accommodate nitrogen guests, causing the phases int.1, int.2 and int.3. The final phase transition, from int.3 to filled, occurs *via* a combination of ligand twisting and a change of metal geometry from square-planar to tetrahedral, illustrating that dynamic motion in metal-organic frameworks often occurs as a result of multiple mechanisms acting simultaneously.

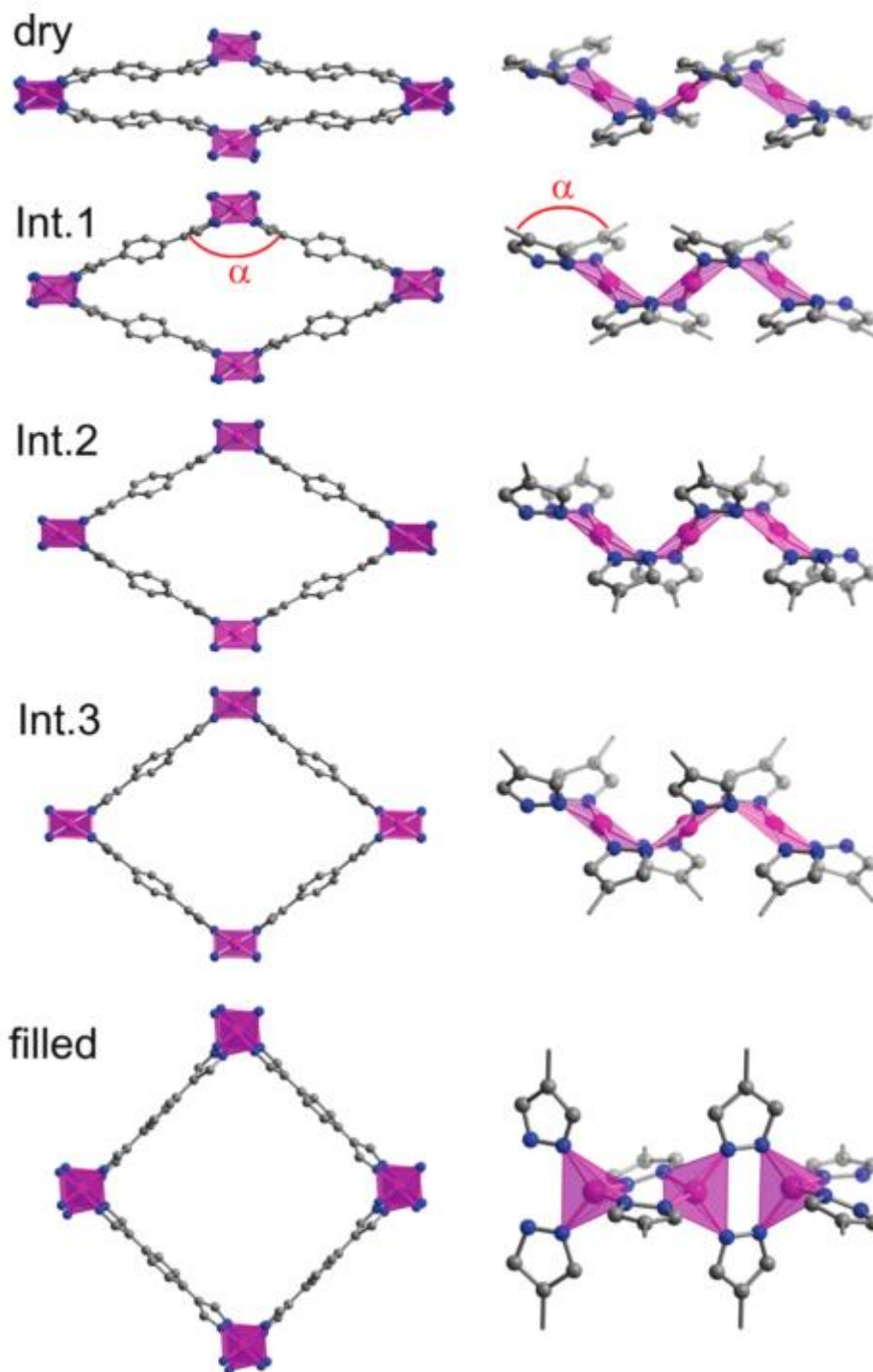


Figure 1.13. The five distinct phases of Co(BDP): left) viewed along the *c*-axis; right) SBU, with metal coordination environment shown in pink. Image reproduced from reference 49 with permission of the American Chemical Society.

In 2010 the nickel and zinc analogues of Co(BDP) were reported by Galli et al.²⁰ The metal coordination geometry in Zn(BDP) is a rigid tetrahedron and is therefore only slightly flexible. Ni(BDP) has square planar geometry and, interestingly, is also only slightly flexible, with no phase

changes apparent from its low-temperature nitrogen adsorption isotherm. This is unexpected, since it appears that ligand twisting alone allows a large degree of flexibility in Co(BDP).⁴⁹ It seems that if the coordination geometry is too rigid, the ligands cannot move enough to twist, and thus flexibility is greatly reduced. The concept of flexible coordination spheres will be returned to later.

Although the MOFs discussed in this section so far have had a rigid chain of metal ions, the same type of flexibility has been achieved in MOFs which have a non-flexible metal-ligand sequence running in one direction. For example, $\text{Zn}_2(\text{BDC})_2(\text{DABCO})$ has zinc paddlewheel SBUs, which are interconnected by DABCO (1,4-diazabicyclo[2.2.2]octane) at the axial sites, and terephthalate at the equatorial sites (Figure 1.14).⁵⁰ A phase change accompanies adsorption of DMF or benzene, and the open, DMF and benzene forms all exhibit temperature-dependent flexibility. In the open and DMF forms, the flexibility is fairly small and caused by ligand twisting perpendicular to the *c*-axis (along the long-axis of the ligand) and ligand bending in the case of the DMF form (Figure 1.15). However, the benzene-loaded form flexes to a much larger degree, accompanied by ligand twisting parallel to the *c*-axis in a knee-cap style hinge reminiscent of the **MIL-53** flexing mechanism (Figure 1.16).³⁹ In all three cases (open, DMF and benzene), the length of the paddlewheel-DABCO repeat unit along the *c*-axis changes very little with temperature, whereas the *a*-axis decreases and *b*-axis increases as the temperature is reduced (Figure 1.17). The negative thermal expansion (NTE) shown by the *b*-axis is a concept that will be explored further in chapter 4.

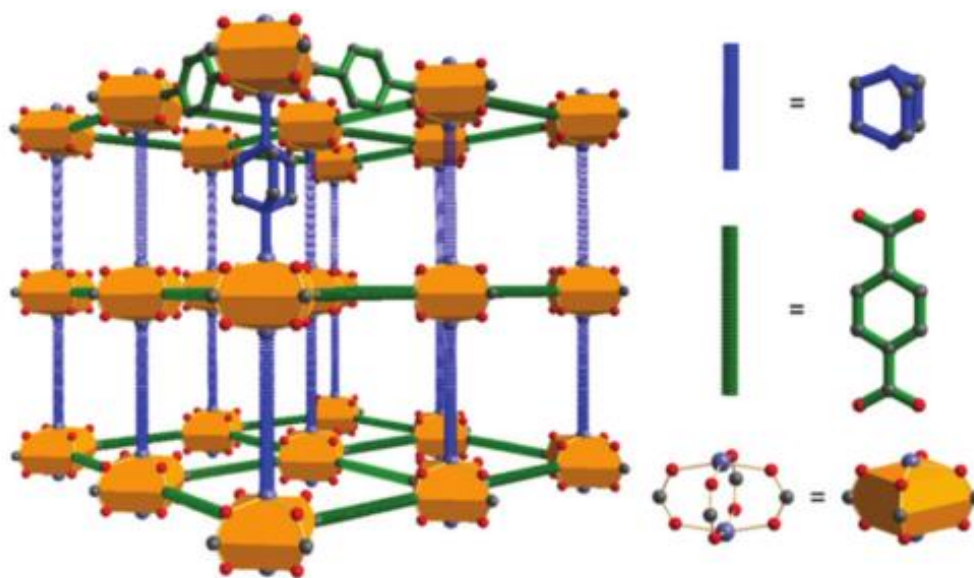


Figure 1.14. The structure of $\text{Zn}_2(\text{BDC})_2(\text{DABCO})$. Green linkers represent terephthalate, blue linkers represent DABCO, and the paddlewheel SBUs are highlighted in yellow. Image reproduced from reference 50 with permission of the Royal Society of Chemistry.

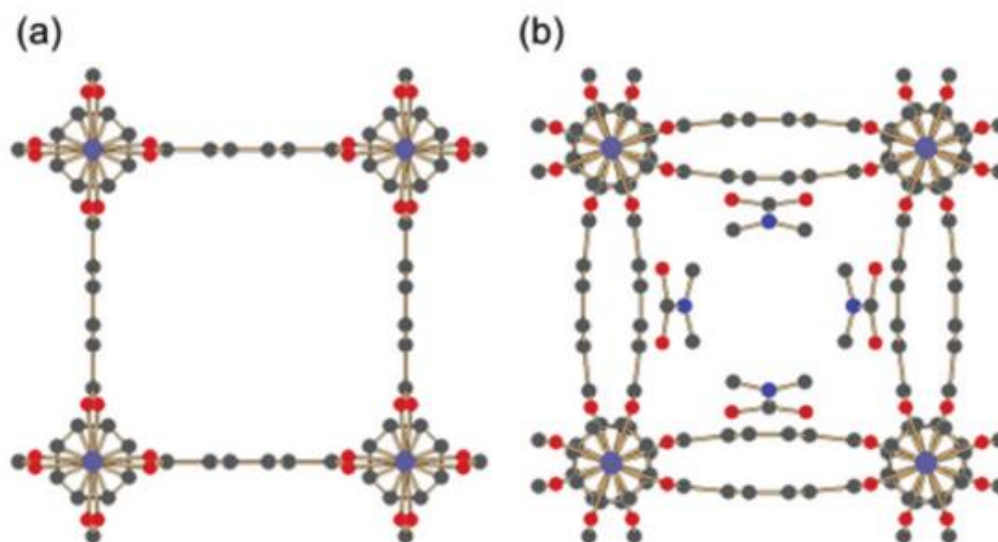


Figure 1.15. Left: $\text{Zn}_2(\text{BDC})_2(\text{DABCO})$ without a guest at 298 K, with the ligands twisted along their long axis. Right: $\text{Zn}_2(\text{BDC})_2(\text{DABCO})$ loaded with DMF, with the ligands bent in an alternating arrangement. Image reproduced from reference 50 with permission of the Royal Society of Chemistry.

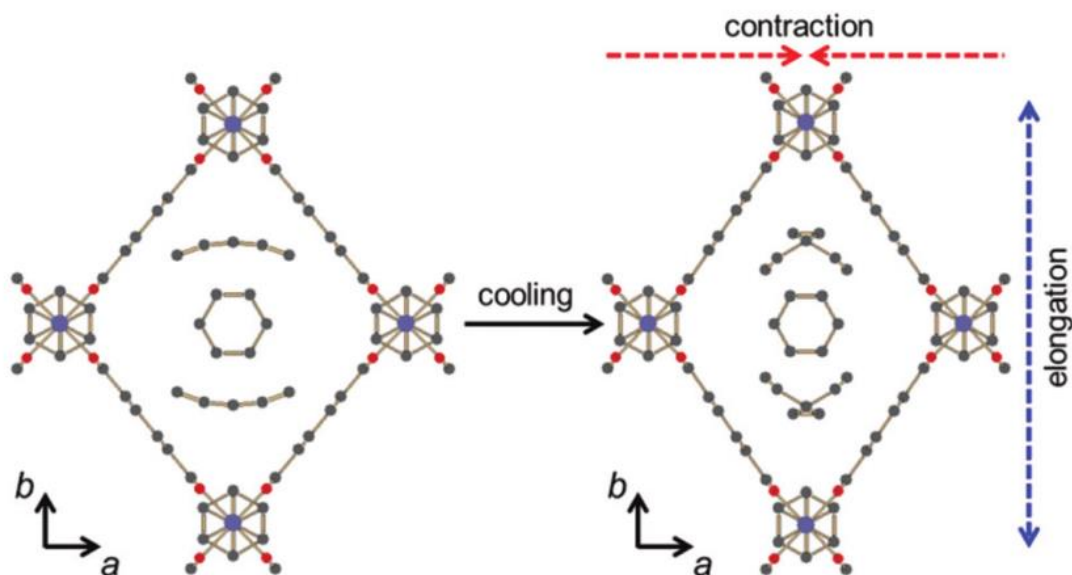


Figure 1.16. $\text{Zn}_2(\text{BDC})_2(\text{DABCO})$ loaded with benzene at 298 K (left) and 100 K (right). Image reproduced from reference 50 with permission of the Royal Society of Chemistry.

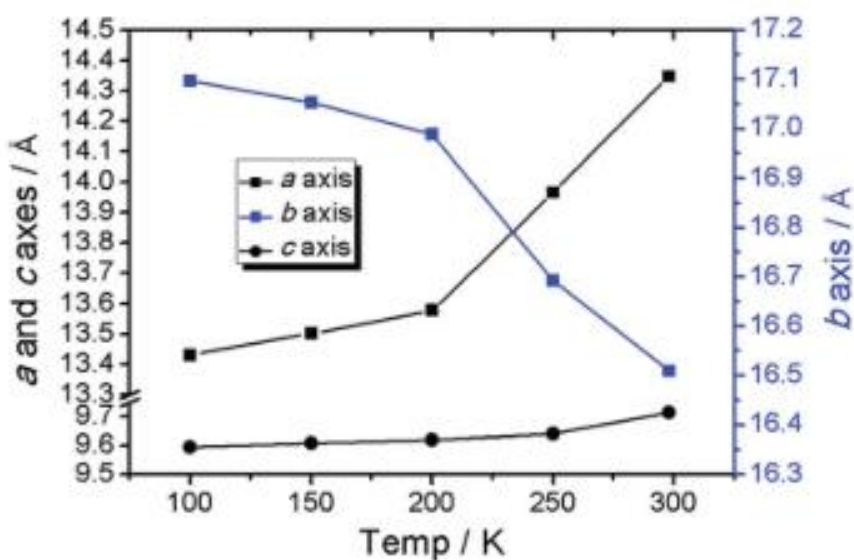


Figure 1.17. The dimensions of the crystallographic axes of benzene-loaded $\text{Zn}_2(\text{BDC})_2(\text{DABCO})$ as a function of temperature. The wine-rack-type flexibility involves the *a*-axis exhibiting positive thermal expansion (PTE), while the *b*-axis exhibits negative thermal expansion (NTE). Image reproduced from reference 50 with permission of the Royal Society of Chemistry.

1.3.4. Flexibility in One Dimension – Pillared/Layered MOFs

Many MOFs comprise two-dimensional layers joined together with pillars in their third dimension. If this pillar is capable of dynamic behaviour, then the framework has the potential for flexibility. For example, $\text{Co}(5\text{-NH}_2\text{BDC})(\text{bpy})_{0.5}$ has two-dimensional rigid layers consisting of cobalt centres interconnected by 5-aminoisophthalate ligands, and the layers are connected in the third dimension by

bpy (4,4'-bipyridine).⁵¹ As-synthesised, the MOF contains one coordinated water molecule per cobalt centre in addition to water molecules within its pores. When heated, it loses all of these guests, and shrinks by approximately 10 % in the direction parallel to the *a*-axis, due to a knee-cap-style twisting of the bpy ligands and a change of metal geometry from pseudo-octahedral to *pseudo*-square planar (Figure 1.18). When exposed to water, the MOF regains its original structure, and will adsorb methanol, ethanol, 2-propynyl alcohol and acetonitrile upon exposure. The rigidity of the two-dimensional layers is likely due to the coordination of the amino substituents to cobalt centres.

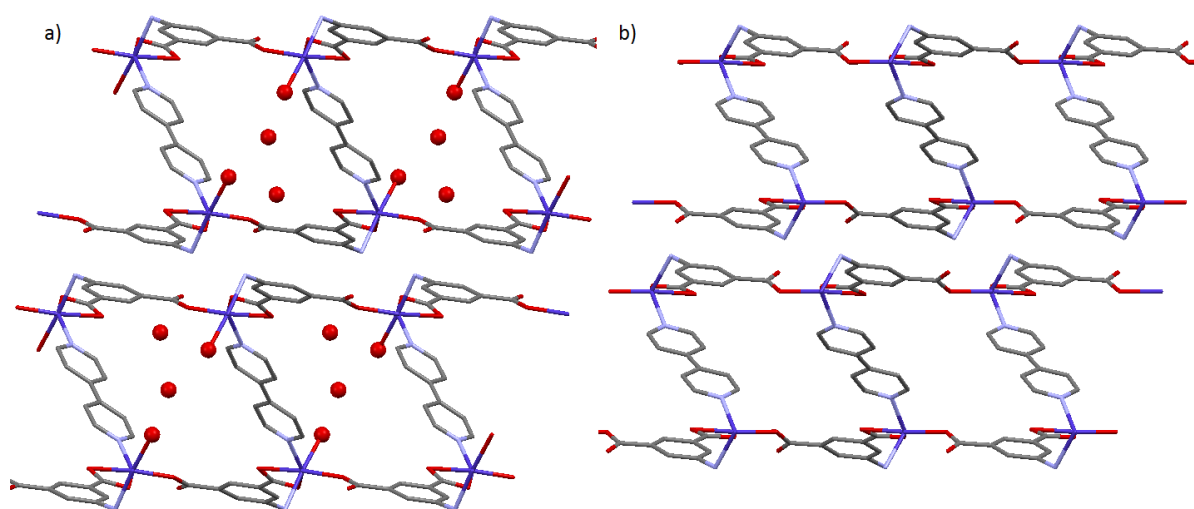


Figure 1.18. $\text{Co}(5\text{-NH}_2)_2\text{BDC}(\text{bpy})_{0.5}$ viewed along the *b*-axis: a) the hydrated form; b) the dehydrated form, where the twisting of the bpy ligands is visible.

Ligands do not have to twist to induce a structural change; other mechanisms are possible, such as a switch of a stereochemical centre. Reported in 2013, $[\text{Zn}_2(\text{bpeb})(\text{obc})_2] \cdot 2\text{DMF} \cdot \text{H}_2\text{O}$ (bpeb = 1,4-bis[2-(4-pyridyl)ethenyl]benzene; obc = 4,4'-oxybisbenzoate) can be prepared solvothermally from zinc nitrate tetrahydrate and the ligands dissolved in DMF, DMSO and water, and consists of two-dimensional layers of zinc and obc pillared by bpeb ligands in the direction perpendicular to the layers (Figure 1.19).⁵² As-synthesised, the interlayer bpeb ligands have a *trans-cis-trans* conformation and the pores are occupied by DMF. Upon soaking the MOF in methanol, the bpeb ligands isomerise to the *trans-trans-trans* conformation, which reduces the cell volume by 6.1 %. This single-crystal-to-single-crystal transformation is accompanied by a blue-shift in the MOF's solid-state emission spectrum, allowing it to be easily detected. Soaking the crystals in DMF reverses the stereochemical switch of the bpeb ligands and restores the original MOF structure.

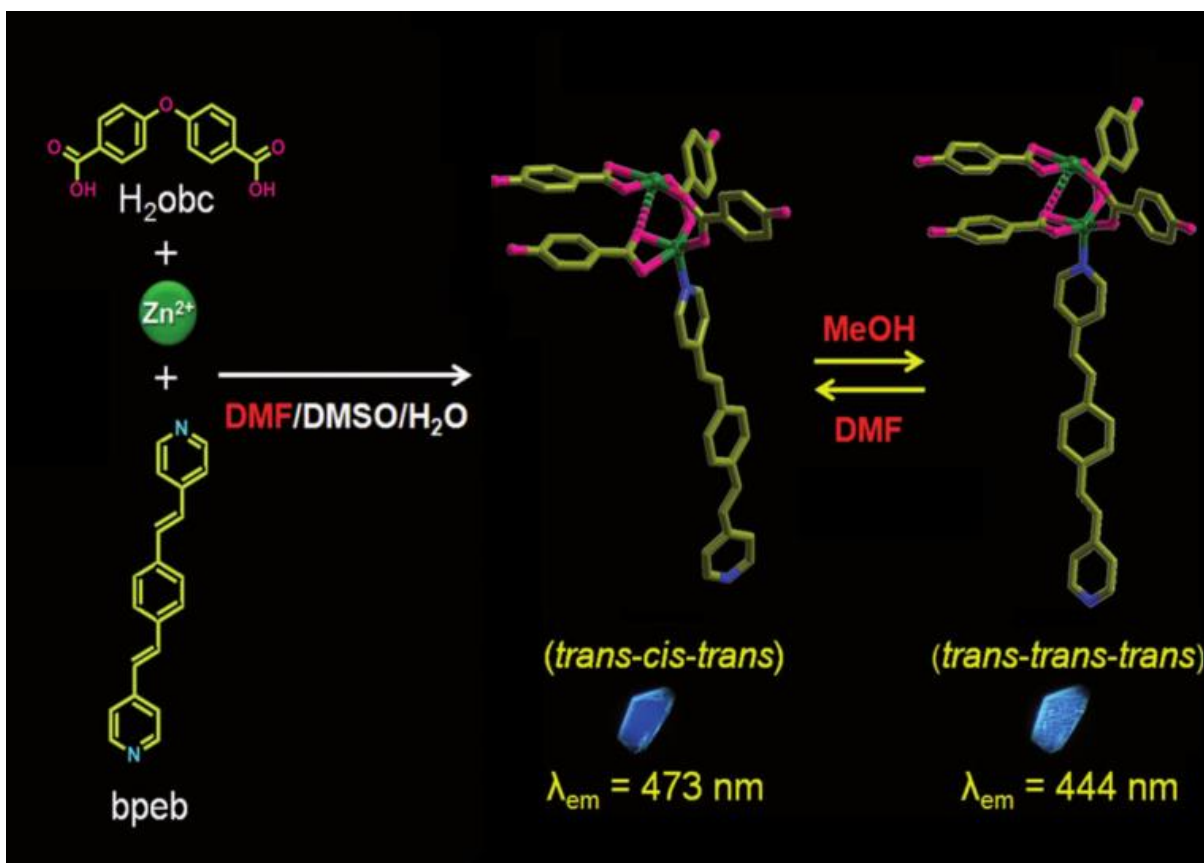


Figure 1.19. The synthetic route to $[\text{Zn}_2(\text{bpeb})(\text{obc})_2] \cdot 2\text{DMF} \cdot \text{H}_2\text{O}$ and a scheme showing the structural change that occurs upon soaking in methanol, and the solid-state emission wavelength for each isomer. The motion of the bpeb ligands is referred to in the article as “pedal-motion”. Image reproduced from reference 52 with permission of Wiley-VCH.

Another interesting two-dimensional flexible MOF worth highlighting was reported by Kitagawa *et al.* in 2009.⁵³ The MOF comprises layers of cadmium and pzdc (2,3-pyrazinedicarboxylate), and pillaring ligands which contain two hydrogen bonding sites, arranged such that when the MOF is evacuated at 383 K, its pores are locked, with the hydrogen-bonding pillars acting as gates (Figure 1.20). Exposure to water vapour at room temperature for 6 hours causes the pillars to rotate, unlocking the pores and allowing inclusion of water molecules. This is a good example of a molecular gate, where a structure is locked in its closed-pore form until a certain set of criteria are reached, at which point the pores are opened and fully accessible.

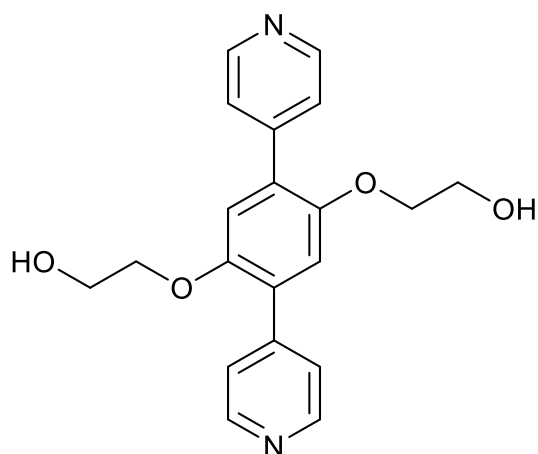


Figure 1.20a. The structure of the pillaring ligand used by Kitagawa *et al.* in the construction of a gated MOF.⁵⁴ The hydroxyl groups act as hydrogen bond donors and acceptors, and the ligand is coordinated to the cadmium centres *via* the nitrogen atoms.

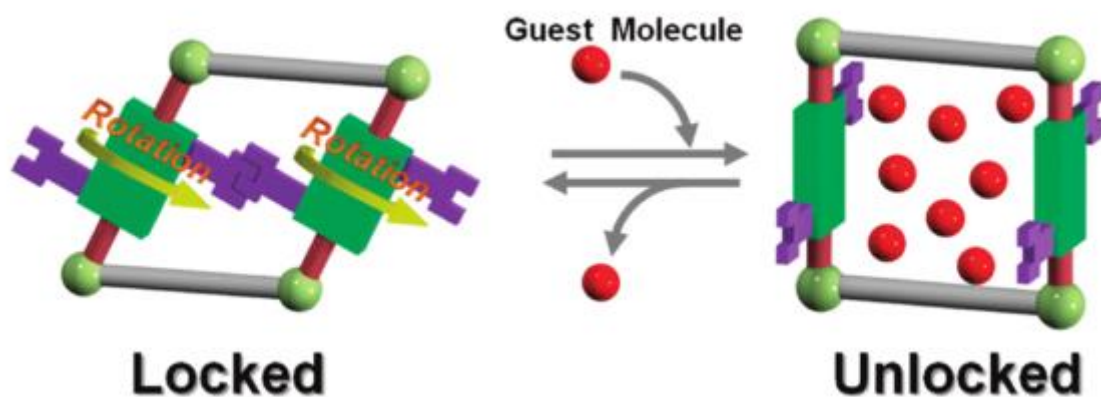


Figure 1.20b. The gate mechanism of the pillaring ligands, opened and closed by rotation of the ligand about its long axis, upon water ad/desorption. Image reproduced from reference 53 with permission of the American Chemical Society.

Flexibility in layered materials is not limited to those with pillared structures, it can also occur in structures with layers stacked *via* intermolecular interactions. $[(\text{NiL}_{\text{allyl}})_2(\text{BuTC})] \cdot 2\text{DEF} \cdot 2\text{H}_2\text{O}$, reported in 2013, contains two-dimensional layers which are intercalated by water and DEF molecules (Figure 1.21).⁵⁴ Heating at 100 °C under vacuum for 7 hours removed the guests and resulted in a collapse in the direction perpendicular to the layers, allowing them to stack together *via* interdigitation of the terminal alkene chains.

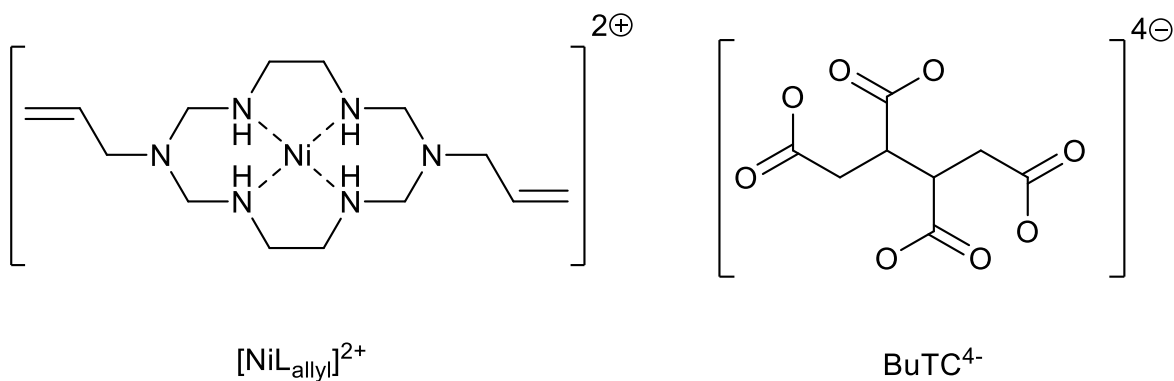


Figure 1.21a. The structures of the subunits that comprise $[(\text{NiL}_{\text{allyl}})_2(\text{BuTC})] \cdot 2\text{DEF} \cdot 2\text{H}_2\text{O}$.

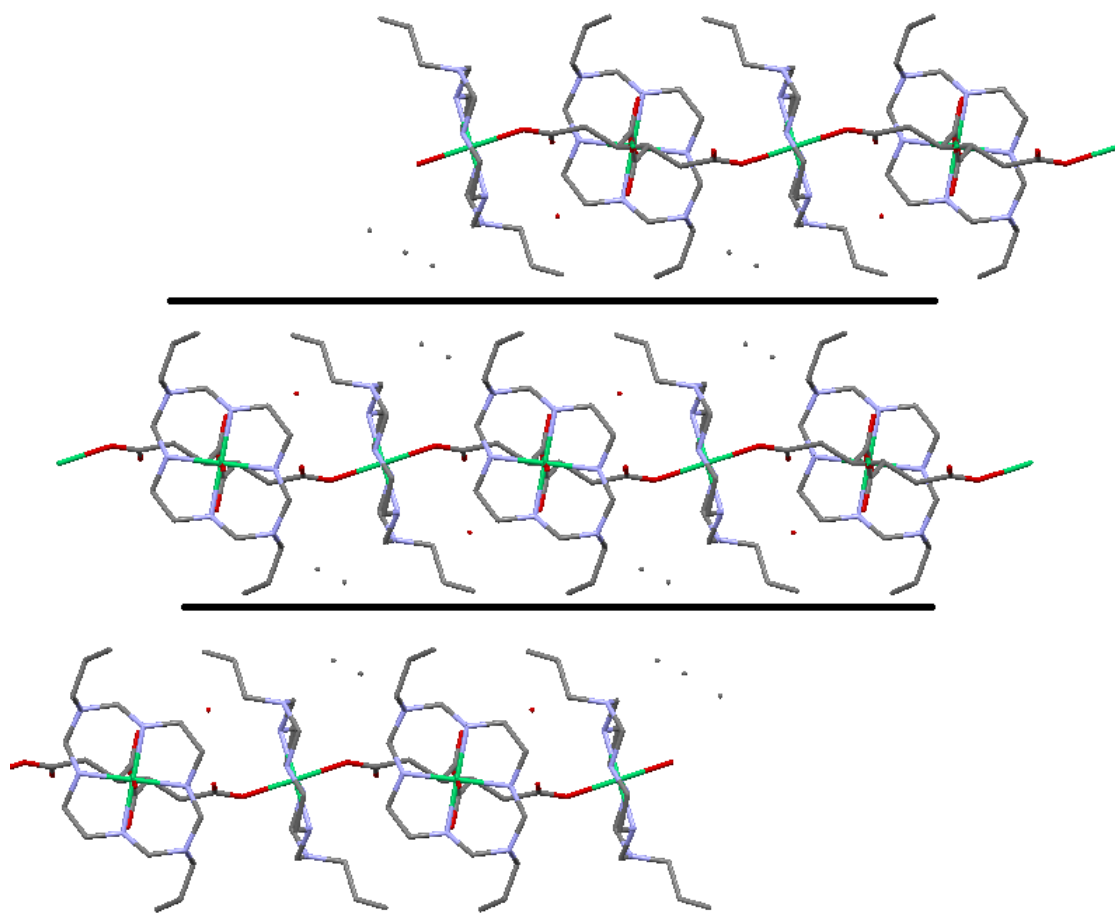


Figure 1.21b. Crystal structure of $[(\text{NiL}_{\text{allyl}})_2(\text{BuTC})] \cdot 2\text{DEF} \cdot 2\text{H}_2\text{O}$. Hydrogen atoms have been omitted for clarity; black lines separate the layers.

1.3.5. Advantages of Flexible MOFs

Section 1.2 made brief mention of a number of rigid metal-organic frameworks currently available for commercial application by the company BASF (Badische Anilin und Soda Fabrik).^{5,35,36} Flexible metal-organic frameworks, however, are still a relatively recent discovery; and therefore at the time of

writing there are no examples of flexible MOFs being used in commercial applications. Nevertheless, MOFs which exhibit dynamic behaviour often afford unique behaviours not observed in rigid frameworks, which could be commercially relevant. Some examples have already been mentioned in this document are: the negative thermal expansion exhibited by $\text{Zn}_2(\text{BDC})_2(\text{DABCO})^{50}$ (*c.f.* Section 1.3.3, Figures 1.14 – 1.17); and the molecular gating phenomenon reported by Kitagawa *et al.* in 2009⁵³ (*c.f.* Section 1.3.4, Figure 1.20).

One of the widely accepted advantages of flexible MOFs over their rigid counterparts is gas separation.²⁵ A flexible MOF which exists in a closed-pore state may exhibit a gate-opening phenomenon upon exposure to CO_2 , but not upon exposure to nitrogen or methane, and therefore appears to be selective for CO_2 . However, in a mixed gas stream, once the framework is opened it is likely to adsorb any small molecules present, and therefore is unlikely to achieve sufficient gas separation for industrial applications.²⁵ Solutions to this problem are possible; in 2018, Taylor *et al.* reported essentially complete separation of CO_2 from CH_4 , in a 50/50 mixture of the two gases at pressure of up to 15 bar, by the framework $\text{Co}(\text{bdp})$.⁵⁵ The success of this material is due to the closed-pore, activated framework expanding to form a CO_2 clathrate, rather than exhibiting a “full” gate-opening effect.

Another useful behaviour is the ability to adopt different activated states. Sakata *et al.* demonstrated this phenomenon in 2013, in the framework $\text{Cu}_2(\text{bdc})_2(\text{bpy})$.⁵⁶ Removing the guest (DMF, methanol or ethanol) induces pore-closure, which can be reversed by re-introducing the guest. However, when the crystalline samples were downsized to *ca.* $700 \times 700 \times 80 \text{ nm}^3$, removal of the solvent guest led to the formation of metastable, open-pore, evacuated crystals. These metastable states could be converted into the expected closed-pore evacuated phase by heating. In crystals of size $\leq 300 \text{ nm}$, the open-pore, evacuated phase could not be converted into the closed-pore phase by heating. This highlights that crystal size can have drastic effects on flexibility, and also that it is possible to switch flexibility on and off by non-chemical methods. The concept of multiple evacuated states will be discussed in more detail in Section 1.5, and in chapters 2 and 3.

Flexibility can also be utilised to initiate self-assembly.⁵⁷ By controlling the spatial distribution of **MIL-88A** crystals on a polymer film, Troyano *et al.* were able to direct the self-assembly of various 3D architectures, including a mechanical gripper and a walking device. Utilising framework swelling in this way could have applications in the fabrication of MOF-based devices for industrial uses.⁵⁷ The same authors demonstrated a similar concept by using the swelling behaviour of **Mil-88A** to fabricate a self-folding polymer composite film, where the degree of folding can be controlled by controlling the relative humidity.⁵⁸

Flexibility can also enhance the tunability of a framework. In 2019, Katsoulidis *et al.* reported a chiral peptide-based framework, ZnGGH (GGH = glycine-glycine-L-histidine), in which flexibility affords nine distinct structures.⁵⁹ These multiple structures are possible due to the flexibility of the tripeptide linker, and chemical control of the linker conformation can trigger guest uptake by modification of the pore geometry. Modification of pore geometry has been shown previously by the same authors, in another peptide-based MOF, ZnCar (Car = carnosine).⁶⁰ In this, example, the material is able to adopt different pore shapes as a response to either water (square-shaped pores) or methanol (parallelogram-shaped pores) guest molecules. This guest-adaptation is induced by the formation of host-guest hydrogen-bonding interactions.⁶⁰

Perhaps the most counter-intuitive behaviour afforded by flexibility is negative gas adsorption. In 2016, Krause *et al.* reported such behaviour in the MOF **DUT-49** (DUT = Dresden University of technology), where a spontaneous, large-scale release of gas occurs from the framework during gas adsorption experiments where pressure is increasing.⁶¹ **DUT-49** adsorbs methane and *n*-butane, forming a metastable state, with large pores and a high energy barrier to the more stable, closed-pore conformation. Overcoming the activation energy occurs due to the higher affinity of the guest for the smaller pores in the closed pore structure, and is accompanied by an overall reduction in pore volume of 61 %. This effect is reproducible, and occurs with a defined temperature and pressure range.⁶¹ This behaviour, along with the other behaviours listed in this section, are only possible due to the flexible nature of the frameworks and/or their component parts, highlighting the importance of flexible MOF research in developing new methodologies and discovering new phenomena.

1.4. Rational Design

1.4.1. The Synthetic Challenge

The main challenge in the preparation of flexible MOFs is the same challenge trying to be solved in the field of crystal engineering: the logical design of a crystalline system from picking specific starting materials.^{1,62-64} MOFs are constructed from metal-ligand coordination bonds, which are relatively strong, making them slightly easier to design than systems involving relatively weak intermolecular interactions. Even so, the preparation of MOFs is not so simple as putting subunits together to make a larger structure, hence the wide range of synthetic conditions required to produce the so-called IRMOF series (IRMOF = isorecticular MOF – **MOF-5** analogues with different metals or functionalised ligands).⁶⁵ Flexible MOFs are even more difficult to design, as a component which is flexible will usually be able to form a number of different crystalline structures, of which only one (if any) will be the desired flexible MOF. It is therefore useful to understand how changing the node or linker can affect the flexibility of the material as a whole.

1.4.2. Choice of Metal

Section 1.3.3 revealed how the choice of metal centre can radically change the dynamic behaviour of a MOF, in the case of M(BDP) (where M = Co, Zn, Ni). Changing the metal centre has also been shown to drastically alter the selectivity of certain MOFs for different guests. In early 2016, a series of honeycomb MOFs with the formula (H₂dab)[M₂(ox)₃] (H₂dab = 1,4-diammonium butane; M = Fe^{II}, Co^{II}, Ni^{II}, Zn^{II}, Mg^{II}; ox = oxalate) were reported, which show guest-dependent flexibility.⁶⁶ When exposed to a positive pressure of water, all MOFs form a dihydrate structure, and all but the nickel framework will further adsorb water to form a hexahydrate structure. When methanol is used, however, all MOFs adsorb four molecules per formula unit, although this occurs much more readily (at lower pressure) in the cobalt and nickel frameworks compared to the iron framework, with the behaviour of the magnesium and zinc frameworks lying between the former and latter. Upon exposure to ethanol, the cobalt, nickel and zinc frameworks all formed trisolvates under a relative pressure (P/P₀) of around 0.4, but the iron and magnesium frameworks did not adsorb any ethanol. The reason provided for the ethanol selectivity relates to the hardness of the metal ions (Co^{II}, Ni^{II} and Zn^{II} have a

more covalent character than Fe^{II} and Mg^{II} , and therefore have a less rigid coordination geometry). However, this is not rationalised mechanistically and does not explain the water or methanol adsorption behaviour. Nevertheless, this study shows that guest-selectivity in MOFs depends heavily on the nature of the framework metal ion.

Oxidation state can also affect flexibility. **COMOC-2** (Center for Ordered Materials, Organometallics and Catalysis, Ghent University) is a V^{IV} -based MOF which displays flexibility upon CO_2 and hexane adsorption.⁶⁷ When a mixed oxidation state analogue (**COMOC-2(V^{IV}/V^{III})**) is used, the structure is not as readily flexible. In contrast, **MIL-47** displays no structural flexibility, despite containing V^{IV} nodes and having a similar structure.⁴² **MIL-47** has an analogous topology to **MIL-53**, but has V^{IV} -oxide, rather than Cr^{III} -hydroxide chains running throughout its structure, and was originally thought to be rigid due to presence of V^{IV} -oxide chains (rather than Cr^{III} -hydroxide chains as found in **MIL-53**). However **COMOC-2** has V^{IV} -oxide chains, and flexes in a manner typical for a wine-rack MOF, so there is still some uncertainty regarding the effect of metal oxidation state on framework flexibility.

Perhaps the most straightforward method to achieve flexible metal centres is to remove directionality and coordination preferences as much as possible. For this, large d^{10} metal centres are the obvious choice. Early in 2016, a flexible, two-fold interpenetrated, indium-based MOF was reported by Hong *et al.*⁶⁸ Interestingly, the ligand is a tetratopic carboxylate TCPBDA⁴⁻ (Figure 1.22) which creates an anionic framework. It is stated that the charge is balanced by MeNH_3^+ ions generated by the decomposition of DMF, however solvothermal decomposition of DMF is known to produce Me_2NH_2^+ ,⁶⁹ and this is well documented in the literature. Upon adsorption of CO_2 , the framework undergoes an irreversible transition accompanied by a significant volume increase.

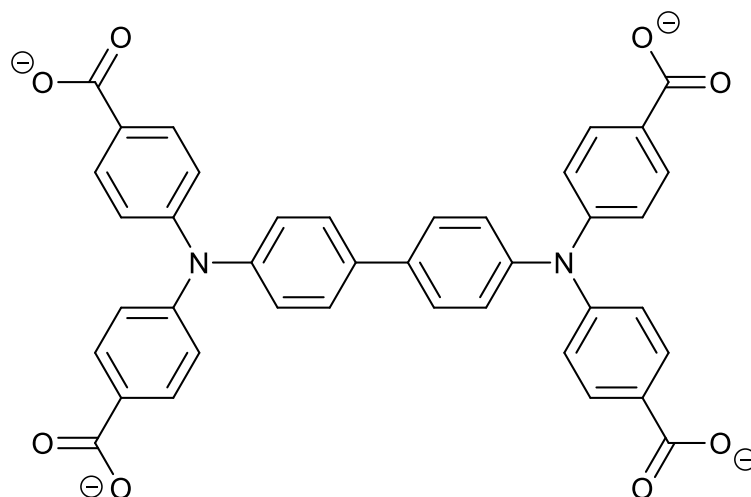


Figure 1.22. The structure of TCPBDA⁴⁻. Rotation about the long axis provides part of the mechanism for flexibility in the framework [In(TCPBDA)]⁻.

The mechanism of flexibility in the MOF has two main components. Firstly, the ligand rotates about its long axis so that the two N(PhCO₂)₂ motifs are almost perpendicular (95°). This results in an apparent flattening of the pseudo-tetrahedral geometry around the indium centre, although it should be noted the bond lengths, angles and atomic positions of the In(O₂CR)₄ SBU remain essentially unchanged. Secondly, the interpenetrated networks shift relative to each other to maximise the surface area available to guest species (Figure 1.23).

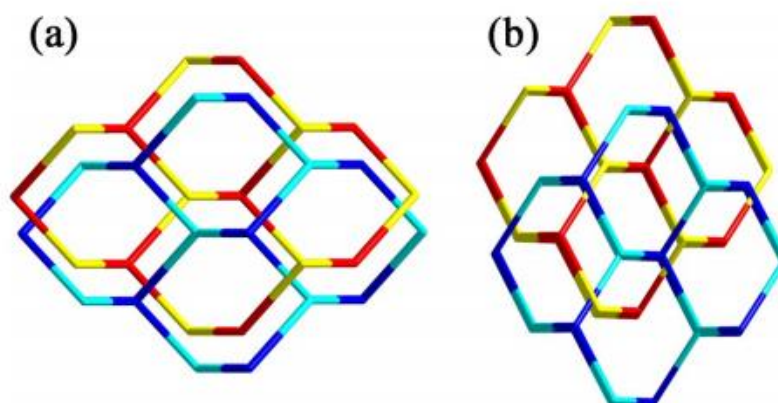


Figure 1.23. A schematic of the interpenetrated networks in [In(TCPBDA)]⁻: a) before CO₂ adsorption, in the closed form; b) the open form, after CO₂ adsorption. Image reproduced from reference 68 with permission of the Royal Society of Chemistry.

With a hydrogen uptake value of 1.80 wt% at 77 K (*c.f.* 1.95 wt% **HKUST-1**), this MOF highlights the potential for flexible MOFs to compete with their rigid analogues in the realm of real-world applications.

1.4.3. Ligand Functionalisation

Besides choosing a suitable node, another way to fine-tune the flexibility of a MOF is to introduce functionality to the ligand. This can be achieved either by direct synthesis (*e.g.* a solvothermal reaction between a metal salt and a functionalised ligand) or by post-synthetic modification (PSM). As Cohen explained in an extensive review, using PSM allows a known MOF to be further modified and often creates synthetic routes to frameworks which are otherwise inaccessible.⁷⁰

Introducing functionality to **MIL-53** has been shown to have profound effects on the MOF flexibility. By comparing the MOF series **Al-MIL-53-X** (where **Al-MIL-53** is the aluminium analogue of **MIL-53**, and **X** = CH₃, NH₂, NO₂, Cl, Br, and (OH)₂ attached to the terephthalate ligand), Stock *et. al.* found that low pressure N₂ adsorption values increased in the following trend: (OH)₂ < Br < Cl ≈ CH₃ < NO₂ < NH₂.⁷¹ These were all lower than the uptake value for the parent **Al-MIL-53** MOF. With the exception of (OH)₂, this result is exactly as expected, considering N₂ adsorption depends on the pore volume available, and this increases in the same trend due to functional group size. Interestingly, however, the CO₂ adsorption isotherms did not follow the same trend. Firstly, **Al-MIL-53-Cl** showed a higher adsorption than the methyl-substituted analogue. Secondly, whilst the **Al-MIL-53-NH₂** showed the highest CO₂ adsorption value at lower pressure, from around 0.5 bar onwards the NO₂-substituted MOF displays the largest CO₂ uptake. The fact that this adsorption occurs more gradually than the other materials indicates that it requires a higher pressure of CO₂ to be active. Additionally, CO₂ adsorption for the Br-substituted MOF is just below that of the CH₃-substituted MOF over the whole pressure range, whilst the difference in their N₂ isotherms is much greater. These results indicate that adsorption CO₂ adsorption increases when using smaller, more electron-rich functional groups. The iron analogue of **MIL-53** has also been investigated for functionalisation by Férey *et. al.*⁷² The parent MOF, **Fe-MIL-53**, was compared with the series **Fe-MIL-53-X** where **X** = NH₂, (CO₂H)₂, Cl, Br and CH₃. The amine and carboxylic acid functionalised

MOFs didn't exhibit any structural change upon exposure to 11.0 bar CO₂, and at pressures below 1.0 bar, the other three functionalised MOFs displayed similar CO₂ adsorption levels, which were higher than the non-functionalised MOF. At higher pressures, however, the non-functionalised MOF adsorbed more CO₂, and all the iron MOFs studied exhibited lower CO₂ adsorption levels than the original chromium-based **MIL-53** discussed in Section 1.3. The lack of CO₂ adsorption in the cases of the NH₂- and (CO₂H)₂-functionalised MOFs is attributed to strong hydrogen-bonding interactions between ligand functional groups and μ_2 -bridging hydroxides. The different CO₂ adsorption behaviours between **Al-MIL-53-NH₂** and **Fe-MIL-53-NH₂** can be explained by considering the metal centre. When the metal is more electropositive, the adjacent μ_2 -OH groups are able to interact more strongly with the ligand functional groups, and this inhibits the flexibility and sustains the closed-pore form. This has been shown by Gascon *et. al.* by comparing the series **M-MIL-53-NH₂** where **M** = Al, Ga, In.⁷³ Gascon *et. al.* have also used PSM to introduce bulky functional groups into **Al-MIL-53-NH₂**, by anchoring diphenylphosphine oxide onto the amine substituent to create **Al-MIL-53-NHP(O)Ph₂**.⁷⁴ Unsurprisingly, adding such a sterically bulky group reduced the pore volume and dramatically reduced the level of CO₂ the MOF could adsorb.

Adding steric bulk to the SBU has also been shown by Kaskel *et. al* to inhibit flexibility.⁷⁵ The zinc pinwheel MOF **JLU-Liu4** (JiLin University) was investigated. The original structure has two formate ligands per SBU, and loses 60 % of its cell volume upon dehydration. By using acetate, benzoate and cinnamate in place of the formate ligands, they were able to reduce the degree to which the structure closed upon dehydration (Figure 1.24). With formate or acetate ligands, the structure adopts a closed-pore phase upon dehydration, which is reflected in the step observed in the CO₂ adsorption isotherms (*c.f.* **MIL-53**³⁹). However, when the larger benzoate or cinnamate ligands are used, the structure is too sterically congested to adopt a closed-pore phase, and CO₂ adsorption occurs at around 0 bar without a stepped isotherm.⁷⁵

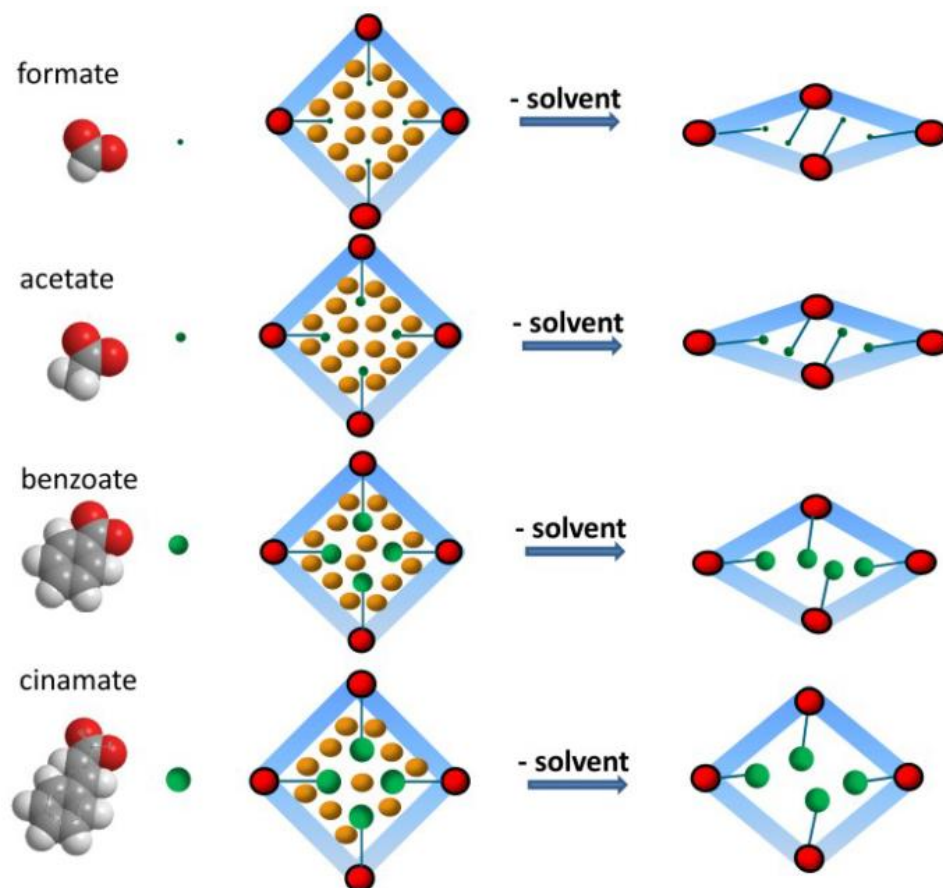


Figure 1.24. A schematic of the flexibility observed for the zinc pinwheel MOF investigated by Kaskel *et al.*⁷⁵ The flexibility correlates directly with the size of the monocarboxylate ligand used. Image adapted from reference 75 with permission of the Royal Society of Chemistry.

It is obvious that adding steric bulk to the pore of a MOF will reduce the available space for guest accommodation and/or dynamic movement of the framework. Unfortunately, the opposite effect is desired, and appears to be significantly harder to achieve. The reason for this is that most flexible MOFs are constructed from small, simple ligands, and adding functionality goes hand-in-hand with adding bulk. It seems that the best approach is to incorporate ligands with electron-rich substituents, which could increase the ability of a MOF to adsorb CO₂ whilst not being so large as to inhibit flexibility or guest uptake.

1.5. SHF-61

SHF-61 (SHF = Sheffield Framework) is an indium-based metal-organic framework whose dynamic behaviour was reported by Carrington *et al.* in 2017.⁷⁶ The material was first reported in

2012 by Yuan *et al.*, but the original authors did not report any dynamic behaviour and used the material solely for gas uptake purposes.⁷⁷ The relevant discussion points from the original 2012 publication were re-addressed in the 2017 publication by Carrington *et al.*, and so the following paragraphs are concerned only with the latter article, unless otherwise stated.

The secondary building unit of **SHF-61** consists of an eight-coordinate indium(III) centre, surrounded by four bidentate carboxylates in pseudo-tetrahedral arrangement (Figure 1.25a). Each indium centre is connected to four other indium centres *via* ditopic aminoterephthalate ($\text{NH}_2\text{BDC}^{2-}$) ligands, forming a diamondoid-type network, and two such networks interpenetrate to form the MOF structure (figure 1.25b). The framework carries an anionic charge, which is balanced by the presence of one dimethylammonium cation *per* indium centre, generated *in situ* by the decomposition of DMF (dimethylformamide) during the synthesis.^{70,76}

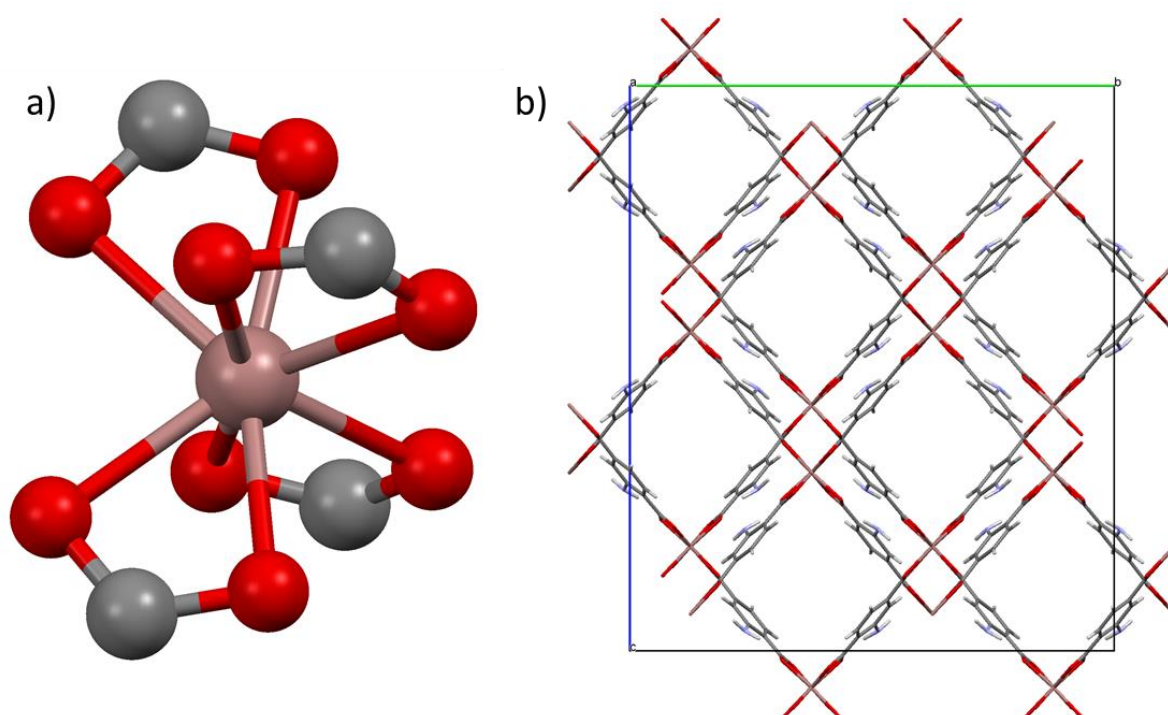


Figure 1.25. a) The eight-coordinate, pseudo-tetrahedral SBU of **SHF-61** – pink = In, red = O, grey = C; b) The doubly interpenetrated structure of the MOF, viewed along the *a*-axis. Note the rhombus-shaped channels running through the structure.

The as-synthesised MOF, **SHF-61-DMF**, resides in the orthorhombic space group *Fddd*, with cell parameters $a \approx 15.1 - 15.3 \text{ \AA}$, $b \approx 26 - 27 \text{ \AA}$ and $c \approx 31 - 32 \text{ \AA}$ (variable due to dynamic nature of the

material), and a combination of DMF and water molecules (1.75 and 1.25 molar equivalents, respectively) residing in its rhombus-shaped channels (these channels also host the dimethylammonium counter-ions). Heating the material at 150 °C for 15 minutes, and then cooling to room temperature causes a phase change *via* a closing of the channels as the solvent molecules are removed (Figure 1.26). The space group is retained throughout this process, but the cell parameters change drastically: $a \approx 14.8 - 14.9 \text{ \AA}$; $b \approx 20 - 22 \text{ \AA}$; $c \approx 34 - 35 \text{ \AA}$. This pore-closure causes a reduction of *c.a.* 13 % in the unit cell volume (*ca.* 13100 Å³ to *ca.* 11000 Å³). It should be clarified that these cell parameters are approximate representatives, as the specific values vary slightly between batches. Not only is this a single-crystal-to-single-crystal transition, but it is also visible macroscopically as a change in crystal shape and dimensions (Figure 1.27). There are two component mechanisms that cause this flexibility. The largest component is a rotation about the O...O vector of the linker carboxylates (the so-called “knee-cap”); two MOFs which display this mechanism have been discussed previously, **MIL-53** and Zn₂(BDC)₂(DABCO).^{39,50} The second component to the flexibility is a distortion of the indium coordination sphere, resulting in a flattening of the pseudo-tetrahedral geometry. Whilst this component is a smaller contributing factor than the former mechanism, it is still a much larger contributor than in most flexible MOFs (*c.f.* [In(TCPBDA)]-⁶⁸ Section 1.4.2, shows essentially no change of coordination sphere), and emphasises the point made in Section 1.4.2, that large d¹⁰ metal centres are suitable candidates for the construction of flexible MOFs. Given the diamondoid-type interconnectivity of **SHF-61**, flexibility might be expected in all three dimensions. However, the change in the *a*-axis is much smaller than in the *b*- and *c*-axes, due to hydrogen-bonding interactions between the amino-substituents of the two networks “locking” the structure in the *a*-direction (Figure 1.28), so the material behaves similarly to a wine-rack-type MOF.⁷⁶

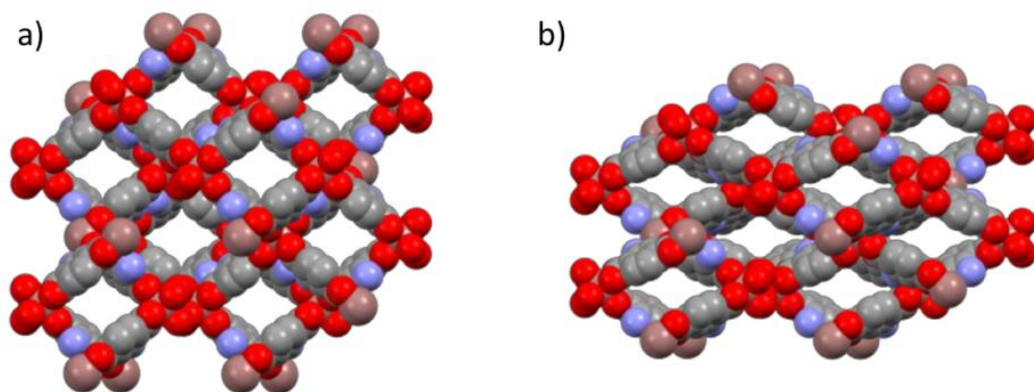


Figure 1.26. A view along the channels (*a*-direction) of the crystal structures of **SHF-61-DMF** before solvent removal (a) and after solvent removal (b). Images reproduced from reference 76 with permission of Nature Publishing Group.

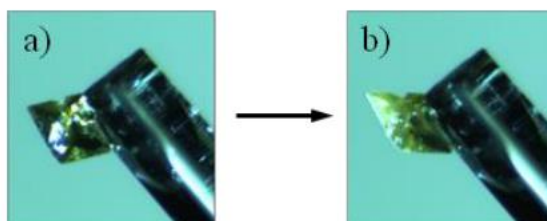


Figure 1.27. Images of a single crystal of **SHF-61** before solvent removal (a) and after solvent removal (b). Images reproduced from reference 76 with permission of Nature Publishing Group.

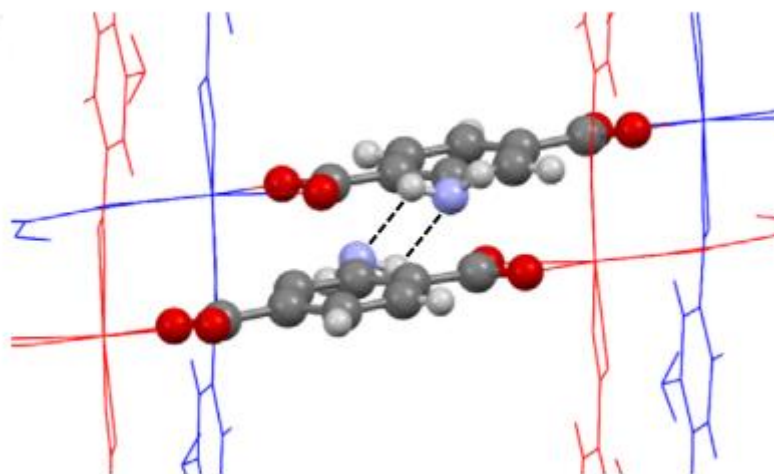


Figure 1.28. The hydrogen-bonding interactions between the amine substituents of the different networks in **SHF-61**, which prevent large-scale flexibility in the *a*-direction. Images reproduced from reference 76 with permission of Nature Publishing Group.

Interestingly, the flexibility that occurs upon solvent removal is *continuous*. Most flexible MOFs exhibit *discrete* flexibility, *i.e.* they have (usually) either open or closed channels, depending on whether they are filled or empty. However, **SHF-61-DMF** adopts a continuous range of states between open and closed as it is desolvated (Table 1.2).

Temperature / °C	<i>a</i> / Å	<i>b</i> / Å	<i>c</i> / Å	<i>V</i> / Å ³
25	15.460(7)	27.214(6)	31.029(6)	13055(8)
40	15.553(6)	26.88(1)	31.244(7)	13062(9)
60	15.21(1)	23.77(1)	33.61(1)	12147(12)
80	15.22(1)	23.45(1)	33.847(9)	12079(10)
100	15.182(8)	22.991(7)	34.116(7)	11909(8)
120	15.142(8)	22.235(13)	34.53(2)	11624(11)

Table 1.2. The cell parameters for **SHF-61** during DMF removal. “Temperature” refers to the temperature the sample was heated to *prior* to data collection; all data were recorded at 298 K. Table reproduced from reference 76.

If the desolvated, closed-pore material is left in air under ambient conditions, it adsorbs atmospheric water and the channels re-open gradually as it does so (Figure 1.29), further highlighting the continuous flexibility of the material.

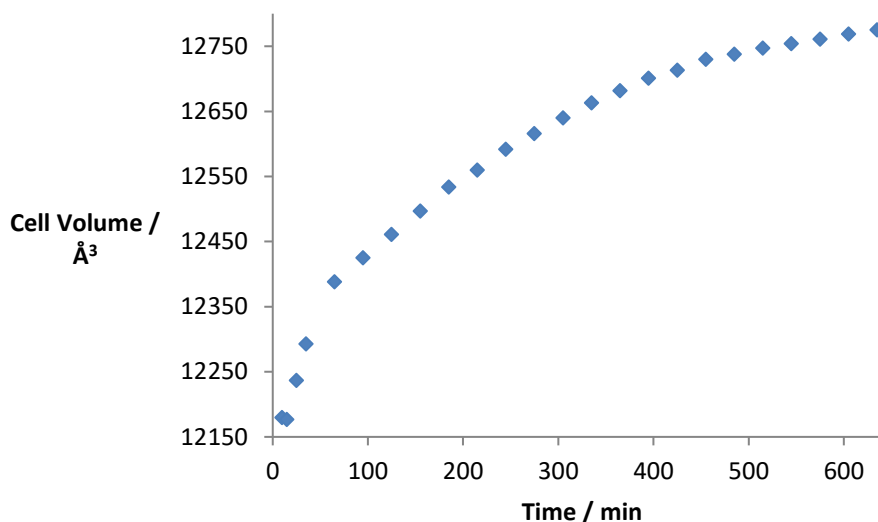


Figure 1.29. The cell volume of **SHF-61** recorded on a sample exposed to ambient moisture, after increasing periods of time. Data extracted from reference 76.

Another remarkable property of **SHF-61** results from solvent-exchange. The DMF/H₂O in the MOF channels can be replaced with chloroform (to form **SHF-61-CHCl₃**) simply by immersing crystals of **SHF-61-DMF** in liquid chloroform. However, when the material is subsequently heated to remove the chloroform, the unit cell volume remains approximately constant (very slight increase). In other words, the MOF retains its open-pore form. It is relatively common for a MOF to have a number of accessible pore states which are guest-dependent; for example, **MIL-53solv** (DMF containing) and **MIL-53lt** (water containing) have different unit cell dimensions (*c.f.* section 1.3.1, Table 1.1).³⁹ However, to the best of our knowledge, **SHF-61** is the only material known to have guest-dependent flexibility, where the choice of guest affects whether or not the pores close or remain open upon guest removal.⁷⁶

Uniquely to this material, gas uptake can be performed on both the open- and closed-pore versions of the activated framework. Volumetric nitrogen isotherms at 77 K confirm that activated **SHF-61-DMF** has closed pores (essentially no uptake) and that activated **SHF-61-CHCl₃** has open pores (significantly higher uptake).⁷⁶ The results are similar in the case of carbon dioxide uptake at room temperature, in that total uptake is almost three times higher in the case of the open-pore form (*c.a.* 6 mmol g⁻¹) than in the closed-pore form (*c.a.* 2 mmol g⁻¹). Interestingly, both isotherms follow a type I

profile, which is typical for a rigid, microporous material (Figure 1.30). These two pieces of information indicate that carbon dioxide uptake does not cause the closed-pore form of the framework to open. The 2012 publication by Yuan *et al.* reported that the open-pore form of the material takes up essentially no methane at 298 K at pressures up to 30 bar,⁷⁷ but Carrington *et al.* found that both the open- and closed-pore forms of the material adsorb methane at pressures of less than 5 bar (Figure 1.30).⁷⁶

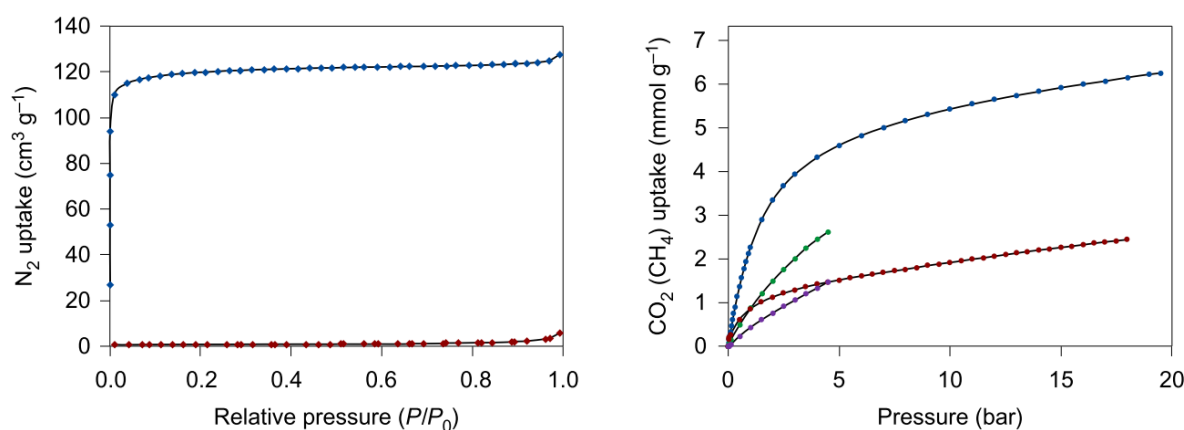


Figure 1.30. Left: Volumetric N₂ adsorption isotherms for **SHF-61** at 77 K; red = activated from DMF, blue = activated from CHCl₃. Right: Gravimetric adsorption isotherms at 298 K for **SHF-61** activated from DMF (red = CO₂, purple = CH₄) and from CHCl₃ (blue = CO₂, green = CH₄). Image reproduced from reference 76 with permission of Nature Publishing Group.

In another series of experiments, Carrington *et al.* performed carbon dioxide uptake experiments at 298 K on partially-desolvated samples of **SHF-61-DMF** with approximately one third of the solvent content removed.⁷⁶ Interestingly (and unlike in the fully-desolvated materials), the gravimetric isotherm shows a gated profile, indicating that adsorption occurs as normal (type I) until the gate pressure (*ca.* 7 bar), at which point the material is converted to the open-pore form and henceforth adsorbs a much larger quantity of carbon dioxide. *In situ* powder diffraction studies elucidate this process in detail, showing that the pore opening process is the reverse of the closing process that occurs upon desolvation (*i.e.* the *b*-axis expands and the *c*-axis contracts upon gas uptake, whilst the *a*-axis changes relatively little). Furthermore, the process is reversible; as the gas is desorbed, the

pores close again, showing a small hysteresis both in the isotherm and the diffraction experiment. This information is summarized in Figure 1.31.

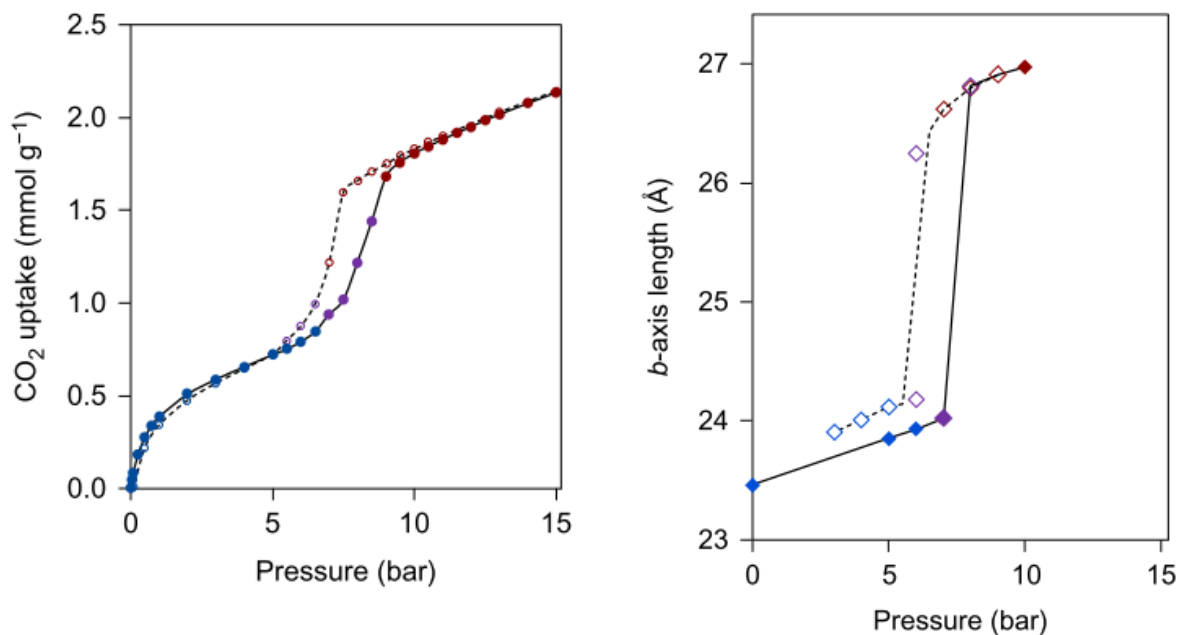
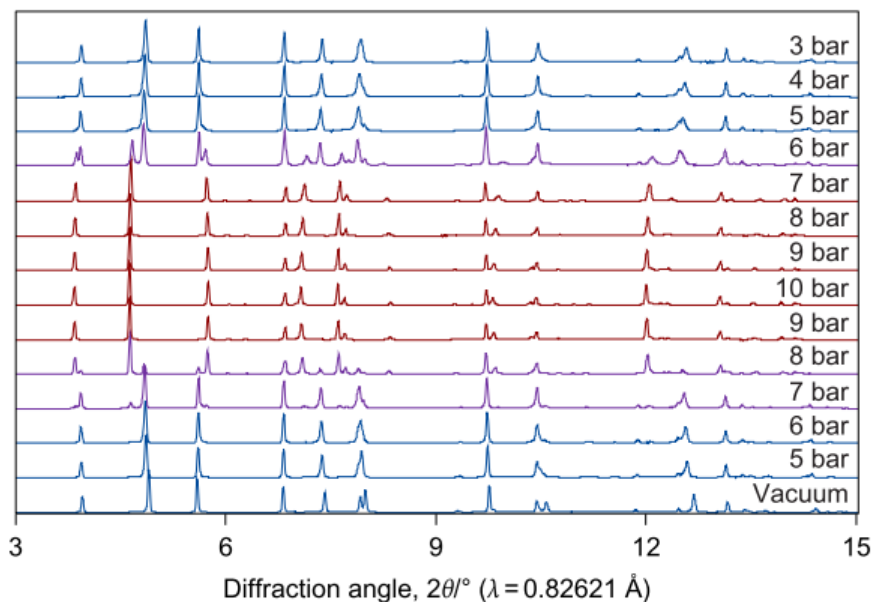


Figure 1.31a. Left: gravimetric CO₂ isotherm for partially-desolvated **SHF-61-DMF** at 298 K. Right: profile of the *b*-axis as a function of pressure. Images reproduced from reference 76 with permission of Nature Publishing Group.



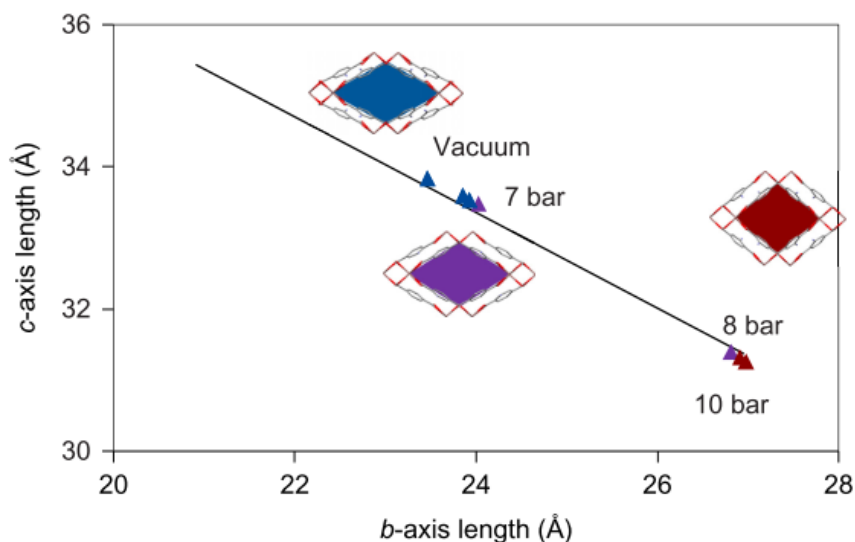


Figure 1.31b. Top: powder diffraction patterns of partially desolvated **SHF-61-DMF** during carbon dioxide adsorption experiment. Bottom: plot of the *b*- and *c*-axes, showing the extent of the wine-rack-type flexibility. Images reproduced from reference 76 with permission of Nature Publishing Group.

Carrington *et al.* proposed that the behaviour of the material originates from guest-framework and cation-framework interactions.⁷⁶ DMF and H₂O are likely to interact strongly with the pore surface of the material due to the polar nature of the amine and carboxylate components. As these guests are removed, in order to maintain their interactions with the framework, the framework pores must narrow. This explains why partial desolvation from DMF/H₂O leads to a partial pore-closure. The strange behaviour upon CO₂ uptake can be explained by cation-framework interactions. In the case of the closed pore material, it was proposed that the dimethylammonium cations act as bridges between the walls of the MOF channels. Since CO₂ is likely to interact less strongly with the framework by comparison, its adsorption is not sufficient to break these framework-cation-framework bridges and allow the framework to open. However, in the partially desolvated material, no such cation-bridges exist, and the material is free to expand to accommodate more CO₂ once a sufficient gate pressure has been reached. Figure 1.32 summarises this information schematically.

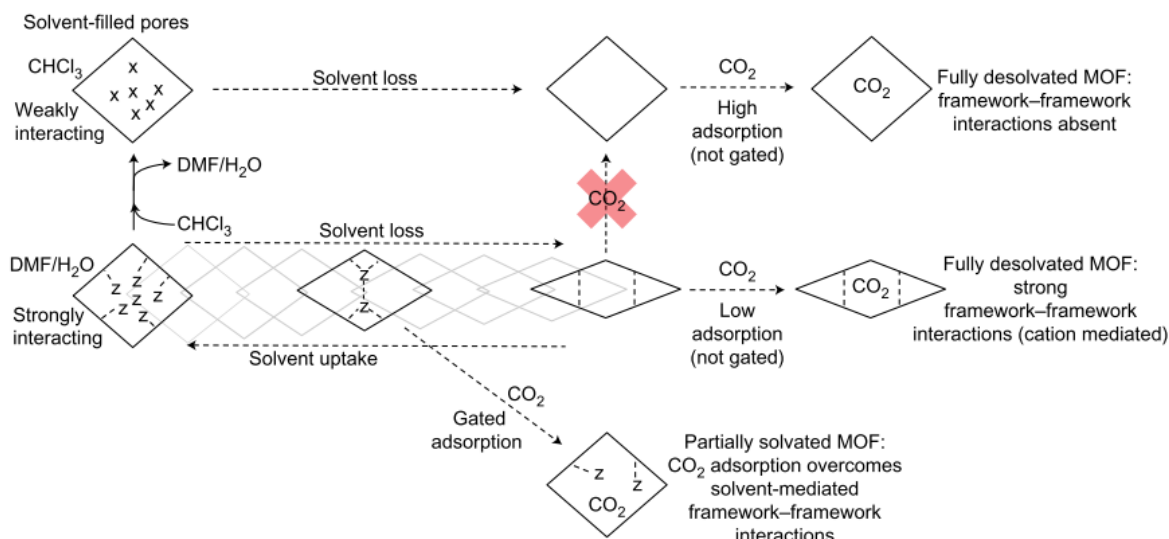


Figure 1.32. A summary of the desolvation and CO₂ uptake behaviour displayed by **SHF-61** and the proposed role of guest-framework and cation-framework interactions. Image reproduced from reference 76 with permission from Nature Publishing Group.

1.6. Conclusions

From their origin as a small sub-group of coordination polymers, metal-organic frameworks have expanded rapidly over only a few decades, becoming a field of chemistry in their own right. The discovery and subsequent study of dynamic, flexible systems such as **MIL-53** has allowed good progress to be made regarding the understanding of this behaviour, such as whether flexibility occurs in one, two or three dimensions, and/or which stimuli can induce it. Efforts to rationalise this dynamic behaviour, and minimise/maximise its extent in a given material are well under way, with various methods employed including adding/removing steric bulk to the pore space, changing the metal centre or ligand (either *via* post-synthetic modification or direct synthesis), and altering various environmental conditions (temperature, pressure etc.).

The study of **SHF-61** has unveiled two remarkable properties, and changed the way that these materials are viewed. Firstly, the existence of continuous flexibility suggests an infinite (theoretically) range of pore states may be accessible in some materials, which could have implications regarding their industrial application. Secondly, the existence of two activated states (dependent on which guest is removed) shows that, in this material at least, the pore shape depends not only on the environmental

conditions present, but also *how* those conditions were obtained. This again, could have implications not only for industrial application, but also for progressing our academic understanding of flexible MOFs.

The published *in situ* X-ray diffraction studies on **SHF-61** describe (among other things) how the activated material behaves when exposed to carbon dioxide at room temperature. However, further work is needed to understand how this adsorption behaviour alters with temperature, and whether it can be reproduced using different guests, such as other gases or solvents. Further work is also needed to understand which part(s) of the pore surface these guests are interacting with, as a number of reasonable suggestions are theoretically possible. This thesis will describe some of the studies carried out on **SHF-61** since the 2017 publication by Carrington *et al.*, namely gas uptake with *in situ* X-ray diffraction and *in situ* infra-red spectroscopy (chapter 2), and solvent-vapour uptake with *in situ* infra-red spectroscopy (chapter 3). Chapter 4 will describe the synthesis and characterisation of a trigonal, cadmium-based metal-organic framework, and its flexibility as a response to solvent removal, gas uptake, and temperature change.

1.7. References

- 1 S. James, *Chem. Soc. Rev.*, 2003, **32**, 276–288.
- 2 H. C. Zhou, J. R. Long and O. M. Yaghi, *Chem. Rev.*, 2012, **112**, 673–674.
- 3 Y. R. Lee, J. Kim and W. S. Ahn, *Korean J. Chem. Eng.*, 2013, **30**, 1667–1680.
- 4 D. J. Tranchemontagne, J. L. Mendoza-Cortés, M. O’Keeffe and O. M. Yaghi, *Chem. Soc. Rev.*, 2009, **38**, 1257–1283.
- 5 A. U. Czaja, N. Trukhan and U. Müller, *Chem. Soc. Rev.*, 2009, **38**, 1284–1293.
- 6 A. Corma, H. Garcia and F. X. Llabres i Xamena, *Chem. Rev.*, 2010, **110**, 4606–4655.
- 7 Y. Liu, W. Xuan and Y. Cui, *Adv. Mater.*, 2010, **22**, 4112–4135.

- 8 J. Liu, L. Chen, H. Cui, J. Zhang, L. Zhang and C. Y. Su, *Chem. Soc. Rev.*, 2014, **43**, 6011–6061.
- 9 Y. Zhao, Z. Song, X. Li, Q. Sun, N. Cheng, S. Lawes and X. Sun, *Energy Storage Mater.*, 2016, **2**, 35–62.
- 10 M. C. So, G. P. Wiederrecht, J. E. Mondloch, J. T. Hupp and O. K. Farha, *Chem. Commun.*, 2015, **51**, 3501–3510.
- 11 B. Garai, A. Mallick and R. Banerjee, *Chem. Sci.*, 2016, **7**, 2195–2200.
- 12 P. P. Bag, D. Wang, Z. Chen and R. Cao, *Chem. Commun.*, 2016, **52**, 3669–3672.
- 13 D. Briones, B. Fernández, A. J. Calahorra, D. Fairen-Jimenez, R. Sanz, F. Martínez, G. Orcajo, E. S. Sebastián, J. M. Seco, C. S. González, J. Llopis and A. Rodríguez-Diéguez, *Cryst. Growth Des.*, 2016, **16**, 537–540.
- 14 L.-Q. Wei, Q. Chen, L.-L. Tang, C. Zhuang, W.-R. Zhu and N. Lin, *Dalton Trans.*, 2016, **45**, 3694–3697.
- 15 A. D. Burrows, M. Jurcic, M. F. Mahon, S. Pierrat, G. W. Roffe, H. J. Windle and J. Spencer, *Dalton Trans.*, 2015, **44**, 13814–13817.
- 16 H. N. Wang, P. X. Liu, H. Chen, N. Xu, Z. Y. Zhou and S. P. Zhuo, *RSC Adv.*, 2015, **5**, 65110–65113.
- 17 A. Douvali, A. C. Tsipis, S. V. Eliseeva, S. Petoud, G. S. Papaefstathiou, C. D. Malliakas, I. Papadas, G. S. Armatas, I. Margiolaki, M. G. Kanatzidis, T. Lazarides and M. J. Manos, *Angew. Chem. Int. Ed.*, 2015, **54**, 1651–1656.
- 18 R. Xu, Y. Wang, X. Duan, K. Lu, D. Micheroni, A. Hu and W. Lin, *J. Am. Chem. Soc.*, 2016, **138**, 2158–2161.

- 19 A. V. Desai, B. Manna, A. Karmakar, A. Sahu and S. K. Ghosh, *Angew. Chem. Int. Ed.*, 2016, **55**, 7811–7815.
- 20 S. Galli, N. Masciocchi, V. Colombo, A. Maspero, G. Palmisano, F. J. López-Garzón, M. Domingo-Garcia, I. Fernández-Morales, E. Barea and J. A. R. Navarro, *Chem. Mater.*, 2010, **22**, 1664–1672.
- 21 C. Montoro, F. Linares, E. Quartapelle Procopio, I. Senkowska, S. Kaskel, S. Galli, N. Masciocchi, E. Barea and J. A. R. Navarro, *J. Am. Chem. Soc.*, 2011, **133**, 11888–11891.
- 22 J. L. C. Rowsell and O. M. Yaghi, *Angew. Chem. Int. Ed.*, 2005, **44**, 4670–4679.
- 23 L. J. Murray, M. Dincă and J. R. Long, *Chem. Soc. Rev.*, 2009, **38**, 1294.
- 24 M. P. Suh, H. J. Park, T. K. Prasad and D. Lim, *Chem. Rev.*, 2012, **112**, 782–835.
- 25 D. M. D’Alessandro, B. Smit and J. R. Long, *Angew. Chem. Int. Ed.*, 2010, **49**, 6058–6082.
- 26 K. Sumida, D. L. Rogow, J. A. Mason, T. M. McDonald, E. D. Bloch, Z. R. Herm, T. H. Bae and J. R. Long, *Chem. Rev.*, 2012, **112**, 724–781.
- 27 S. S-Y Chui, S. M-F Lo, J. P. H Charmant, A. Guy Orpen and I. D. Williams, *Science*, 1999, **283**, 1148–1150.
- 28 H. Li, M. Eddaoudi, M. O’Keeffe and O. M. Yaghi, *Nature*, 1999, **402**, 276–279.
- 29 K. S. Lin, A. K. Adhikari, C. N. Ku, C. L. Chiang and H. Kuo, *Int. J. Hydrogen Energy*, 2012, **37**, 13865–13871.
- 30 C. Prestipino, L. Regli, J. G. Vitillo, F. Bonino, A. Damin, C. Lamberti, A. Zecchina, P. L. Solari, K. O. Kongshaug and S. Bordiga, *Chem. Mater.*, 2006, **18**, 1337–1346.
- 31 J. Lee, J. Li and J. Jagiello, *J. Solid State Chem.*, 2005, **178**, 2527–2532.
- 32 J. L. C. Rowsell and O. M. Yaghi, *J. Am. Chem. Soc.*, 2006, **128**, 1304–1315.

- 33 N. L. Rosi, J. Eckert, M. Eddaoudi, D. T. Vodak, J. Kim, M. O'Keefe and O. M. Yaghi, *Science*, 2003, **300**, 1127–1129.
- 34 B. Panella and M. Hirscher, *Adv. Mater.*, 2005, **17**, 538–541.
- 35 A. Schneemann, V. Bon, I. Schwedler, I. Senkovska, S. Kaskel and R. A. Fischer, *Chem. Soc. Rev.*, 2014, **43**, 6062–6096.
- 36 G. Férey, *Dalton Trans.*, 2016, **45**, 4073–4089.
- 37 E. Alvarez, N. Guillou, C. Martineau, B. Bueken, B. Vandevoorde, C. Leguillouzer, P. Fabry, F. Nouar, F. Taulelle, D. Devos, J. S. Chang, K. H. Cho, N. Ramsahye, T. Devic, M. Daturi, G. Maurin and C. Serre, *Angew. Chem. Int. Ed.*, 2015, **54**, 3664–3668.
- 38 S. Kitagawa, R. Kitaura and S. I. Noro, *Angew. Chem. Int. Ed.*, 2004, **43**, 2334–2375.
- 39 C. Serre, F. Millange, C. Thouvenot, M. Noguès, G. Marsolier, D. Louër and G. Férey, *J. Am. Chem. Soc.*, 2002, **124**, 13519–13526.
- 40 F. Millange, C. Serre, N. Guillou, G. Férey and R. I. Walton, *Angew. Chem. Int. Ed.*, 2008, **47**, 4100–4105.
- 41 G. Férey and C. Serre, *Chem. Soc. Rev.*, 2009, **38**, 1380–1399.
- 42 S. Bourrelly, P. L. Llewellyn, C. Serre, F. Millange, T. Loiseau and G. Férey, *J. Am. Chem. Soc.*, 2005, **127**, 13519–13521.
- 43 Z. Chang, D. H. Yang, J. Xu, T. L. Hu and X. H. Bu, *Adv. Mater.*, 2015, **27**, 5432–5441.
- 44 M. Alhamami, H. Doan and C. H. Cheng, *Materials*, 2014, **7**, 3198–3250.
- 45 C. R. Murdock, B. C. Hughes, Z. Lu and D. M. Jenkins, *Coord. Chem. Rev.*, 2014, **258–259**, 119–136.

- 46 S. A. Moggach, T. D. Bennett and A. K. Cheetham, *Angew. Chem. Int. Ed.*, 2009, **48**, 7087–7089.
- 47 C. Mellot-Draznieks, C. Serre, S. Surblé, N. Audebrand and G. Férey, *J. Am. Chem. Soc.*, 2005, **127**, 16273–16278.
- 48 H. J. Choi, M. Dincă and J. R. Long, *J. Am. Chem. Soc.*, 2008, **130**, 7848–7850.
- 49 F. Salles, G. Maurin, C. Serre, P. L. Llewellyn, C. Knöfel, H. J. Choi, Y. Filinchuk, L. Oliviero, A. Vimont, J. R. Long and G. Férey, *J. Am. Chem. Soc.*, 2010, **132**, 13782–13788.
- 50 Y. Kim, R. Haldar, H. Kim, J. Koo and K. Kim, *Dalton Trans.*, 2016, **45**, 4187–4192.
- 51 M. H. Zeng, S. Hu, Q. Chen, G. Xie, Q. Shuai, S. L. Gao and L. Y. Tang, *Inorg. Chem.*, 2009, **48**, 7070–7079.
- 52 I. H. Park, S. S. Lee and J. J. Vittal, *Chem. Eur. J.*, 2013, **19**, 2695–2702.
- 53 J. Seo, R. Matsuda, H. Sakamoto, C. Bonneau and S. Kitagawa, *J. Am. Chem. Soc.*, 2009, **131**, 12792–12800.
- 54 S. M. Hyun, T. K. Kim, Y. K. Kim, D. Moon and H. R. Moon, *Inorg. Chem. Commun.*, 2013, **33**, 52–56.
- 55 M. K. Taylor, T. Runčevski, J. Oktawiec, J. E. Bachman, R. L. Siegelman, H. Jiang, J. A. Mason, J. D. Tarver and J. Long, *J. Am. Chem. Soc.*, 2018, **140**, 10324–10331.
- 56 Y. Sakata, S. Furukawa, M. Kondo, K. Hirai, N. Horike, Y. Takashima, H. Uehara, N. Louvain, M. Mailikhov, T. Tsuruoka, S. Isoda, W. Kosaka, O. Sakata and S. Kitagawa, *Science*, 2013, **339**, 193–196.
- 57 J. Troyano, A. Carné-Sánchez and D. Maspoch, *Adv. Mater.*, 2019, **31**, 1808235.
- 58 J. Troyano, A. Carné-Sánchez, J. Pérez-Carvajal, L. León-Reina, I. Imaz, A. Cabeza and D. Maspoch, *Angew. Chem. Int. Ed.*, 2018, **57**, 15420–15424.

- 59 A. P. Katsoulidis, D. Antypov, G. F. S. Whitehead, E. J. Carrington, D. J. Adams, N. G. Berry, G. R. Darling, M. S. Dyer and M. J. Rosseinsky, *Nature*, 2019, **565**, 7738, 213–217.
- 60 A. P. Katsoulidis, K. S. Park, D. Antypov, C. Martí-Gastaldo, G. J. Miller, J. E. Warren, C. M. Robertson, F. Blanc, G. R. Darling, N. G. Berry, J. A. Purton, D. J. Adams and M. J. Rosseinsky, *Angew. Chem. Int. Ed.*, 2014, **53**, 193–198.
- 61 S. Krause, V. Bon, I. Senkovska, U. Stoeck, D. Wallacher, D. M. Töbrens, S. Zander, R. S. Pillai, G. Maurin, F-X. Coudert and S. Kaskel, *Nature*, 2016, **532**, 348–352.
- 62 R. Robson, *J. Chem. Soc., Dalton Trans.*, 2000, 3735–3744.
- 63 G. R. Desiraju, *Angew. Chem., Int. Ed. Engl.*, 1995, **34**, 2311–2327.
- 64 L. Brammer, *Chem. Soc. Rev.*, 2004, **33**, 476–489.
- 65 M. Eddaoudi, J. Kim, N. Rosi, D. Vodak, J. Wachter, M. O’Keeffe and O. M. Yaghi, *Science*, 2002, **295**, 469–472.
- 66 M. Sadakiyo, T. Yamada, K. Kato, M. Takata and H. Kitagawa, *Chem. Sci.*, 2015, **5**, 476–482.
- 67 Y. Y. Liu, S. Couck, M. Vandichel, M. Grzywa, K. Leus, S. Biswas, D. Volkmer, J. Gascon, F. Kapteijn, J. F. M. Denayer, M. Waroquier, V. Van Speybroeck and P. Van Der Voort, *Inorg. Chem.*, 2013, **52**, 113–120.
- 68 X. Li, X. Chen, F. Jiang, L. Chen, S. Lu, Q. Chen, M. Wu, D. Yuan and M. Hong, *Chem. Commun.*, 2016, **52**, 2277–2280.
- 69 A. D. Burrows, K. Cassar, R. M. W. Friend, M. F. Mahon, S. P. Rigby and J. E. Warren, *CrystEngComm*, 2005, **7**, 548.
- 70 S. M. Cohen, *Chem. Rev.*, 2012, **112**, 970–1000.
- 71 S. Biswas, T. Ahnfeldt and N. Stock, *Inorg. Chem.*, 2011, **50**, 9518–9526.

- 72 T. Devic, F. Salles, S. Bourrelly, B. Moulin, G. Maurin, P. Horcajada, C. Serre, A. Vimont, J. C. Lavalley, H. Leclerc, G. Clet, M. Daturi, P. L. Llewellyn, Y. Filinchuk and G. Férey, *J. Mater. Chem.*, 2012, **22**, 10266–10273.
- 73 P. Serra-Crespo, E. Gobechiya, E. V. Ramos-Fernandez, J. Juan-Alcañiz, A. Martinez-Joaristi, E. Stavitski, C. E. A. Kirschhock, J. A. Martens, F. Kapteijn and J. Gascon, *Langmuir*, 2012, **28**, 12916–12922.
- 74 S. Castellanos, K. B. Sai Sankar Gupta, A. Pustovarenko, A. Dikhtiarenko, M. Nasalevich, P. Atienzar, H. García, J. Gascon and F. Kapteijn, *Eur. J. Inorg. Chem.*, 2015, 4648–4652.
- 75 V. Bon, N. Kavooosi, I. Senkovska, P. Müller, J. Schaber, D. Wallacher, D. M. Többens, U. Mueller and S. Kaskel, *Dalton Trans.*, 2016, **45**, 4407–4415.
- 76 E. J. Carrington, C. A. McAnally, A. J. Fletcher, S. P. Thompson, M. Warren and L. Brammer, *Nat. Chem.*, 2017, **9**, 882–889.
- 77 B. Yuan, D. Ma, X. Wang, Z. Li, Y. Li, H. Liu and D. He, *Chem. Commun.*, 2012, **48**, 1135–1137.

2. Gas uptake in SHF-61: *in situ* Diffraction Studies

2.1. Abstract

The dynamic response of activated **SHF-61-DMF** (**SHF-61** = $[\text{NMe}_2\text{H}_2][\text{In}(\text{NH}_2\text{BDC})_2]$) to CO_2 and SO_2 is monitored at temperatures of 195 K and 273 K, respectively, with *in situ* X-ray single-crystal and powder diffraction, using a range of pore states as starting points. These studies reveal the presence of a gate pressure, which does not seem to be guest or temperature dependent, and also a *b*-axis threshold for gated uptake, which is *ca.* 0.6 Å in the SO_2 experiments. A single CO_2 uptake study at 298 K is performed with *in situ* single-crystal X-ray diffraction to build upon a previous study of **SHF-61-DMF**, and the published studies at 298 K are compared to the 195 K studies presented here. CO_2 uptake at 298 K monitored *in situ* by infra-red spectroscopy supports the published gravimetric adsorption studies, and further reveals that CO_2 interacts relatively weakly with the amine substituents of the MOF framework.

2.2. Introduction

The carbon dioxide uptake behaviour of **SHF-61-DMF** is both intriguing and bemusing. Carrington *et al.* reported various carbon dioxide studies uptake on activated **SHF-61-DMF**, all with different levels of pore-closure.¹ The length of the *b*-axis is a reasonable indication of pore size – typically between 27 and 28 Å in the solvated material, and as low as 20 Å after activation. In some of the studies, when $b \approx 24$ Å at the start of the experiment, carbon dioxide adsorption induces a gated opening of the framework, but in other studies where $b \approx 22$ Å, either: no gate is observed, and instead a small continuous opening is observed with a final pore size of $b \approx 23.5$ Å, or; a gated opening occurs with a final pore size of $b \approx 25.5$ Å. In order to further understand and clarify this behaviour, CO_2 uptake was performed with *in situ* single crystal X-ray diffraction at 298 K to complement the initial reported studies. In separate experiments, CO_2 uptake in single crystals was monitored *in situ* by infra-red spectroscopy on both activated **SHF-61-DMF** and activated **SHF-61-CHCl₃**, to determine whether the guest species interacts with the framework amine groups. It is well documented that amine-functionalised materials generally display greater CO_2/CH_4 selectivity than

their non-functionalised analogues (even though the incorporation of amine-functionalisation can reduce the overall uptake capacity of the material).^{2,3} However, interaction of adsorbed CO₂ with framework amine groups doesn't always occur when the two are present, and may not be an important mechanism in CO₂ binding.⁴⁻⁶

Additionally, given that the published *in situ* crystallographic studies of CO₂ adsorption were performed at room temperature, a complementary set of experiments were performed at 195 K. The first reason for this was to try to determine whether or not the temperature affected the position of the gate or the degree of pore opening, and the second reason was that it allowed the experiment to be monitored at pressures up to the vapour pressure of carbon dioxide, which wasn't possible at 298 K due to instrument limitations (vapour pressure of CO₂ = 1 bar at 195 K, or *ca.* 64 bar at 298 K).

Finally, sulphur dioxide adsorption was performed at 273 K, with *in situ* monitoring by single-crystal and powder X-ray diffraction, on activated **SHF-61-DMF** after both partial, and full (more thorough) desolvation. Very few studies of SO₂ uptake in metal-organic frameworks have been reported,⁷⁻¹⁰ despite SO₂ being a potent environmental pollutant, so it is important to determine which materials might be viable as encapsulating agents. Additionally, we hypothesized that the stronger dipole of SO₂ compared to CO₂ could lead to stronger framework interactions, and potentially shift the gate to lower pressures in the partially desolvated material. It was additionally hoped that the position of SO₂ molecules within the unit cell would be deducible from the single-crystal diffraction studies, due to the higher electron density of SO₂ compared to CO₂, although this did not prove possible.

By combining all of the gas uptake data currently collected on **SHF-61-DMF**, the aim of this chapter is to provide further insight into how gaseous species might interact with the framework, and what factors cause the framework to exhibit gated or ungated opening as a response. Almost all of the data presented in this chapter were collected at Diamond Light Source; at Beamlines I19 (single-crystal X-ray diffraction), I11 (powder X-ray diffraction) and B22 (infra-red spectroscopy).

2.3. Experimental

2.3.1. Synthesis & General Procedures

The preparation of both **SHF-61-DMF** and **SHF-61-CHCl₃** was performed according to the published literature, unless otherwise stated.^{1,11} All reagents and solvents were supplied by Sigma-Aldrich, Alfa Aesar, Acros Organics, Fisher Scientific, Fluorochem or Manchester Organics, and were used without additional purification, except chloroform, which was obtained from the departmental Grubbs dry solvent service.

2.3.2. Single-Crystal Diffraction Experiments

Single-crystal X-ray diffraction data were recorded at Beamline I19, Diamond Light Source. Full hemispheres of data were collected using three 132 ° and one 180 ° omega scans, with 0.4 ° slicing, on a Newport diffractometer using a Pilatus 300K detector. Data processing and absorption correction was performed using Aligent Crysalis Pro. Each crystal was glued to a Mylar loop, carefully minimising coverage of the crystal with glue, and loaded into the 0.7 mm quartz capillary of a gas cell to allow CO₂ uptake. Sample temperature was controlled using an Oxford Cryosystems cryostream. Crystal structures were solved, and refined against F^2 values using the program SHELX 2013 implemented via OLEX-2.^{12,13} All non-hydrogen atoms were refined anisotropically, with the exception of non-framework dimethylammonium counter-ions in some structures. In many structures, data quality was not sufficient to model the position of the counter-ion. Crystallographic restraints and constraints were applied to some structures where necessary. Positions of hydrogen atoms were calculated with idealised geometries and refined using a riding model with isotropic displacement parameters. Final structure files (.CIFs) were checked with PLATON¹⁴ and checkCIF¹⁵. The PLATON function SQUEEZE was used only to determine residual electron densities and solvent accessible void space. The below equations define the measures of agreement between calculated and experimental data presented in Tables 2.1–2.6:

$$R1(F) = \frac{\sum(|F_o| - |F_c|)}{\sum|F_o|} \quad wR2(F^2) = \sqrt{\frac{\sum(F_o^2 - F_c^2)^2}{\sum w F_o^4}} \quad S(F^2) = \sqrt{\frac{\sum w(F_o^2 - F_c^2)^2}{(n+r-p)}}$$

Experiment A1 – CO₂ Uptake at 298 K

A single crystal of **SHF-61-DMF** was selected directly from the mother liquor, placed in the gas cell, and placed under dynamic vacuum (10^{-7} mbar) at room temperature. Data were collected at 298 K under vacuum, and at 0.5, 1 and 2 bar CO₂ pressures. Crystal data are reported in Table 2.1.

Table 2.3. Crystal data for MOF SHF-61 in CO₂ uptake study **A1**. **A1-0** = vacuum; **A1-0.5** = 0.5 bar CO₂; **A1-1** = 1 bar CO₂; **A1-2** = 2 bar CO₂.

	A1-0	A1-0.5	A1-1
Crystal Size / mm	0.20 x 0.15 x 0.10	0.20 x 0.15 x 0.10	0.20 x 0.15 x 0.10
Crystal System	Orthorhombic	Orthorhombic	Orthorhombic
Space Group	<i>Fddd</i>	<i>Fddd</i>	<i>Fddd</i>
<i>a</i> / Å	15.1662(5)	15.2044(3)	15.2129(3)
<i>b</i> / Å	23.8591(8)	24.5999(6)	24.8680(6)
<i>c</i> / Å	33.4475(9)	32.9660(7)	32.7745(8)
α (°)	90	90	90
β (°)	90	90	90
γ (°)	90	90	90
<i>V</i> / Å ³	12103.1(7)	12330.1(5)	12399.1(5)
<i>Z</i>	16	16	16
Radiation	$\lambda = 0.6889$ Å	$\lambda = 0.6889$ Å	$\lambda = 0.6889$ Å
Density / g cm ⁻³	1.039	1.019	1.014
Temperature /K	298	298	298
μ / mm ⁻¹	0.749	0.735	0.731
2 θ range (°)	3.302 – 58.95	3.278 – 58.95	3.272 – 58.95

Reflns collected	40017	41633	41734
Independent reflns	4617	4711	4739
Reflns used in refinement, n	4617	4711	4739
L.S. parameters, p	123	123	123
No. of restraints, r	0	0	0
R_{int}	0.0535	0.0614	0.1128
R_{sigma}	0.0304	0.0307	0.0469
$R1(F) I > 2\sigma(I)$	0.0830	0.0861	0.0929
$wR2(F^2)$, all data	0.2791	0.2867	0.2974
$S(F^2)$, all data	1.100	1.101	1.106

A1-2

Crystal Size / mm	0.20 x 0.15 x 0.10
Crystal System	Orthorhombic
Space Group	$Fddd$
$a / \text{\AA}$	15.2216(3)
$b / \text{\AA}$	25.2032(7)
$c / \text{\AA}$	32.5309(8)
α ($^\circ$)	90
β ($^\circ$)	90
γ ($^\circ$)	90
$V / \text{\AA}^3$	12479.9(5)
Z	16

Radiation	$\lambda = 0.6889 \text{ \AA}$
Density / g cm ⁻³	1.007
Temperature /K	298
μ / mm ⁻¹	0.727
2 θ range (°)	3.264 – 58.95
Reflns collected	41992
Independent reflns	4757
Reflns used in refinement, n	4757
L.S. parameters, p	123
No. of restraints, r	0
R_{int}	0.0596
R_{sigma}	0.0321
$R1(F)^a$ $I > 2\sigma(I)$	0.0899
$wR2(F^2)^a$, all data	0.3002
$S(F^2)^a$, all data	1.115

Experiment C1a – CO₂ Uptake at 195 K

A single crystal of **SHF-61-DMF** was desolvated by heating in a temperature-controlled oven at 150 °C. X-ray diffraction data were collected at a series of CO₂ gas pressures from vacuum up to 1 bar, and an additional data collection was performed under vacuum after desorption. Unfortunately, due to sample degradation, data quality was sufficient only to determine the lattice parameters, which are listed in Table 2.2.

Table 2.4. Lattice parameters obtained from study **C1a**. For all X-ray data sets, crystal system = orthorhombic. R_{int} values are shown to indicate data quality.

Pressure / bar	R_{int}	Lattice Parameters			
		$a / \text{\AA}$	$b / \text{\AA}$	$c / \text{\AA}$	$V / \text{\AA}^3$
Vacuum	0.1759	14.888(2)	22.180(8)	34.669(4)	11448(5)
0.05	0.1572	14.835(2)	23.187(9)	34.163(6)	11751(5)
0.1	0.1537	14.831(2)	23.145(10)	34.138(6)	11718(6)
0.2	0.1976	14.849(3)	23.618(14)	33.855(8)	11873(8)
0.4	0.2050	14.877(3)	23.953(13)	33.669(9)	11998(8)
0.6	0.2094	14.899(3)	24.349(14)	33.416(9)	12122(8)
0.8	0.2351	14.924(3)	24.837(18)	33.186(11)	12301(10)
1.0	0.1922	14.920(3)	24.816(16)	33.119(10)	12263(9)
Vacuum	0.1860	14.810(3)	24.418(13)	33.365(9)	12066(8)

Experiment C1b – CO₂ Uptake at 195 K

A single crystal of **SHF-61-DMF** was selected directly from the mother liquor, placed in the gas cell, and placed under dynamic vacuum. X-ray diffraction data were collected at a series of CO₂ gas pressures from vacuum up to 1 bar. Crystal data are listed in Table 2.3.

Table 2.5. Crystal data for MOF SHF-61 in CO₂ uptake study **C1b**. Numerical suffix refers to the CO₂ pressure (bar) during data collection.

	C1b-0	C1b-0.02	C1b-0.1
Crystal Size / mm	0.07 x 0.05 x 0.04	0.07 x 0.05 x 0.04	0.07 x 0.05 x 0.04
Crystal System	Orthorhombic	Orthorhombic	Orthorhombic
Space Group	<i>Fddd</i>	<i>Fddd</i>	<i>Fddd</i>
<i>a</i> / Å	15.0903(4)	15.4005(3)	15.4308(3)
<i>b</i> / Å	23.0714(6)	27.3234(3)	27.5240(4)
<i>c</i> / Å	33.9269(8)	30.8336(6)	30.6363(6)
α (°)	90	90	90
β (°)	90	90	90
γ (°)	90	90	90
<i>V</i> / Å ³	11811.7(5)	12974.6(4)	13011.7(4)
<i>Z</i>	16	16	16
Radiation	$\lambda = 0.6889$ Å	$\lambda = 0.6889$ Å	$\lambda = 0.6889$ Å
Density / g cm ⁻³	1.168	0.969	1.060
Temperature /K	195	195	195
μ / mm ⁻¹	0.774	0.699	0.702
2 θ range (°)	3.336 – 58.95	3.208 – 58.95	3.204 – 58.95
Reflns collected	39623	43610	43427
Independent reflns	4512	4948	4975
Reflns used in refinement, <i>n</i>	4512	4948	4975
L.S. parameters, <i>p</i>	137	123	123
No. of restraints, <i>r</i>	0	0	0

R_{int}	0.0571	0.0565	0.0604
R_{sigma}	0.0312	0.0271	0.0294
$R1(F) I > 2\sigma(I)$	0.0848	0.0610	0.0652
$wR2(F^2)$, all data	0.2697	0.2296	0.2447
$S(F^2)$, all data	1.077	1.092	1.152

	C1b-0.4	C1b-1.0
Crystal Size / mm	0.07 x 0.05 x 0.04	0.07 x 0.05 x 0.04
Crystal System	Orthorhombic	Orthorhombic
Space Group	<i>Fddd</i>	<i>Fddd</i>
$a / \text{\AA}$	15.4095(3)	15.4309(4)
$b / \text{\AA}$	27.4621(4)	27.5088(5)
$c / \text{\AA}$	30.6946(7)	30.6362(7)
α (°)	90	90
β (°)	90	90
γ (°)	90	90
$V / \text{\AA}^3$	12989.3(5)	13004.6(5)
Z	16	16
Radiation	$\lambda = 0.6889 \text{\AA}$	$\lambda = 0.6889 \text{\AA}$
Density / g cm ⁻³	0.968	1.061
Temperature /K	195	195
μ / mm^{-1}	0.698	0.703
2 θ range (°)	3.206 – 58.95	3.204 – 58.95
Reflns collected	43007	43881

Independent reflns	4963	4972
Reflns used in refinement, n	4963	4972
L.S. parameters, p	123	123
No. of restraints, r	0	0
R_{int}	0.0606	0.0618
R_{sigma}	0.0314	0.312
$R1(F)^a I > 2\sigma(I)$	0.0652	0.0665
$wR2(F^2)^a$, all data	0.2424	0.2472
$S(F^2)^a$, all data	1.153	1.160

Experiment C1c – CO₂ Uptake at 195 K

A single crystal of **SHF-61-DMF** was selected directly from the mother liquor, placed in the gas cell, and placed under dynamic vacuum. X-ray diffraction data were collected at a series of CO₂ gas pressures from vacuum up to 1 bar. Crystal data are listed in Table 2.4.

Table 2.6. Crystal data for MOF SHF-61 in CO₂ uptake study **C1c**. Numerical suffix refers to the CO₂ pressure (bar) during data collection.

	C1c-0	C1c-0.02	C1c-0.05
Crystal System	Orthorhombic	Orthorhombic	Orthorhombic
Space Group	<i>Fddd</i>	<i>Fddd</i>	<i>Fddd</i>
$a / \text{\AA}$	15.0911(7)	15.4390(12)	15.4643(10)
$b / \text{\AA}$	23.0911(12)	27.5703(18)	27.6708(14)
$c / \text{\AA}$	33.879(2)	30.536(3)	30.430(2)
α (°)	90	90	90

β (°)	90	90	90
γ (°)	90	90	90
$V / \text{Å}^3$	11805.9(11)	12997.9(18)	13021.1(14)
Z	16	16	16
Radiation	$\lambda = 0.6889 \text{ Å}$	$\lambda = 0.6889 \text{ Å}$	$\lambda = 0.6889 \text{ Å}$
Density / g cm ⁻³	1.065	0.967	0.965
Temperature /K	195	195	195
μ / mm^{-1}	0.768	0.698	0.696
2 θ range (°)	3.336 – 51.00	3.204 – 51.00	3.204 – 51.00
Reflns collected	28097	31969	32223
Independent reflns	3021	3329	3338
Reflns used in refinement, n	3021	3329	3338
L.S. parameters, p	123	123	123
No. of restraints, r	0	0	0
R_{int}	0.1757	0.1781	0.1746
R_{sigma}	0.0823	0.0908	0.0899
$R1(F)^a I > 2\sigma(I)$	0.1256	0.1099	0.1204
$wR2(F^2)^a$, all data	0.3517	0.3530	0.3645
$S(F^2)^a$, all data	1.286	1.230	1.285

	C1c-0.1	C1c-0.3	C1c-0.7
Crystal System	Orthorhombic	Orthorhombic	Orthorhombic
Space Group	<i>Fddd</i>	<i>Fddd</i>	<i>Fddd</i>
<i>a</i> / Å	15.4870(10)	15.4855(10)	15.5141(11)
<i>b</i> / Å	27.7072(15)	27.6554(15)	27.7532(17)
<i>c</i> / Å	30.369(2)	30.426(2)	30.340(2)
α (°)	90	90	90
β (°)	90	90	90
γ (°)	90	90	90
<i>V</i> / Å ³	13031.2(14)	13030.2(15)	13063.4(15)
<i>Z</i>	16	16	16
Radiation	$\lambda = 0.6889$ Å	$\lambda = 0.6889$ Å	$\lambda = 0.6889$ Å
Density / g cm ⁻³	0.965	1.059	0.962
Temperature /K	195	195	195
μ / mm ⁻¹	0.696	0.701	0.694
2 θ range (°)	3.196 – 51.00	3.196 – 51.00	3.192 – 51.00
Reflns collected	32070	31942	31893
Independent reflns	3338	3338	3326
Reflns used in refinement, <i>n</i>	3338	3338	3326
L.S. parameters, <i>p</i>	123	123	123
No. of restraints, <i>r</i>	0	0	0
<i>R</i> _{int}	0.1624	0.1610	0.1968

R_{sigma}	0.0823	0.0835	0.1115
$R1(F) I > 2\sigma(I)$	0.1158	0.1115	0.1180
$wR2(F^2)$, all data	0.3653	0.3578	0.3565
$S(F^2)$, all data	1.291	1.268	1.117

C1c-1.0

Crystal System	Orthorhombic
Space Group	<i>Fddd</i>
$a / \text{\AA}$	15.5501(8)
$b / \text{\AA}$	27.7924(12)
$c / \text{\AA}$	30.3120(19)
α (°)	90
β (°)	90
γ (°)	90
$V / \text{\AA}^3$	13100.1(12)
Z	16
Radiation	$\lambda = 0.6889 \text{\AA}$
Density / g cm^{-3}	0.959
Temperature /K	195
μ / mm^{-1}	0.692
2θ range (°)	3.188 – 50.99
Reflns collected	32337
Independent reflns	3350

Reflns used in refinement, n	3350
L.S. parameters, p	123
No. of restraints, r	0
R_{int}	0.1527
R_{sigma}	0.0826
$R1(F) I > 2\sigma(I)$	0.1126
$wR2(F^2)$, all data	0.3660
$S(F^2)$, all data	1.261

Experiment D1a – SO₂ Uptake at 273 K

Single crystals of **SHF-61-DMF** were removed from the mother liquor, heated at 155 °C in a temperature-controlled oven for 4 hours. A single crystal was then selected and mounted in the gas cell. X-ray diffraction data were collected at a series of SO₂ gas pressures from vacuum up to 1 bar. Unfortunately, due to sample degradation, data quality was sufficient only to determine the lattice parameters, which are reported in Table 2.5.

Table 2.7. Lattice parameters obtained from study **D1a**. For all X-ray data sets, crystal system = orthorhombic. R_{int} values are shown to indicate data quality.

Pressure / bar	R_{int}	Lattice Parameters			
		$a / \text{Å}$	$b / \text{Å}$	$c / \text{Å}$	$V / \text{Å}^3$
Vacuum	0.0942	14.981(1)	22.391(4)	34.488(3)	11568(2)
0.20	0.1103	14.966(1)	22.445(4)	34.467(3)	11578(2)
0.41	0.1247	14.931(2)	22.619(5)	34.422(4)	11625(1)
0.60	0.1471	14.897(3)	22.909(7)	34.304(5)	11707(4)

0.80	0.1834	14.870(3)	23.208(8)	34.118(6)	11774(5)
1.00	0.1861	14.869(3)	23.418(9)	33.998(7)	11838(6)

Experiment D1b – SO₂ Uptake at 273 K

A single crystal of **SHF-61-DMF** was removed from the mother liquor and placed under vacuum in the gas cell. This was sufficient to achieve the desired level of pore-closure without heating. X-ray diffraction data were recorded at SO₂ pressures from vacuum up to 0.9 bar. Crystal data are listed in Table 2.6.

Table 2.8. Crystal data for MOF SHF-61 in SO₂ uptake study **D1b**. Numerical suffix refers to the pressure (bar) of SO₂ during data collection.

	D1b-0	D1b-0.2	D1b-0.4
Crystal Size / mm	0.17 × 0.17 × 0.15	0.17 × 0.17 × 0.15	0.17 × 0.17 × 0.15
Crystal System	Orthorhombic	Orthorhombic	Orthorhombic
Space Group	<i>Fddd</i>	<i>Fddd</i>	<i>Fddd</i>
<i>a</i> / Å	15.208(2)	15.331(3)	15.396(2)
<i>b</i> / Å	25.028(4)	26.412(5)	26.806(3)
<i>c</i> / Å	32.777(4)	31.683(4)	31.387(4)
α (°)	90	90	90
β (°)	90	90	90
γ (°)	90	90	90
<i>V</i> / Å ³	12476(3)	12829(4)	12954(3)
<i>Z</i>	16	16	16
Radiation	$\lambda = 0.6889$ Å	$\lambda = 0.6889$ Å	$\lambda = 0.6889$ Å
Density / g cm ⁻³	1.008	0.980	0.970

Temperature /K	273	273	273
μ / mm ⁻¹	0.727	0.707	0.700
2 θ range (°)	3.268 – 33.33	3.228 – 33.34	3.214 – 33.35
Reflns collected	10936	8154	11293
Independent reflns	950	979	985
Reflns used in refinement, <i>n</i>	950	979	985
L.S. parameters, <i>p</i>	123	123	123
No. of restraints, <i>r</i>	117	123	123
R_{int}	0.0784	0.0912	0.0484
R_{sigma}	0.0280	0.0520	0.0172
$R1(F) I > 2\sigma(I)$	0.1618	0.1254	0.1044
$wR2(F^2)$, all data	0.5046	0.3800	0.3406
$S(F^2)$, all data	2.589	1.669	1.201

	D1b-0.6	D1b-0.8	D1b-0.9
Crystal Size / mm	0.17 × 0.17 × 0.15	0.17 × 0.17 × 0.15	0.17 × 0.17 × 0.15
Crystal System	Orthorhombic	Orthorhombic	Orthorhombic
Space Group	<i>Fddd</i>	<i>Fddd</i>	<i>Fddd</i>
<i>a</i> / Å	15.4020(16)	15.4224(15)	15.4851(11)
<i>b</i> / Å	26.984(2)	27.081(2)	27.2066(18)
<i>c</i> / Å	31.218(3)	31.125(3)	31.012(2)
α (°)	90	90	90
β (°)	90	90	90

γ (°)	90	90	90
$V / \text{Å}^3$	12974(2)	13000(2)	13065.3(16)
Z	16	16	16
Radiation	$\lambda = 0.6889 \text{ Å}$	$\lambda = 0.6889 \text{ Å}$	$\lambda = 0.6889 \text{ Å}$
Density / g cm^{-3}	0.969	0.967	0.962
Temperature /K	273	273	273
μ / mm^{-1}	0.699	0.698	0.694
2θ range (°)	3.21 – 33.35	3.208 – 33.36	3.198 – 33.35
Reflns collected	11400	11679	11948
Independent reflns	987	989	998
Reflns used in refinement, n	987	989	998
L.S. parameters, p	123	123	123
No. of restraints, r	117	126	117
R_{int}	0.0476	0.0430	0.0387
R_{sigma}	0.0173	0.0151	0.0136
$R1(F) I > 2\sigma(I)$	0.1058	0.1037	0.1033
$wR2(F^2)$, all data	0.3873	0.3880	0.3918
$S(F^2)$, all data	1.942	1.966	2.004

2.3.3. Powder Diffraction Experiments

Powder X-ray diffraction data were collected at Beamline I11, Diamond Light Source, using a wide-angle position sensitive detector comprising 18 Mythen-2 modules.^{16,17} A pair of scans was collected for each measurement, related by a 0.25 ° detector offset, to account for gaps between modules. The two patterns were summed together prior to analysis. Samples were packed into 0.7 mm

quartz capillaries, built into a gas rig to allow CO₂ uptake. The sample temperature was controlled using an Oxford Cryosystems cryostream. All powder diffraction data were analysed by Pawley refinement,¹⁸ using TOPAS 4.1.¹⁹ The equations below define R_{wp} and R_{wp}' , the measures of agreement between calculated and experimental diffraction data:

$$R_{wp} = \sqrt{\frac{\sum[w(Y_{obs}-Y_{calc})^2]}{\sum[wY_{obs}^2]}} \quad R_{wp}' = \sqrt{\frac{\sum[w(Y_{obs}-Y_{calc})^2]}{\sum[w(Y_{obs}-bkg)^2]}}$$

Experiment C2a – CO₂ Uptake at 195 K

A powdered sample of **SHF-61-DMF** was packed into the capillary, placed under dynamic vacuum, and heated *in situ* on the beamline at temperatures between 140 °C and 165 °C for a total of 5.5 hours. The sample was intermittently cooled and scans performed at various stages to monitor pore closure. After sufficient desolvation had been achieved, the material was cooled to 195 K and left for 10 minutes to equilibrate before the first X-ray diffraction measurement at vacuum. X-ray diffraction data were recorded at a series of CO₂ pressures from vacuum up to 1 bar, and then a second measurement was performed at vacuum after desorption. Inspection of the patterns indicated that two phases of the MOF were present until 0.4 bar, and these two phases reappeared again upon desorption. The stacked patterns are shown in Figure 2.1, and the data from Pawley refinement shown in Table 2.7.

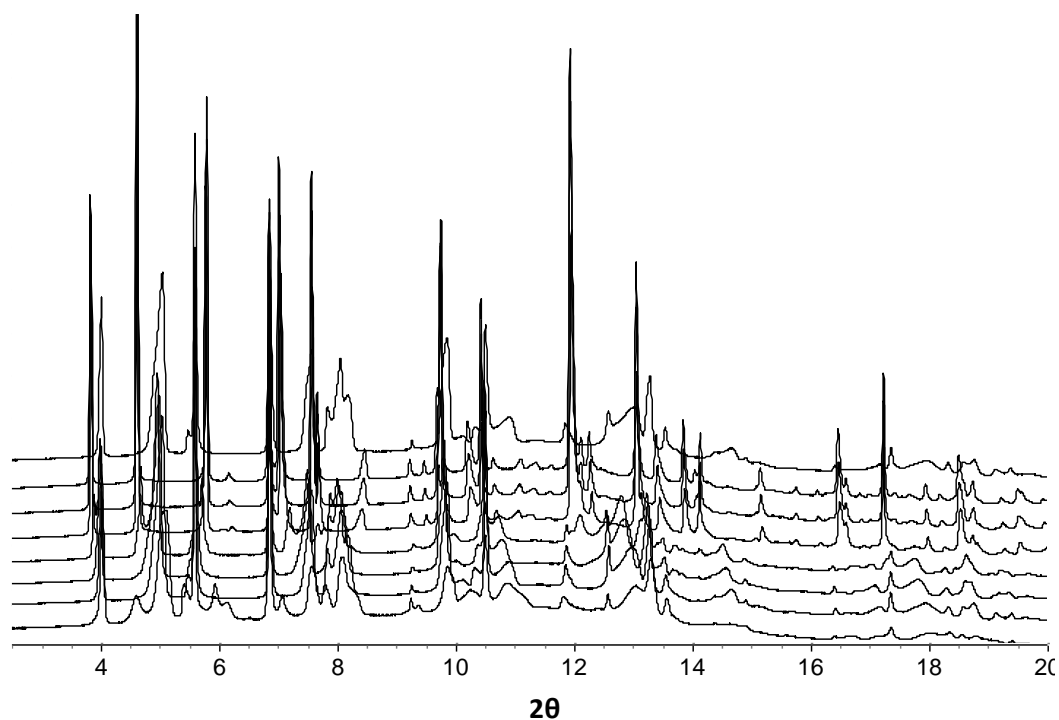


Figure 2.1. Stacked powder patterns obtained in study **C2a**, in ascending order (*i.e.* bottom = first measurement, top = last measurement); between the range $2^\circ \leq 2\theta \leq 20^\circ$.

Table 2.9. Pawley refinement results for study **C2a**.*

Pressure / bar		R_{wp}	R_{wp}'	Lattice Parameters			$V / \text{\AA}^3$
				$a / \text{\AA}$	$b / \text{\AA}$	$c / \text{\AA}$	
Vacuum	Phase 1	0.0575	0.1730	15.1013(123)	21.9859(222)	34.6204(335)	11494.5(186)
	Phase 2			15.0998(140)	22.8791(208)	33.7936(333)	11674.6(190)
0.06	Phase 1	0.0533	0.1422	15.0545(24)	22.3456(45)	34.4708(62)	11596.0(36)
	Phase 2			15.0694(35)	22.9103(69)	34.0722(148)	11763.2(68)
0.1	Phase 1	0.0561	0.1427	15.0821(34)	22.7421(50)	34.3422(81)	11779.4(46)
	Phase 2			15.1529(108)	23.3453(195)	33.7636(727)	11943.8(289)
0.2	Phase 1	0.0761	0.2533	15.1170(25)	23.1144(47)	34.0142(68)	11885.3(39)
	Phase 2			15.3266(23)	26.1946(52)	31.9450(87)	12825.1(47)
0.4		0.0825	0.2254	15.3911(13)	27.2470(23)	31.0063(29)	13002.8(19)

0.7	0.0743	0.1998	15.4377(9)	27.4602(16)	30.8223(21)	13066.3(14)
1.0	0.0694	0.1904	15.4616(7)	27.5567(14)	30.7344(15)	13095.0(11)
Vacuum	Phase 1		15.0628(19)	22.3207(42)	34.4245(54)	11574.0(32)
	Phase 2	0.0601	0.1796	15.0603(36)	22.9838(79)	33.9836(174)

*For all measurements: temperature = 195 K; $\lambda = 0.824528 \text{ \AA}$; 18 background parameters; *ca.* 230 reflections per phase; 1 zero error parameter; 5 profile parameters for single phase fits, 9 profile parameters for two-phase fits; lattice = orthorhombic; 3 lattice parameters refined (a , b , c).

Experiment C2b – CO₂ Uptake at 195 K

A powdered sample of **SHF-61-DMF** was packed into a capillary and the capillary heated in a temperature-controlled oven with one end open at 150 °C for 12.5 hours. A very minor phase is present which, by visual inspection, is consistent with the open-pore form of the material (possibly due to atmospheric water uptake as the capillary was cooling and being assembled into the gas cell). Attempts to fit this phase were unsuccessful as only the first three reflections are distinguishable from the major phase. Stacked patterns are shown in Figure 2.2, Pawley refinement results in Table 2.8.

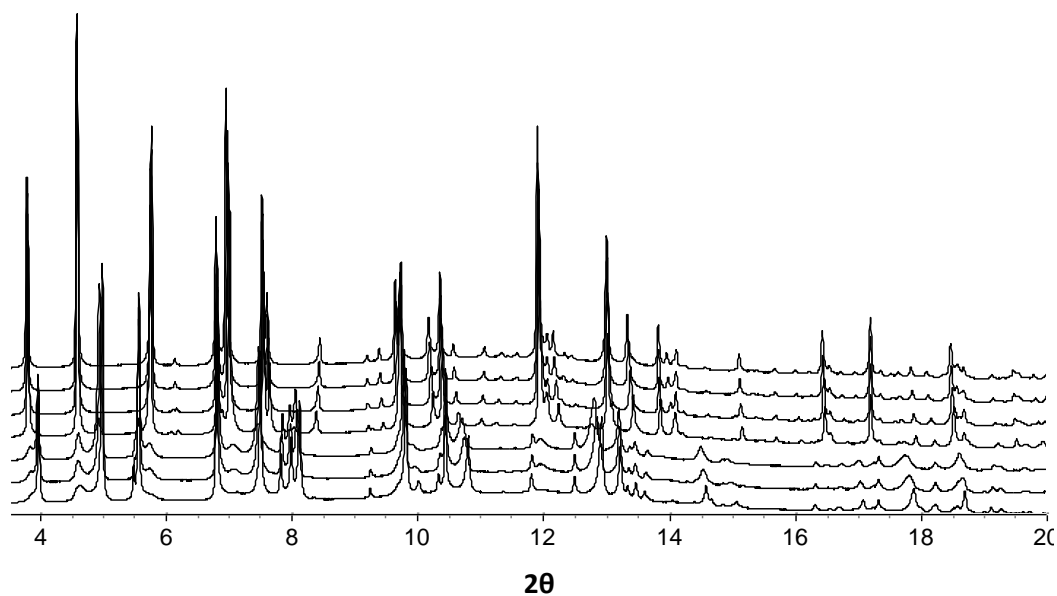


Figure 2.2. Stacked patterns obtained in study **C2b**, in ascending order (*i.e.* bottom = first measurement, top = last measurement); between the range $2^\circ \leq 2\theta \leq 20^\circ$.

Table 2.10. Pawley refinement results for study **C2b**.*

Pressure / bar	R_{wp}	R_{wp}'	Lattice Parameters			
			$a / \text{Å}$	$b / \text{Å}$	$c / \text{Å}$	$V / \text{Å}^3$
Vacuum	0.0588	0.1817	15.1322(6)	22.5792(1)	34.342(2)	11733.7(10)
0.05	0.0674	0.1971	15.1253(9)	22.789(2)	34.234(3)	11800(1)
0.1	0.0678	0.1882	15.1212(9)	22.956(2)	34.145(3)	11852(2)
0.2	0.0472	0.1421	15.4414(5)	27.2998(9)	30.963(1)	13052.4(7)
0.4	0.0455	0.1287	15.4942(4)	27.4593(8)	30.8165(10)	13111.2(6)
0.7	0.0421	0.1208	15.5310(3)	27.5612(7)	30.7274(8)	13153.0(5)
1.0	0.0429	0.1229	15.5549(3)	27.6234(7)	30.6696(7)	13178.1(5)

*For all measurements: temperature = 195 K; $\lambda = 0.82471 \text{ Å}$; 12 background parameters; ca. 450 reflections; 1 zero error parameter; 5 profile parameters; lattice = orthorhombic; 3 lattice parameters refined (a , b , c).

Experiment C2c – CO₂ Uptake at 195 K

A powdered sample of **SHF-61-DMF** was packed in a gas cell and placed under vacuum for 29 hours, after which the material was heated at 150 °C under vacuum for 10 minutes. X-ray diffraction data were collected at a series of CO₂ pressures from vacuum up to 1 bar, followed by desorption to vacuum. Stacked patterns are shown in Figure 2.3; Pawley refinement results are documented in Table 2.9.

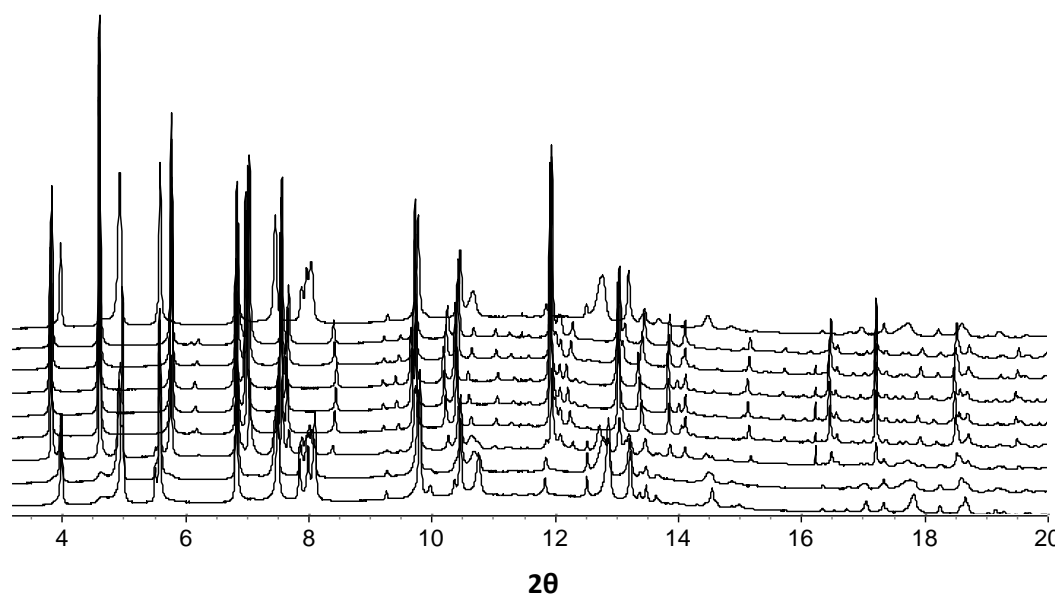


Figure 2.3. Stacked patterns obtained in study **C2c**, in ascending order (*i.e.* bottom = first measurement, top = last measurement); between the range $2^\circ \leq 2\theta \leq 20^\circ$.

Table 2.11. Pawley refinement results for study **C2c**.*

Pressure / bar	Lattice Parameters					
	R_{wp}	R_{wp}'	$a / \text{\AA}$	$b / \text{\AA}$	$c / \text{\AA}$	$V / \text{\AA}^3$
Vacuum	0.0517	0.1495	15.1191(5)	22.7878(8)	34.2462(15)	11798.9(8)
0.1	Phase 1		15.1180(16)	23.0062(36)	34.1185(58)	11866.6(30)
	Phase 2	0.0650	0.1521	15.4537(18)	27.0907(38)	30.9914(42)
0.2	Phase 1		15.1171(18)	23.2091(29)	34.0444(57)	11944.6(29)
	Phase 2	0.0532	0.1831	15.4039(12)	27.2511(21)	31.0389(27)
0.4	0.0397	0.1205	15.4586(3)	27.4627(6)	30.8452(7)	13094.9(5)
0.7	0.0402	0.1218	15.5045(3)	27.5686(6)	30.7457(7)	13141.8(5)
1.0	0.0390	0.1180	15.5341(3)	27.6320(6)	30.6875(6)	13172.2(4)
0.3	0.0384	0.1162	15.4415(3)	27.4372(5)	30.8678(7)	13077.8(4)
0.2	0.0377	0.1136	15.4029(3)	27.3443(6)	30.9532(7)	13036.9(4)

Vacuum 0.0636 0.2051 15.1329(9) 23.1566(17) 34.0335(30) 11926.2(15)

*For all measurements: temperature = 195 K; $\lambda = 0.824528 \text{ \AA}$; 14 background parameters; *ca.* 250 reflections per phase; 1 zero error parameter; 5 profile parameters for single phase fits, 9 profile parameters for two-phase fits; lattice = orthorhombic; 3 lattice parameters refined (*a*, *b*, *c*).

Experiment D2a – SO₂ Uptake at 273 K

A powdered sample of **SHF-61-DMF** was packed in a gas cell and placed under vacuum for 2 hours, after which the material was heated at 150 °C under vacuum for 6 hours. X-ray data were collected at a series of SO₂ pressures from vacuum up to 1 bar. Stacked patterns are shown in Figure 2.4. Pawley refinement results are reported in Table 2.10.

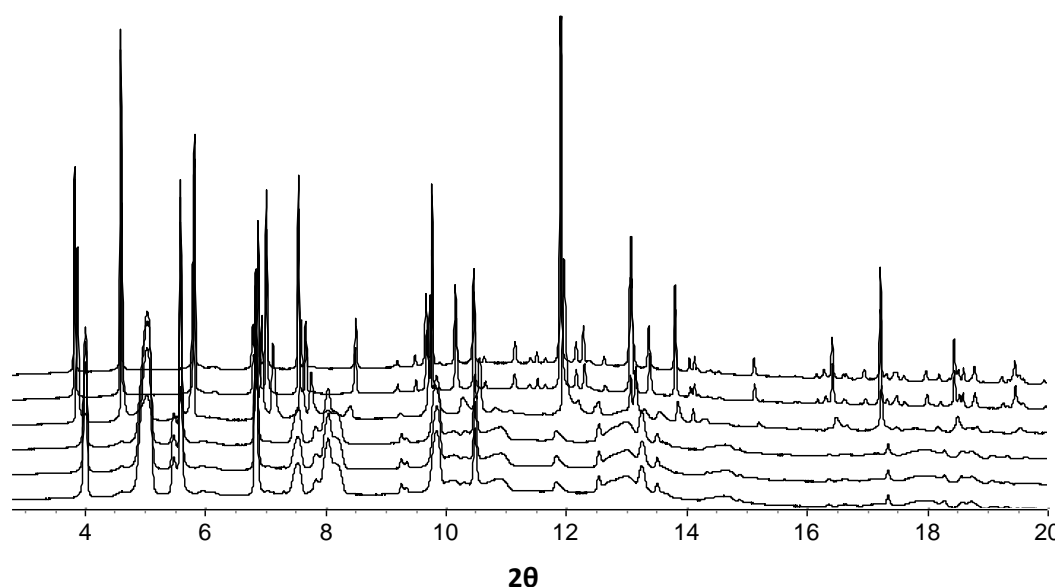


Figure 2.4. Stacked patterns obtained in study **D2a**, in ascending order (*i.e.* bottom = first measurement, top = last measurement); between the range $3^\circ \leq 2\theta \leq 20^\circ$.

Table 2.12. Pawley refinement results for study **D2a**.*

Pressure / bar	Lattice Parameters					
	R_{wp}	R_{wp}'	$a / \text{\AA}$	$b / \text{\AA}$	$c / \text{\AA}$	$V / \text{\AA}^3$
Vacuum	0.1286	0.2538	15.0992(31)	22.5521(61)	34.3340(99)	11691.4(52)
0.1	0.1319	0.3064	15.1000(33)	22.5063(69)	34.3701(104)	11680.5(56)
0.2	0.1234	0.2821	15.1024(29)	22.5546(60)	34.3455(90)	11699.1(49)

0.4	Phase 1			15.1661(8)	27.2342(17)	31.1024(19)	12846.4(13)
		0.0548	0.1630				
	Phase 2			15.0802(31)	22.6672(55)	34.2941(122)	11722.6(56)
0.6		0.0499	0.1366	15.3989(3)	27.8150(5)	30.5851(5)	13100.2(4)
0.8		0.0489	0.1401	15.4205(3)	27.8691(5)	30.5412(5)	13125.2(4)
1.0		0.0479	0.1362	15.4296(2)	27.8979(4)	30.5145(5)	13135.0(4)

*For all measurements: temperature = 273 K; $\lambda = 0.824528 \text{ \AA}$; 14 background parameters; *ca.* 250 reflections per phase; 1 zero error parameter; 5 profile parameters for single phase fits, 9 profile parameters for two-phase fits; lattice = orthorhombic; 3 lattice parameters refined (*a*, *b*, *c*).

Experiment D2b – SO₂ Uptake at 273 K

A powdered sample of **SHF-61-DMF** was packed in a capillary and the capillary heated at 150 °C in a temperature-controlled oven for 1 hour. X-ray data were recorded at a series of SO₂ pressures from vacuum up to 1 bar. The powder patterns measured at vacuum and 0.1 bar SO₂ contain a trace amount of a minor phase which, by visual inspection corresponds to the open-pore form of the material (likely due to incomplete desolvation or atmospheric water uptake during the assembly of the gas cell). This minor phase was in too small a quantity to be Pawley fitted. The measurement at 0.2 bar exhibits significant peak broadening, indicating that a wide range of pore states were present at this step. Stacked patterns are shown in Figure 2.5. Pawley refinement results are reported in Table 2.11.

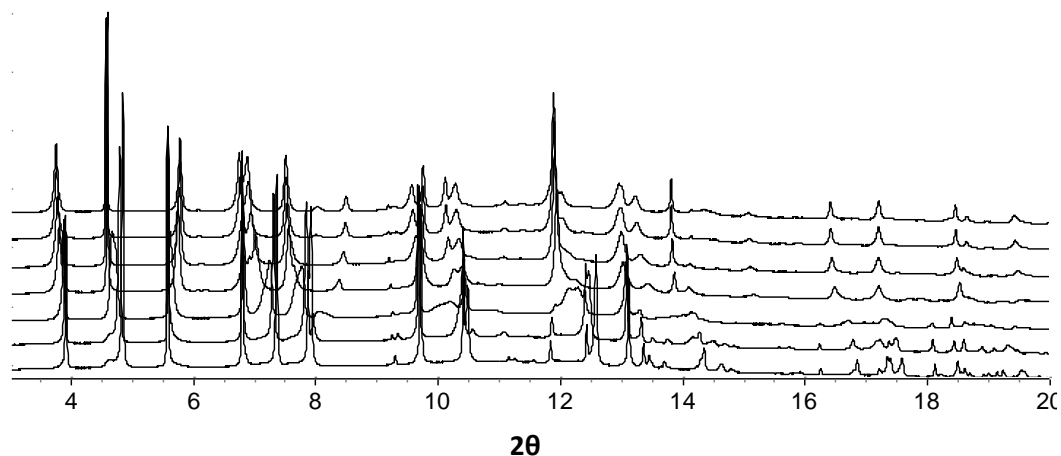


Figure 2.5. Stacked patterns obtained in study **D2a**, in ascending order (*i.e.* bottom = first measurement, top = last measurement); between the range $2^\circ \leq 2\theta \leq 20^\circ$.

Table 2.13. Pawley refinement results for study **D2b**.*

Pressure / bar	R_{wp}	R_{wp}'	Lattice Parameters			
			$a / \text{Å}$	$b / \text{Å}$	$c / \text{Å}$	$V / \text{Å}^3$
Vacuum	0.0585	0.1675	15.2065(3)	23.7303(8)	33.658(1)	12145.7(6)
0.1	0.0798	0.2315	15.2336(5)	24.223(13)	33.339(2)	12303(1)
0.2	0.1290	0.4076	15.38(1)	26.16(2)	31.84(3)	12806(19)
0.4	0.0747	0.1679	15.432(2)	27.229(4)	31.029(5)	13038(4)
0.6	0.0784	0.2274	15.600(3)	27.634(5)	30.632(6)	13205(4)
0.8	0.0741	0.2329	15.696(2)	27.830(3)	30.442(3)	13298(2)
1.0	0.0702	0.2531	15.737(1)	27.882(2)	30.382(3)	13331(2)

*For all measurements: temperature = 273 K; $\lambda = 0.824528 \text{ Å}$; 14 background parameters; *ca.* 450 reflections per phase; 1 zero error parameter; 5 profile parameters; lattice = orthorhombic; 3 lattice parameters refined (a , b , c).

2.3.4. Infra-red Spectroscopy Studies

Infra-red spectroscopy studies were performed at Beamline B22, Diamond Light Source,* using a polarised IR source connected to a Hyperion 3000 IR microscope and liquid nitrogen cooled MCT

detector. Single-crystal samples were loaded into a variable-temperature Linkham flow-cell with zinc selenide windows. The cell was connected to an input tube, enabling gas feeding from both nitrogen and carbon dioxide cylinders, and an output tube for exhaust of the gases. The partial pressure of the two gases in the cell was controlled using separate mass-flow controllers. Spectra were collected at room temperature under ambient pressure, in the range $650 - 4000 \text{ cm}^{-1}$, using a $20 \times 20 \text{ }\mu\text{m}$ beam. In both studies, measurements were made sequentially at the following relative pressures: $\text{CO}_2/\text{N}_2 = 0.0/1.0$; $\text{CO}_2/\text{N}_2 = 0.2/0.8$; $\text{CO}_2/\text{N}_2 = 0.4/0.6$; $\text{CO}_2/\text{N}_2 = 0.6/0.4$; $\text{CO}_2/\text{N}_2 = 0.8/0.2$; $\text{CO}_2/\text{N}_2 = 1.0/0.0$. Wavenumber at peak maximum was analysed manually using the Omnic32 program. Peak integration was performed using Origin Pro.* Model fitting of the spectra was performed only on the region containing the MOF framework amine bands ($3549 \text{ cm}^{-1} - 3304 \text{ cm}^{-1}$), by fitting the spectra to the following equation:

$$\text{Spectrum} = C1(A) + C2(B).$$

Where: *Spectrum* = the spectrum to be fitted; *A* = the spectrum at the start of the study, before exposure to CO_2 ; *B* = the spectrum at the end of the study ($\text{CO}_2/\text{N}_2 = 1.0/0.0$). The coefficients *C1* and *C2* therefore represent the how closely the spectrum resembles the start or end (respectively) of the study. This approach is based on the assumption that any spectrum measured between the start and end of the study can be treated as a composite of the first and final measurements.

*These experiments were performed as part of a collaborative study with Dr Tim Easun and Alex Tansell, at Cardiff University. Data collection was performed collaboratively at the Diamond Light Source, and subsequent data analysis was shared between myself and Alex Tansell. In this chapter, the peak integration of the CO_2 bands was performed by Alex Tansell.

Experiment B1 – CO_2 Uptake in narrow-pore SHF-61

Intra-red spectra were acquired from a single crystal of **SHF-61-DMF** (experiment **B1**), after heating at 40, 60, 80 and 100 for 20 minutes each, and then heating at $150 \text{ }^\circ\text{C}$ for 125 minutes. This procedure was chosen as it replicated the activation procedure used in some experiments by Carrington *et al.*,¹ and allowed *in situ* monitoring of solvent removal. Stacked spectra are shown in

Figure 2.6. Peak integration results for the CO₂ ($\nu_1 + \nu_3$) and ($2\nu_2 + \nu_3$) combination bands²⁰ are provided in Table 2.12. Results of the model-fit approach of the amine bands are provided in Table 2.13.

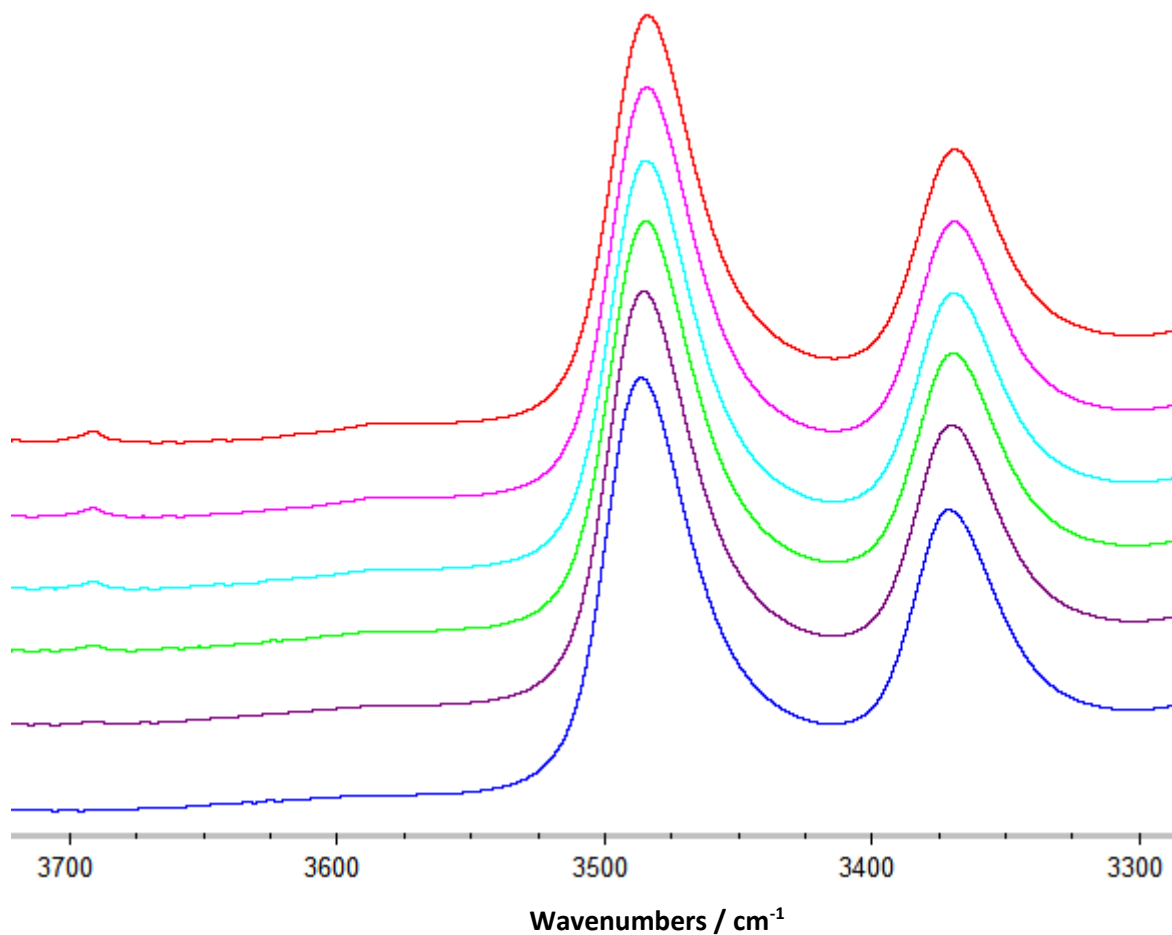


Figure 2.6. Stacked IR spectra obtained in study **B1**, in order of increasing CO₂ partial pressure (*i.e.* bottom = first measurement at CO₂/N₂ = 0.0/1.0, top = final measurement at CO₂/N₂ = 1.0/0.0). For clarity, only the region between 3300 and 3700 cm⁻¹ is shown, as this region contains all the bands relevant to analysis. The y-axis is absorbance.

Table 2.14. Peak integration results for experiment **B1**. The ($\nu_1 + \nu_3$) combination band was integrated in the range 3568 – 3608 cm⁻¹; the ($2\nu_2 + \nu_3$) combination band was integrated in the range 3672 – 3712 cm⁻¹. FWHM (Width at half maximum), Centre and Height refer to profile of the integrated band.

Band Integrated	Pressure / CO ₂ /N ₂	Area / Abs cm ⁻¹	FWHM / cm ⁻¹	Centre / cm ⁻¹	Height / Abs
($\nu_1 + \nu_3$)	0.0/1.0	0.040	3593.2	3608	0.0030

$(\nu_1 + \nu_3)$	0.2/0.8	0.153	27.6	3589	0.0065
$(\nu_1 + \nu_3)$	0.4/0.6	0.217	29.1	3589	0.0084
$(\nu_1 + \nu_3)$	0.6/0.4	0.233	23.6	3587	0.0099
$(\nu_1 + \nu_3)$	0.8/0.2	0.263	21.9	3587	0.0115
$(\nu_1 + \nu_3)$	1.0/0.0	0.294	21.9	3587	0.0128
$(2\nu_2 + \nu_3)$	0.0/1.0	-0.073	6.7	3697	-0.0035
$(2\nu_2 + \nu_3)$	0.2/0.8	0.004	5.9	3691	0.0053
$(2\nu_2 + \nu_3)$	0.4/0.6	0.073	7.5	3693	0.0101
$(2\nu_2 + \nu_3)$	0.6/0.4	0.156	8.8	3693	0.0150
$(2\nu_2 + \nu_3)$	0.8/0.2	0.205	9.7	3693	0.0174
$(2\nu_2 + \nu_3)$	1.0/0.0	0.258	10.1	3693	0.0209

Table 2.15. Results of the model-fit approach to the spectral region containing the MOF framework amine bands in study **B1**. Values are quoted to 3 significant figures.

Pressure / CO ₂ /N ₂	C1	C1 error (σ)	C2	C2 error (σ)	Reduced χ^2	Adjusted R ²
0.0/1.0	1.00	4.22 x 10 ⁻¹⁶	2.53 x 10 ⁻¹⁴	3.68 x 10 ⁻¹⁶	5.47 x 10 ⁻³¹	1.00
0.2/0.8	0.589	6.65 x 10 ⁻³	0.417	6.46 x 10 ⁻³	4.52 x 10 ⁻⁶	1.00
0.4/0.6	0.244	0.0208	0.777	0.0202	4.42 x 10 ⁻⁵	1.00
0.6/0.4	0.0381	0.0341	1.00	0.0331	1.18 x 10 ⁻⁴	0.998
0.8/0.2	0.0343	0.0258	1.00	0.0251	6.79 x 10 ⁻⁵	0.999
1.0/0.0	2.60 x 10 ⁻¹⁴	3.18 x 10 ⁻¹⁶	1.00	3.42 x 10 ⁻¹⁶	5.49 x 10 ⁻³¹	1.00

Experiment B2 – CO₂ Uptake in open-pore SHF-61

Experiment **B2** was performed on **SHF-61-CHCl₃**, after heating at 40, 60, 80, 100 and 120 °C for 20 minutes. This procedure was chosen as it replicated the activation procedure used in some experiments by Carrington *et al.*,¹ and allowed *in situ* monitoring of solvent removal. Stacked spectra are shown in Figure 2.7. Peak integration results for the CO₂ ($\nu_1 + \nu_3$) and ($2\nu_2 + \nu_3$) combination bands²⁰ are provided in Table 2.14. Results of the model-fit approach of the amine bands are provided in Table 2.15.

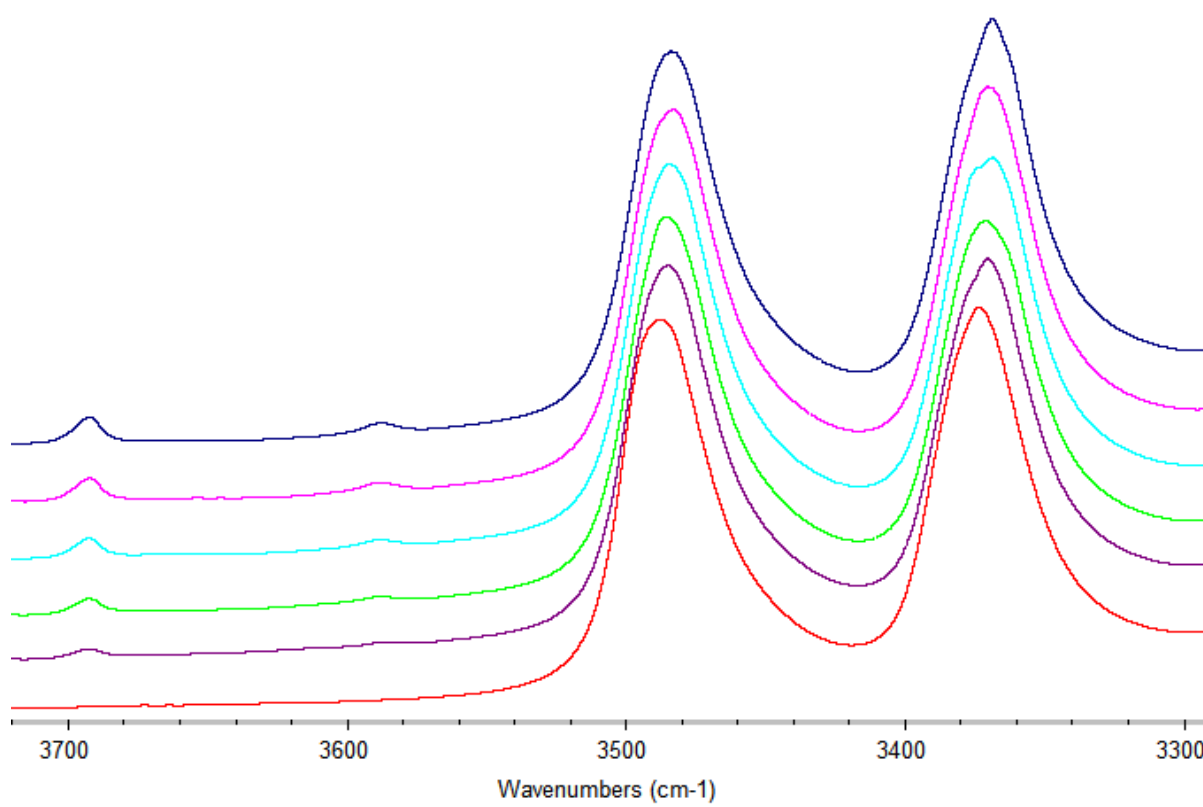


Figure 2.7. Stacked spectra obtained in study **B2**, in ascending order (*i.e.* bottom = first measurement at CO₂/N₂ = 0.0/1.0, top = final measurement at CO₂/N₂ = 1.0/0.0). For clarity, only the region between 3300 and 3700 cm⁻¹ is shown, as this region contains all the bands relevant to analysis. The y-axis is absorbance.

Table 2.14. Peak integration results for experiment **B2**. The ($\nu_1 + \nu_3$) combination band was integrated in the range 3568 – 3608 cm^{-1} ; the ($2\nu_2 + \nu_3$) combination band was integrated in the range 3672 – 3712 cm^{-1} . WHM (Width at half maximum), Centre and Height refer to profile of the integrated band.

Band Integrated	Pressure / CO₂/N₂	Area / Abs cm⁻¹	FWHM / cm⁻¹	Centre / cm⁻¹	Height / Abs
($\nu_1 + \nu_3$)	0.0/1.0	-0.280	35.3	3595	-0.0084
($\nu_1 + \nu_3$)	0.2/0.8	0.040	8.2	3589	0.0102
($\nu_1 + \nu_3$)	0.4/0.6	0.314	11.7	3589	0.0255
($\nu_1 + \nu_3$)	0.6/0.4	0.506	12.6	3589	0.0378
($\nu_1 + \nu_3$)	0.8/0.2	0.659	13.0	3589	0.0472
($\nu_1 + \nu_3$)	1.0/0.0	0.762	13.1	3589	0.0540
($2\nu_2 + \nu_3$)	0.0/1.0	-0.010	4.8	3708	-0.0018
($2\nu_2 + \nu_3$)	0.2/0.8	0.593	10.5	3693	0.0493
($2\nu_2 + \nu_3$)	0.4/0.6	0.989	10.3	3693	0.0843
($2\nu_2 + \nu_3$)	0.6/0.4	1.305	10.4	3693	0.1101
($2\nu_2 + \nu_3$)	0.8/0.2	1.589	10.5	3693	0.1329
($2\nu_2 + \nu_3$)	1.0/0.0	1.853	10.7	3693	0.1514

Table 2.15. Results of the model-fit approach to the spectral region containing the MOF framework amine bands in study **B2**. Values are quoted to 3 significant figures.

Pressure / CO₂/N₂	C1	C1 error (σ)	C2	C2 error (σ)	Reduced χ^2	Adjusted R²
0.0/1.0	1.00	0.00	3.15×10^{-17}	0.00	0.00	1.00
0.2/0.8	0.381	0.0159	0.623	0.0144	9.76×10^{-4}	0.998

0.4/0.6	0.252	0.0159	0.750	0.0143	9.68×10^{-4}	0.998
0.6/0.4	0.175	9.38×10^{-3}	0.819	8.49×10^{-3}	3.40×10^{-4}	1.00
0.8/0.2	0.108	6.77×10^{-3}	0.886	6.13×10^{-3}	1.78×10^{-4}	1.00
1.0/0.0	2.89×10^{-15}	7.15×10^{-18}	1.00	3.18×10^{-17}	2.60×10^{-31}	1.00

2.3.5. Volumetric Gas Adsorption

Volumetric CO₂ adsorption was performed using a Micromeritics ASAP 2020Plus Analyser (Figure 2.13, Section 2.4.2). **SHF-61-DMF** (*ca.* 100 mg) was activated according to the literature procedure for bulk-phase activation,¹ and then further activated (*in situ* on the analyser) by applying vacuum for an additional 16 hours at 150 °C. CO₂ adsorption and desorption was measured at 195 K using a dry ice/acetone bath for temperature control.

2.4. Results & Discussion

2.4.1. CO₂ Uptake at 298 K

Carrington *et al.* showed that partially desolvated **SHF-61-DMF** fully opens as a response to CO₂ uptake at 298 K (Figure 2.8).¹ In their study, data set **N1.2** was taken under vacuum, and data set **N1.4**, **N1.5** and **N1.6** were measured under 5 bar, 10 bar and 20 bar of CO₂ respectively (**N1.1** is the sample before desolvation). As can be seen in Figure 2.9, by the 5 bar measurement, the MOF pores are virtually fully open. An intermediate point was measured at 1 bar CO₂ (**N1.3**), but data quality was not sufficient to determine the unit cell parameters. Since full structure solutions were possible for points **N1.1**, **N1.2**, **N1.4** and **N1.5**, it seems unlikely that the poor data quality of **N1.3** is due to sample degradation, and it is more likely that the sample either: is changing during the measurement; or exists with a range of pore states at 1 bar CO₂.

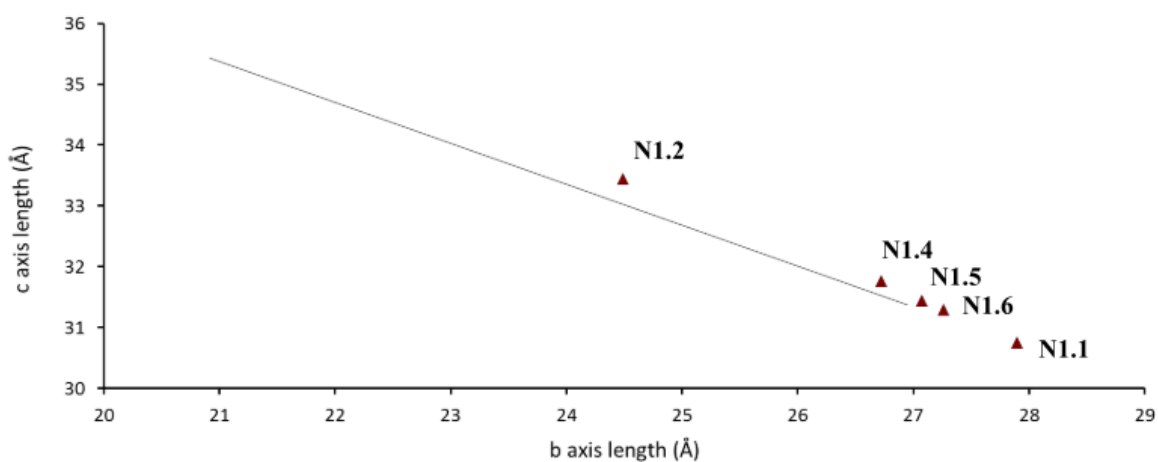


Figure 2.8. Study **N1** from the article by Carrington *et al.*,¹ monitoring framework expansion of partially-desolvated **SHF-61-DMF** as a response to CO₂ pressure at 298 K. The trend line indicates the profile of desolvation from the *ex situ* single crystal desolvation studies by Carrington *et al.* **N1.1** = sample before desolvation; **N1.2**, **N1.4**, **N1.5**, **N1.6** = vacuum, 5 bar, 10 bar, 20 bar respectively. Figure reproduced from reference 1 with permission from Nature Publishing Group.

To answer this question, we performed *in situ* single crystal-ray diffraction study **A1**, in which **SHF-61-DMF** was monitored under vacuum and at CO₂ pressures of 0.5, 1 and 2 bar at 298 K. The results are provided in Table 2.1 (Section 2.3.2), and shown graphically in Figure 2.9.

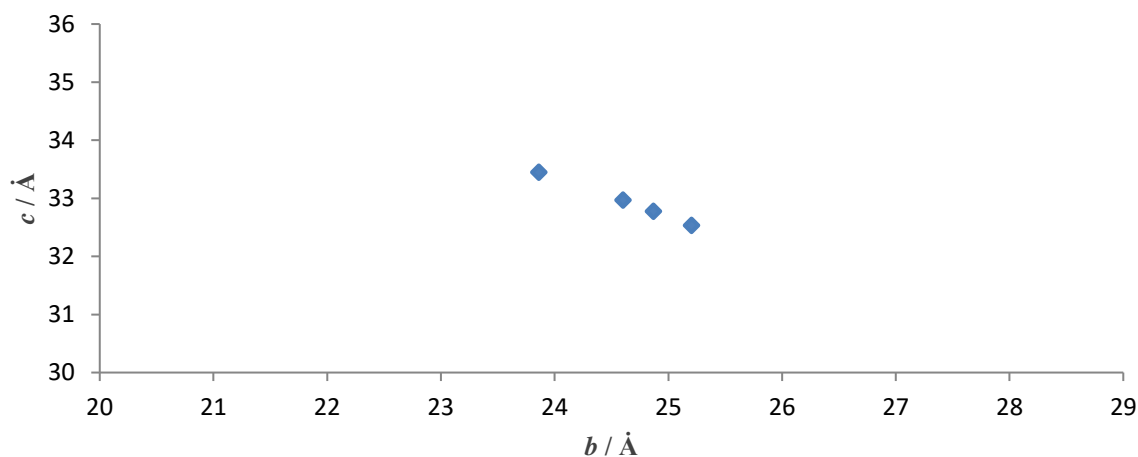


Figure 2.9. *b*- and *c*-axes of **SHF-61-DMF** during study **A1**. Left to right = vacuum, 0.5, 1, 2 bar CO₂.

Although study **A1** starts slightly more closed than the previously reported study **N1** ($b = 23.8591(8)$ for **A1**, $b = 24.490(2)$ for **N1**), it is clear from the continuous nature of the profile that intermediate states do exist at low pressure, and that the partially desolvated MOF opens in a continuous fashion up to CO₂ pressures of 2 bar at 298 K. This degree of opening seen in study **A1**

contrasts that of the bulk-phase material when monitored by *in situ* powder X-ray diffraction by Carrington *et al.*, in which the *b*-axis only reaches a value of *ca.* 24 Å at a pressure of 5 bar, despite starting at a similar value under vacuum (Figure 2.10).¹

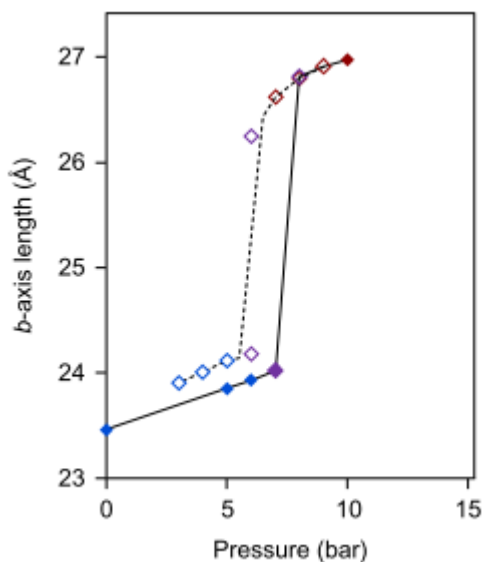


Figure 2.10. *b*-axis as a function of CO₂ pressure at 298 K in bulk-phase partially-desolvated **SHF-61-DMF**. Image reproduced from reference 1 with permission from Nature Publishing Group.

CO₂ uptake as a function of partial pressure was also monitored by *in situ* infra-red spectroscopy, in studies **B1** (activated **SHF-61-DMF**) and **B2** (activated **SHF-61-CHCl₃**). In both experiments, a single crystal of the sample was monitored at CO₂/N₂ partial pressures of 0.0/1.0, 0.2/0.8, 0.4/0.6, 0.6/0.4, 0.8/0.2 and 1.0/0.0. Integration of the CO₂ ($2\nu_2 + \nu_3$) combination bands showed that in the closed framework (activated **SHF-61-DMF**), the amount of CO₂ absorbed was *ca.* 35 % of that absorbed by the open framework (activated **SHF-61-CHCl₃**) (Figure 2.11), which is essentially the same result found in the gravimetric absorption studies performed by Carrington *et al.*,¹ despite this experiment being done in the presence of nitrogen, and only sampling pressures up to 1 bar (gravimetric adsorption studies used CO₂ pressures up to 20 bar). It should be noted that the crystal of activated **SHF-61-CHCl₃** used in **B2** had an absorbance *ca.* 2.5 times stronger than the crystal of activated **SHF-61-DMF** used in **B1**, and this factor has been applied to the data in Figure 2.12; the *unnormalized* data can be found in Table 2.12, Section 2.3.4.

As stated in Section 2.3.4, the peak integration for studies **B1** and **B2** was performed by Alex Tansell, Cardiff University.

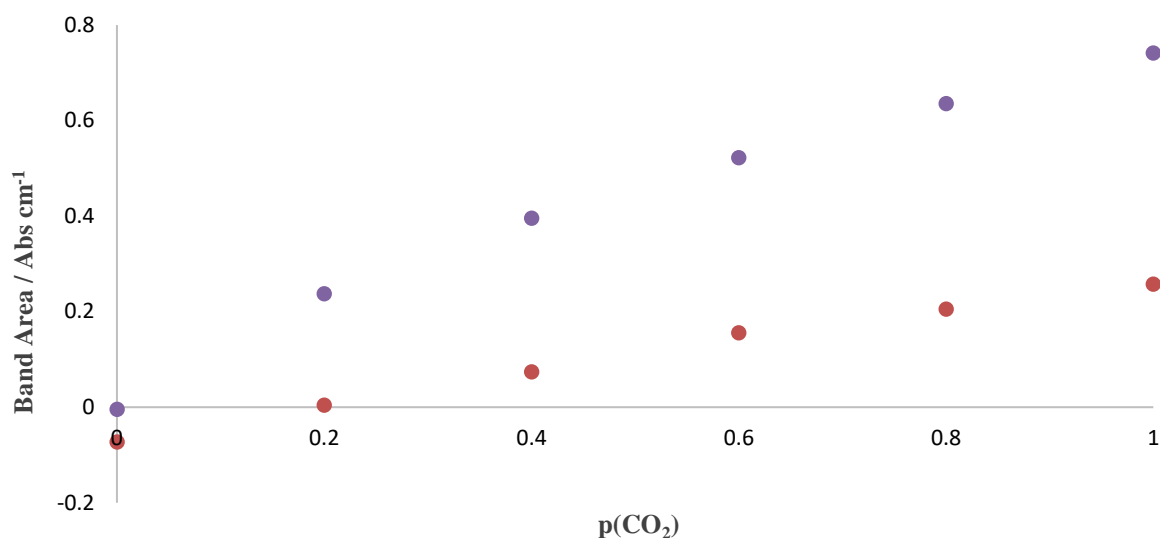


Figure 2.11. Band area from peak integration of the CO₂ ($2\nu_2 + \nu_3$) combination bands in study **B1** (red circles) and **B2** (blue circles – normalised to account for crystal maximum absorption) as a function of partial pressure of CO₂.

The framework amine bands were unsuitable for normal peak fitting approaches, as the resolution between bands arising from saturated (*i.e.* interacting with guest) and unsaturated (non-interacting) framework amine groups was too small. Additionally, these experiments provide no information regarding the unit cell dimensions of the MOF, but it cannot be ruled out that changes in MOF pore dimensions could be affecting the shape of the framework amine bands, since the two interpenetrated diamondoid networks of the framework interact via weak hydrogen-bonding interactions between these amine groups.¹ Instead, we used a “model-fit” approach, where each spectrum in the study was fitted using the following equation:

$$Spectrum = C1(A) + C2(B).$$

Where: *Spectrum* = the spectrum to be fitted; *A* = the spectrum at the start of the study, before exposure to CO₂; *B* = the spectrum at the end of the study (CO₂/N₂ = 1.0/0.0). The coefficients C1 and C2 therefore represent how closely the spectrum resembles the start or end (respectively) of the study. This approach is based on the assumption that any spectrum measured between the start and end of the study can be treated as a composite of the initial and final measurements. It is important to note

that this model-fit was only carried out only for the region containing the framework amine bands (more information is available in Section 2.3.4). The data are tabulated in Tables 2.13 and 2.15, Section 2.3.4, and shown graphically in Figure 2.12. In both studies, errors are small, and the reduced χ^2 and adjusted R^2 values indicate a good fit. Interestingly, in study **B1**, the amine bands stop changing after a pressure $\text{CO}_2/\text{N}_2 = 0.6/0.4$, implying that saturation of the amine bands by CO_2 has already been achieved at this stage. A single-crystal X-ray diffraction study by Carrington *et al.* (**N2** in their report) showed that if **SHF-61-DMF** is activated more thoroughly (b -axis = 22.398(7) Å), then adsorption of CO_2 at 298 K doesn't fully open the framework; instead an expansion of only *ca.* 1 Å is observed in the b -axis at a pressure of 20 bar.¹ Considering this information in light of the infra-red spectroscopy studies here, a reasonable conclusion would be that initial saturation of the framework amine bands with CO_2 occurs at low pressure. At higher pressures, the CO_2 is absorbed into the remaining pore space without significant interaction with the framework, and therefore there is no cause for large-scale expansion. This would also explain why the gravimetric absorption for activated **SHF-61-DMF** has a Type I isotherm, reminiscent of a rigid microporous material. In contrast, the model-fitting results of study **B2** (open framework – activated **SHF-61-CHCl₃**) indicate that the amine bands are still changing at the end of the experiment, suggesting that in the open framework saturation does not occur at such low pressures. It is possible that the reason for this is the presence of nitrogen: Since both N_2 and CO_2 are present in the infra-red spectroscopy studies, there may be an equilibrium between the two gases and the amine groups, the position of which changes with each pressure step. Each time the pressure changes to a higher $p(\text{CO}_2)$, the amine bands become more saturated with CO_2 . Whilst it seems unlikely that nitrogen would compete with another guest, it has been shown that CO_2 does not bind strongly to amine bands.⁴⁻⁶ This interplay between the two gases would not occur in experiment **B1**, as activated **SHF-61-DMF** is non-porous to nitrogen.¹

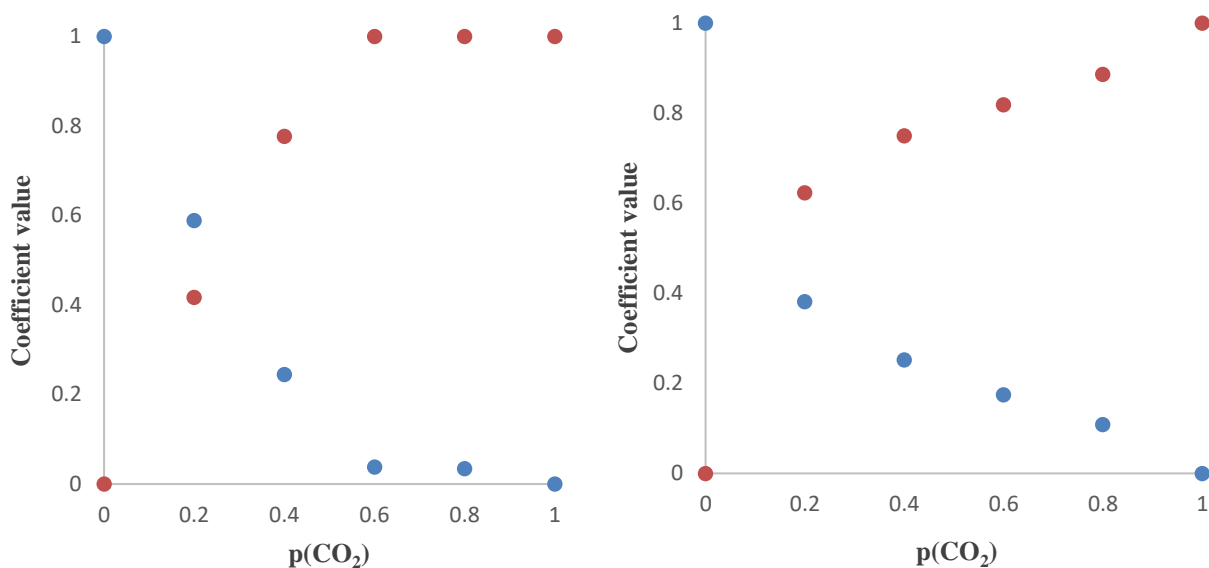


Figure 2.12. Left: Model-fitting results for the amine bands in study **B1**. Right: Model-fitting results for the amine bands in study **B2**. In both studies: coefficient C1 (first spectrum) = blue circles; coefficient C2 (last spectrum) = red circles.

The wavenumber position (at peak maximum) of the symmetric and asymmetric NH₂ stretches (*ca.* 3370 cm⁻¹ and *ca.* 3480 cm⁻¹ respectively) shift by 2 – 4 cm⁻¹ over the course of experiments **B1** and **B2**. This is similar to an analogous study by Greenaway *et al.* on another amine-functionalised MOF, Sc₂(NH₂BDC)₃, and indicates that the adsorbed CO₂ is interacting weakly with the framework amine substituents.²¹ A similar study on **NH2-MIL-53(Al)** (an amino-functionalised, aluminium based **MIL-53** analogue) found that adsorbed CO₂ did not interact with the amine substituents, binding instead to the hydroxyl groups of the framework.⁶ Given that weak NH₂⋯CO₂ interactions *are* observed in **SHF-61**, it follows that the amine substituents must be the preferential site of adsorption for CO₂.

2.4.2. CO₂ Uptake at 195 K

Volumetric CO₂ adsorption was performed on activated **SHF-61-DMF** at 195 K (Figure 2.13). The amount of CO₂ adsorbed reaches a plateau at *ca.* 1.75 mmol g⁻¹, which indicates that the material remains in a narrow-pore state, which is consistent with the published data.¹ However, this uptake is smaller than expected. In the published gravimetric studies, the amount of CO₂ adsorbed at 20 bar is *ca.* 2.5 mmol g⁻¹ at 298 K, and *ca.* 3 mmol g⁻¹ at 258 K. Clearly, with an even lower temperature of 195 K, a higher CO₂ capacity would be expected. This is further exaggerated by the fact that 20 bar of

CO₂ at 298 K corresponds to a relative pressure, p/p_0 , of only *ca.* 0.31, whereas 1 bar at 195 K is a relative pressure of 1.0. The activation procedure for this volumetric adsorption experiment was the same as for the gravimetric studies. It is possible that atmospheric moisture uptake is the cause; activated **SHF-61-DMF** is known to expand in air due to adsorption of water.¹ The presence of a hysteresis indicates that carbon dioxide is involved in some interactions with the pore surface.

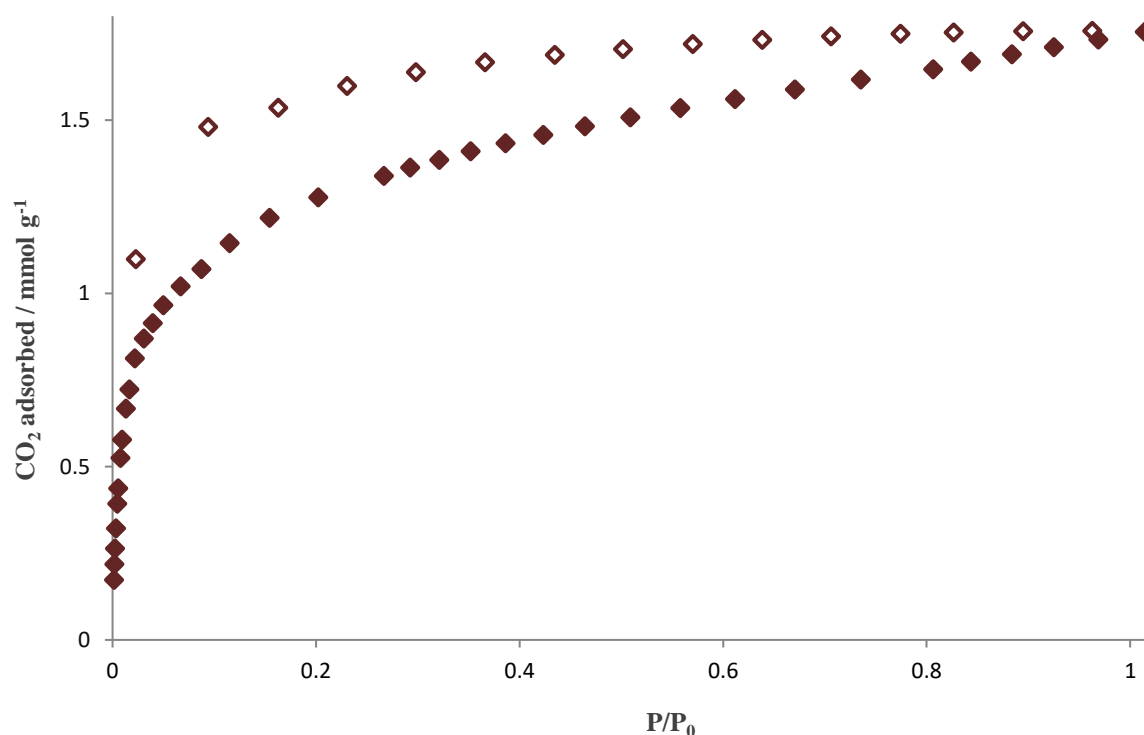


Figure 2.13. Volumetric CO₂ adsorption isotherm for activated **SHF-61-DMF** at 195 K. Filled markers = adsorption, hollow markers = desorption.

Six separate X-ray diffraction studies monitoring *in situ* the structural changes during CO₂ uptake by activated **SHF-61-DMF** were performed at 195 K; three single-crystal experiments, numbered **C1a**, **C1b** and **C1c**, and three powder diffraction experiments, numbered **C2a**, **C2b** and **C2c**. The main differences between these experiments is the level of desolvation in the samples prior to CO₂ uptake. This was achieved by using different activation methods, which are detailed in Sections 2.3.2 and 2.3.3. The degree of pore opening is presented graphically in Figures 2.14 and 2.15. To simplify the situation and allow comparisons to be made easily, the *b*-axis dimension of the MOF is plotted as a function of CO₂ pressure.

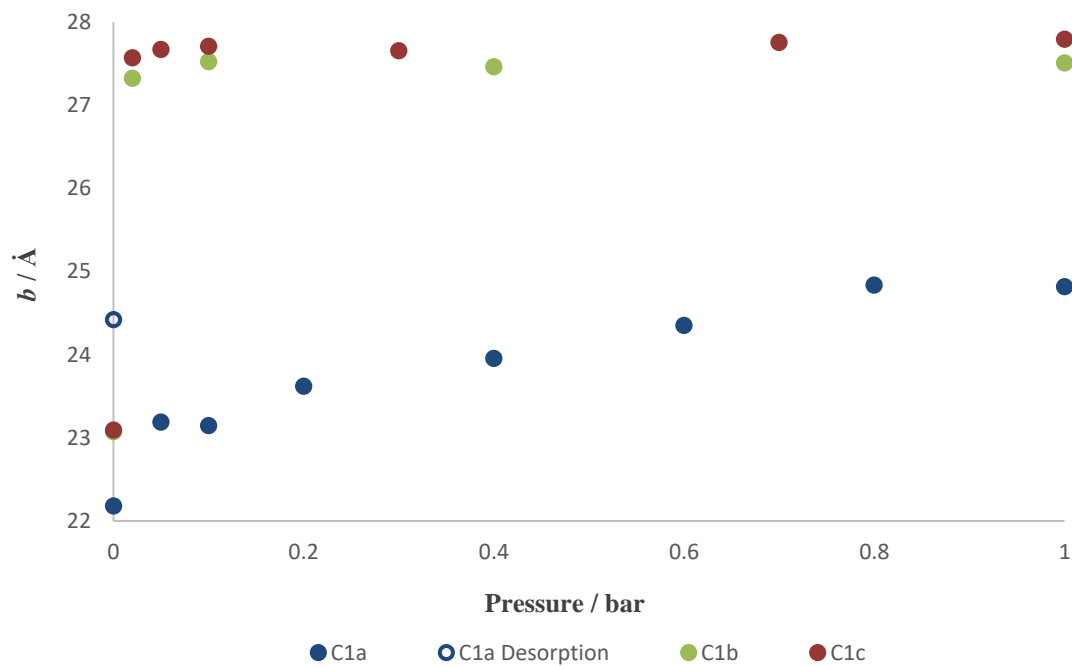


Figure 2.14. Single-crystal X-ray diffraction studies **C1a**, **C1b** and **C1c**, showing change in b -axis (\AA) as a function of CO_2 pressure at 195 K. The vacuum measurements for **C1b** and **C1c** are almost identical.

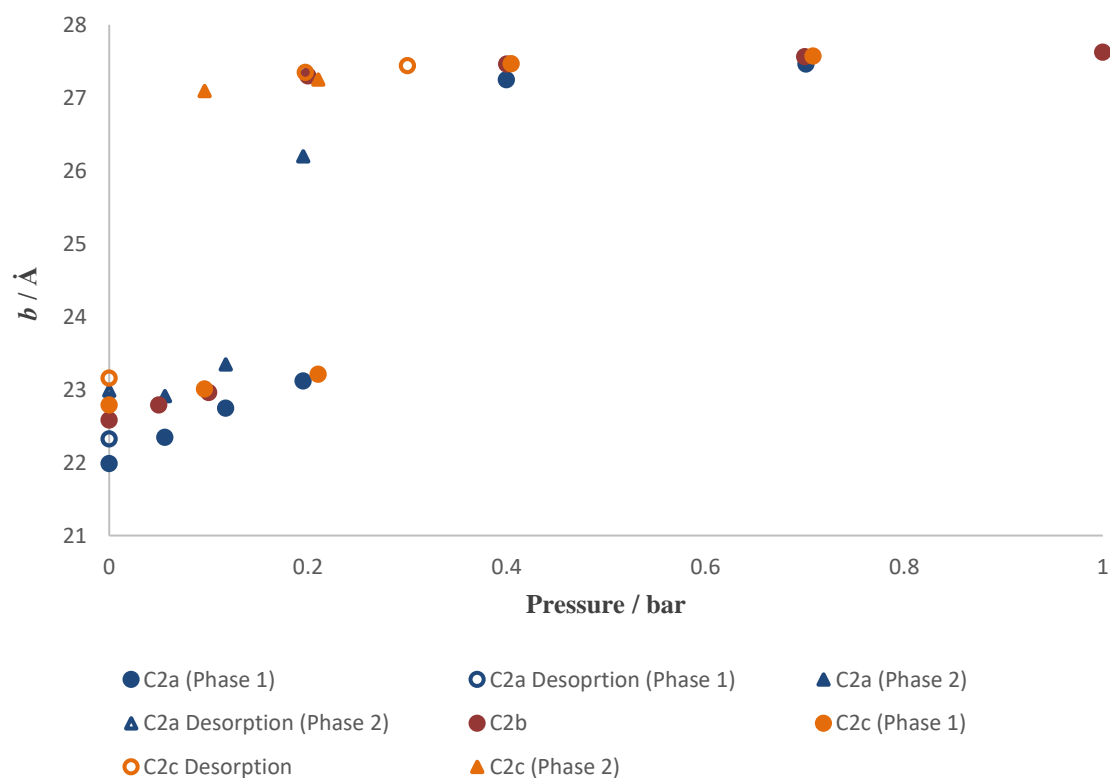


Figure 2.15. Powder X-ray diffraction studies **C2a**, **C2b** and **C2c**, showing change in b -axis (\AA) as a function of CO_2 pressure at 195 K.

The powder X-ray diffraction studies on the bulk-phase material at 195 K all show a gated expansion at a CO₂ pressure between 0.1 and 0.2 bar. In some studies (**C2a** and **C2c**), the patterns around this region contain two phases corresponding to closed- and open-pore forms of the MOF. The maximum *b*-axis value *before* this gate is 23.3 Å, and in each experiment, a small degree of continuous flexibility occurs at low pressure, until the *b*-axis is around this value. In the volumetric CO₂ uptake experiment at 195 K (and the published gravimetric studies at higher temperatures¹), a low uptake was observed, indicating no/very little framework expansion. It therefore follows that the samples used for the *in situ* powder X-ray diffraction studies were not *fully* desolvated. This is not unsurprising – the first measurement in experiment **C2a** has two phases, clearly indicating incomplete desolvation, and our general experience of this material is that complete removal of guest DMF is very difficult to achieve when the sample is packed inside a capillary. It can therefore be concluded at this stage that bulk-phase, partially-desolvated **SHF-61-DMF** exhibits a gated expansion upon CO₂ uptake at 195 K, at a pressure of around 0.1 – 0.2 bar, and at a *b*-axis value of *ca.* 23 Å. This is in fact similar to most flexible metal-organic frameworks;²² such as **MIL-53**²³ and **In(TCPBDA)**⁻ (discussed in Chapter 1).²⁴ Single-crystal *in situ* studies **C1b** and **C1c** are very similar. They have very similar start and end points, and by the second measurement at 0.02 bar (*i.e.* the first measurement after CO₂ exposure), a gated expansion takes place, and the MOF fully opens. This initially appears to contradict the powder diffraction data; however, the starting points of the experiments are different. At the start of the single-crystal experiments **C1b** and **C1c**, *b* ≈ 23.1 Å. As they already fulfil this criterion for the gate to occur, it does so at the first CO₂ dosing. However, in the powder X-ray diffraction studies, the samples start in a more closed state ($22.0 \text{ \AA} \leq b \leq 22.8 \text{ \AA}$), and the first few pressure steps are spent gradually opening the sample until the gate threshold is reached. The outlier in these data sets is experiment **C1a**, which starts at *b* ≈ 22.1 Å, and undergoes a smaller, continuous (non-gated) expansion throughout the study, reaching a plateau of *b* ≈ 24.8 Å at 0.8 bar. This is *not* due to the starting point of the experiment, as PXRD study **C2a** has a starting value of *b* ≈ 22.0 Å, and shows a gated expansion (fully opening) at 0.2 bar. It is possible that a particle-size effect is occurring; Carrington *et al.* hypothesized that fully desolvated **SHF-61-DMF** is prevented from opening due to strong framework-cation-framework interactions,¹ if these interactions are present in

the partially desolvated material as well, then they may have a cumulative effect on larger particles. This is obviously speculative, and with only one data set it is impossible to draw a conclusion. Additionally, it should not be ignored that this effect was also observed in the 298 K SCXRD experiment **N2** in the publication by Carrington *et al.*,¹ and in both experiments, data quality was insufficient to allow full structure solutions.

Comparing the data at 195 K and 298 K, some similarities are observed. Firstly, 298 K study **N2** reported by Carrington *et al.*¹ is actually very similar to study 195 K **C1c** in this thesis. The starting points differ by only *ca.* 0.2 Å in the *b*-axis, and at 20 bar ($p/p^0 \approx 0.31$) in the 298 K experiment, the *b*-axis has reached a value of *ca.* 23.4 Å, compared to 23.6 Å at $p/p^0 = 0.2$ in the 195 K study. Neither sample displays full pore-opening under the monitored pressure ranges. The simplest way to compare full-opening at the two temperatures is to compare study **C2a** in this thesis with 298 K study **N5** by Carrington *et al.*¹ Again, both are powder diffraction experiments on samples which start at similar levels of pore closure, differing by less than 0.02 Å in the *b*-axis. At 298 K, the open-pore form first appears as a minor phase at 5 bar ($p/p^0 \approx 0.078$); and at 20 bar ($p/p^0 \approx 0.31$) the material has a *b*-axis of 25.56(4) Å. In contrast, at 195 K, the open-pore form first appears as a minor phase at the higher relative pressure of 0.2. By the next measurement at $p/p^0 = 0.4$, the material has fully opened, with a *b*-axis of 27.557(1) Å. Comparison of the other data sets is difficult as the 298 K studies **N1**, **N3** and **N4** have starting points that are less closed than 195 K powder diffraction studies presented here, and there is no clear *b*-axis threshold for gated expansion (*cf.* 23 Å at 195 K). It is entirely plausible, however, that the difference in starting points is a temperature effect. If that is the case, then it seems that the gate upon CO₂ uptake is moved to a higher relative pressure by lowering the temperature; the three 298 K studies **N1**, **N3** and **N4** all have pore-opening by $p/p^0 \approx 0.078$ (5 bar), as either the only phase (**N1**) or as minor phases (**N3** and **N4**), whereas in the 195 K powder diffraction studies presented here, the lowest pressure gate is at $p/p^0 = 0.1$ in study **C2c**, and the open-pore MOF is only present at this pressure as a minor phase (the rest of the sample still residing in the narrow-pore form). In contrast, the 195 K single crystal diffraction studies **C1b** and **C1c** presented here both have gated

openings at $p/p_0 = 0.02$, far lower than in all the analogous experiments at either 195 K or 298 K, despite starting in more closed states ($b \approx 23.1 \text{ \AA}$) than all 298 K studies except **N5**.

2.4.3. SO₂ Uptake at 273 K

Four SO₂ uptake studies were monitored *in situ* by X-ray diffraction: two single crystal experiments, **D1a** and **D1b**, summarised in Figure 2.16; and two powder experiments, **D2a** and **D2b**, summarised in Figure 2.17.

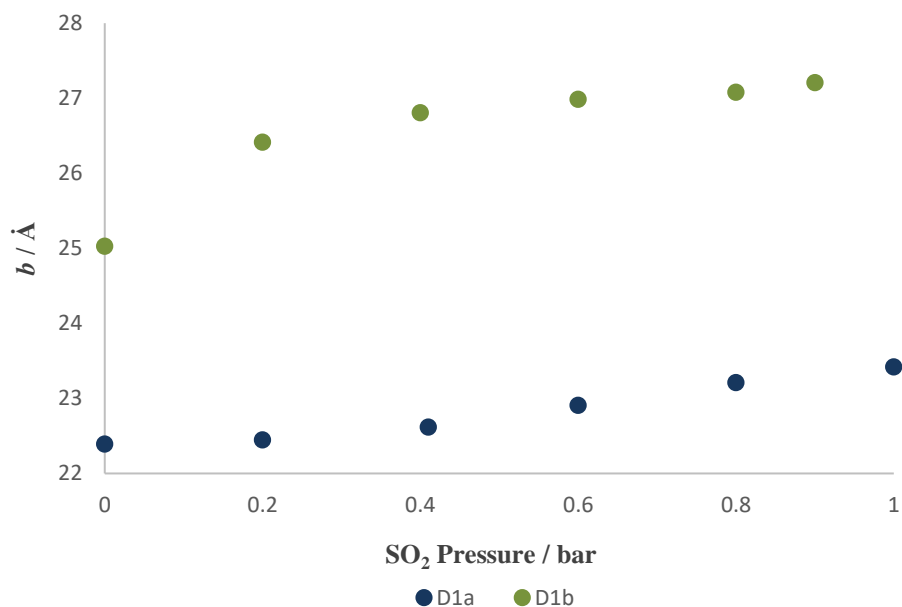


Figure 2.16. Single crystal X-ray diffraction studies **D1a** and **D1b**, showing change in b -axis (\AA) as a function of CO₂ pressure at 273 K.

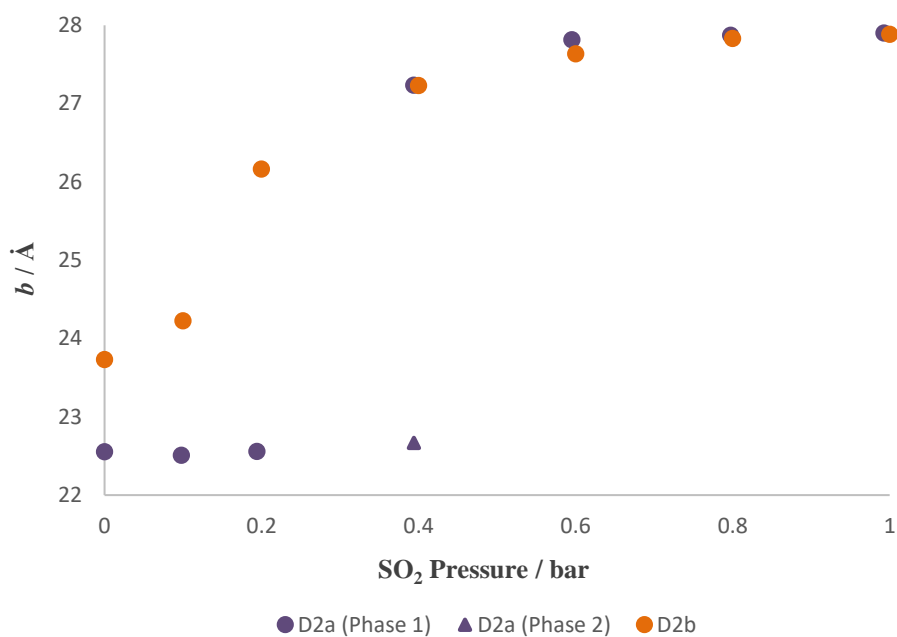


Figure 2.17. Powder X-ray diffraction studies **D2a** and **D2b**, showing change in b -axis (Å) as a function of CO₂ pressure at 273 K.

Powder diffraction study **D2a** shows the presence of a gate at 0.4 bar SO₂ ($p/p_0 \approx 0.17$) at a b -axis value of *ca.* 22.5 Å. Study **D2b** has a starting b -axis of 23.7 Å, and instead shows the largest change occurring between 0.1 and 0.2 bar. While the profile of **D2b** looks continuous by visual inspection, there could indeed be a gate between these pressures that is not directly observed due to the relatively open starting point of the experiment coupled with the sparseness of pressure steps monitored (compared to a gravimetric or volumetric adsorption study, for example). Single-crystal experiment **D1a** starts in a similar pore state to study **D2a**, but doesn't undergo gated expansion, instead opening continuously by only 1 Å (in the b -axis) over the course of the experiment. For reference, 1.0 bar of SO₂ at 273 K is equivalent to a relative pressure of 0.42. Study **D1b** starts with a relatively open-pore material, and therefore is opened after the first pressure step. As in the case of CO₂ uptake, it seems that there may be a particle-size effect which prevents pore-opening in macrocrystalline samples which have been more thoroughly activated (*i.e.* had more solvent removed). Similarly, the gate at $p/p_0 = 0.17$ is in the same range as the gate for expansion upon CO₂ uptake at 195 K (0.1 – 0.2 bar). Therefore, at this stage, there is insufficient evidence to suggest that the framework opens at a different gate pressure as a response to SO₂ relative to CO₂. Study **D2a** shows very little continuous

expansion before the gated opening at $b \approx 22.5 \text{ \AA}$, whereas in the analogous 195 K CO₂ experiments, continuous opening occurred in samples that started with $b < 23 \text{ \AA}$, and gated expansion only occurred once this b -axis threshold had been reached. It is therefore possible that rather than shifting the gate *pressure*, the effect of using SO₂ rather than CO₂ has been to shift the b -axis threshold for gated opening. To be sure of this conclusion, however, more studies would be needed to support the results of **D2a**. A report by Savage *et al.* on a different metal-organic framework, **MFM-300(In)** (MFM = Manchester Framework Material), found that SO₂ was adsorbed with high selectivity over CO₂ when a 1:1 ratio of the two guests was used at 298 K.²⁵ It was further shown that SO₂ is involved in interactions with the framework hydroxyl groups of **MFM-300(In)**, and additionally involved in interactions with other adsorbed SO₂ molecules. Given that in **SHF-61**, there does not seem to be much difference between CO₂ uptake at 195 K and SO₂ uptake at 273 K, it follows that there must not be any strong binding sites for SO₂ in **SHF-61**. This mirrors the infra-red spectroscopy studies performed with CO₂ at 298 K (**B1** and **B2**), in which it is evident that CO₂ is not involved in strong interactions with the MOF framework.

2.5. Conclusion

The work presented in this chapter has shown that gated expansion of **SHF-61** upon CO₂ uptake occurs even in relatively narrow-pore versions, but supports the original findings that fully activated **SHF-61-DMF** does not open in response to CO₂ pressure. It is evident that this is the case at both 195 K and 298 K, from both *in situ* X-ray diffraction studies and volumetric and gravimetric adsorption experiments. Single-crystal infra-red spectroscopic studies during CO₂ adsorption indicate that adsorbed CO₂ interacts relatively weakly with the framework amine substituents, and quantification of the CO₂ combination bands in the open and closed MOF experiments supports the difference in adsorption observed in the gravimetric studies of the open- and closed-pore forms, and by extension supports the observation that fully activated **SHF-61-DMF** does not open as a response to CO₂ uptake. Additionally, whether a partially-desolvated sample fully opens in a gated fashion or partially opens in a continuous fashion is not consistent across single-crystal and powder X-ray diffraction studies, leading to the hypothesis that a particle-size effect is occurring, which hinders full-opening in

larger crystals. This effect is also observed in SO₂ uptake experiments at 273 K. The gate pressure appears unchanged when switching to SO₂ (relative to CO₂), but a tentative conclusion is that there is a *b*-axis threshold for gated expansion, and that this is *ca.* 0.6 Å lower for SO₂ at 273 K than CO₂ at 195 K. In other MOF materials that interact strongly with CO₂ and SO₂ *via* framework hydroxyl groups, SO₂ is adsorbed selectively, than CO₂. The absence of this effect in **SHF-61**, coupled with the lack of evidence for strong amine-CO₂ interactions, suggests that SO₂ does not interact strongly with **SHF-61**.

2.6. References

- 1 E. J. Carrington, C. A. McAnally, A. J. Fletcher, S. P. Thompson, M. Warren and L. Brammer, *Nat. Chem.*, 2017, **9**, 882–889.
- 2 C. Chen, J. Kim and W. S. Ahn, *Korean J. Chem. Eng.*, 2014, **31**, 1919–1934.
- 3 Z. Qiao, N. Wang, J. Jiang and J. Zhou, *Chem. Commun.*, 2016, **52**, 974–977.
- 4 K. Sumida, D. L. Rogow, J. A. Mason, T. M. McDonald, E. D. Bloch, Z. R. Herm, T. H. Bae and J. R. Long, *Chem. Rev.*, 2012, **112**, 724–781.
- 5 E. Stavitski, E. A. Pidko, S. Couck, T. Remy, E. J. M. Hensen, B. M. Weckhuysen, J. Denayer, J. Gascon and F. Kapteijn, *Langmuir*, 2011, **27**, 3970–3976.
- 6 M. Mihaylov, K. Chakarova, S. Andonova, N. Drenchev, E. Ivanova, A. Sabetghadam, B. Seoane, J. Gascon, F. Kapteijn and K. Hadjiivanov, *J. Phys. Chem. C*, 2016, **120**, 23584–23595.
- 7 J. H. Carter, X. Han, F. Y. Moreau, I. Da Silva, A. Nevin, H. G. W. Godfrey, C. C. Tang, S. Yang and M. Schröder, *J. Am. Chem. Soc.*, 2018, **140**, 15564–15567.
- 8 M. Wang, L. Guo and D. Cao, *Anal. Chem.*, 2018, **90**, 3608–3614.
- 9 P. Brandt, A. Nuhnen, M. Lange, J. Möllmer, O. Weingart and C. Janiak, *ACS Appl. Mater. Interfaces*, 2019, **11**, 17350–17358.
- 10 B. Supronowicz, A. Mavrandonakis and T. Heine, *J. Phys. Chem. C*, 2013, **117**, 14570–14578.
- 11 B. Yuan, D. Ma, X. Wang, Z. Li, Y. Li, H. Liu and D. He, *Chem. Commun.*, 2012, **48**, 1135–1137.

- 12 O. V. Dolomanov, L. J. Bourhis, R. J. Gildea, J. A. K. Howard & H. Puschmann, *J. Appl. Cryst.*, 2009, **42**, 339–341.
- 13 G. M. Sheldrick, *Acta Cryst. A.*, 2008, **64**, 112–22.
- 14 A. L. Spek, *Acta Cryst. C*, 2015, **71**, 9–18.
- 15 A. L. Spek, *Acta Cryst. D.*, 2009, **65**, 148–155.
- 16 S. P. Thompson, J. E. Parker, J. Potter, T. P. Hill, A. Birt, T. M. Cobb, F. Yuan & C. C. Tang, *Rev. Sci. Instrum.*, 2009, **80**, 075107.
- 17 S. P. Thompson, J. E. Parker, J. Marchal, J. Potter, A. Birt, F. Yuan, R. D. Fearn, A. R. Lennie, S. R. Street & C. C. Tang, *J. Synchrotron Radiat.*, 2011, **18**, 637–648.
- 18 G. S. Pawley, *J. Appl. Cryst.*, 1981, **14**, 357–361.
- 19 A. A. Coelho, TOPAS Academic. Version 4.1, 2007.
- 20 K. Isokoski, C. A. Poteet and H. Linnartz, *Astron. Astrophys.*, 2013, **555**, 4–9.
- 21 A. Greenaway, B. Gonzalez-Santiago, P. M. Donaldson, M. D. Frogley, G. Cinque, J. Sotelo, S. Moggach, E. Shiko, S. Brandani, R. F. Howe and P. A. Wright, *Angew. Chem. Int. Ed.*, 2014, **53**, 13483–13487.
- 22 A. Schneemann, V. Bon, I. Schwedler, I. Senkovska, S. Kaskel and R. A. Fischer, *Chem. Soc. Rev.*, 2014, **43**, 6062–6096.
- 23 C. Serre, F. Millange, C. Thouvenot, M. Noguès, G. Marsolier, D. Louër and G. Férey, *J. Am. Chem. Soc.*, 2002, **124**, 13519–13526.
- 24 X. Li, X. Chen, F. Jiang, L. Chen, S. Lu, Q. Chen, M. Wu, D. Yuan and M. Hong, *Chem. Commun.*, 2016, **52**, 2277–2280.
- 25 M. Savage, Y. Cheng, T. L. Easun, J. E. Eyley, S. P. Argent, M. R. Warren, W. Lewis, C. Murray, C. C. Tang, M. D. Frogley, G. Cinque, J. Sun, S. Rudić, R. T. Murden, M. J. Benham, A. N. Fitch, A. J. Blake, A. J. Ramirez-Cuesta, S. Yang and M. Schröder, *Adv. Mater.*, 2016, **28**, 8705–8711.

3. Solvent-Uptake in SHF-61: *in situ* Spectroscopy Studies

3.1. Abstract

A series of solvent uptake experiments are presented, monitored using *in situ* infra-red spectroscopy at Beamline B22, Diamond Light Source. DMF uptake is found to induce a gated opening in closed-pore **SHF-61**. Open-pore **SHF-61** is found to accommodate DMF and cyclopentanone by forming interactions with the ligand amine substituents; these interactions being stronger in the case of DMF. Water is also found to bind to the ligand amine groups, and may produce a pore-closing effect, similar to that seen in **MIL-53**. The open framework is found to also adsorb chloroform and isopropanol. The solvent dependence of **SHF-61** activation is discussed, along with a discussion of some of the limits of *in situ* infra-red spectroscopy on the **SHF-61** system, and suggestions for future directions of the project.

3.2. Introduction

Arguably the most interesting property of the MOF **SHF-61** is the presence of two desolvated states – open or closed.¹ This is, to our knowledge, the first instance of such path-dependent activation behaviour; conventionally MOFs only have one desolvated state (which can be either open or closed pore depending on the material).²⁻⁶ The two solvents discussed in the **SHF-61** publication are chloroform and DMF; **SHF-61-DMF** adopts a closed-pore state upon activation whereas **SHF-61-CHCl₃** remains in an open-pore state. One of the obvious differences between DMF and chloroform is their polarity, and before the publication by Carrington *et al.*¹ this was considered as a possibility for the difference in desolvation behaviour between **SHF-61-DMF** and **SHF-61-CHCl₃**. There are numerous ways to measure/estimate the polarity of a material; a suitable parameter for this work is the $E_T(30)$ value, first proposed by Dimroth *et al.* in 1966.⁷ This was chosen as it represents not only the molecular dipole, but also more specific properties, such as the ability of the species to form hydrogen-bonds, or donate electron density.⁸ A higher $E_T(30)$ indicates a higher polarity and/or a greater ability to interact with other species. To investigate whether solvent polarity was the cause of the selective desolvation behaviour of **SHF-61**, a 4th year undergraduate MChem project was

performed by Amelia Newman, in which the activation of **SHF-61** from a number of different solvents was monitored.⁹ The solvents chosen were isopropanol (ⁱPrOH), dichloromethane (DCM), nitromethane (NO₂Me) and cyclohexane (CyH), as these represented a range of polarities and functional groups that may interact with the pore surface of **SHF-61**; the $E_T(30)$ values of these solvents, as well as those of DMF, chloroform and cyclopentanone (CyP – relevant to later discussions), are detailed in Table 3.1. Included also are the $E_T(30)$ values of water, and vacuum (*i.e.* the lowest possible value) for context.

Table 3.16. $E_T(30)$ values for relevant solvents. Water is the second highest value listed by Markus,⁸ and “vacuum” represents the lowest theoretical possible value.

Solvent	$E_T(30)$
Water	63.1
ⁱ PrOH	48.4
NO ₂ Me	46.3
DMF	43.2
DCM	40.7
CyP	39.4
CHCl ₃	39.1
CyH	30.9
Vacuum	27.1

The conclusion of the project was that **SHF-61** remained open after removal of all the solvents, even though isopropanol and nitromethane are more polar than DMF.⁹ Therefore, solvent polarity must not be the factor that causes different desolvation behaviour in **SHF-61-DMF**. The next reasonable hypothesis, proposed by Carrington *et al.*,¹ is that the difference in desolvation behaviour arises from host-guest interactions. DMF has strong enough interactions with the framework to “pull”

the framework shut as it gradually leaves the material (*i.e.* in order to maintain interactions with the decreasing amount of DMF guest as it is removed, the framework is forced to close). Chloroform is not expected to interact very strongly with the framework, and therefore does not induce pore-closing.

In an attempt to further understand the nature of any framework-solvent interactions in the **SHF-61** system, a series of solvent uptake experiments were performed at Beamline B22, Diamond Light Source. These experiments were performed collaboratively with Dr Tim Easun and Alex Tansell, of Cardiff University, and whilst the data analysis presented in this chapter is my own work, sincere acknowledgement is made to Tim and Alex for their help, guidance and advice regarding this aspect of the project.

3.3. Experimental

3.3.1. Synthesis and General Procedures

The preparation of both **SHF-61-DMF** and **SHF-61-CHCl₃** was performed according to the published literature, unless otherwise stated.^{1,10} All reagents and solvents were supplied by Sigma-Aldrich, Alfa Aesar, Acros Organics, Fisher Scientific, Fluorochem or Manchester Organics, and were used without additional purification, except chloroform, which was obtained from the departmental Grubbs dry solvent service.

3.3.2. General Information on Uptake Experiments

Infra-red spectroscopy studies were performed at Beamline B22, Diamond Light Source,* using a polarised IR source connected to a Hyperion 3000 IR microscope and liquid nitrogen cooled MCT detector. Single crystal samples were loaded into a variable temperature Linkham flow-cell with zinc selenide windows. An input tube was connected from a nitrogen cylinder, and the flow of nitrogen passed through a bubbler of the specified solvent, such that a flow of solvent vapour was passed through the sample-containing cell and passed out through an exhaust. Spectra were collected at room temperature under ambient pressure, in the range 650 – 4000 cm⁻¹, using a 20 x 20 μm beam, approximately every 18.8 seconds (every 30 seconds in the case of DMF uptake on the closed

framework). Wavenumber at peak maximum was analysed manually using Omnic32. Peak integration was performed using Origin Pro. Where data quality allowed, peaks were fitted to a Lorentzian shape using Origin Pro. Model fitting of the spectra was performed only on the region containing the MOF framework amine bands (3549 cm⁻¹ – 3304 cm⁻¹), by fitting the spectra to the following equation:

$$Spectrum = C1(A) + C2(B).$$

Where: *Spectrum* = the spectrum to be fitted; *A* = the spectrum at the start of the study; *B* = the spectrum at the end of the study. The coefficients *C1* and *C2* therefore represent the how closely the spectrum resembles the start or end (respectively) of the study. This approach is based on the assumption that any spectrum measured between the start and end of the study can be treated as a composite of the first and final measurements. A slightly different model-fitting approach was applied in the case of DMF uptake in the closed framework – this is specified in the experiment details in Section 3.3.3.

*These experiments were performed as part of a collaborative study with Dr Tim Easun and Alex Tansell, at Cardiff University. Data collection was performed collaboratively at the Diamond Light Source.

3.3.3. DMF Uptake on Activated SHF-61-DMF (closed framework)

The sample (**SHF-61-DMF**) was activated by heating at 40, 60, 80 and 100 °C for 20 minutes each, and then heating at 150 °C for 125 minutes. This procedure was chosen as it replicated the activation procedure used in some experiments by Carrington *et al.*,¹ and allowed *in situ* monitoring of solvent removal. Peak integration and model fitting results are presented and discussed in Section 3.4.1. For this experiment only, the model-fitting was performed slightly differently to the approach for the studies adsorption by the open-framework MOF. Spectra in this study were fitted according to the following equation:

$$Spectrum = C1(cE) + C2(cD) + C3(oE) + C4(oD).$$

Where: *cE* = closed, empty framework model; *cD* = closed, DMF-containing framework model; *oE* = open, empty framework model; *oD* = open, DMF-containing framework model. *cE* is simply the

spectrum measured at the start of this study, and *oD* is the spectrum measured at the end of this study. *oE* is a spectrum of activated **SHF-61-CHCl₃** measured at the start of another experiment (scaled to account for differences in absorption). *cD* is a calculated spectrum taken by subtracting the start spectrum (*cE*) from spectrum number 75. Spectrum number 75 was measured 164 minutes into the experiment, just before the onset of rapid (gated) DMF uptake. Logically, at this point, there exist two extreme states: closed-pore framework with DMF present in 100 % occupancy; and closed-pore *without* DMF present (*cE*). The result of the calculation is therefore the spectrum of a hypothetical closed-pore framework *with* DMF present in 100 % occupancy (which may or may not exist in reality).

3.3.4. Experiments on Open-Pore SHF-61

Uptake experiments were performed on open-pore **SHF-61** using the following solvent vapours: DMF; chloroform; cyclopentanone; cyclopentanone (DMF present); isopropanol (DMF present); and water (DMF present). The intention in these experiments was to monitor solvents separately, but unfortunately, the latter two experiments contain DMF vapour as a contaminant in the Linkham cell itself. This was identified during the analysis stage, after the data had been collected. The contamination in the cyclopentanone experiment was due to absorbent tubing, which was noticed during the beamtime, and hence the experiment was repeated without the presence of DMF.

The sample (**SHF-61-CHCl₃**) was activated by heating at 120 °C. Due to the time-based logistics of performing experiments at the Beamline, activation times for **SHF-61-CHCl₃** differed in the experiments. These are detailed *per* (adsorbed) solvent as follows: DMF (182 minutes); chloroform (67 minutes); cyclopentanone (203 minutes); cyclopentanone with DMF contamination (348 minutes); isopropanol with DMF contamination (330 minutes); and water with DMF contamination (333 minutes). Due to the immense number of spectra collected (> 1000 in some cases), the data are not tabulated, but instead presented graphically in Section 3.4 alongside the discussion. Experiments were continued until spectra appeared unchanged by visual inspection, the time for which naturally

differed depending on the solvent used. The length of each experiment is apparent from the graphs presented in Section 3.4.

3.4. Results & Discussion

3.4.1. DMF Uptake in Narrow-Pore SHF-61

Closed pore **SHF-61** (activated **SHF-61-DMF**) was exposed to DMF vapour in a flow of nitrogen gas at room temperature. Spectra were recorded successively at roughly 30 second intervals. As the experiment progressed, new bands appeared at 1667 cm^{-1} and 1096 cm^{-1} , consistent with DMF solvent (Figure 3.1). Peak fitting the carbonyl band (1667 cm^{-1}) showed that growth was gradual for the first 164 minutes, and then rapidly increased in a gated fashion, consistent with gated expansion of the framework (Figure 3.2). At 200 minutes, the detector required refilling with liquid nitrogen, and data collection was not possible for the next 45 minutes. After this detector fill, the carbonyl band has reached saturation. A similar trend is seen also in the DMF (C-N-CHO) deformation band at 1096 cm^{-1} (Figure 3.3), although this peak was too small to fit for the first 89 minutes of the experiment, and its area continues to increase after the detector fill, showing that DMF is still being adsorbed by the framework at this stage. The DMF carbonyl band in particular has a rather broad profile, which could indicate that the carbonyl group is involved in an interaction with another species.

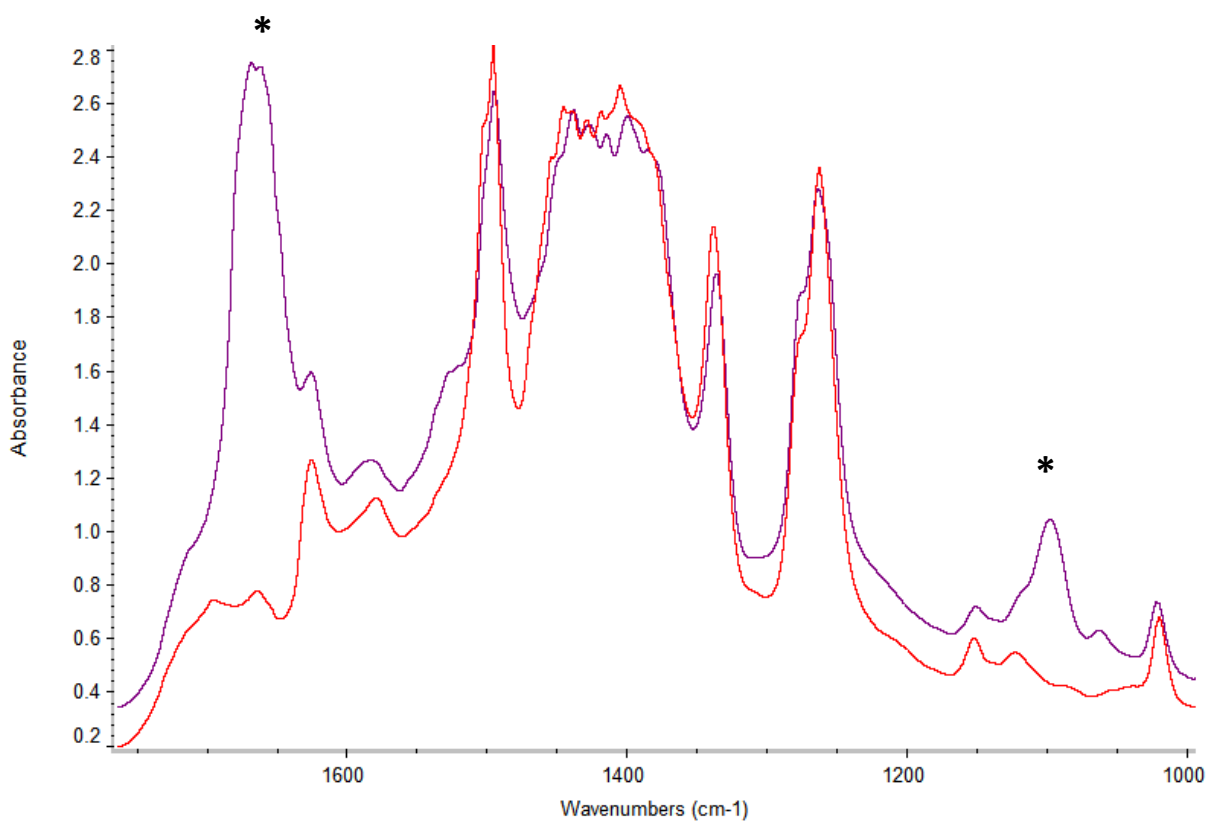


Figure 3.1. Selected region of the spectra collected at the start (red) and end (blue) of the DMF uptake experiment on closed-pore **SHF-61**, showing the DMF bands at 1667 cm^{-1} and 1096 cm^{-1} (both marked).

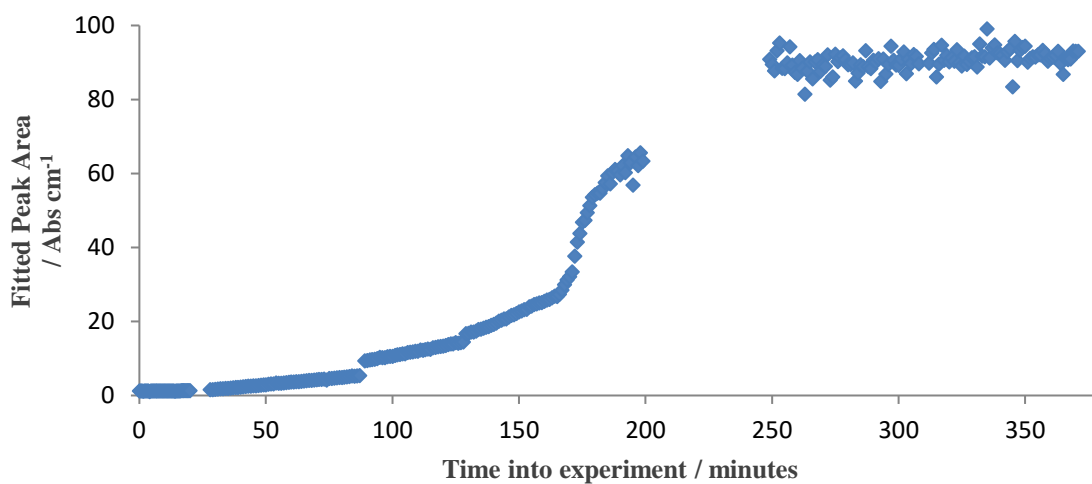


Figure 3.2. Peak fitted area of the DMF carbonyl band at 1667 cm^{-1} as function of experiment time. The gap in data acquisition (approx. 40 mins) is necessitated by the requirement to refill the detector with liquid N_2 coolant and allow an equilibration period before continuing measurements.

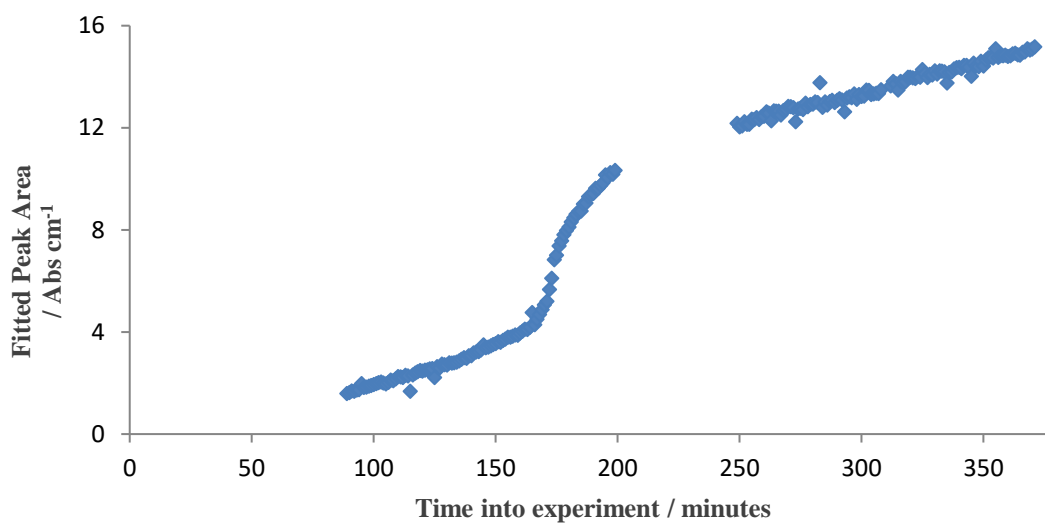


Figure 3.3. Peak fitted area of the DMF (C-N-CHO) deformation band at 1096 cm^{-1} as function of experiment time in the DMF uptake experiment on closed-pore **SHF-61**.

The wavenumber of the framework amine bands (symmetric and asymmetric NH_2 stretches) at peak maxima decreases during the study, consistent with the ligand amine groups interacting with DMF (Figure 3.4). The wavenumber positions of these bands is similar to those reported values for the MOF $\text{Sc}_2(\text{NH}_2\text{BDC})_3$, providing confidence that these amine bands are not due to the dimethylammonium counter-ion.¹¹ Additionally, the profile of the wavenumber shift of the amine bands mirrors the gate observed in the DMF bands (Figures 3.5 and 3.6).

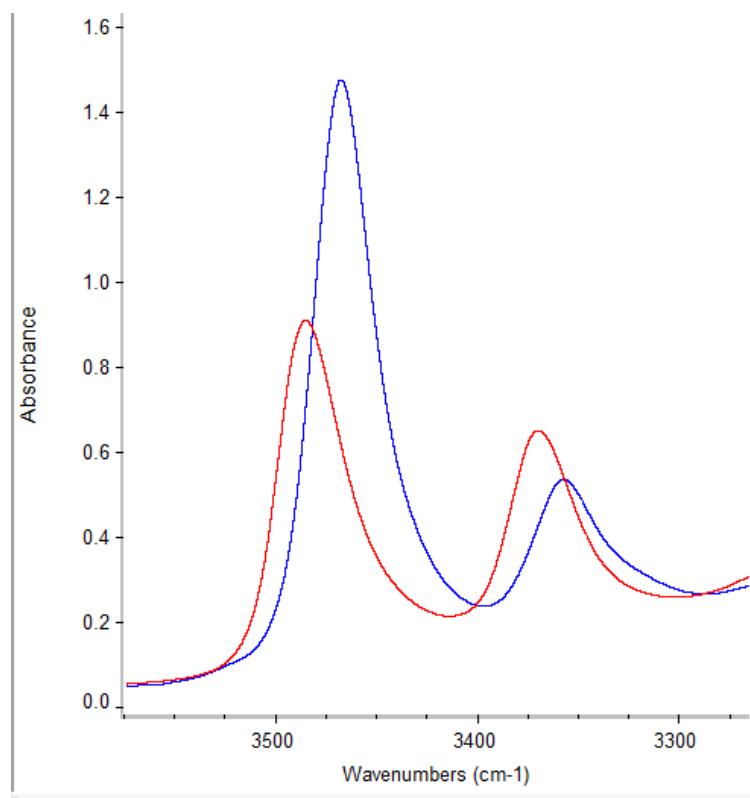


Figure 3.4. Comparison of framework NH_2 symmetric and asymmetric stretch bands in the closed framework at the start of the experiment (red) and in the DMF-filled open framework at the end of the experiment (blue).

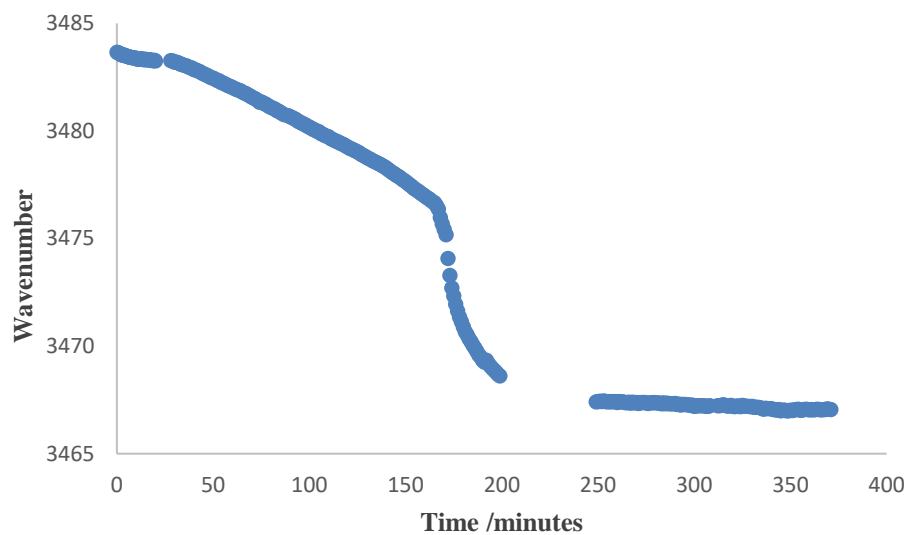


Figure 3.5. The wavenumber of the fitted framework NH_2 asymmetric stretch over the course of the DMF uptake experiment on closed **SHF-61**.

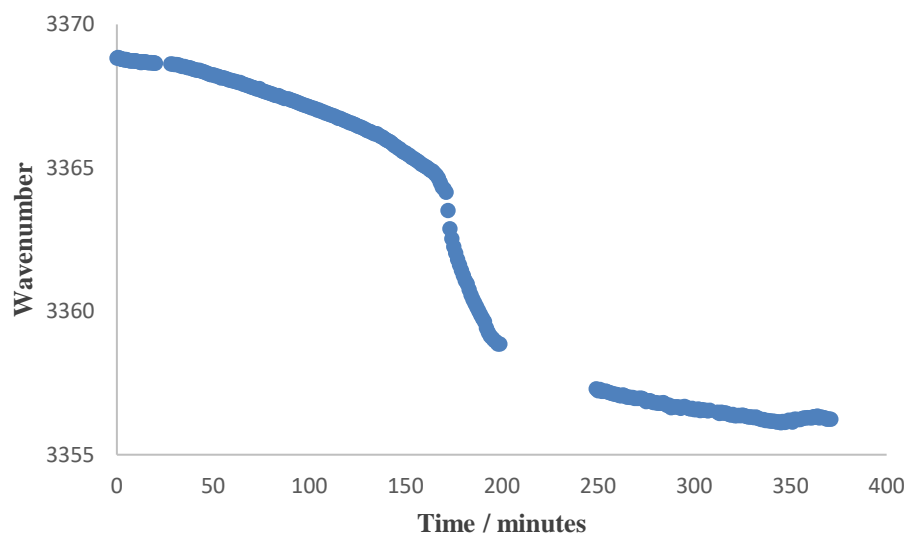


Figure 3.6. The wavenumber of the fitted framework NH_2 symmetric stretch over the course of the DMF uptake experiment on closed **SHF-61**.

The framework amine groups in **SHF-61** exist in two states in this experiment – either they are *not* interacting with DMF (start of the experiment), or they *are* interacting with DMF (end of the experiment). Their apparent continuous shift between 164 and 200 minutes is actually the product of a decrease in the non-interacting stretches, and an increase in the interacting-stretches. Peak fitting these as separate bands was not possible due to both the broadness of the bands (likely due to inter-network hydrogen-bonding which limits flexibility in the *a*-axis, *cf.* chapter 1),¹ and their proximity to each other (only *ca.* 15 cm^{-1} difference in position). Instead, a model-fitting approach was used, where four model spectra were obtained: *cE*, *cD*, *oE*, and *oD* (lower case o = open, lower case c = closed, upper case E = empty, upper case D = DMF-bound). Models *oE*, *oD* and *cE* were measured and model *cD* was calculated using measured data sets. A more detailed explanation is provided in Section 3.3.3. All data sets in the study were fitted as a function of these four model spectra, and the results are shown graphically in Figure 3.6. Only the region containing the amine bands was subject to model fitting.

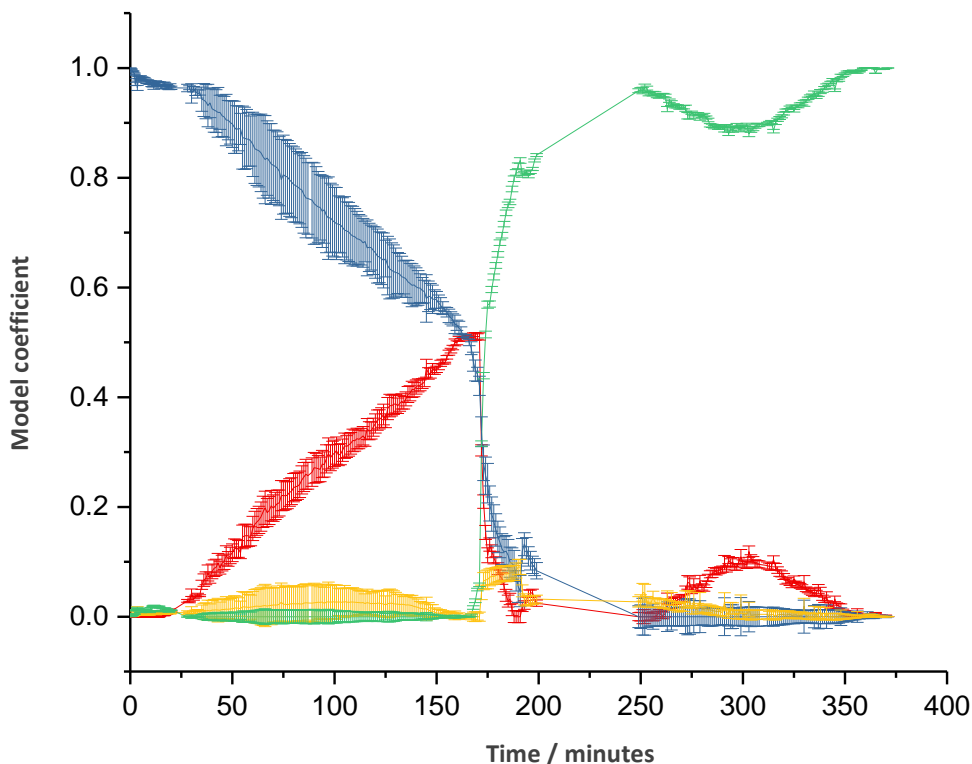


Figure 3.7. Model fitting results on framework NH_2 stretches in the DMF uptake study on closed-pore **SHF-61**. Blue = cE ; red = cD ; yellow = oE ; and green = oD . Error bars are included.

For the first 164 minutes, cE decreases and cD increases, both at a constant rate, until they reach a value of 0.5. At this point they both drop to zero fairly quickly, coupled with an immediate rise of oD . This suggests that closed-pore **SHF-61** exhibits a gated opening upon DMF uptake that occurs once 50 % of the framework amine groups have been bound by DMF. During the gate, between 164 and 200 minutes, there is also a small rise and fall of the oE model (maximum coefficient 0.1), suggesting that the MOF opens more rapidly than it is filled under these conditions.

3.4.2. DMF Uptake in Open-Pore **SHF-61**

DMF uptake was studied for open-pore **SHF-61** in a similar fashion to the experiment on the closed-pore MOF (Section 3.4.1). As in the closed-pore experiment, the DMF carbonyl and C-N-CHO deformation bands (1667 cm^{-1} and 1096 cm^{-1} respectively) both increase throughout the study (Figures 3.8 and 3.9). In this case, however, no gated uptake is observed. This is consistent with the open framework adsorbing DMF vapour with little/no energy barrier.

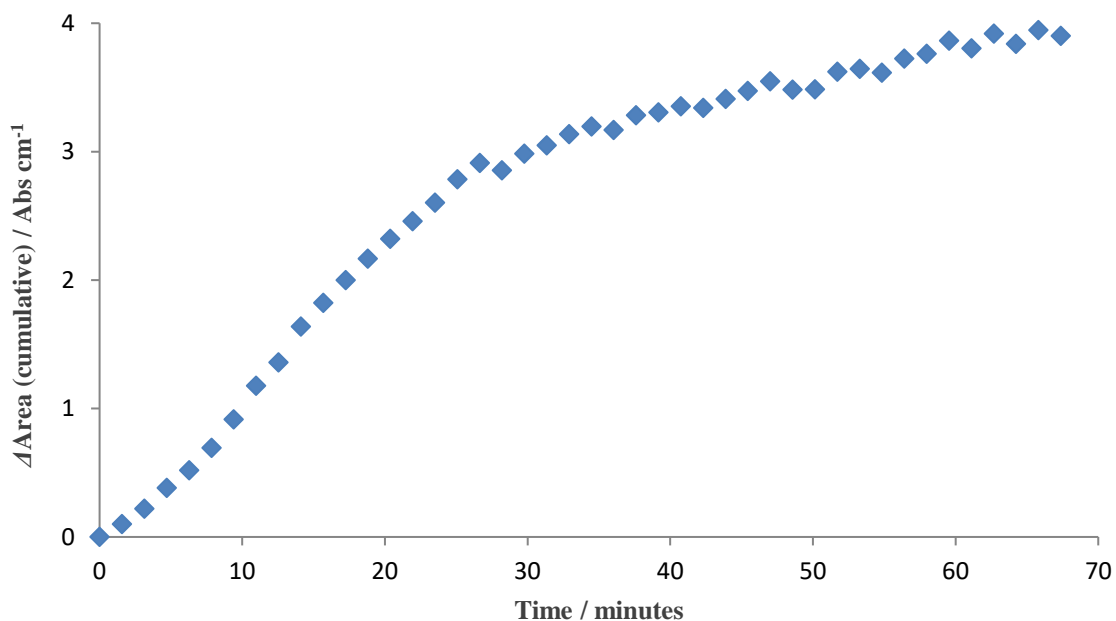


Figure 3.8. Cumulative area of the 1667 cm^{-1} DMF carbonyl band over the course of the DMF uptake experiment on open-pore **SHF-61**. For this band, direct peak integration was found to be more suitable than peak fitting. The y-axis represents the successive, cumulative area increase in the band over time.

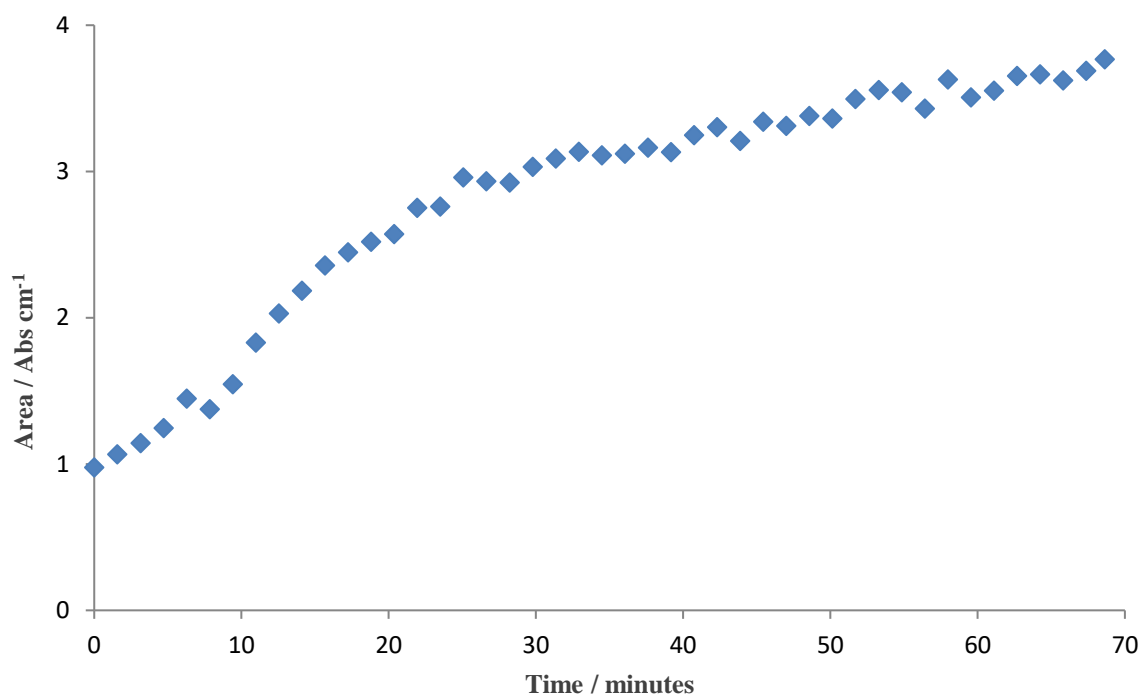


Figure 3.9. The fitted band area of the 1096 cm^{-1} DMF C-N-CHO deformation band over the course of the DMF uptake experiment on open-pore **SHF-61**.

Additionally, the amine bands shift in the same manner as was observed in the closed MOF experiment (*cf.* Section 3.4.1), although they do not reach the same wavenumber values, falling short

by *ca.* 4 cm^{-1} (Figures 3.10–3.12). The reason for this is unknown, but could be due to the experiment time. Unfortunately, in this experiment, the sample crystal was moved slightly after 69 minutes, and the spectra recorded afterwards were unsuitable for analysis. In the analogous study on the closed MOF, the experiment was run for over 6 hours.

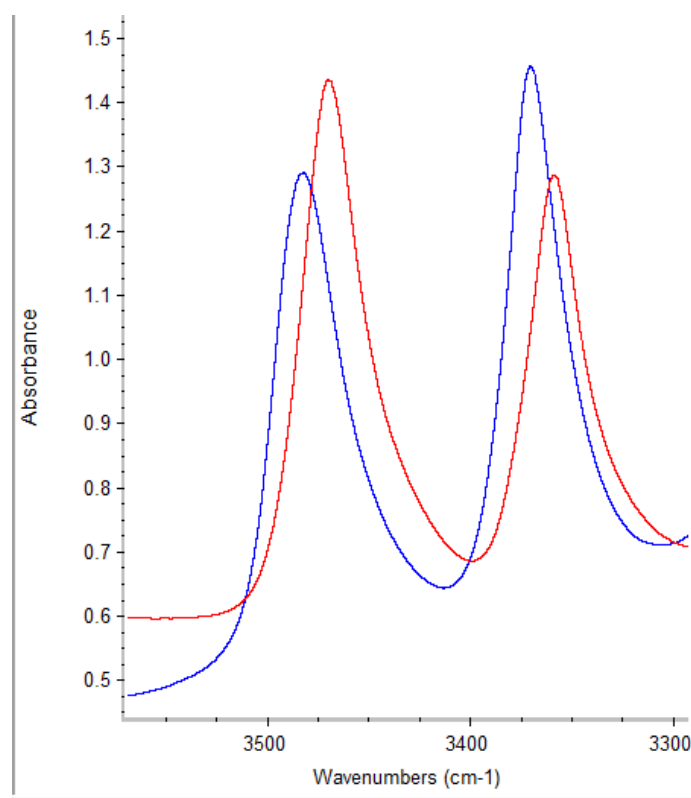


Figure 3.10. Comparison of framework NH_2 symmetric and asymmetric stretch bands in the empty open framework at the start of the experiment (blue) and in the DMF-filled open framework at the end of the experiment (red).

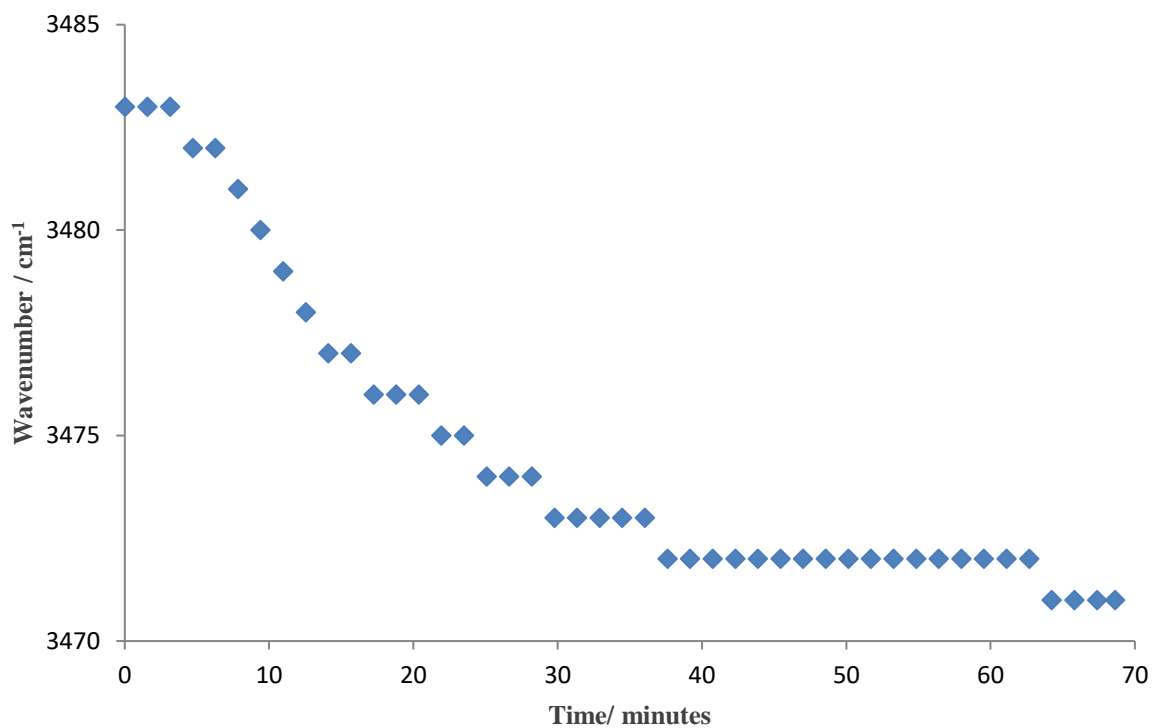


Figure 3.11. Wavenumber at peak maximum of the asymmetric framework NH_2 over the course of the DMF uptake experiment on open-pore **SHF-61**. The stepped appearance is an artefact of experiment accuracy (rounding).

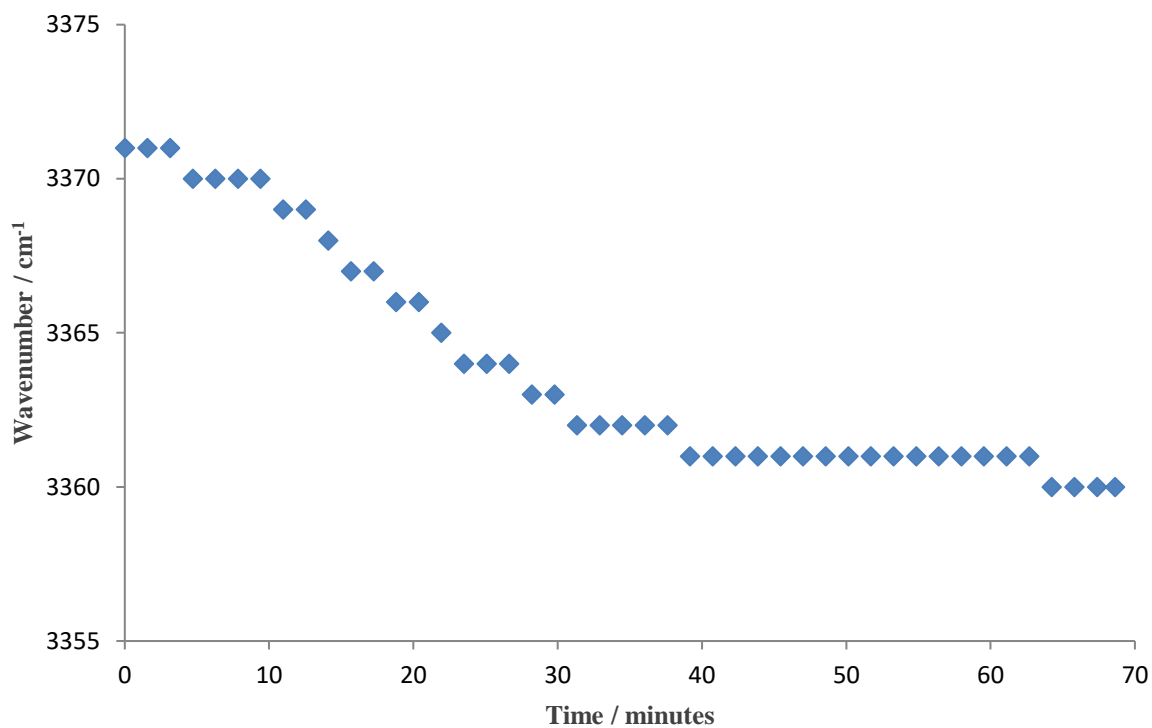


Figure 3.12. Wavenumber at peak maximum of the symmetric framework NH_2 stretch over the course of the DMF uptake experiment on open-pore **SHF-61**. The stepped appearance is an artefact of experiment accuracy (rounding).

The amine band regions of the spectra were also fitted as function of two models: the first spectrum in the study, and the last. This enabled the change in the amine bands to be monitored over time (rather than just their wavenumber). The resultant plot of the relative contribution of the starting and ending models as a function of time (Figure 3.13) confirms that there is no gated expansion occurring, as was observed in the case of closed-pore **SHF-61**. There was a possibility that open-pore **SHF-61** would close upon DMF adsorption, and then exhibit a gated opening, akin to the effect seen in activated **MIL-53** upon exposure to water or CO₂.¹² However, this appears not to be the case – the analyses performed on this experiment indicate that the open framework adsorbs DMF vapour *without* contracting.

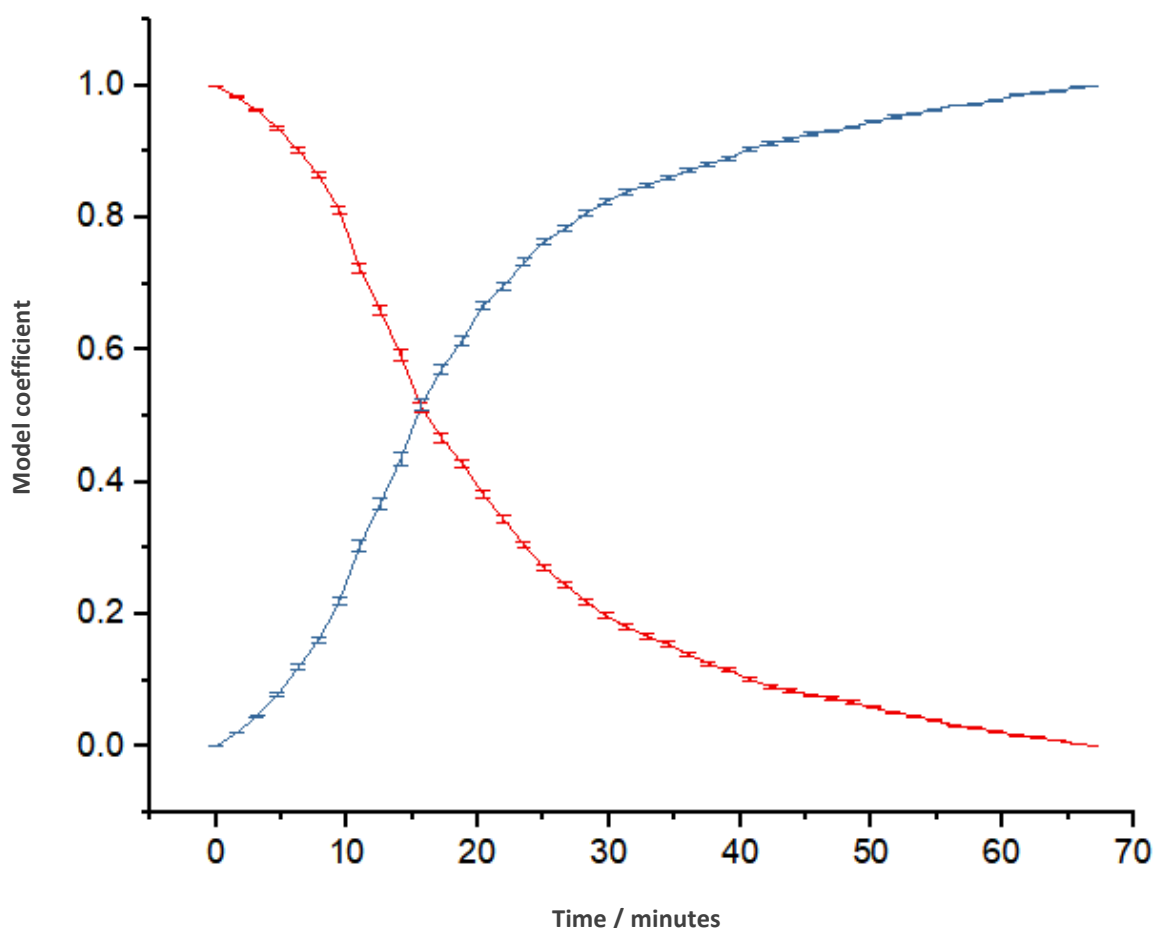


Figure 3.13. Model-fit approach of the framework amine band region over the course of the DMF uptake experiment on open-pore **SHF-61**. Red = first measurement in study (oE); blue = last measurement in study (oD).

Interestingly, in this experiment, the rate of DMF uptake increases in the first 10 minutes. This cannot be gated expansion of the material, as it is already in its open-pore form. A possible explanation could be design of the experiment: these experiments are not performed with pressure steps, but with a continuous flow of vapour using a carrier gas. The first measurement was recorded as soon as the carrier gas was set to flow, and it will have taken a short period of time for a constant vapour pressure to be attained in the sample-containing cell. During this time, solvent uptake will have been lower as there would be less solvent available in the cell.

3.4.3. Chloroform Uptake in Open-Pore SHF-61

The chloroform uptake on open-pore **SHF-61** has interesting results. The chloroform C-H stretch at 3031 cm^{-1} is observed to first appear after 6.5 minutes, and the intensity of the band reaches a plateau after 8 minutes (Figures 3.14 and 3.15). A simultaneous growth is observed in a band at 3015 cm^{-1} (Figures 3.14 and 3.16), which is not found in the framework *or* in chloroform reference spectra. However, in this band, a small area increase is observed in the first 6 minutes.

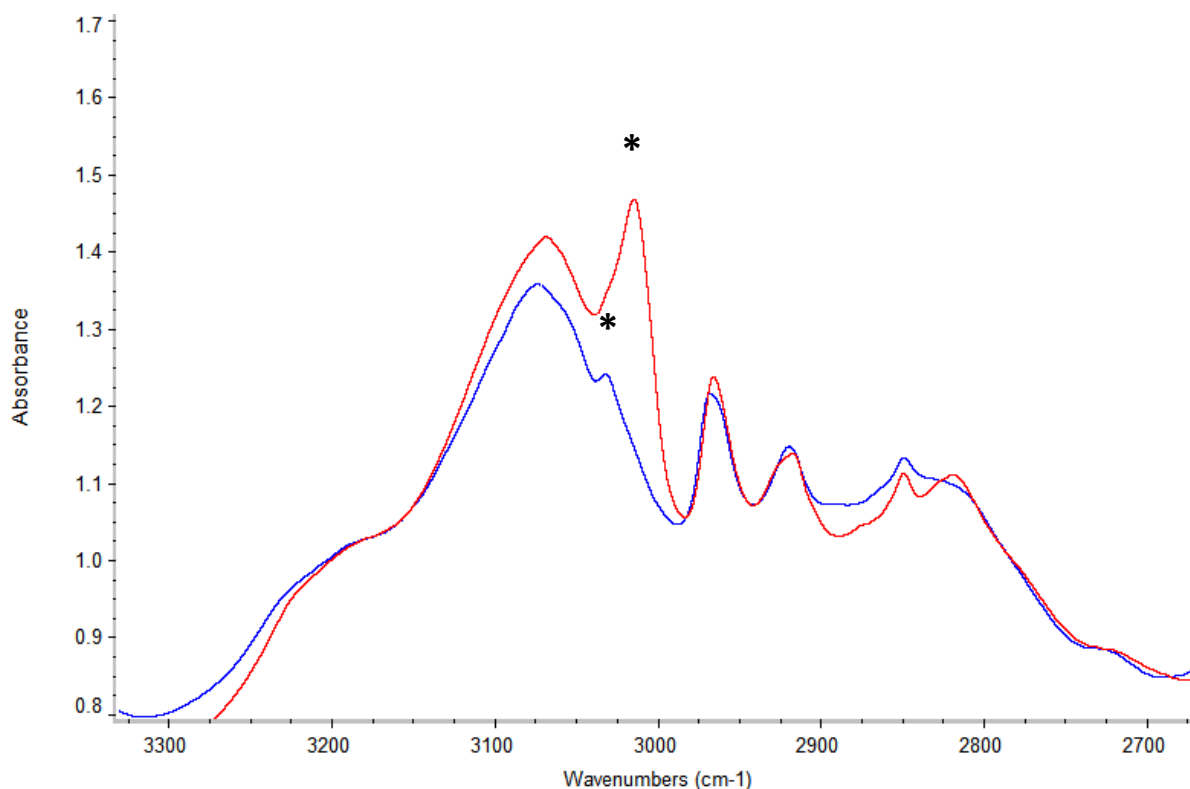


Figure 3.14. Comparison of the first (blue) and last (red) spectrum in the experiment, showing the growth of both bands at 3031 cm^{-1} and 3015 cm^{-1} (marked) in the chloroform uptake experiment on open-pore **SHF-61**.

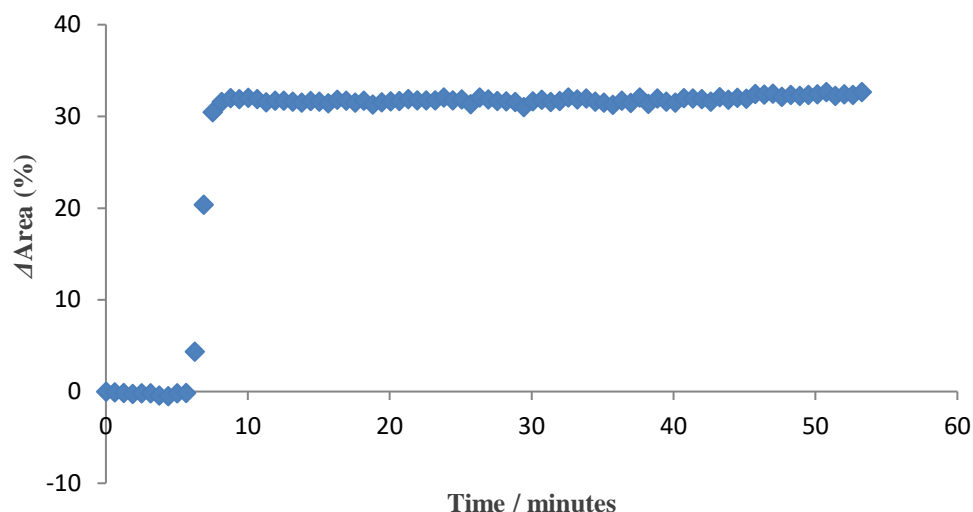


Figure 3.15. Peak integration results of the 3031 cm^{-1} chloroform C-H stretch over the course of the chloroform uptake experiment on open-pore **SHF-61**.

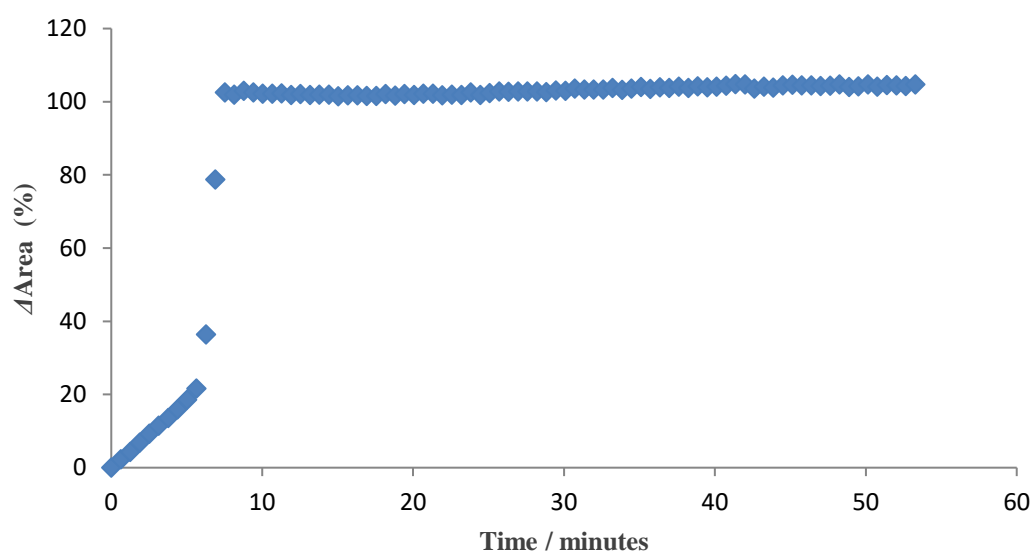


Figure 3.16. Peak integration results of the 3015 cm^{-1} band, suspected to be a C-H stretch of chloroform involved in a hydrogen-bonding interaction, over the course of the chloroform uptake experiment on open-pore **SHF-61**.

Additionally, a framework band at 1627 cm^{-1} undergoes a sharp decrease, combined with the growth of another band at 1623 cm^{-1} (Figures 3.17 and 3.18). Although the numerous framework bands have not been assigned in these studies, the location of these bands is consistent with the expected position of framework carboxyl stretches.

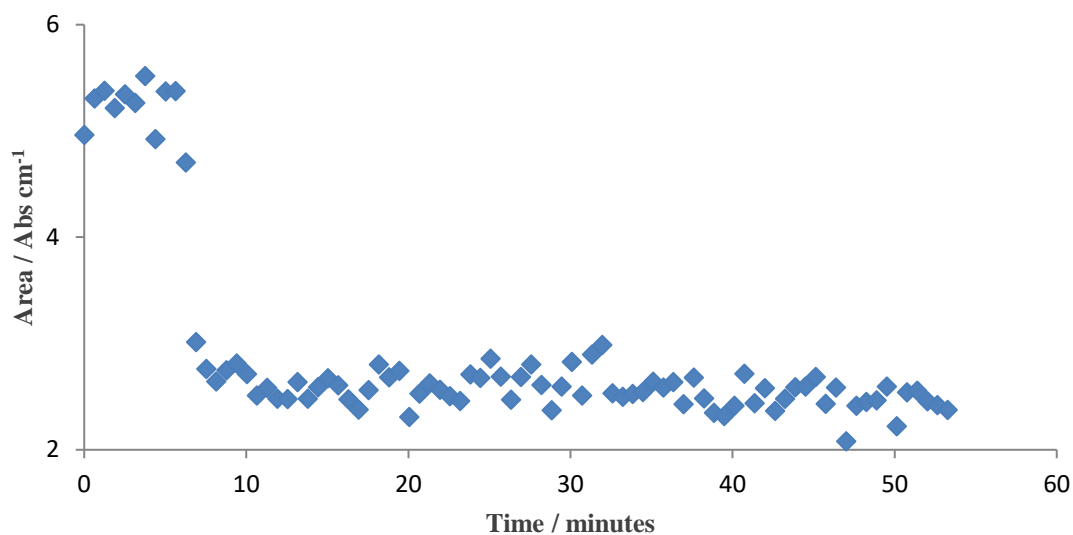


Figure 3.17. Peak fitted area of the band at 1627 cm^{-1} , potentially a framework carboxyl group, over the course of the chloroform uptake experiment on open-pore **SHF-61**.

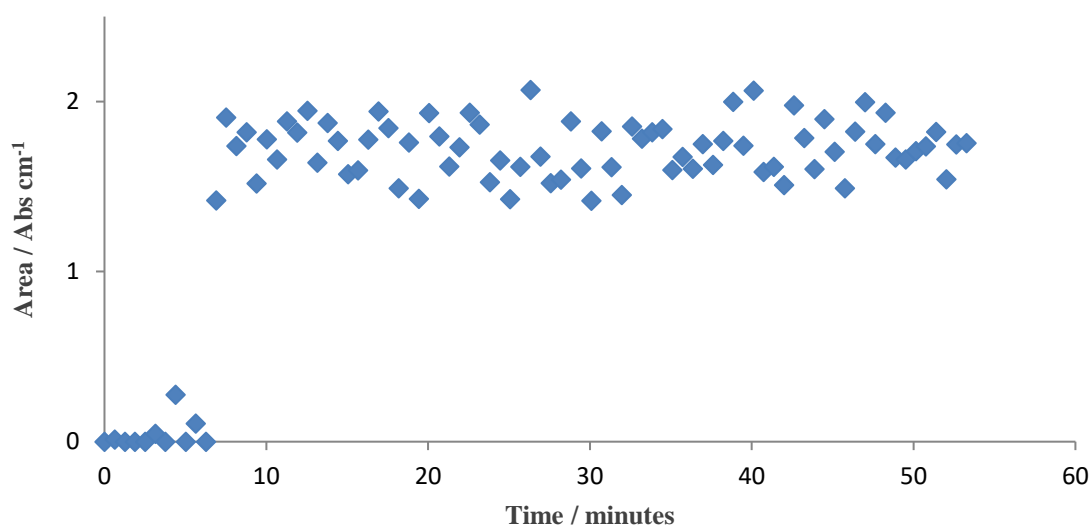


Figure 3.18. Peak fitted area of the band at 1623 cm^{-1} , potentially a framework carboxyl group involved in an interaction with chloroform, over the course of the chloroform uptake experiment on open-pore **SHF-61**.

A tentative suggestion at this stage is that chloroform is acting as a hydrogen-bond donor, and a linker carboxyl group acting as a hydrogen-bond acceptor. The band at 3015 cm^{-1} could be the C-H stretch of chloroform molecules bound to framework carboxyls, and the 1627 cm^{-1} and 1623 cm^{-1} bands could be non-interacting, and chloroform-bound framework carboxyl stretches respectively. There are, however, a few problems with this hypothesis. Firstly, the interaction between chloroform and a carboxyl group is likely to be weaker than interactions between DMF and an aromatic amine,

yet in the analogous DMF uptake experiment (Section 3.4.2), uptake occurs much more slowly. Secondly, the fact that the 3031 cm^{-1} and 3015 cm^{-1} bands reach a plateau in intensity at 8 minutes suggests that uptake has stopped at this point. The only rational explanation for this is if the framework snaps shut around chloroform, in the same fashion as **MIL-53** does in response to water and CO_2 .¹² However, open-pore **SHF-61** does not respond in this fashion to DMF, which is likely a more strongly bound guest, and is certainly a stronger hydrogen-bond acceptor than chloroform is a donor. Thirdly, data quality in these experiments was insufficient to get a result from the amine band region, which naturally casts suspicion over the other results. The near-instant nature of the changes in this data set are very odd, and it is not impossible that some instrumental/human error occurred (such as a slight movement of sample stage). It will be very interesting to see if repetitions of this experiment produce similar results.

3.4.4. Cyclopentanone Uptake in Open-Pore SHF-61

A total of four bands appeared over the course of the cyclopentanone uptake experiment – all of these in the region between 1700 and 1800 cm^{-1} (Figure 3.19). Reference spectra of cyclopentanone indicate that the main carbonyl stretch is at 1750 cm^{-1} , with a large shoulder at 1730 cm^{-1} . These bands are observed in our uptake experiment. Peak fitting was not possible due to the presence of a more intense framework band nearby, but peak integration revealed that these two bands have a very similar growth profile over the course of the experiment (Figures 3.20 and 3.21).

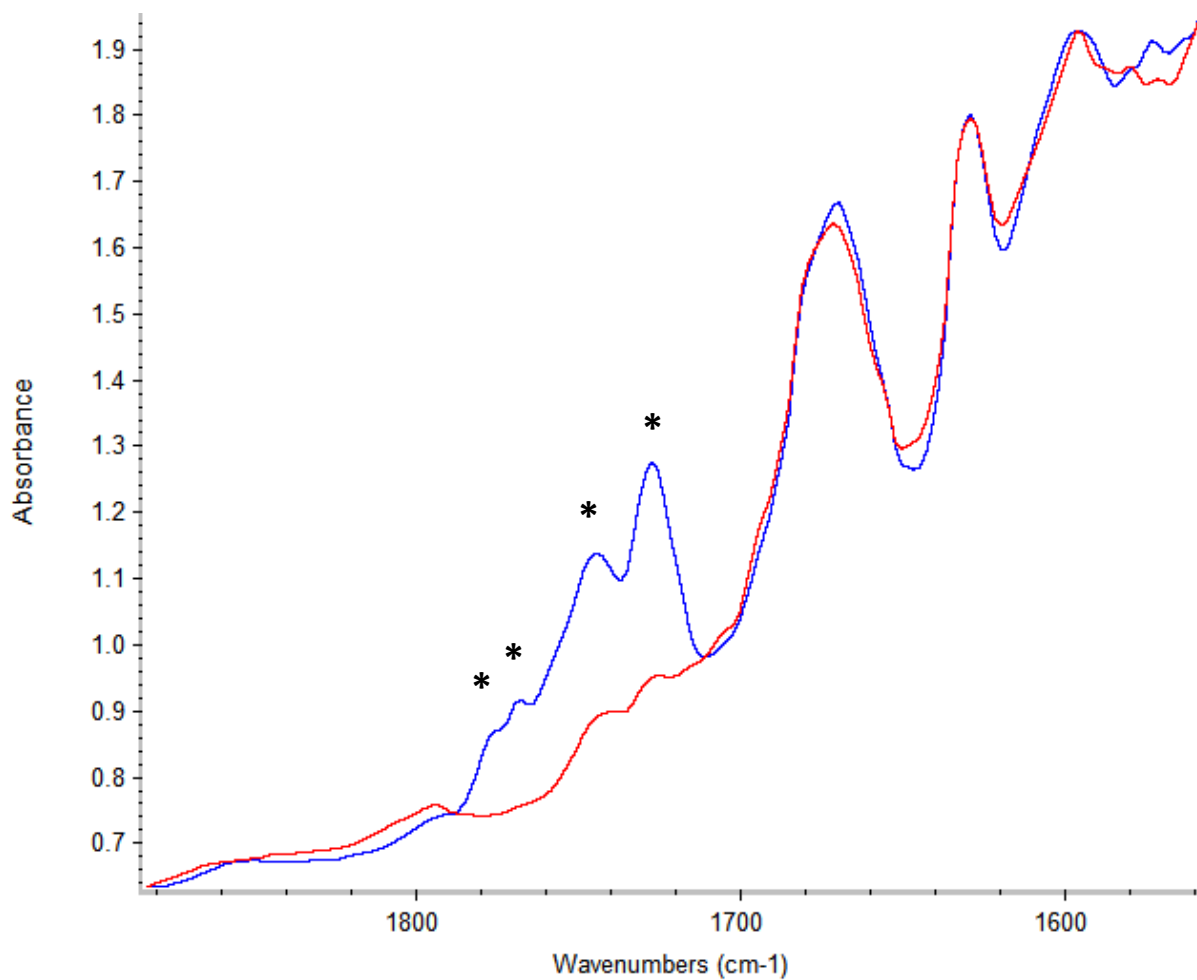


Figure 3.19. A comparison of the first (red) and last (red) measurement in the cyclopentanone uptake experiment in open-pore SHF-61, showing the four new bands which appear over the course of the study (marked).

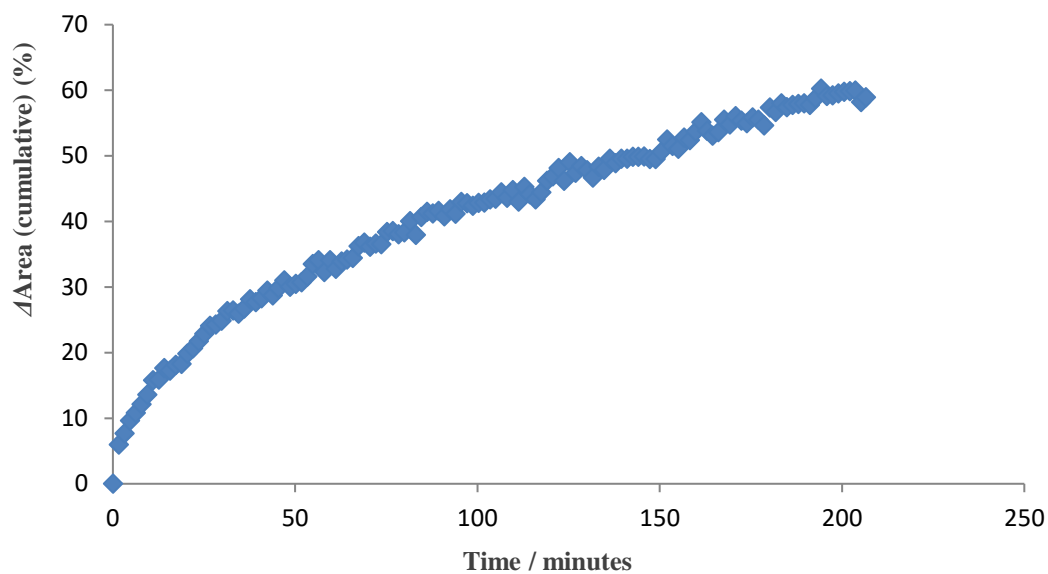


Figure 3.20. Integrated peak area for the 1750 cm^{-1} cyclopentanone carbonyl stretch over the course of the cyclopentanone uptake experiment on open-pore **SHF-61**.

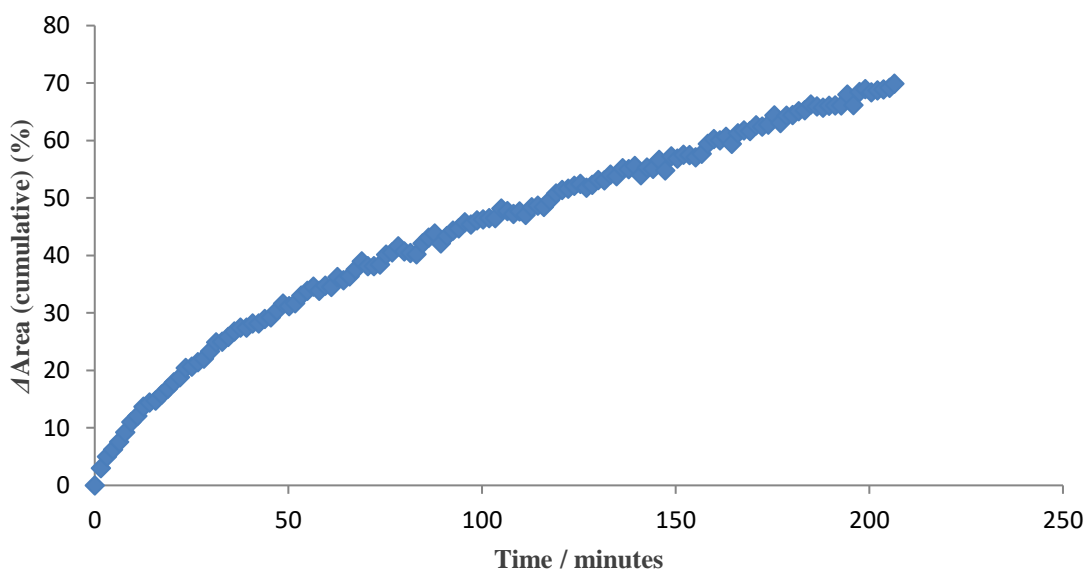


Figure 3.21. Integrated peak area for the 1730 cm^{-1} cyclopentanone carbonyl stretch over the course of the cyclopentanone uptake experiment on open-pore **SHF-61**.

The two remaining bands are at 1770 cm^{-1} and 1776 cm^{-1} , and these change in a similar manner to each other (Figures 3.22 and 3.23), but a different manner to the 1750 cm^{-1} and 1730 cm^{-1} bands.

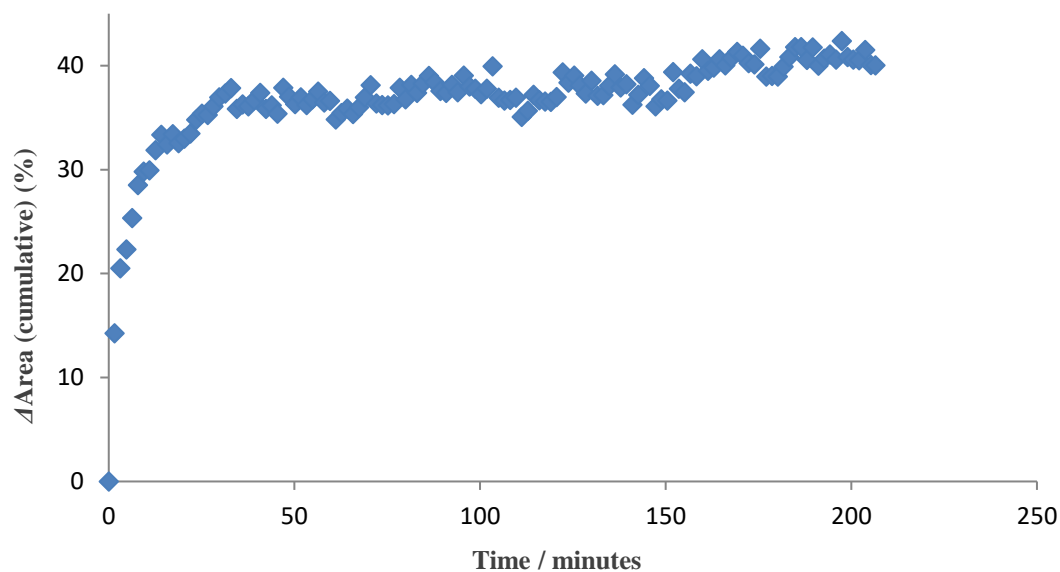


Figure 3.22. Integrated peak area for the 1770 cm^{-1} band over the course of the cyclopentanone uptake experiment on open-pore **SHF-61**.

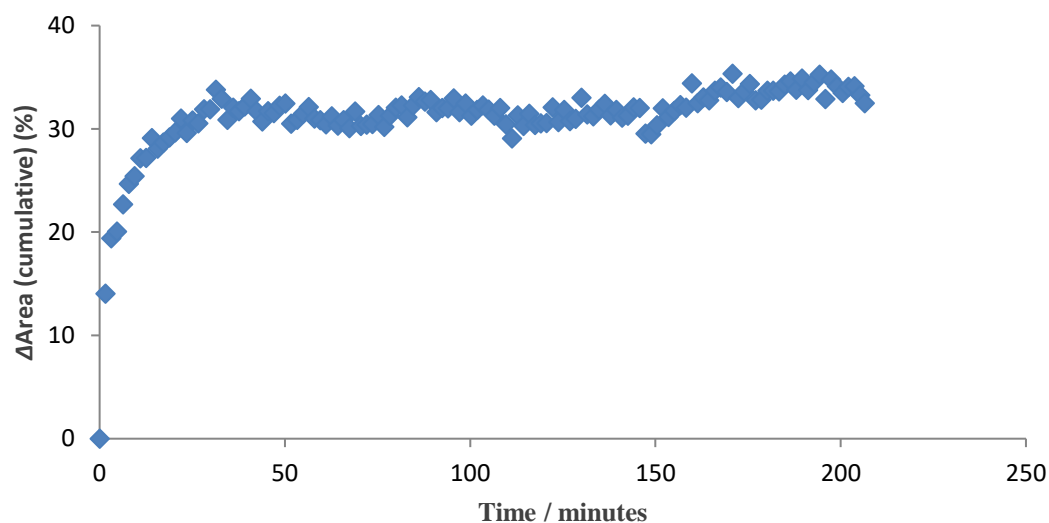


Figure 3.23. Integrated peak area for the 1776 cm^{-1} band over the course of the cyclopentanone uptake experiment on open-pore **SHF-61**.

Self-enolisation of cyclopentanone accounts for the two bands at 1750 cm^{-1} and 1730 cm^{-1} , but the assignment of the others is unknown. Given that they have different rates of growth to the cyclopentanone carbonyl bands, they must be associated with a separate entity. However, any interaction of the carbonyl is likely to lower the wavenumber of the carbonyl stretch, and these two bands are higher in wavenumber. In any case, the wavenumber positions of the framework amine

stretches each change by less than 3 cm^{-1} (Figures 3.24 and 3.25), showing that any hydrogen-bonding interactions are weak in nature.

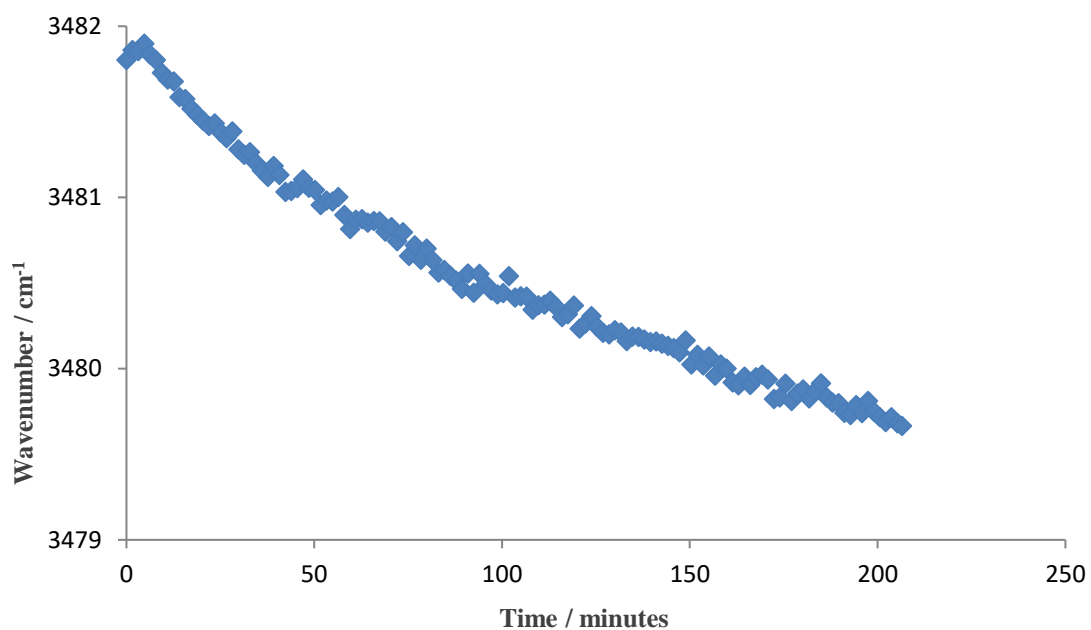


Figure 3.24. Wavenumber position of the asymmetric framework NH_2 stretch over the course of the cyclopentanone uptake experiment on open-pore **SHF-61**.

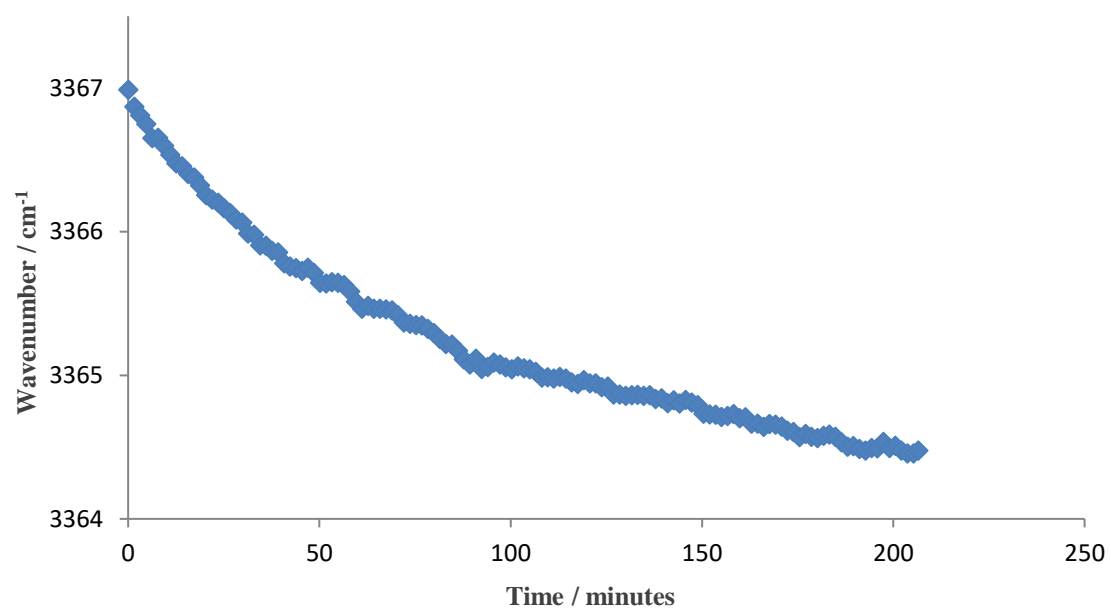


Figure 3.25. Wavenumber position of the symmetric framework NH_2 stretch over the course of the cyclopentanone uptake experiment on open-pore **SHF-61**.

The amine region of the spectra was analysed by the model-fitting approach used in the DMF uptake studies (Sections 3.4.1 and 3.4.2), using the first and last measurement as model spectra in order to observe the progression of the bands over time (Figure 3.26). The results indicate that interaction with cyclopentanone occurs immediately upon uptake. Figures 3.24 – 3.26 indicate that the uptake is “unfinished” at the end of the experiment (*i.e.* a plateau has not been reached) – this leads to the conclusion that the MOF is not fully saturated with cyclopentanone, as was observed in the DMF uptake experiments (Sections 3.4.1 and 3.4.2). The two bands at 1770 cm^{-1} and 1776 cm^{-1} , however, both reach a plateau in intensity after 28 minutes. This suggests they are not guest cyclopentanone within the framework. A suggestion for their identity at this stage is that they are gas-phase cyclopentanone, either free in the atmosphere of the cell, or bound to the surface of the MOF crystal. It is noted, however, that such phenomena have not been observed in the other vapour uptake studies.

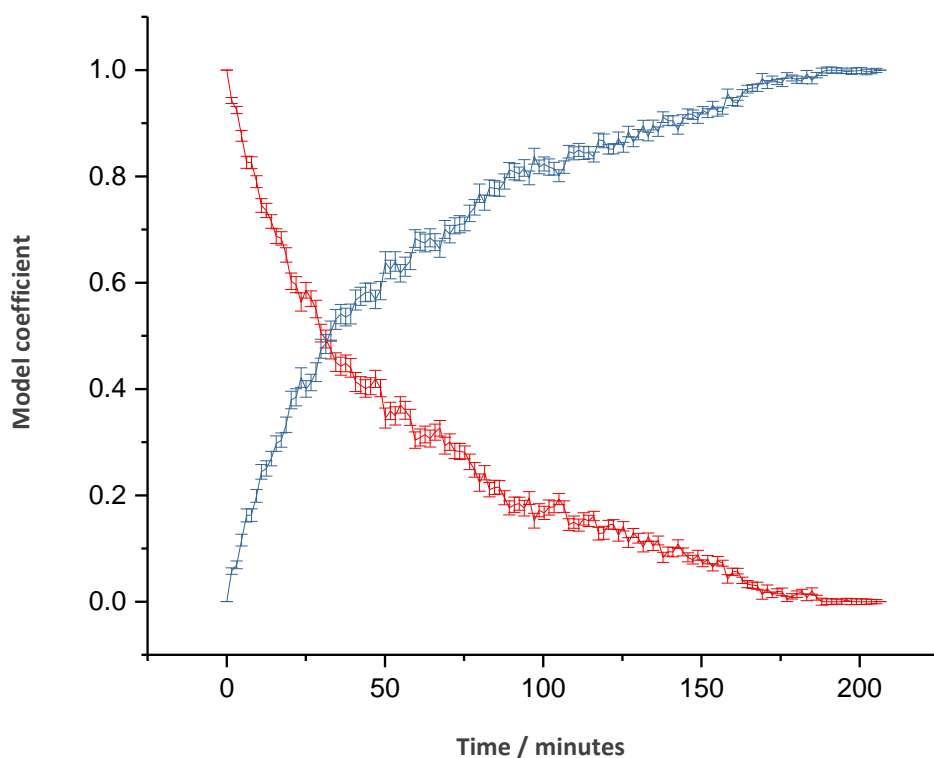


Figure 3.26. Model fitting results of the cyclopentanone uptake experiment on open-pore **SHF-61**. Red = first measurement model (oE); blue = final measurement model (oCyP).

3.4.5. Cyclopentanone Uptake in Open-Pore SHF-61 (DMF Contaminated)

This experiment is analogous to the cyclopentanone experiment discussed in Section 3.4.4, but was undertaken in the presence of DMF, which had been absorbed in a small section of plastic tubing used to supply the solvent in a previous experiment and was released during this cyclopentanone experiment. Just as in the uncontaminated experiment, two cyclopentanone carbonyl stretches are observed at 1750 cm^{-1} and 1730 cm^{-1} , and two additional bands at 1770 and 1776 cm^{-1} (Figures 3.27 - 3.30).

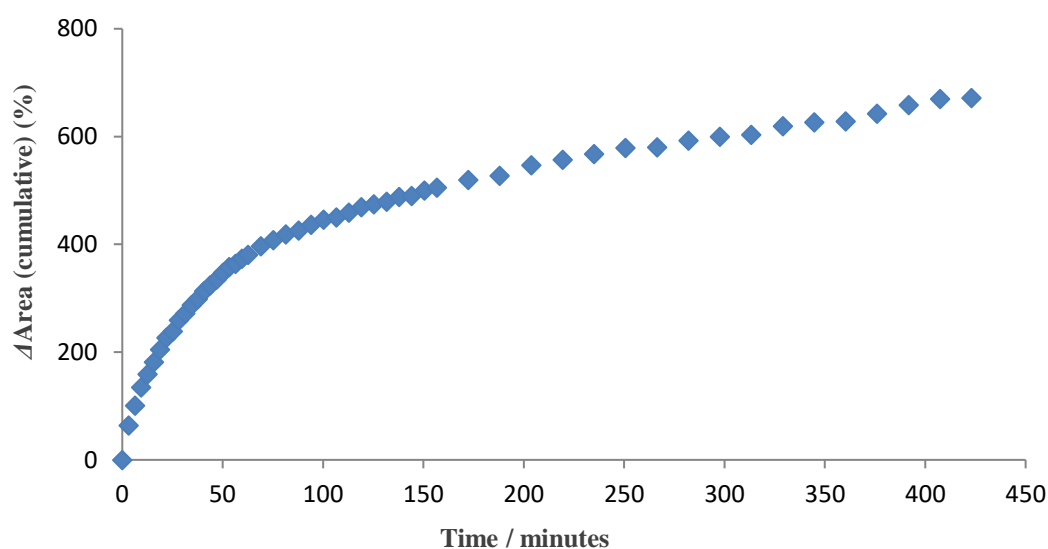


Figure 3.27. Integrated peak area of the 1750 cm^{-1} cyclopentanone carbonyl stretch over the course of the DMF-contaminated cyclopentanone uptake experiment on open-pore **SHF-61**.

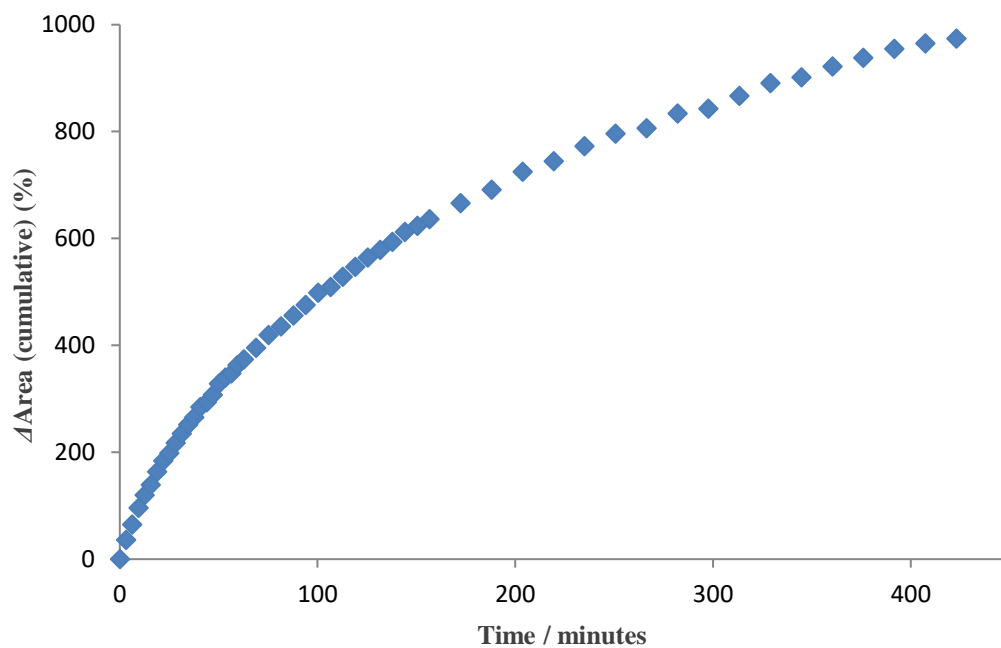


Figure 3.28. Integrated peak area of the 1750 cm^{-1} cyclopentanone carbonyl stretch over the course of the DMF-contaminated cyclopentanone uptake experiment on open-pore **SHF-61**.

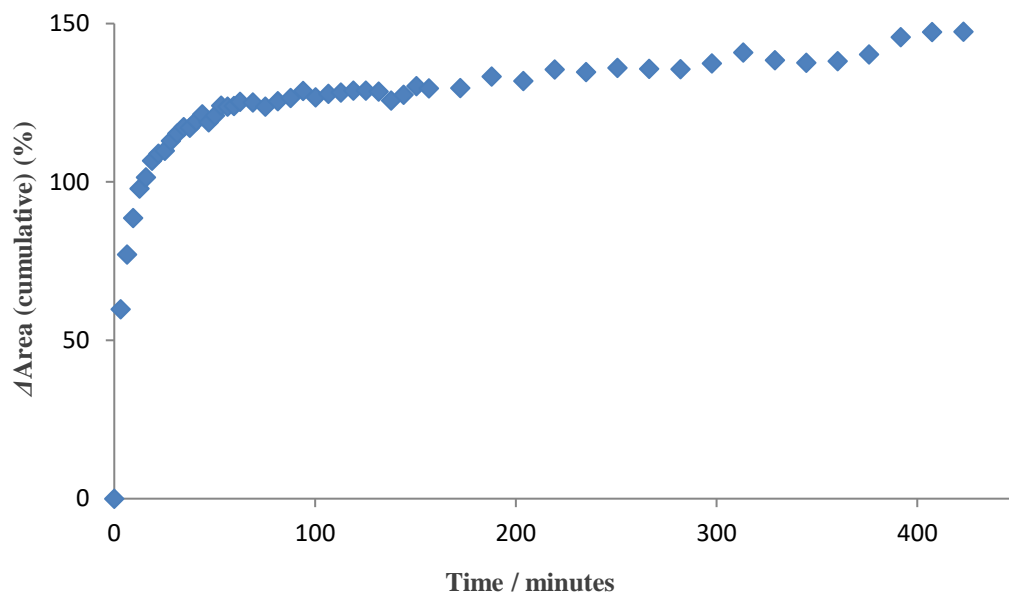


Figure 3.29. Integrated peak area of the 1770 cm^{-1} band over the course of the DMF-contaminated cyclopentanone uptake experiment on open-pore **SHF-61**.

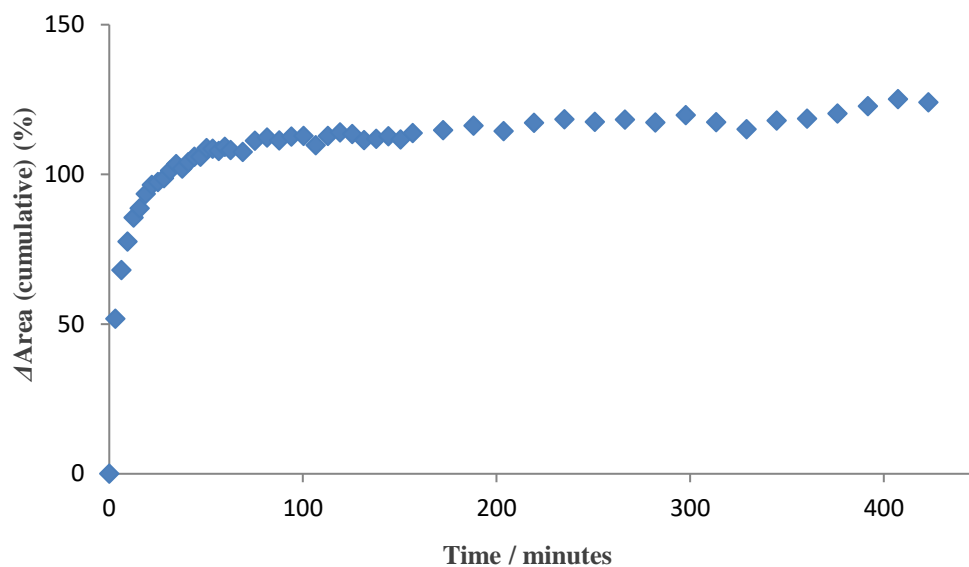


Figure 3.30. Integrated peak area of the 1776 cm^{-1} band over the course of the DMF-contaminated cyclopentanone uptake experiment on open-pore **SHF-61**.

Additionally, the DMF carbonyl stretch at 1667 cm^{-1} is observed, growing sharply at first, and reaching saturation at 145 minutes (Figure 3.31). The DMF C-N-CHO deformation band increases in area beyond this point; reaching a plateau after *ca.* 300 minutes (Figure 3.32).

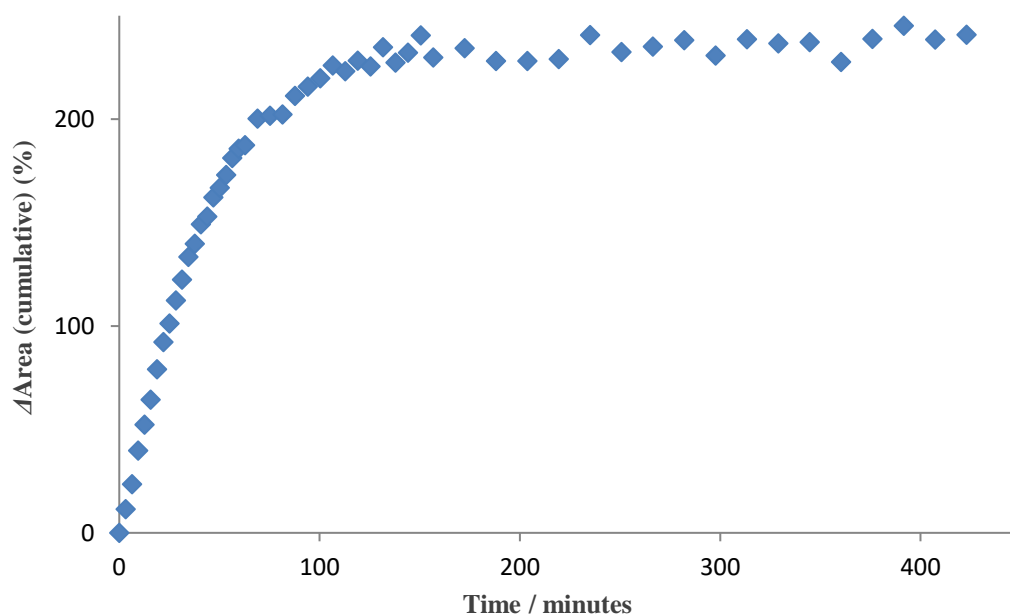


Figure 3.31. Integrated peak area of the 1667 cm^{-1} DMF carbonyl stretch over the course of the DMF-contaminated cyclopentanone uptake experiment on open-pore **SHF-61**.

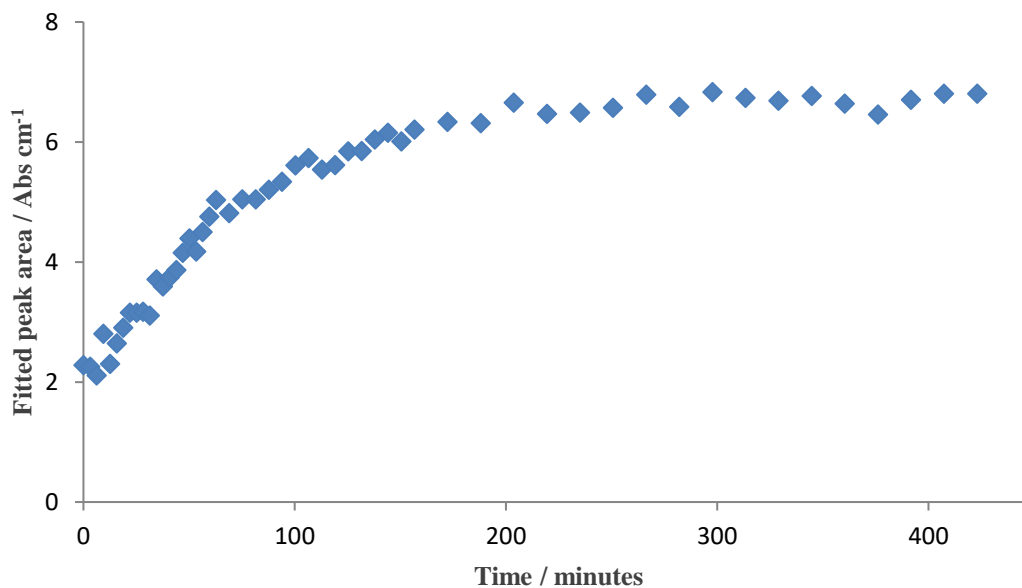


Figure 3.32. Peak fitted area of the 1098 cm^{-1} DMF C-N-CHO deformation band over the course of the DMF-contaminated cyclopentanone uptake experiment on open-pore **SHF-61**.

Analysis of the symmetric and asymmetric framework amine stretches reveals that they interact with guest solvent immediately, reaching their final position after *ca.* 250 minutes (Figures 3.33 – 3.35). Given that in the uncontaminated experiment, cyclopentanone did not interact strongly with the framework amine groups, the interaction observed here must be with DMF. This is interesting, as it shows that DMF is able to successfully compete with cyclopentanone despite being present in a much smaller quantity. Additionally, both this experiment and the uncontaminated version (Section 3.4.4) have shown that the solvent dependence of **SHF-61** does not simply depend on the functional groups present, as cyclopentanone and DMF both have carbonyl groups, yet only DMF induces pore-closure upon desolvation.

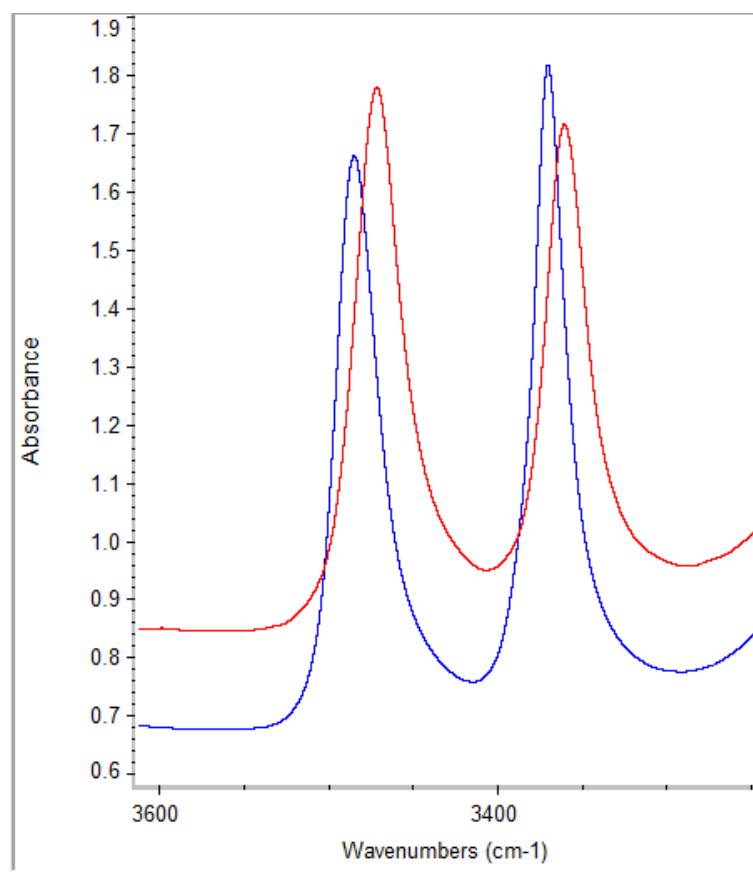


Figure 3.33. Comparison of framework NH_2 symmetric and asymmetric stretch bands in the empty open framework at the start of the experiment (blue) and in the DMF/CyP-filled open framework at the end of the experiment (red).

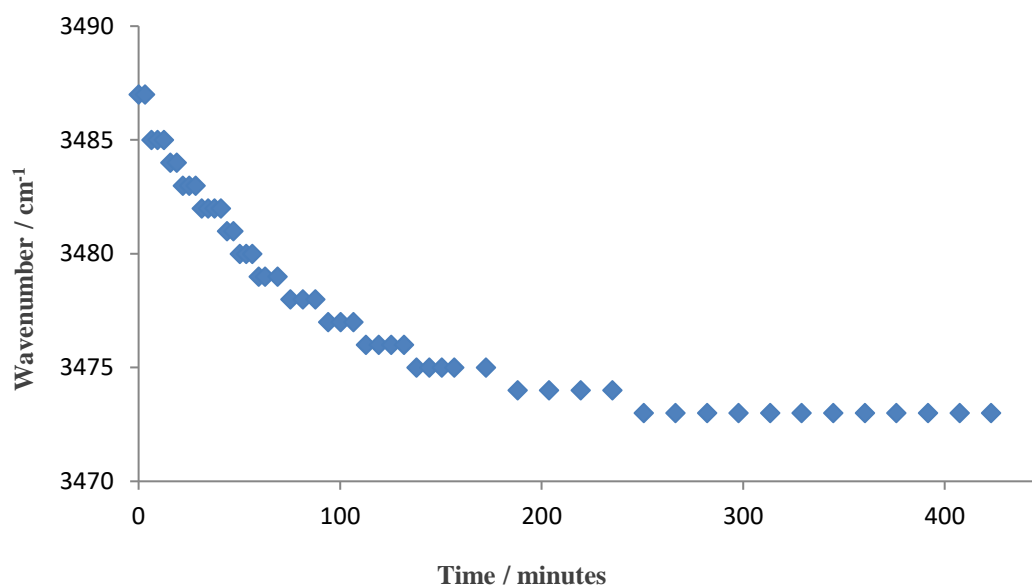


Figure 3.34. Wavenumber of the asymmetric framework NH_2 stretch over the course of the DMF-contaminated cyclopentanone uptake experiment on open-pore **SHF-61**. The stepped appearance is an artefact of experiment accuracy (rounding).

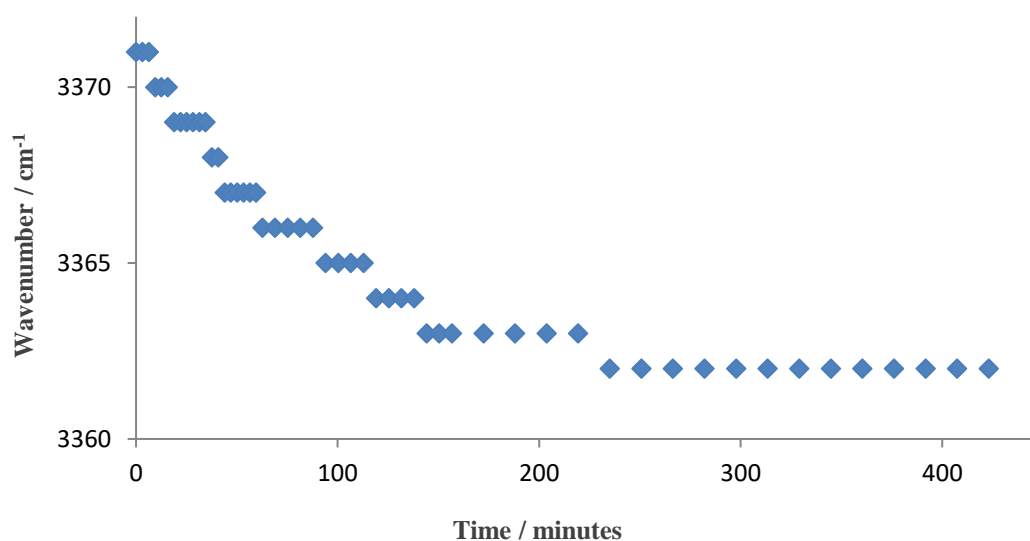


Figure 3.35. Wavenumber of the symmetric framework NH_2 stretch over the course of the DMF-contaminated cyclopentanone uptake experiment on open-pore **SHF-61**. The stepped appearance is an artefact of experiment accuracy (rounding).

3.4.6. Isopropanol Uptake in Open-Pore SHF-61 (DMF Contaminated)

Isopropanol uptake was monitored in the same manner as the previous experiments on open-pore **SHF-61** (Sections 3.4.2 - 3.4.5). During data analysis, however, the presence of DMF was observed, characterised by its distinctive 1667 cm^{-1} carbonyl band and 1096 cm^{-1} C-N-CHO deformation band. Additionally, the framework amine bands have starting values consistent with DMF-interaction (3476 cm^{-1} and 3365 cm^{-1}). This contamination was likely due to DMF vapour residing in the sample stage, leftover from the previous uptake experiment (Section 3.4.2), despite a lengthy heating cycle between experiments (*ca.* 6 hours), which expected to remove any residual solvent in the cell. The framework amine bands remain essentially constant throughout the experiment, as does the area of the DMF bands, which indicates that isopropanol does not replace the existing DMF during the course of the experiment. Isopropanol is nevertheless adsorbed into the free pore space of the material, evidenced by the growth of a C-H stretch at 2962 cm^{-1} , a C-C stretch at 1160 cm^{-1} and a C-O stretch at 950 cm^{-1} (Figure 3.36).

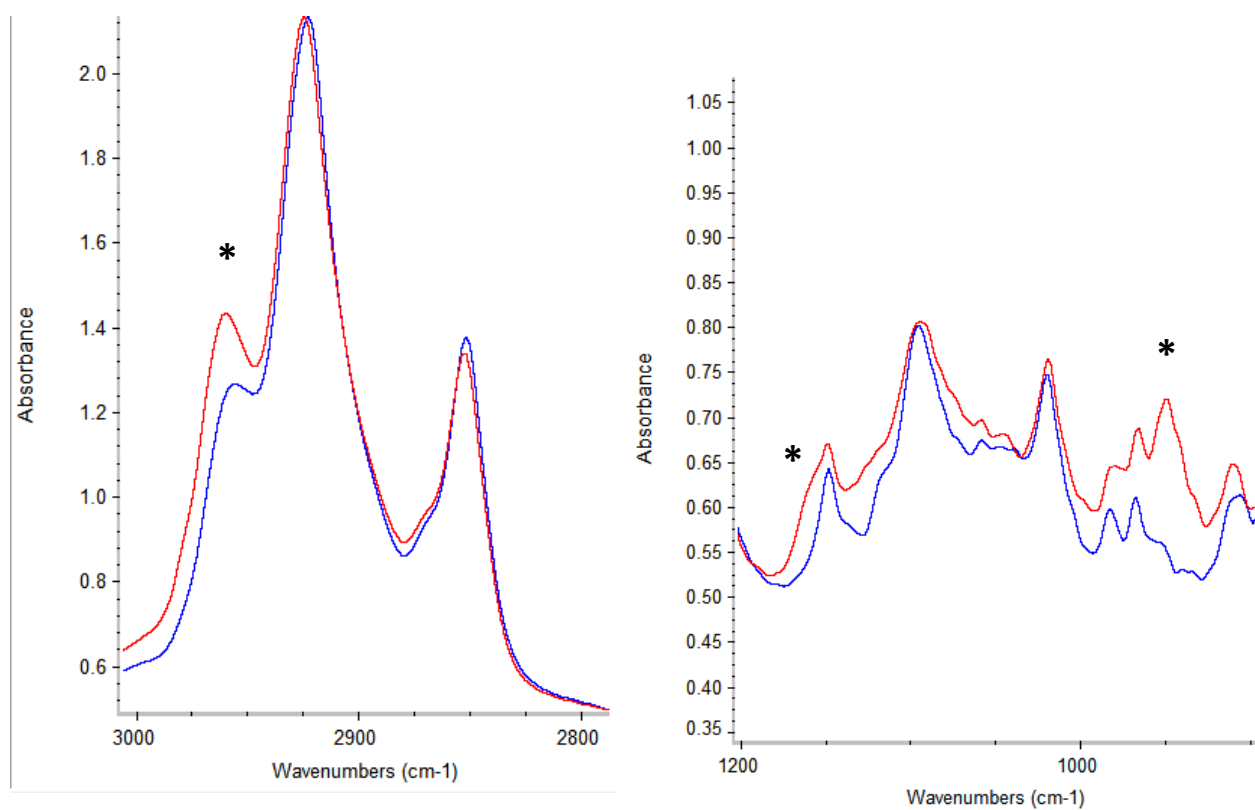


Figure 3.36. The three isopropanol peaks monitored in the isopropanol uptake experiment on open-pore **SHF-61**. Reading from left: C-H stretch, 2962 cm^{-1} ; C-C stretch, 1160 cm^{-1} ; C-O stretch, 950 cm^{-1} (all marked).

Peak fitting the isopropanol bands reveals that the solvent is adsorbed readily from the start of the experiment, with a profile that resembles a type I gas uptake isotherm, suggesting no/little barrier to adsorption (Figures 3.37 – 3.39).¹³

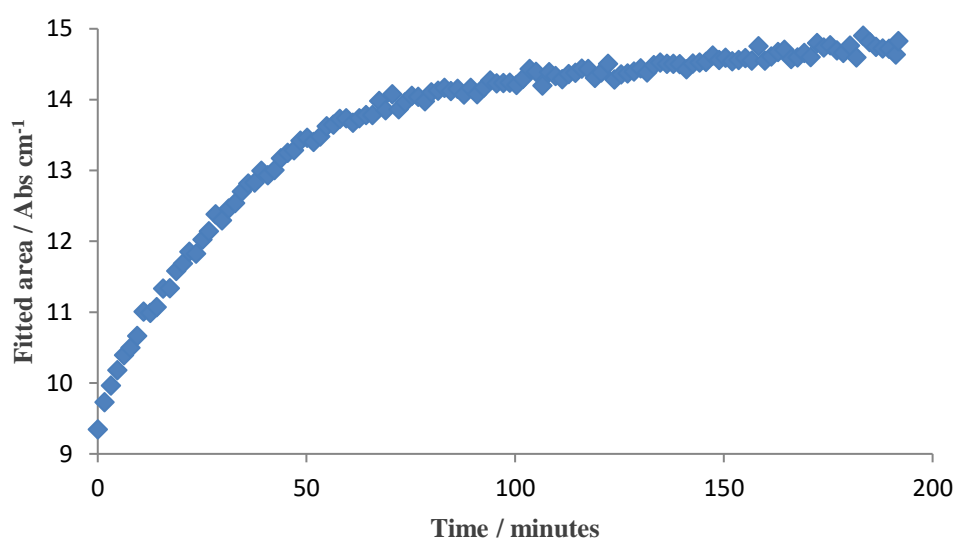


Figure 3.37. Peak fitted area of the isopropanol C-H stretch at 2962 cm^{-1} over the course of the isopropanol uptake experiment on open-pore **SHF-61**.

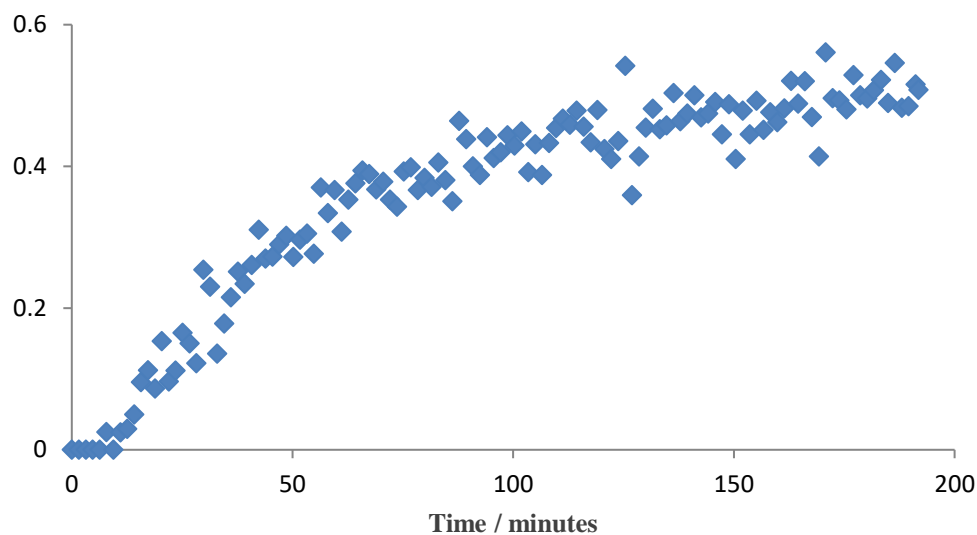


Figure 3.38. Fitted peak area of the isopropanol C-C stretch vibration at 1160 cm^{-1} over the course of the isopropanol uptake experiment on open-pore **SHF-61**.

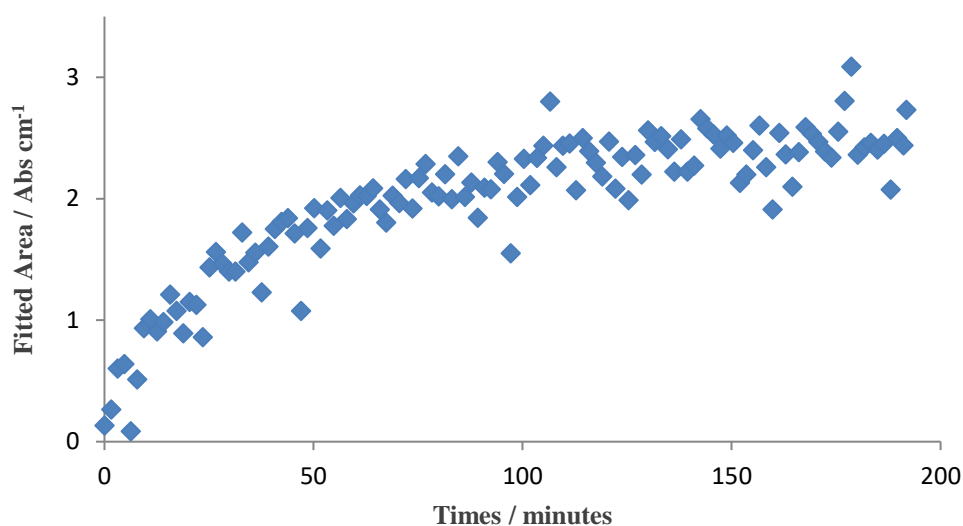


Figure 3.39. Fitted peak area of the isopropanol C-O stretch at 950 cm^{-1} over the course of the isopropanol uptake experiment on open-pore **SHF-61**.

3.4.7. Water Uptake in Open-Pore SHF-61

Analysis of water uptake in **SHF-61** was non-trivial, since the only distinguishing feature of water in an infra-red spectrum is the broad O-H band at high energy. Visual inspection shows that the baseline rises sharply in the initial stages of the experiment, simultaneously with the amine bands shifting to a lower energy (Figure 3.40). Quantification of this water uptake was not possible; but by

considering the whole region in addition to the usual amine band model-fitting approach used in some of the other uptake experiments, an additional model-based fit was performed on the entire 3699-2500 cm^{-1} region. The profiles of the two fits are exceptionally similar to each other (Figures 3.41 and 3.42), suggesting that the change in the amine bands occurs simultaneously with the rising water O-H stretch. This further implies that water is adsorbed onto amine groups first (otherwise the amine band model fit would reach a plateau earlier than the model fit for the entire 3699-2500 cm^{-1} region). This is unsurprising given the high hydrogen-bond acceptor capability of water.⁸

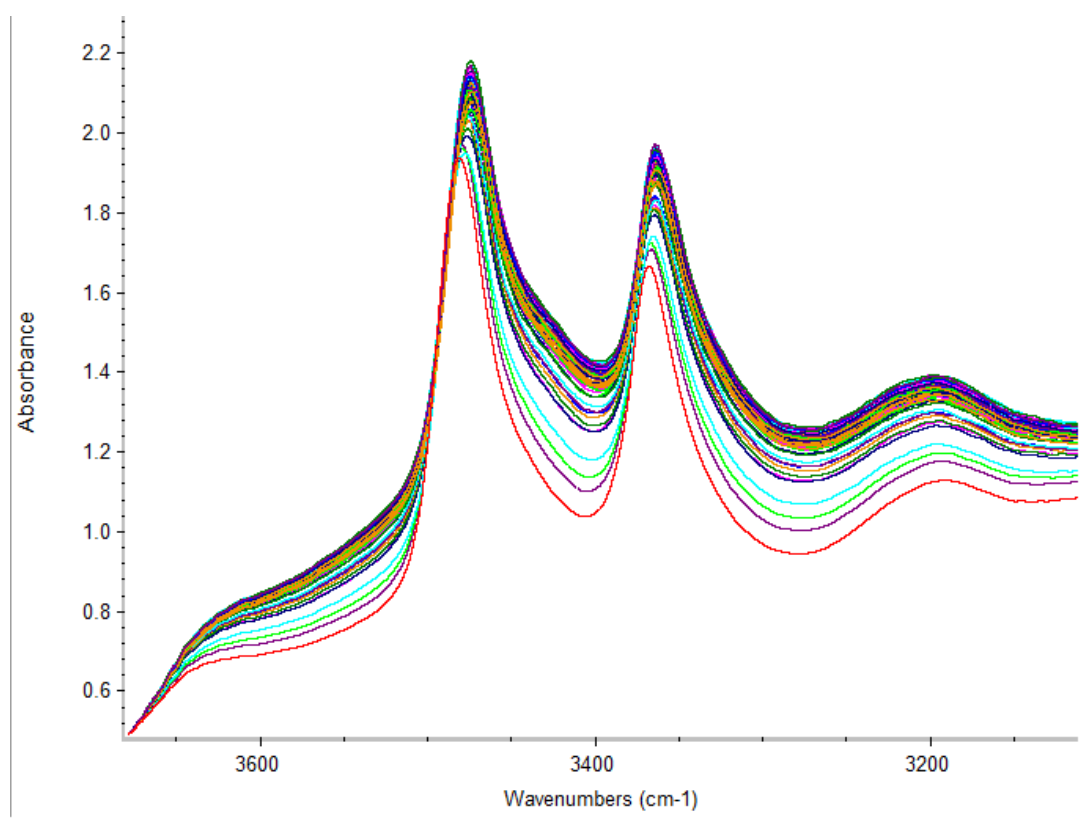


Figure 3.40. High-energy region of the spectra collected in the water uptake study on open-pore **SHF-61**, in ascending order (*i.e.* first measurement at the bottom, final measurement at the top).

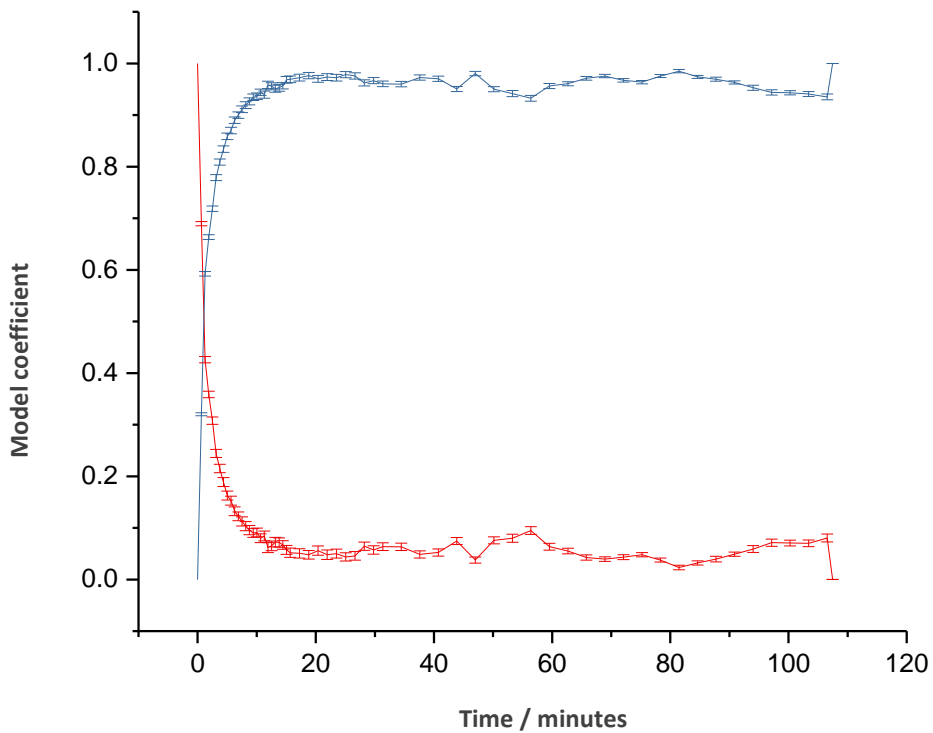


Figure 3.41. Results of the model-fit approach on the water uptake study experiment on open-pore **SHF-61**, using only the amine bands. Red = first measurement model (oE); blue = final measurement model (oH₂O).

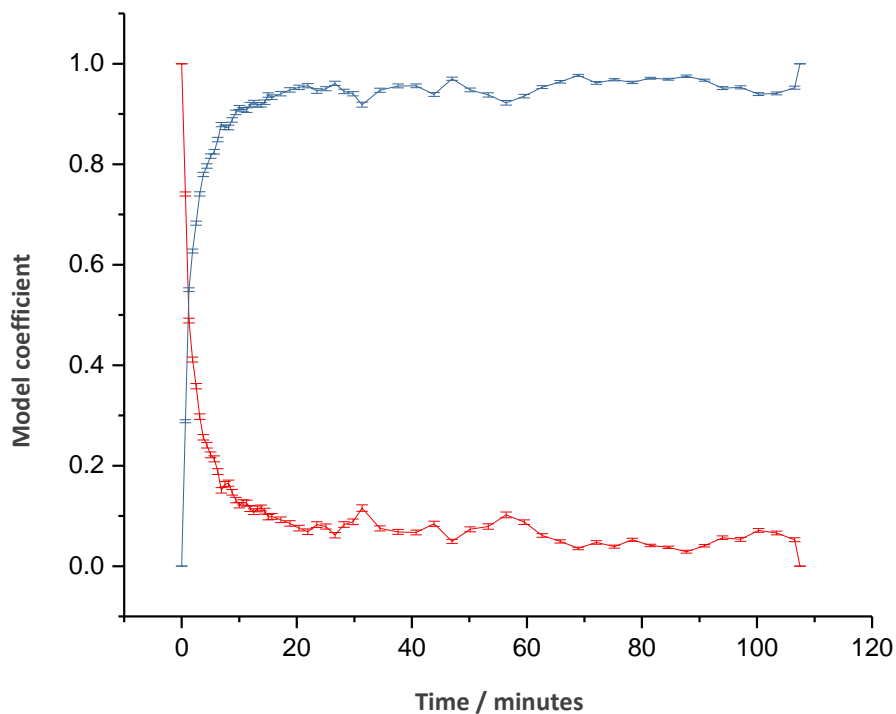


Figure 3.42. Results of the model-fit approach on the water uptake study experiment on open-pore **SHF-61**, using only the amine bands. Red = first measurement model (oE); blue = final measurement model (oH₂O).

Immediately upon exposure to water, the framework amine bands shift to a lower wavenumber (Figures 3.43 and 3.44). Interestingly, their final values at the end of the experiment are 3 – 4 cm^{-1} higher than in the analogous DMF uptake experiment on open-pore **SHF-61** (Section 3.4.2). Additionally, the fact that the two model fitting methods produced essentially the same result suggests that water uptake does not occur after the framework amine bands are saturated. These two pieces of evidence suggest the possibility that or the open MOF closes upon water uptake, in the same fashion as **MIL-53**.¹² However, more detailed studies, using a variety of analytical methods (particularly diffraction studies) would be needed to confirm this.

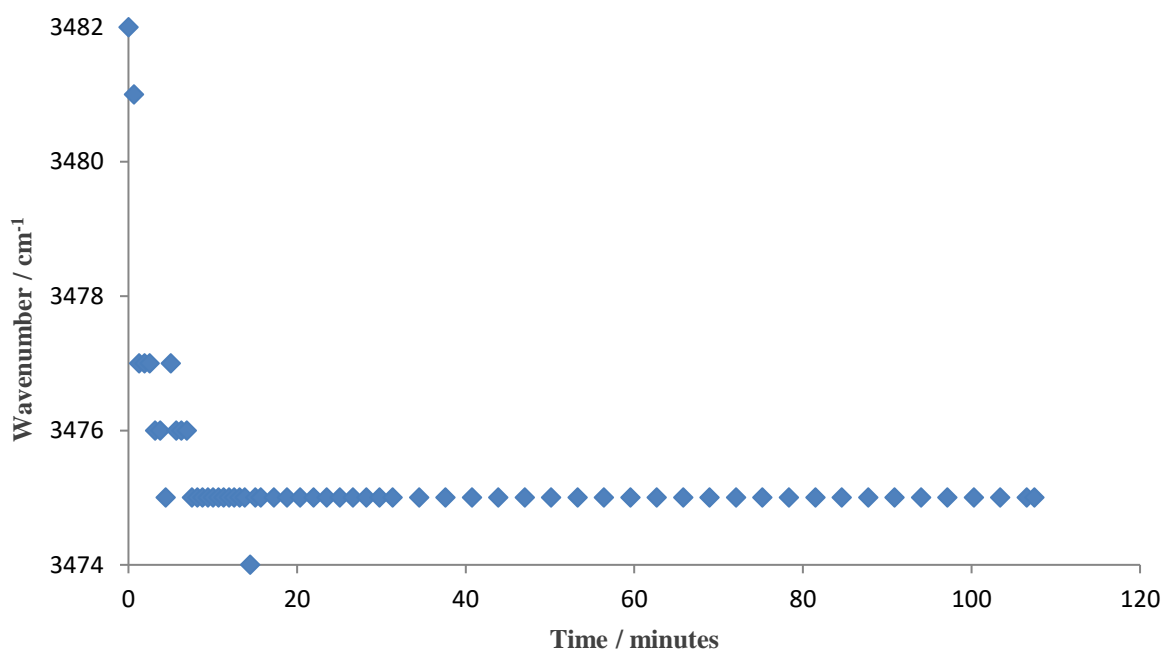


Figure 3.43. Wavenumber of the asymmetric framework amine stretch in the water uptake experiment on open-pore **SHF-61**. The stepped appearance is an artefact of experiment accuracy (rounding).

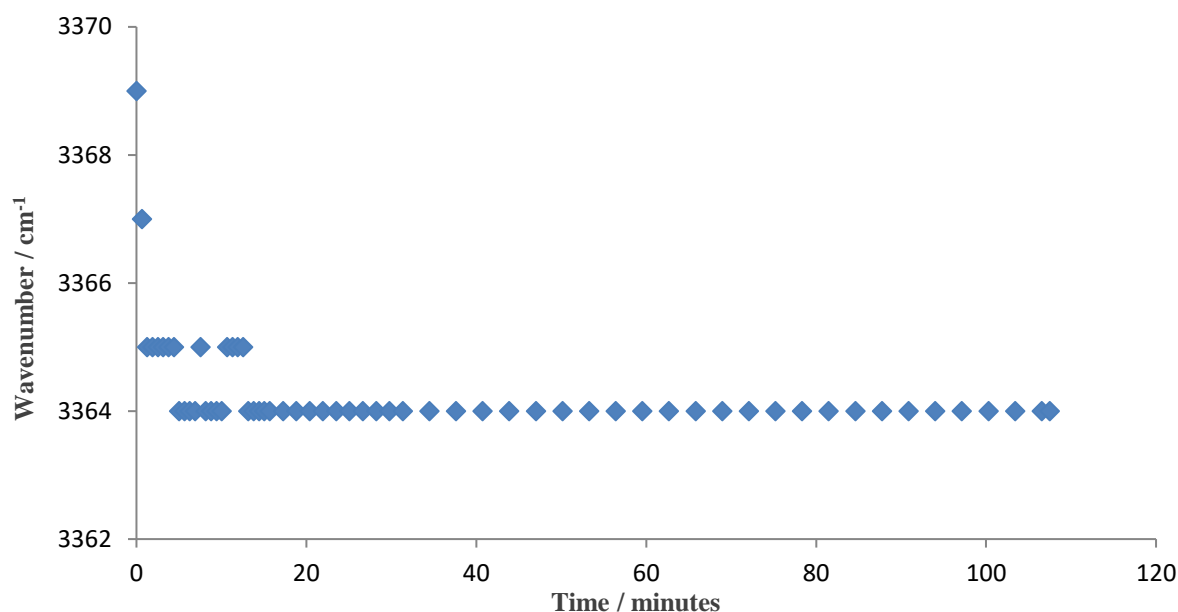


Figure 3.44. Wavenumber of the symmetric framework amine stretch in the water uptake experiment on open-pore **SHF-61**. The stepped appearance is an artefact of experiment accuracy (rounding).

3.4.8. Discussion of SHF-61 Solvent Dependence

The confusion regarding the solvent dependence of **SHF-61** can be demonstrated by the following series of statements. Each argument is chemically sound, and yet together they do not fully account for the behaviour of **SHF-61**:

Referring back to the introduction (Section 3.2), DMF is less polar than isopropanol,⁸ yet isopropanol does not induce pore closing upon desolvation.⁹ The infra-red spectroscopy studies presented here have revealed that DMF interacts with the framework amine bands, and logically, this interaction must be *via* the carbonyl, as this is the strongest hydrogen-bond acceptor on the molecule. However, cyclopentanone also has a carbonyl group, yet does not interact as strongly with the amine groups. Therefore, it must be the strength of the solvent as a hydrogen-bond acceptor which induces pore-closure; and yet, isopropanol is also a relatively strong hydrogen-bond acceptor,⁸ and might be expected to induce pore closure, but it does not.⁹

Clearly, more work is needed. To progress further, isopropanol uptake needs completing without DMF contamination, and more solvents need investigating that are good H-bond acceptors, and/or have high polarity, such as formamide, *n*-alcohols (series where R = Et, Pr, Bu, Pe (?) etc.).

Another factor to consider is the cation, which is not directly observable in our SCXRD studies (*cf.* chapter 2 and Carrington *et al.*)¹ or our IR studies (this chapter). Perhaps the most straightforward way to monitor this is with a computational approach. The most energetically favourable position of the cation could be deduced in both open and closed empty framework models, and then solvent molecules could be introduced to these models, in order to determine if the most favourable interactions are with the framework or the cation, and also determine the nature of these interactions. This approach could be extended to other guests as well, such as CO₂, SO₂ and CH₃, which would complement the existing crystallographic studies (*cf.* chapter 2 and Carrington *et al.*)¹

3.5. Conclusion

The infra-red studies presented in this chapter, monitoring *in situ* solvent uptake in **SHF-61**, have produced some interesting results. Specifically, we have shown that DMF is likely the most strongly interacting guest in our studies, despite other candidates being either similarly highly polar or similarly strong hydrogen-bond acceptors. DMF uptake produces a gated opening in closed-pore **SHF-61**, yet enters the open-pore material without causing any pore-closure, despite the closed-pore structure only being attainable from DMF desolvation. Additionally, we have shown that trace amounts of DMF (as a contaminant) are able to compete with both cyclopentanone and isopropanol, despite the latter solvents being in far greater excess. Cyclopentanone interacts fairly weakly with the framework amine groups, whereas chloroform may interact with a framework carboxyl group instead. Finally, the possibility has been raised that water uptake in open-pore **SHF-61** may in fact cause the material to close, similar to the well-studied **MIL-53** system.¹²

The next stage in this project needs to focus on the factors that infra-red spectroscopy could not monitor. Quantification of the amount of solvent adsorbed could be achieved using gravimetric or volumetric approaches. Similarly, the hypotheses formed regarding the pore-state of the material could be confirmed (or refuted) using *in situ* crystallographic studies, akin to those described in chapters 2 and 4 of this thesis. Finally, computational studies could reveal the location of the elusive

dimethylammonium counter-ion, providing insight into the role it plays in **SHF-61**, as well as revealing the favourable binding sites for the guest species studied thus far by practical methods.

3.6. References

- 1 E. J. Carrington, C. A. McAnally, A. J. Fletcher, S. P. Thompson, M. Warren and L. Brammer, *Nat. Chem.*, 2017, **9**, 882–889.
- 2 A. Schneemann, V. Bon, I. Schwedler, I. Senkovska, S. Kaskel and R. A. Fischer, *Chem. Soc. Rev.*, 2014, **43**, 6062–6096.
- 3 G. Férey, *Chem. Soc. Rev.*, 2008, **37**, 191–214.
- 4 G. Férey and C. Serre, *Chem. Soc. Rev.*, 2009, **38**, 1380–1399.
- 5 M. Alhamami, H. Doan and C. H. Cheng, *Materials*, 2014, **7**, 3198–3250.
- 6 G. Férey, *Dalton Trans.*, 2016, **45**, 4073–4089.
- 7 K. Dimroth, C. Reichardt, T. Siepmann and F. Bohlmann, *Liebigs Ann. Chem.*, 1966, **661**, 1.
- 8 Y. Marcus, *The Properties of Solvents*, John Wiley & Sons, Chichester, 1998.
- 9 A. Newman, *Solvent effects on a “breathing” metal-organic framework*, 4th Year MChem Thesis, Department of Chemistry, The University of Sheffield, 2017.
- 10 B. Yuan, D. Ma, X. Wang, Z. Li, Y. Li, H. Liu and D. He, *Chem. Commun.*, 2012, **48**, 1135–1137.
- 11 A. Greenaway, B. Gonzalez-Santiago, P. M. Donaldson, M. D. Frogley, G. Cinque, J. Sotelo, S. Moggach, E. Shiko, S. Brandani, R. F. Howe and P. A. Wright, *Angew. Chem. Int. Ed.*, 2014, **53**, 13483–13487.
- 12 C. Serre, F. Millange, C. Thouvenot, M. Noguès, G. Marsolier, D. Louër and G. Férey, *J. Am. Chem. Soc.*, 2002, **124**, 13519–13526.

13 M. D. Donohue and G. L. Aranovich, *Adv. Colloid Interface Sci.*, 1998, **76-77**, 137-152.

4. The Dynamic Behaviour of a Trigonal Metal-Organic Framework: Response to Solvent Removal, Gas Uptake and Temperature

4.1. Abstract

The synthesis and characterisation of trigonal metal-organic framework, $[\text{NMe}_2\text{H}_2][\text{Cd}(\text{NO}_2\text{BDC})_2]$, is described. *In situ* and *ex situ* X-ray diffraction studies on both single crystal and powder samples show that $[\text{NMe}_2\text{H}_2][\text{Cd}(\text{NO}_2\text{BDC})_2]$ adopts a narrow-pore structure upon the removal of its solvent guests, with the transition to the desolvated structure occurring *via* negative area expansion (NAE) of the crystallographic *ab*-plane and positive linear expansion (PLE) of the *c*-axis. The narrow structure is shown to adsorb CO_2 at both 195 K and 298 K and *in situ* X-ray diffraction experiments on both single crystal and powder samples show that this partially reverses the transition observed upon desolvation; i.e. NLE of the *c*-axis and PAE of the *ab*-plane. Volumetric adsorption data is used alongside crystallographic data to rationalise a mechanism for CO_2 uptake. Additionally, $[\text{NMe}_2\text{H}_2][\text{Cd}(\text{NO}_2\text{BDC})_2]$ is shown to display temperature-dependent flexibility, occurring *via* negative thermal expansion (NTE) of the *c*-axis and positive thermal expansion (PTE) of the *ab*-plane. This is similar to reported behaviour of an analogous material, **QMOF-2** (Q = Quartz-type), but is expressed to a greater extent. This chapter therefore shows that dynamic behaviour in $[\text{NMe}_2\text{H}_2][\text{Cd}(\text{NO}_2\text{BDC})_2]$ can be induced by three different stimuli: solvent-removal; gas-uptake; and temperature change.

4.2. Introduction

In 2002, Sun *et al* reported the synthesis and structure of **QMOF-2** (Q = quartz-like, formula $\text{H}[\text{In}(\text{BDC})_2]$).¹ The material has a molecular structure reminiscent of **SHF-61**,² with eight-coordinate In^{III} centres surrounded by four terephthalate ligands in a pseudo-tetrahedral arrangement (Figure 4.1). However, where **SHF-61** has a diamondoid network topology and resides in the orthorhombic space group *Fddd*,² **QMOF-2** has a β -quartz topology and resides in the hexagonal space group *P6₄22*.¹ Like **SHF-61**, **QMOF-2**, is two-fold interpenetrated. The hexagonal β -quartz topology results in the presence of hexagonal channels aligned parallel to the crystallographic *c*-axis (Figure 4.1), which are

reported to be filled with 1.5 equivalents of DMF and 4 equivalents of water, based on thermogravimetric analysis.¹

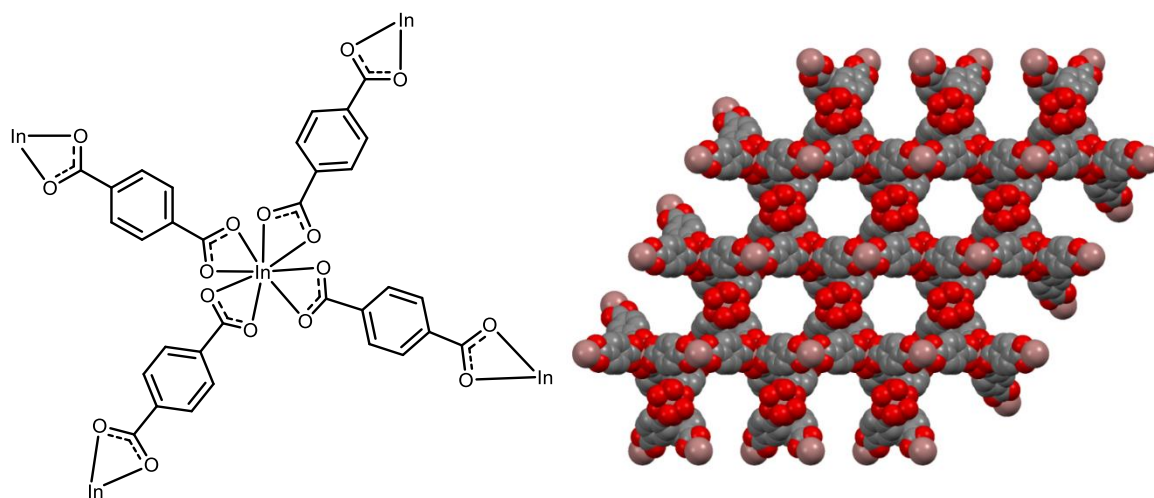


Figure 4.3. Left: Representation of the In^{III} coordination sphere and immediate environment in QMOF-2. Right: The crystal structure of QMOF-2 viewed along the c-axis, showing the hexagonal channels that propagate through the material.

The counter-ion of the anionic framework in **QMOF-2** is reported as H⁺.¹ Protonated frameworks have been reported in the past, for example, Ingleson *et al.* used infra-red spectroscopy to show that the linker carboxylate of a nickel-based MOF had been protonated.³ However, in the case of **QMOF-2**, no evidence is provided for the existence of a protonated carboxylate. Additionally, the generation of dimethylammonium from DMF decomposition during solvothermal reactions is well documented in the literature,⁴ and would be consistent with **SHF-61** and other similar published materials.^{2,5-8} Thus, it may be more reasonable to assume in the absence of experimental evidence that the formula for **QMOF-2** is (Me₂NH₂)[In(BDC)₂].

The authors correctly note that the preparation of a chiral structure from achiral components is challenging, and highlight that **QMOF-2** could be a step forwards in this field. However, a paper by Ji *et al* in 2013 on gas sorption in **QMOF-2** reports the synthesis of the enantiomeric form, *i.e.* space group *P*6₂22.⁹ It is likely that both teams produced a racemic batch of material, and happened (by chance) to select crystals of opposite enantiomers for single-crystal X-ray diffraction. This will be discussed in more detail in Section 4.4.1. It is worth mentioning that Ji *et al.* report the guest species

of the framework to be water and dimethylamine, although they do not mention how they came to this conclusion.⁹

In 2014, Collings *et al.* reported dynamic behaviour in the deuterium-exchanged analogue of **QMOF-2** (reported as InD(BDC)₂, although it is unclear whether there exists a deuterated carboxylate linker or instead a NMe₂D₂⁺ counter-ion) as a response to temperature.¹⁰ Before discussing the temperature-induced flexibility, however, it is worth mentioning the cell parameters obtained upon activation. After heating the material at 100 °C for 24 hours, the resultant unit cell was 70 Å³ (*ca.* 3 %) smaller than that of the solvated structure reported originally by Sun *et al.*,¹ despite being measured at very similar temperatures (Table 4.1). Additionally, this desolvated structure was found by neutron diffraction to contain residual guest,¹⁰ although it is unclear whether this is un-removed solvent or a NMe₂D₂⁺ counter-ion. This 3 % decrease in unit cell volume was not alluded to by Collings *et al.*, and it is a factor of 4 smaller than that which occurs upon desolvation of **SHF-61-DMF**. Nevertheless, it does imply that a hexagonal β-quartz-type MOF is capable of guest-induced flexibility.

Table 4.17. Unit cell parameters for solvated **QMOF-2** and activated, deuterated **QMOF-2** from different publications.

	<i>a</i> / Å	<i>c</i> / Å	<i>V</i> / Å ³	Temperature / K	Pre-treatment
Sun <i>et al.</i> (2002)¹	15.087(4)	12.032(5)	2371.7(13)	293	None
Collings <i>et al.</i> (2014)¹⁰	14.7900(13)	12.152(2)	2302.0(5)	285	100 °C, 24 hrs

The main focus of the 2014 paper by Collings *et al.* was the temperature-dependent dynamic behaviour of two materials with quartz-type topology: Zn(ISN)₂ (ISN = isonicotinate); and the aforementioned deuterated **QMOF-2**. By conducting variable temperature experiments with *in situ* powder neutron diffraction, the authors showed that as the temperature is increased from 10 to 300 K, deuterated **QMOF-2** exhibits negative thermal expansion (NTE) in the *c*-axis and positive thermal expansion (PTE) in the *a*- and *b*-axes (Table 4.2), similar to the behaviour of Zn₂(BDC)₂(DABCO) discussed in Section 1.3.3.¹¹

Table 4.18. Unit cell parameters of activated, deuterated **QMOF-2** as a function of temperature. Table reproduced from reference 10 with permission of The Royal Society of Chemistry.

Temperature / K	$a / \text{\AA}$	$c / \text{\AA}$	$V / \text{\AA}^3$
11.96(7)	14.5291(11)	12.2738(17)	2243.8(5)
42(3)	14.5475(12)	12.2628(19)	2247.5(5)
95.8(8)	14.5838(11)	12.2472(17)	2255.8(5)
138(4)	14.6285(12)	12.2296(19)	2266.4(5)
188(2)	14.6818(12)	12.2035(19)	2278.1(5)
238(3)	14.7335(12)	12.1809(19)	2289.9(5)
285.2(5)	14.7900(13)	12.152(2)	2302.0(5)

Conversely, Collings *et al.* found that $\text{Zn}(\text{ISN})_2$ behaved in the opposite manner to deuterated **QMOF-2**, in that positive thermal expansion was observed in the c -axis, and negative thermal expansion in the ab -plane.¹⁰ The authors then demonstrate that the reason for this difference is purely geometrical, and results from the ρ value ($\rho = c/a$) of the material. When ρ is lower than a critical value ρ_{crit} (0.53) the material exhibits negative thermal expansion in the ab -plane (ρ for $\text{Zn}(\text{ISN})_2$ is 0.40); when ρ is greater than 0.53, negative thermal expansion is observed in the c -axis (ρ for activated deuterated **QMOF-2** is 0.82). Negative thermal expansion is rare, and interesting from an industrial/commercial viewpoint due to the potential for high control over the thermal properties of materials.¹²

A small number of MOFs have been reported which are isostructural to **QMOF-2**, in that they have either In^{III} or Cd^{II} ions linked by terephthalate-based ligands in a two-fold interpenetrated, β -quartz-type arrangement.⁵⁻⁷ This chapter describes a modified synthesis and revised structure for one of these materials, $[\text{NMe}_2\text{H}_2][\text{Cd}(\text{NO}_2\text{BDC})_2]$,⁶ and its novel dynamic behaviour as a response to solvent removal, gas uptake, and temperature.

4.3. Experimental

4.3.1. General Techniques

Reagents and solvents were obtained from Sigma-Aldrich, Alfa Aesar, Acros Organics, Fisher Scientific, Fluorochem or Manchester Organics, and were used without additional purification.

Samples used for elemental analysis, thermogravimetric analysis, volumetric adsorption and in-house powder X-ray diffraction were ground into a powder using a mortar and pestle immediately prior to analysis, to ensure consistency of solvent content in the bulk material. For solution-phase NMR spectroscopy, the sample (*ca.* 3 mg) was acid-digested in 50 μ L deuterium chloride (35 % in D₂O) in 1 mL DMSO-d₆.

Thermogravimetric analysis (Figure 4.4) was performed in air using a Perkin Elmer Thermogravimetric Analyser. Elemental analysis was performed by combustion in pure oxygen using a Perkin Elmer 24000 CHNS/O Series II Analyser or an Elementar Vario MICRO cube analyser. NMR spectroscopy (400 MHz) was performed using Bruker AVANCE III 400 HD or AVANCE 400 HD Spectrometers and analysed using MestReNova. Volumetric gas adsorption was performed on a Micromeritics ASAP 2020Plus Analyser. The sample (*ca.* 100 mg) was desolvated at 80 °C under vacuum overnight (*ca.* 16 hours) using standard Schlenk techniques, transferred to the analyser and degassed for a further 16 hours under vacuum at 80 °C prior to analysis. Nitrogen uptake was performed at 77 K using a liquid N₂ bath for temperature control; CO₂ uptake was performed at 195 K using a dry ice/acetone bath.

In-house single-crystal X-ray diffraction experiments were performed using either a Bruker X8 APEX-II CCD diffractometer with SMART or KAPPA platform, with a Mo-K α sealed-tube X-ray source, or a Bruker D8 Venture diffractometer with a PHOTON 100 dual-CMOS chip detector, operating a Cu-K α I μ S microfocus X-ray source. Data were processed using the APEX-2 suite of programs. Sample temperature was maintained using an Oxford Cryosystems Cryostream 700 device. Samples were mounted directly from the mother liquor, unless stated otherwise. Absorption correction was performed using empirical methods (SADABS) based on symmetry-equivalent

reflections combined with measurements at different azimuthal angles.^{13,14} Synchrotron single-crystal X-ray diffraction data were recorded at Beamline I19, Diamond Light Source. The crystal was glued to a Mylar loop and loaded into a 0.7 mm quartz capillary built into a gas cell to allow CO₂ uptake. Full hemispheres of data were collected using three 132 ° and one 180 ° omega scans, with 0.4 ° slicing, on a Newport diffractometer using a Pilatus 300K detector. Data processing and absorption correction was performed using Rigaku Oxford Diffraction CrysAlis Pro. Crystal structures were solved, and refined against F^2 values the program SHELX 2013¹⁶ implemented via OLEX-2.¹⁵ All non-hydrogen atoms were refined anisotropically unless stated otherwise. Crystallographic restraints and constraints were applied to some structures where necessary. Positions of hydrogen atoms were calculated with idealised geometries and refined using a riding model with isotropic displacement parameters. Final structure files (CIFs) were checked with PLATON¹⁷ and checkCIF.¹⁸ The PLATON function SQUEEZE was used only to determine residual electron densities and solvent accessible void space. The below equations define the measures of agreement between calculated and experimental data:

$$R1(F) = \frac{\sum(|F_o| - |F_c|)}{\sum|F_o|} \quad wR2(F^2) = \sqrt{\frac{\sum(F_o^2 - F_c^2)^2}{\sum w F_o^4}} \quad S(F^2) = \sqrt{\frac{\sum w(F_o^2 - F_c^2)^2}{(n+r-p)}}$$

In-house powder X-ray diffraction experiments were performed using a Bruker D8 Advance, equipped with Göbel mirrors and recorded in the range $3^\circ < 2\theta < 60^\circ$ using Cu-K α radiation. Data collection was performed with Debye-Scherrer geometry, with a rotating capillary stage. Samples were loaded in 0.7 mm borosilicate capillaries. Temperature was either ambient (routine collections), or controlled using an Oxford Cryosystems Cryostream Plus device. Synchrotron powder X-ray diffraction data were collected at Beamline I11, Diamond Light Source using a wide-angle position sensitive detector comprising 18 Mythen-2 modules.^{19,20} Samples were packed into 0.7 mm quartz capillaries, built into a gas rig to allow sample evacuation and CO₂ uptake. A pair of scans was collected for each measurement, related by a 0.25 ° detector offset, to account for gaps between modules. The two patterns were summed together prior to analysis. All powder diffraction data were

analysed by Pawley refinement,²¹ using TOPAS 4.1.²² The below equations define R_{wp} and R_{wp}' , the measures of agreement between calculated and experimental diffraction data:

$$R_{wp} = \sqrt{\frac{\sum[w(Y_{obs}-Y_{calc})^2]}{\sum[wY_{obs}^2]}} \quad R_{wp}' = \sqrt{\frac{\sum[w(Y_{obs}-Y_{calc})^2]}{\sum[w(Y_{obs}-bkgr)^2]}}$$

4.3.2. Synthesis and Characterisation

Cadmium nitrate hexahydrate (0.3072 g, 0.9926 mmol), 2-nitroterephthalic acid (0.4210 g, 1.994 mmol), dimethylamine hydrochloride (0.0080 g, 98 μ mol) and *N,N*-dimethylformamide (DMF) (10 mL) were stirred for *ca.* 5 minutes (until dissolution of the solids) in a 23 mL Teflon vessel. The Teflon vessel was then sealed inside a stainless steel autoclave, heated to 130 °C at a rate of 1 °C min⁻¹ and held at 130 °C for 24 hours. The vessel was then cooled to room temperature at a rate of 0.1 °C min⁻¹ and the product (orange crystalline needles; 0.5621 g, 0.7381 mmol, 74 %)* washed with DMF and stored under DMF. Expected*: C, 40.16 %; H, 4.73 %; N, 10.75 %. Found: C, 40.16 %; H, 4.74 %; N, 10.74 %. *Yield and expected elemental analysis results calculated using the formula:



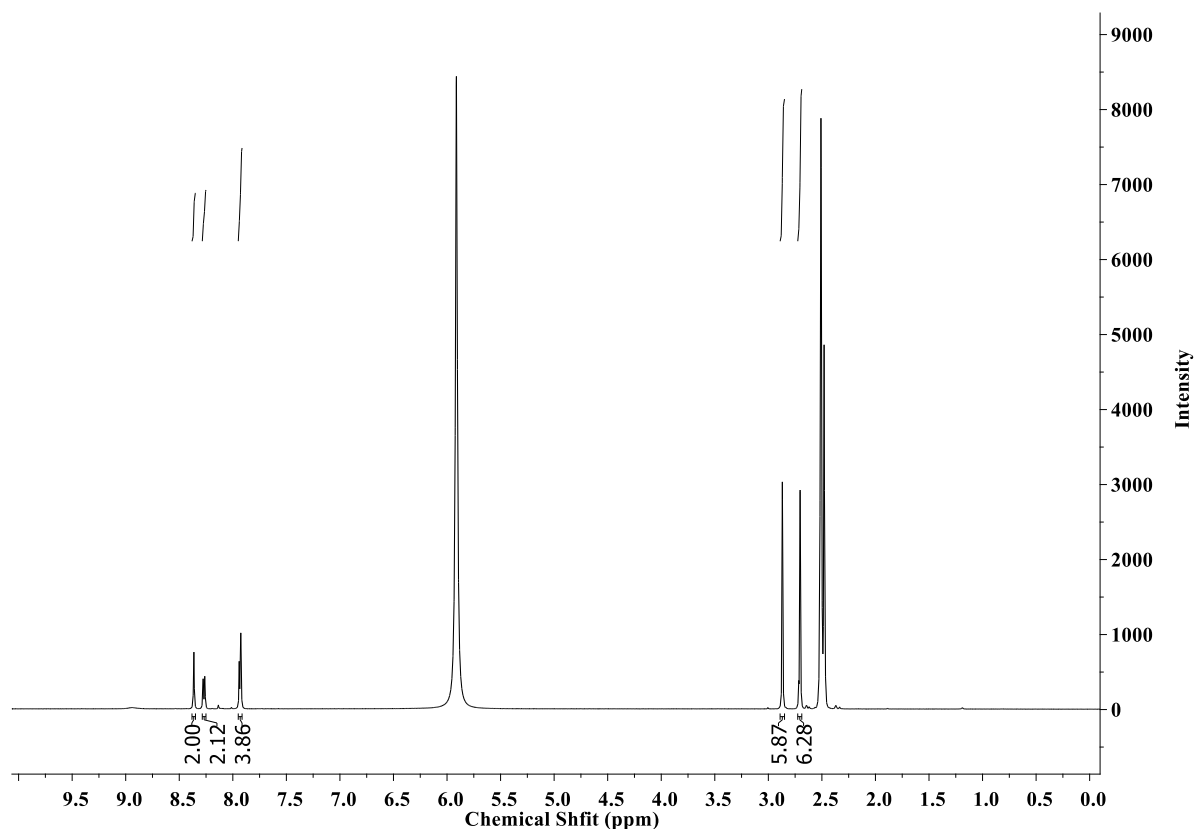


Figure 4.2. ^1H NMR spectrum of solvated $[\text{NMe}_2\text{H}_2][\text{Cd}(\text{NO}_2\text{BDC})_2]$. The aromatic region is expanded and assigned in Figure 4.17, Section 4.4.1. The peak at 2.5 ppm is DMSO; the peak at *ca.* 2.45 ppm is NMe_2H_2^+ ; the peak at *ca.* 5.8 ppm is $\text{H}_2\text{O}/\text{H}_3\text{O}^+$. The DMF peaks can be seen at 7.5 (formyl proton), 2.8 (methyl) and 2.7 (methyl).

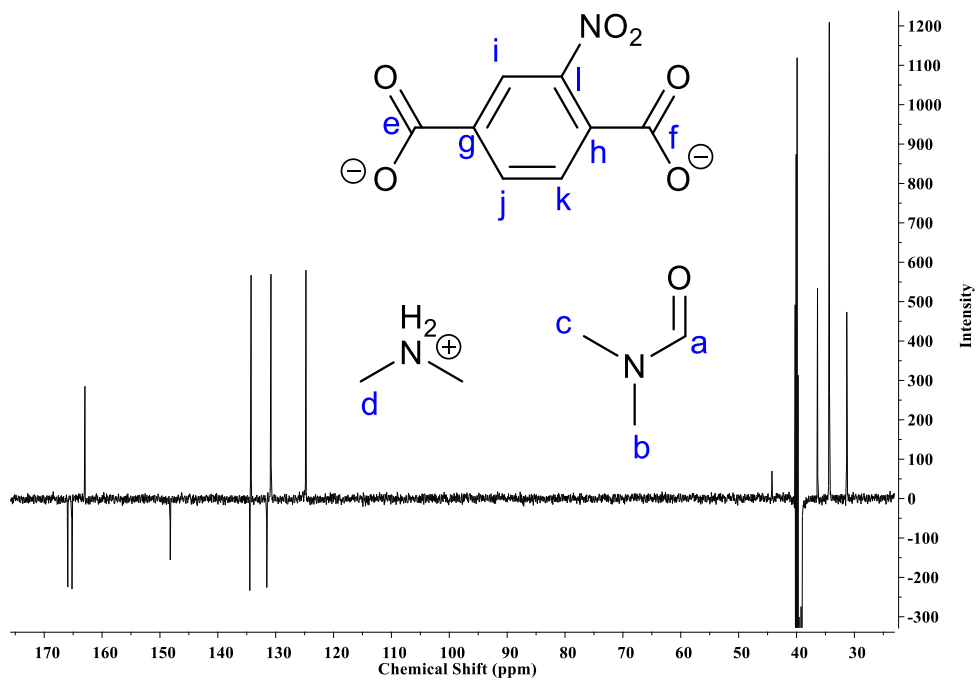


Figure 4.3. Solution-phase ^{13}C NMR spectrum of $[\text{NMe}_2\text{H}_2][\text{Cd}(\text{NO}_2\text{BDC})_2]$. Assignment as follows: 166 ppm, f; 165.2 ppm, e; 163 ppm, a; 148.2 ppm, l; 134.5 ppm, h; 134.2 ppm, g; 131.5 ppm, i; 130.8 ppm, j; 124.7 ppm, k; 39.7 ppm, DMSO; 36.4 ppm, b; 34.3 ppm, d; 31.3 ppm, c.

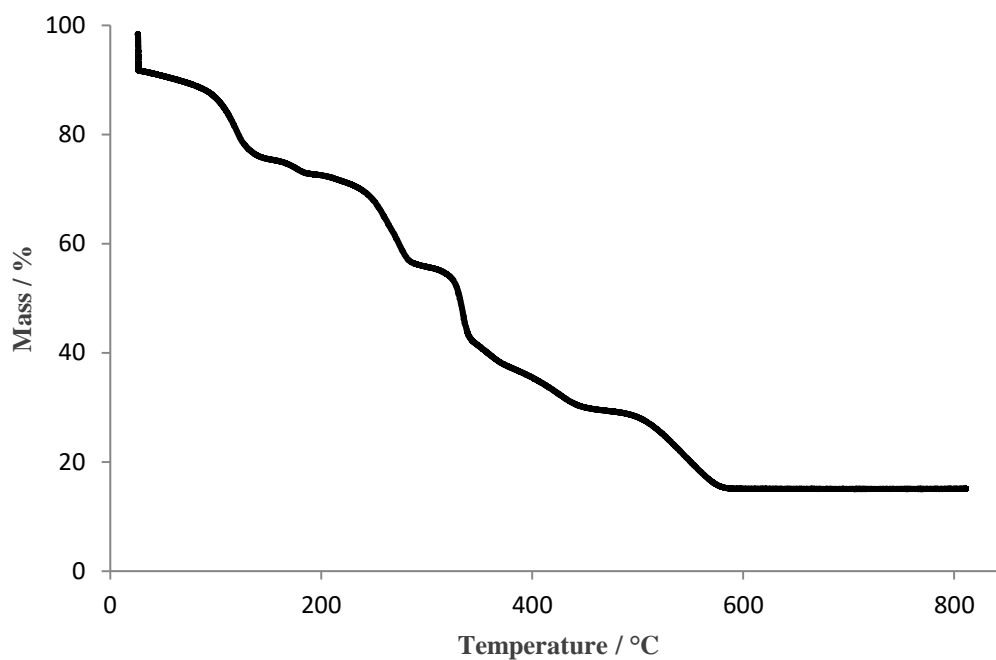


Figure 4.4. Thermogravimetric analysis of $[\text{NMe}_2\text{H}_2]_2[\text{Cd}(\text{NO}_2\text{BDC})_2]$. Sample (5 mg) was loaded into a pan, and heated in air from 25 °C to 800 °C at a rate of 3 °C min⁻¹. The sample was held at ambient temperature for 10 minutes prior to heating to allow the loss of surface-bound solvent. The stepped profile indicates the expected stepwise loss of MOF components (e.g. pore-bound solvent, dimethylamine, nitroterephthalic acid etc.) leaving behind cadmium oxide.

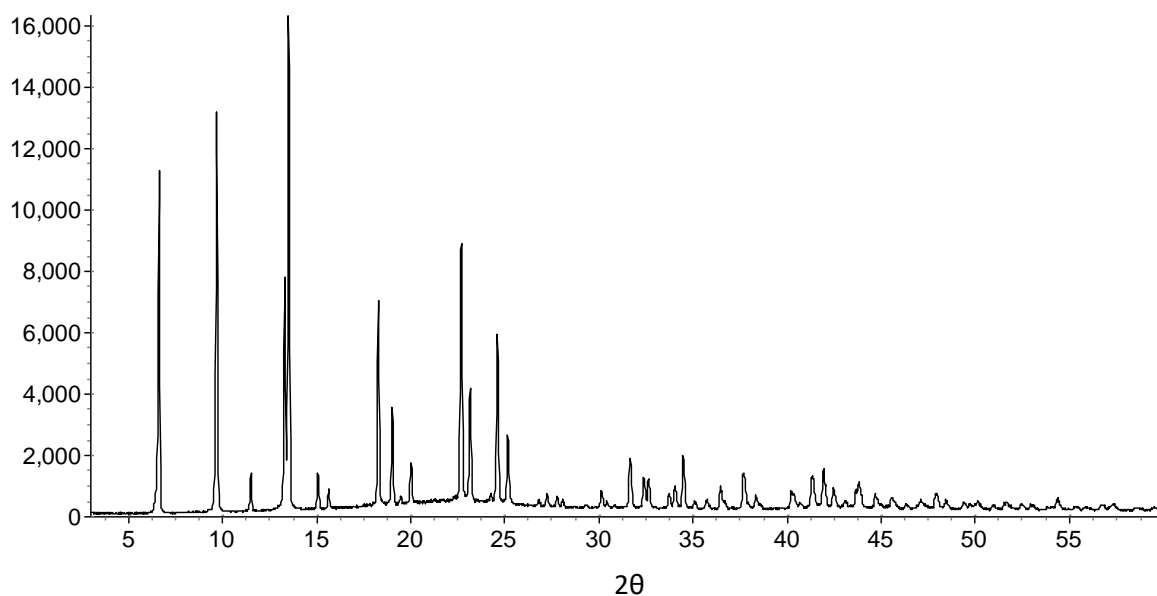


Figure 4.5. Powder X-ray diffraction pattern of solvated $[\text{NMe}_2\text{H}_2]_2[\text{Cd}(\text{NO}_2\text{BDC})_2]$ under ambient conditions. 196 parameters were used in refinement (13 background, 1 zero error, 5 profile, 2 cell and ca. 175 reflections). Trigonal/hexagonal lattice – unit cell parameters are detailed in Table 4.16, Section 4.4.2. $R_{\text{wp}} = 0.0502$; $R_{\text{wp}}' = 0.0836$.

Table 4.3. Crystal structure data tables for solvated $[\text{NMe}_2\text{H}_2]_2[\text{Cd}(\text{NO}_2\text{BDC})_2]$ at 100 K (A_1 = trigonal solution; A_2 = hexagonal solution), and at 195 K (B).

	A₁	A₂	B
Crystal Size / mm ³	0.5 x 0.2 x 0.2	0.5 x 0.2 x 0.2	0.5 x 0.3 x 0.3
Crystal System	Trigonal	Hexagonal	Trigonal
Space Group	<i>P</i> 3 ₂ 21	<i>P</i> 6 ₂ 22	<i>P</i> 3 ₂ 21
<i>a</i> / Å	14.8922(7)	14.8917(7)	15.0467(5)
<i>b</i> / Å	14.8922(7)	14.8917(7)	15.0467(5)
<i>c</i> / Å	12.7663(6)	12.7663(6)	12.6619(4)
α (°)	90	90	90
β (°)	90	90	90
γ (°)	120	120	120
<i>V</i> / Å ³	2452.0(3)	2451.8(3)	2482.63(18)
<i>Z</i>	3	3	3
Radiation	Mo-K α (λ = 0.71073 Å)	Mo-K α (λ = 0.71073 Å)	Cu- K α (λ = 1.54178 Å)
Density / g cm ⁻³	1.265	1.078	1.250
Temperature /K	100	100	195
μ / mm ⁻¹	0.721	0.709	5.758
2 θ range (°)	3.158 – 55.794	3.158 – 55.794	6.784 – 133.384
Reflns collected	22669	22669	42505
Independent reflns	2900	1967	2919
Reflns used in refinement, <i>n</i>	2900	1967	2919
L.S. parameters, <i>p</i>	157	55	157
No. of restraints, <i>r</i>	135	9	135
Flack parameter	-0.06(3)	0.00(3)	-0.028(9)
<i>R</i> _{int}	0.0514	0.0642	0.0384
<i>R</i> _{sigma}	0.0339	0.0318	0.0153
<i>R</i> 1(<i>F</i>) ^a <i>I</i> >2 σ (<i>I</i>)	0.0655	0.0922	0.0565
<i>wR</i> 2(<i>F</i> ²) ^a , all data	0.2230	0.3046	0.1676
<i>S</i> (<i>F</i> ²) ^a , all data	1.249	1.244	1.232

^a*R*1(*F*), *wR*2(*F*²) and *S*(*F*²) defined in section 4.3.1.

4.3.3. Solvent Removal

Solvent removal was performed on bulk-phase $[\text{NMe}_2\text{H}_2]_2[\text{Cd}(\text{NO}_2\text{BDC})_2]$ by vacuum filtering the crystals from the mother liquor, grinding to a fine powder, and subsequently heating the powdered

sample at 80 °C under vacuum for ≥ 16 hours using standard Schlenk techniques. Elemental analysis indicates solvent removal. Any alternative methods of monitoring bulk-phase desolvation are described in the text (*e.g. in situ* PXRD study, volumetric gas adsorption).

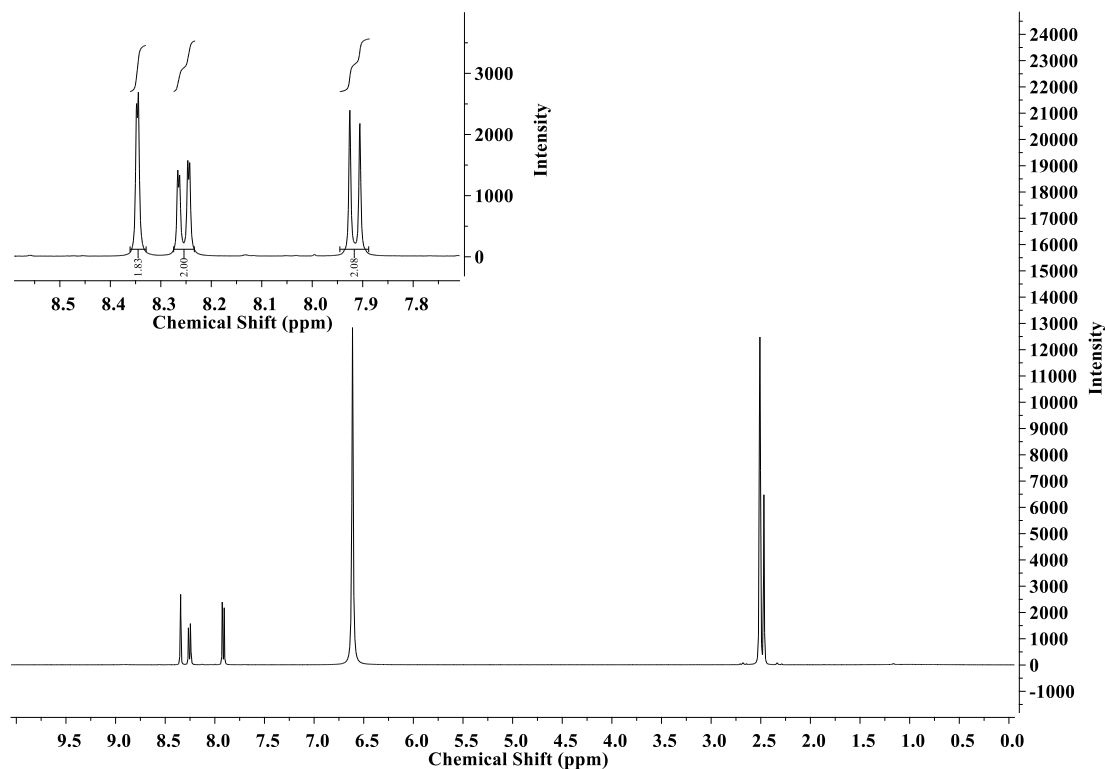


Figure 4.6. ^1H NMR of desolvated $[\text{NMe}_2\text{H}_2]_2[\text{Cd}(\text{NO}_2\text{BDC})_2]$ after acid-digestion. The aromatic region is expanded for better clarity. The peak at 2.5 ppm is DMSO; the peak at *ca.* 2.45 ppm is NMe_2H_2^+ ; and the peak at *ca.* 6.6 ppm $\text{H}_2\text{O}/\text{H}_3\text{O}^+$.

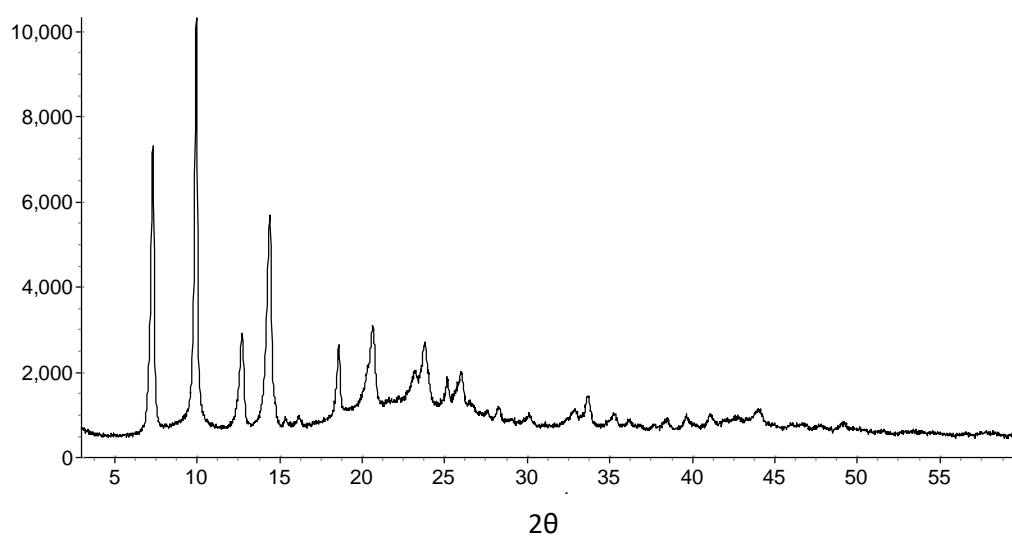


Figure 4.7. In-house powder X-ray diffraction pattern at room temperature of desolvated $[\text{NMe}_2\text{H}_2]_2[\text{Cd}(\text{NO}_2\text{BDC})_2]$. 199 parameters were used in Pawley refinement (16 background, 1 zero error, 5 profile, 2 cell and *ca.* 175 reflections). Trigonal/hexagonal lattice – unit cell parameters are detailed in Table 4.16, Section 4.4.2. $R_{\text{wp}} = 0.0592$; $R_{\text{wp}}' = 0.1298$.

Table 4.4. Crystal Structure Data Table for desolvated [NMe₂H₂]₂[Cd(NO₂BDC)₂] at 100 K (C) and 195 K (D).

	C	D
Crystal Size / mm ³	0.36 x 0.18 x 0.18	0.1 x 0.1 x 0.1
Crystal System	Trigonal	Trigonal
Space Group	<i>P</i> 3 ₁ 21	<i>P</i> 3 ₁ 21
<i>a</i> / Å	13.6137(13)	13.7699(3)
<i>b</i> / Å	13.6137(13)	13.7699(3)
<i>c</i> / Å	13.2281(13)	13.2048(3)
α (°)	90	90
β (°)	90	90
γ (°)	120	120
<i>V</i> / Å ³	2123.1(4)	2168.3(1)
<i>Z</i>	3	3
Radiation	Cu-K α (λ = 1.54178 Å)	Mo-K α (λ = 0.71073 Å)
Density / g cm ⁻³	1.461	1.431
Temperature /K	99.96	195.01
μ / mm ⁻¹	6.733	0.815
2 θ range (°)	6.682 – 133.428	3.084 – 54.138
Reflns collected	72379	24627
Independent reflns	2519	3196
Reflns used in refinement, <i>n</i>	2519	3196
L.S. parameters, <i>p</i>	157	157
No. of restraints, <i>r</i>	135	129
Flack parameter	0.032(7)	0.00(3)
<i>R</i> _{int}	0.0517	0.1092
<i>R</i> _{sigma}	0.0123	0.0708
<i>R</i> 1(<i>F</i>) ^a <i>I</i> >2 σ (<i>I</i>)	0.0637	0.0704
<i>wR</i> 2 (<i>F</i> ²) ^a , all data	0.1715	0.1894
<i>S</i> (<i>F</i> ²) ^a , all data	1.132	1.091

^a*R*1(*F*), *wR*2(*F*²) and *S*(*F*²) defined in section 4.3.1.

An in-house *in situ* single-crystal X-ray diffraction desolvation study was carried out using the following procedure. A single crystal was allowed to dry (in air, from mother liquor) on a glass slide, and subsequently attached with 2-part epoxy resin to a glass fibre, viewed using a light microscope.

The crystal was then mounted on the diffractometer in a temperature-controlled nitrogen stream at 298 K. A short sequence of scans, sufficient for accurate determination of the orientation matrix and unit cell parameters (such scans subsequently will be referred to as “matrix scans”) were recorded, and the temperature increased to 313 K and held for 30 minutes. The temperature was then cooled to 298 K, and a set of matrix scans recorded after a 5-minute equilibration time. This cycle was repeated for the temperatures 333 K, 353 K, 373 K, 393 K, 413 K and 433 K. The unit cell parameters determined from reflection positions obtained from the matrix scans are listed in Section 4.4.2, Table 4.17

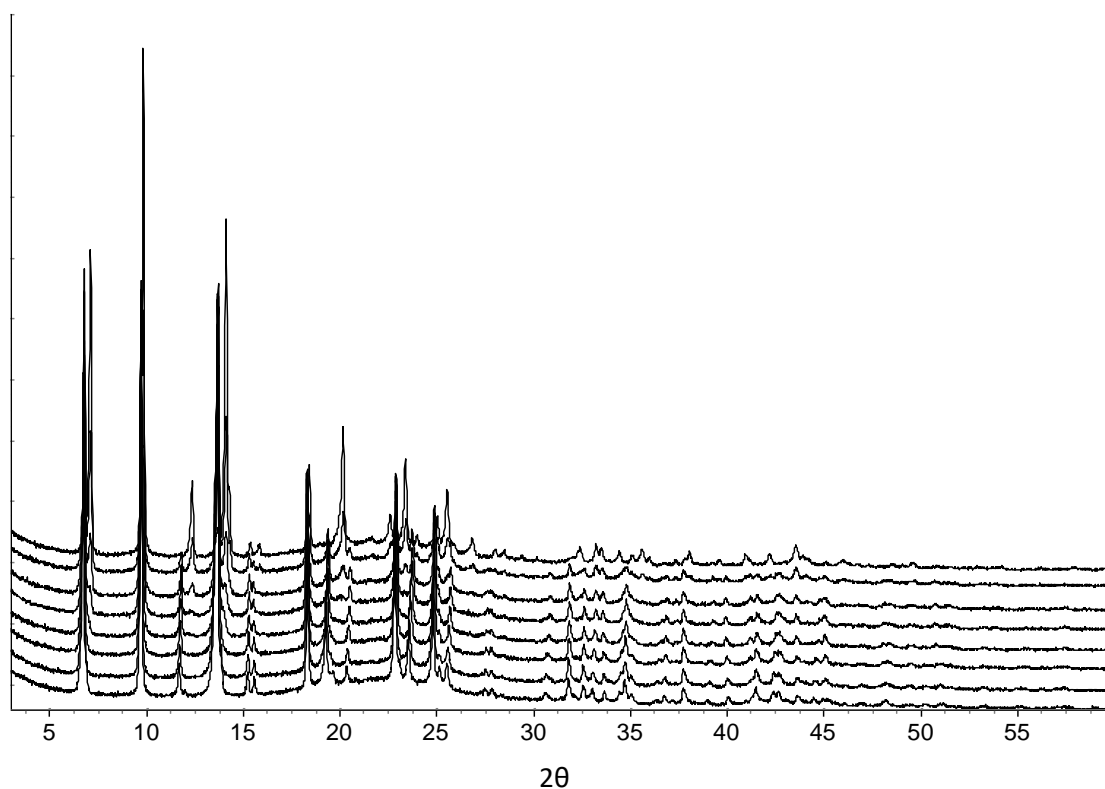


Figure 4.8. Powder X-ray diffraction patterns obtained during *in situ* desolvation study. Patterns are in ascending order; *i.e.* bottom is first pattern before heating, top is final pattern after heating to 433 K.

Table 4.5. Number of Pawley refinement parameters used for each pattern in *in situ* powder X-ray diffraction desolvation study. All patterns fitted to a trigonal/hexagonal lattice, and used 1 zero error parameter.

Temperature* / °C	R_{wp}	R_{wp}'	No. Parameters			
			Background	Profile	Cell	Reflections
25	6.496	16.320	14	5	2	<i>ca.</i> 175
40	5.663	14.012	14	5	2	<i>ca.</i> 175
60	5.392	13.506	13	5	2	<i>ca.</i> 175
80	4.382	10.094	12	9	4	<i>ca.</i> 350
100	4.594	10.449	14	9	4	<i>ca.</i> 350
120	4.578	7.668	14	9	4	<i>ca.</i> 350
140	5.930	12.324	11	9	4	<i>ca.</i> 350
160	7.196	17.084	14	5	2	<i>ca.</i> 175

4.3.4. Gas Uptake with *in situ* X-ray Diffraction

An *in situ* powder X-ray diffraction study during CO₂ uptake at 195 K was performed immediately after the analogous 298 K experiment, and on the same sample (see later). To ensure thorough removal of CO₂ between experiments, the sample was placed under vacuum (*ca.* 10⁻⁷ mbar) for one hour. The experiments were performed on beamline I11 at Diamond Light Source.

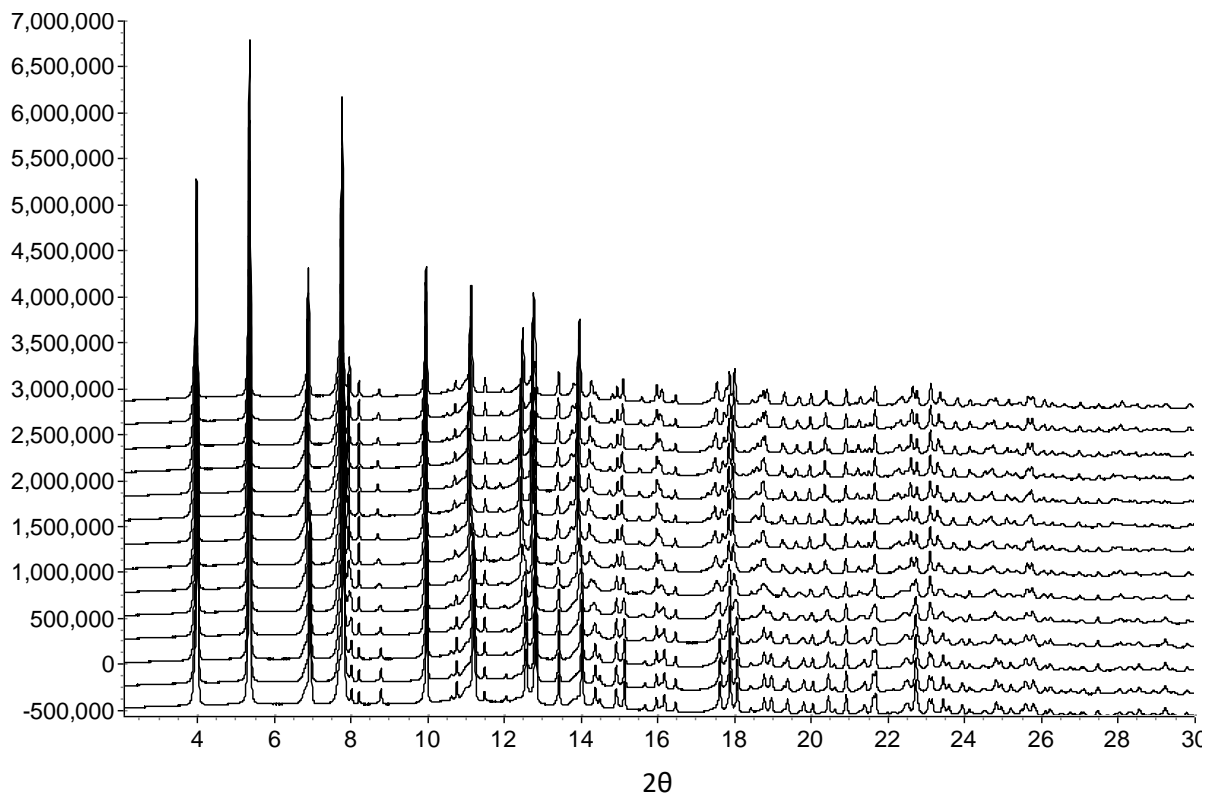


Figure 4.9. Powder patterns obtained in the *in situ* 195 K CO₂ uptake study, in ascending order; *i.e.* bottom is first measurement under vacuum, top is final measurement under vacuum after CO₂ uptake and subsequent desorption. Details of Pawley refinements are provided in Table 4.6.

Table 4.6. Details of Pawley refinements for *in situ* 195 K powder X-ray diffraction with CO₂ uptake study.*

Pressure / bar	R_{wp}	R_{wp}'	Lattice Parameters		
			$a / \text{Å}$	$c / \text{Å}$	$V / \text{Å}^3$
0 (vac)	0.0980	0.2130	13.6202(4)	13.2071(6)	2121.8(2)
0.0524	0.0979	0.2131	13.6204(4)	13.2075(6)	2121.9(2)
0.1004	0.0990	0.2221	13.6285(5)	13.2039(7)	2123.9(2)
0.1607	0.1002	0.2336	13.6435(6)	13.2009(9)	2128.1(2)
0.1993	0.1031	0.2377	13.6771(9)	13.1979(12)	2138.1(3)
0.301	0.0971	0.2212	13.7273(9)	13.1869(11)	2152.0(3)
0.3994	0.0846	0.1962	13.7641(6)	13.1747(7)	2161.6(2)

0.6994	0.0767	0.1833	13.7851(4)	13.1655(5)	2166.7(1)
1	0.0786	0.1908	13.8041(4)	13.1588(5)	2171.5(1)
0.4023	0.0794	0.1932	13.7983(4)	13.1592(5)	2169.8(1)
0.2082	0.0793	0.1919	13.7850(3)	13.1622(5)	2166.1(1)
0.0951	0.0789	0.1889	13.7684(3)	13.1653(4)	2161.4(1)
0.0531	0.0789	0.1881	13.7541(3)	13.1671(5)	2157.2(1)
0 (vac)	0.0793	0.1888	13.7216(3)	13.1731(5)	2148.0(1)

*For all patterns: $\lambda = 0.824528 \text{ \AA}$; 14 background parameters; *ca.* 150 reflections; 1 zero error; 5 profile parameters; trigonal/hexagonal lattice; 2 unit cell parameters refined.

For the *in situ* powder X-ray diffraction CO₂ uptake study at 298 K, the sample was activated as normal according to the procedure outlined in Section 4.3.3 for bulk phase material. Afterwards, the material was decanted carefully under a semi-inert argon atmosphere (argon flow through an upturned funnel over a small area) and packed into a 0.7 mm quartz capillary, which was sealed with wax. The sample was stored in this fashion during transport to Diamond Light Source, and the capillary loaded into a gas cell before the experiment.

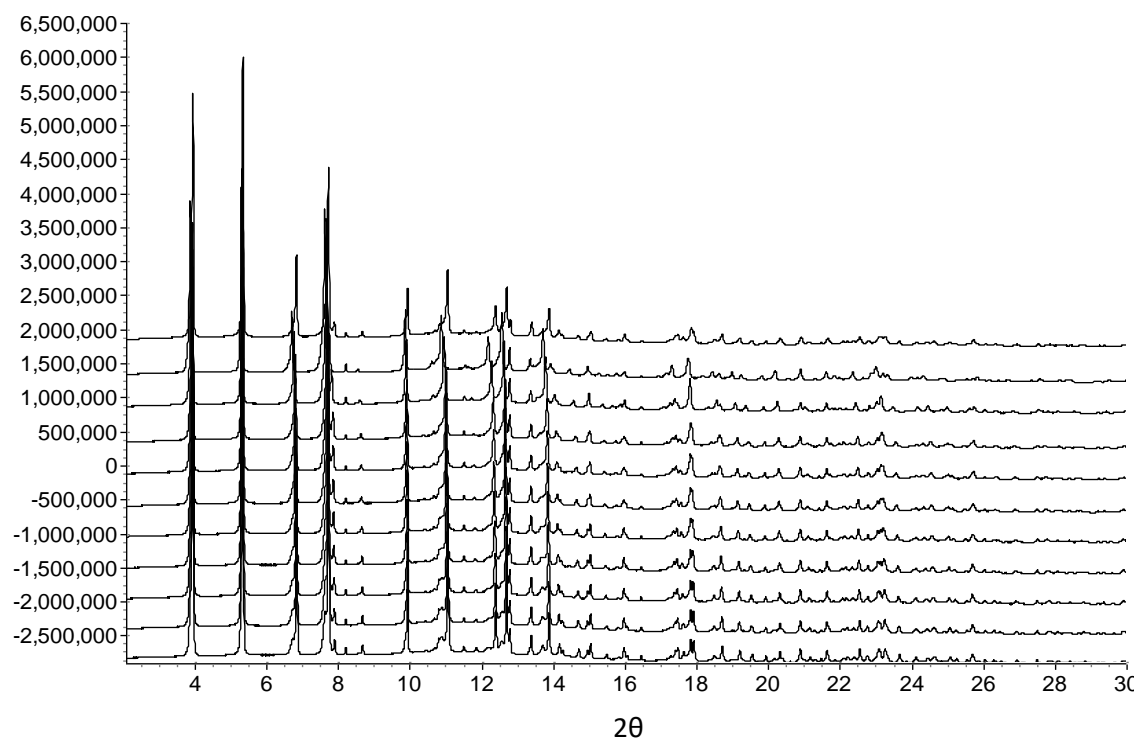


Figure 4.10. Powder patterns obtained in the *in situ* 298 K CO₂ uptake study, in ascending order; *i.e.* bottom is first measurement under vacuum, top is final measurement under vacuum after CO₂ uptake and subsequent removal. Details of Pawley refinements are provided in Table 4.7.

Table 4.7. Details of Pawley refinements for *in situ* 298 K powder X-ray diffraction with CO₂ uptake study.*

Pressure / bar	R_{wp}	R_{wp}'	Lattice Parameters		
			$a / \text{Å}$	$c / \text{Å}$	$V / \text{Å}^3$
0 (vac)	0.0994	0.2266	13.8276(4)	13.1535(6)	2178.0(2)
0.5233	0.0962	0.2195	13.8407(6)	13.1501(9)	2181.6(2)
1.0093	0.0926	0.2134	13.8536(4)	13.1465(5)	2185.1(2)
2.09	0.0884	0.2064	13.8683(4)	13.1426(6)	2189.0(2)
5.42	0.0847	0.1996	13.8854(4)	13.1382(6)	2193.7(2)
10.14	0.0815	0.1965	13.8995(5)	13.1340(6)	2197.5(2)
15.01	0.0790	0.1936	13.9092(5)	13.1308(6)	2200.0(2)
20.02	0.0751	0.1901	13.9201(5)	13.1260(6)	2202.7(2)

40.45	0.0701	0.1865	13.9843(5)	13.1073(6)	2219.9(2)
49.84	0.0721	0.2026	14.1024(6)	13.0718(7)	2251.4(2)
0 (vac)	0.0771	0.2046	13.8500(6)	13.1276(7)	2180.8(2)

*For all patterns: $\lambda = 824528 \text{ \AA}$; 14 background parameters; *ca.* 150 reflections; 1 zero error; 5 profile parameters; trigonal/hexagonal lattice; 2 unit cell parameters refined.

The CO₂ uptake study with *in situ* single-crystal X-ray diffraction was performed at beamline I19 at Diamond Light Source. A crystal was selected from the mother liquor, allowed to dry in air, and mounted using 2-part epoxy resin to a Mylar loop, which was then threaded into a quartz capillary fashioned into a gas cell. The gas cell was evacuated and the atmosphere replaced with pure nitrogen using standard Schlenk techniques. The cell was heated to 100 °C for two hours; during which time the atmosphere was evacuated and replaced with fresh pure nitrogen (3 purges) after one hour. At the end of the study, the atmosphere was again replaced with nitrogen and then subsequently removed by vacuum, before mounting the cell onto the diffractometer at the start of the experiment. Table 4.8 lists the crystal data tables for the final structures.

Table 4.8. Crystal data tables for CO₂ uptake study with *in situ* single-crystal X-ray diffraction. E0 = vacuum; E1 = 1 bar; E2 = 5 bar; E3 = 10 bar; E4 = 20 bar; E5 = 40 bar.

	E0	E1	E2
Crystal Size / mm ³	0.20 x 0.13 x 0.13	0.20 x 0.13 x 0.13	0.20 x 0.13 x 0.13
Crystal System	Trigonal	Trigonal	Trigonal
Space Group	<i>P</i> ₃ ₁ ₂ ₁	<i>P</i> ₃ ₁ ₂ ₁	<i>P</i> ₃ ₁ ₂ ₁
<i>a</i> / Å	13.9484(7)	13.9775(9)	14.0982(10)
<i>b</i> / Å	13.9484(7)	13.9775(9)	14.0982(10)
<i>c</i> / Å	13.1157(4)	13.0994(5)	13.0538(6)
α (°)	90	90	90
β (°)	90	90	90
γ (°)	120	120	120
<i>V</i> / Å ³	2209.9(2)	2216.4(3)	2247.0(3)
<i>Z</i>	3	3	3
Radiation	$\lambda = 6889 \text{ \AA}$	$\lambda = 6889 \text{ \AA}$	$\lambda = 6889 \text{ \AA}$
Density / g cm ⁻³	1.404	1.400	1.381

Temperature /K	298	298	298
μ / mm ⁻¹	0.741	0.739	0.729
2 θ range (°)	3.01 – 59.88	3.014 – 59.892	3.024 – 59.884
Reflns collected	31932	31828	32158
Independent reflns	4705	4713	4766
Reflns used in refinement, <i>n</i>	4705	4713	4766
L.S. parameters, <i>p</i>	157	157	157
No. of restraints, <i>r</i>	129	129	129
Flack Parameter	-0.011(19)	0.00(2)	0.01(2)
R_{int}	0.0613	0.0668	0.0729
R_{sigma}	0.0375	0.0423	0.0483
$R1(F)^a$ $I > 2\sigma(I)$	0.0542	0.0661	0.0748
$wR2(F^2)^a$, all data	0.1676	0.2159	0.2451
$S(F^2)^a$, all data	1.007	1.031	1.031

^a $R1(F)$, $wR2(F^2)$ and $S(F^2)$ defined in section 4.3.1.

	E3	E4	E5
Crystal Size / mm ³	0.20 x 0.13 x 0.13	0.20 x 0.13 x 0.13	0.20 x 0.13 x 0.13
Crystal System	Trigonal	Trigonal	Trigonal
Space Group	$P3_121$	$P3_121$	$P3_121$
a / Å	14.2180(12)	14.366(3)	14.515(3)
b / Å	14.2180(12)	14.366(3)	14.515(3)
c / Å	13.0014(6)	12.8607(10)	12.8247(10)
α (°)	90	90	90
β (°)	90	90	90
γ (°)	120	120	120
V / Å ³	2276.1(4)	2298.5(8)	2340.0(9)
Z	3	3	3
Radiation	$\lambda = 6889$ Å	$\lambda = 6889$ Å	$\lambda = 6889$ Å
Density / g cm ⁻³	1.363	1.350	1.326
Temperature /K	298	298	298
μ / mm ⁻¹	0.720	0.713	0.700
2 θ range (°)	3.206 – 59.884	4.416 – 40.292	4.398 – 40.29
Reflns collected	32634	14756	15010
Independent reflns	4844	1607	1645

Reflns used in refinement, <i>n</i>	4844	1607	1645
L.S. parameters, <i>p</i>	157	157	127
No. of restraints, <i>r</i>	129	153	119
Flack Parameter	0.02(3)	-0.05(7)	-0.06(5)
R_{int}	0.0830	0.1260	0.1075
R_{sigma}	0.0580	0.0506	0.0438
$R1(F)^a$ $I > 2\sigma(I)$	0.0851	0.1239	0.1291
$wR2(F^2)^a$, all data	0.2857	0.3564	0.3757
$S(F^2)^a$, all data	1.024	1.196	1.200

^a $R1(F)$, $wR2(F^2)$ and $S(F^2)$ defined in section 4.3.1.

4.3.5. Variable Temperature Studies

Study VT1: A single-crystal structure of $[\text{NMe}_2\text{H}_2]_2[\text{Cd}(\text{NO}_2\text{BDC})_2]$ was determined at 170 K (**VT1-1**). Additional data sets were collected on the same crystal, immediately afterwards, at 140 K (**VT1-2**) and 100K (**VT1-3**).

Table 4.9. Crystal data tables for study **VT1**.

	VT1-1	VT1-2	VT1-3
Crystal Size / mm ³	0.2 x 0.15 x 0.15	0.2 x 0.15 x 0.15	0.2 x 0.15 x 0.15
Crystal System	Trigonal	Trigonal	Trigonal
Space Group	$P3_121$	$P3_121$	$P3_121$
$a / \text{\AA}$	14.9689(4)	14.9210(5)	14.8744(10)
$b / \text{\AA}$	14.9689(4)	14.9210(5)	14.8744(10)
$c / \text{\AA}$	12.6934(4)	12.7118(5)	12.7248(9)
α (°)	90	90	90
β (°)	90	90	90
γ (°)	120	120	120
$V / \text{\AA}^3$	2463.14(15)	2450.94(19)	2438.1(4)
Z	3	3	3
Radiation	Cu-K α ($\lambda = 1.54178 \text{ \AA}$)	Cu-K α ($\lambda = 1.54178 \text{ \AA}$)	Cu-K α ($\lambda = 1.54178 \text{ \AA}$)
Density / g cm ⁻³	1.260	1.688	1.084
Temperature /K	170	140	100
μ / mm^{-1}	5.804	7.777	5.775
2θ range (°)	6.818 – 133.314	6.84 – 133.41	6.862 – 133.32

Reflns collected	33600	30993	32861
Independent reflns	2915	2901	2877
Reflns used in refinement, <i>n</i>	2915	2901	2877
L.S. parameters, <i>p</i>	130	130	130
No. of restraints, <i>r</i>	130	121	119
Flack Parameter	-0.002(12)	0.023(12)	0.013(13)
R_{int}	0.0555	0.0574	0.0587
R_{sigma}	0.0240	0.0251	0.0247
$R1(F)^a$ $I > 2\sigma(I)$	0.0753	0.0773	0.0785
$wR2(F^2)^a$, all data	0.2311	0.2345	0.2450
$S(F^2)^a$, all data	1.189	1.219	1.176

^a $R1(F)$, $wR2(F^2)$ and $S(F^2)$ defined in section 4.3.1.

Study VT2: Sets of matrix scans were performed on a single crystal of $[\text{NMe}_2\text{H}_2]_2[\text{Cd}(\text{NO}_2\text{BDC})_2]$ at successively lower temperatures between 160 K and 85 K. The unit cell parameters determined from these matrix scans are detailed in Table 4.10.

Table 4.10. Lattice parameters for study VT2.

Temperature / K	Lattice Parameters		
	$a / \text{\AA}$	$c / \text{\AA}$	$V / \text{\AA}^3$
160	14.976(3)	12.6880(11)	2464.5(5)
130	14.927(3)	12.7089(14)	2452.5(6)
120	14.915(3)	12.7149(18)	2449.4(6)
110	14.903(3)	12.7193(16)	2446.4(6)
100	14.889(3)	12.7246(15)	2443.0(6)
90	14.881(3)	12.7273(15)	2441.0(6)
85	14.859(4)	12.7234(19)	2432.7(8)

Study VT3: Sets of matrix scans were performed on a single crystal of $[\text{NMe}_2\text{H}_2]_2[\text{Cd}(\text{NO}_2\text{BDC})_2]$ at successively lower temperatures between 300 K and 90 K. The unit cell parameters determined from these matrix scans are detailed in Table 4.11.

Table 4.11. Lattice parameters for study VT3.

Temperature / K	Lattice Parameters		
	$a / \text{Å}$	$c / \text{Å}$	$V / \text{Å}^3$
300	15.166(4)	12.592(7)	2508.1(1.5)
280	15.041(3)	12.676(4)	2483.5(9)
260	14.988(2)	12.697(4)	2470.0(9)
240	14.935(2)	12.725(4)	2458.0(9)
220	14.883(2)	12.754(4)	2446.7(9)
200	14.836(2)	12.778(4)	2435.7(9)
180	14.787(2)	12.793(4)	2422.4(9)
160	14.750(2)	12.816(4)	2414.7(9)
140	14.716(2)	12.829(5)	2406.1(1.0)
120	14.686(3)	12.837(5)	2397.7(1.0)
100	14.666(3)	12.834(5)	2390.7(1.1)
90	14.650(3)	12.843(5)	2387.3(1.1)

Study VT4: Sets of matrix scans were performed on a single crystal of desolvated $[\text{NMe}_2\text{H}_2]_2[\text{Cd}(\text{NO}_2\text{BDC})_2]$ (procedure outlined in section 4.3.2) at 100 K. The temperature was then lowered to 85 K and sets of matrix scans performed at successively higher temperatures up to 300 K.

A final set of matrix scans was performed at 298 K. The unit cell parameters determined from these matrix scans are detailed in Table 4.12.

Table 4.12. Lattice parameters for study VT4.

Temperature / K	Lattice Parameters		
	$a / \text{\AA}$	$c / \text{\AA}$	$V / \text{\AA}^3$
100	13.645(5)	13.211(4)	2130.1(9)
85	13.623(4)	13.212(3)	2123.5(7)
90	13.643(4)	13.211(4)	2129.7(9)
100	13.647(5)	13.210(4)	2130.6(10)
120	13.678(4)	13.202(3)	2138.8(7)
140	13.709(3)	13.203(3)	2149.0(6)
160	13.738(3)	13.193(3)	2156.4(7)
180	13.776(4)	13.181(3)	2166.1(7)
200	13.809(4)	13.172(3)	2175.3(7)
220	13.833(4)	13.162(3)	2181.3(8)
240	13.879(4)	13.149(3)	2193.6(8)
260	13.908(4)	13.149(3)	2202.9(7)
280	13.945(4)	13.143(3)	2213.5(8)
300	13.986(6)	13.128(5)	2224.0(13)
298	13.984(7)	13.123(6)	2222.4(15)

Study VT5: Powder diffraction was performed on a sample of $[\text{NMe}_2\text{H}_2]_2[\text{Cd}(\text{NO}_2\text{BDC})_2]$ at temperatures between 300 K and 90 K at Beamline I11, Diamond Light Source. After the 90 K

measurement, the temperature was then raised to 300 K, with measurements performed at the same temperatures for comparison. The results are shown in Figure 4.11 and Table 4.13.

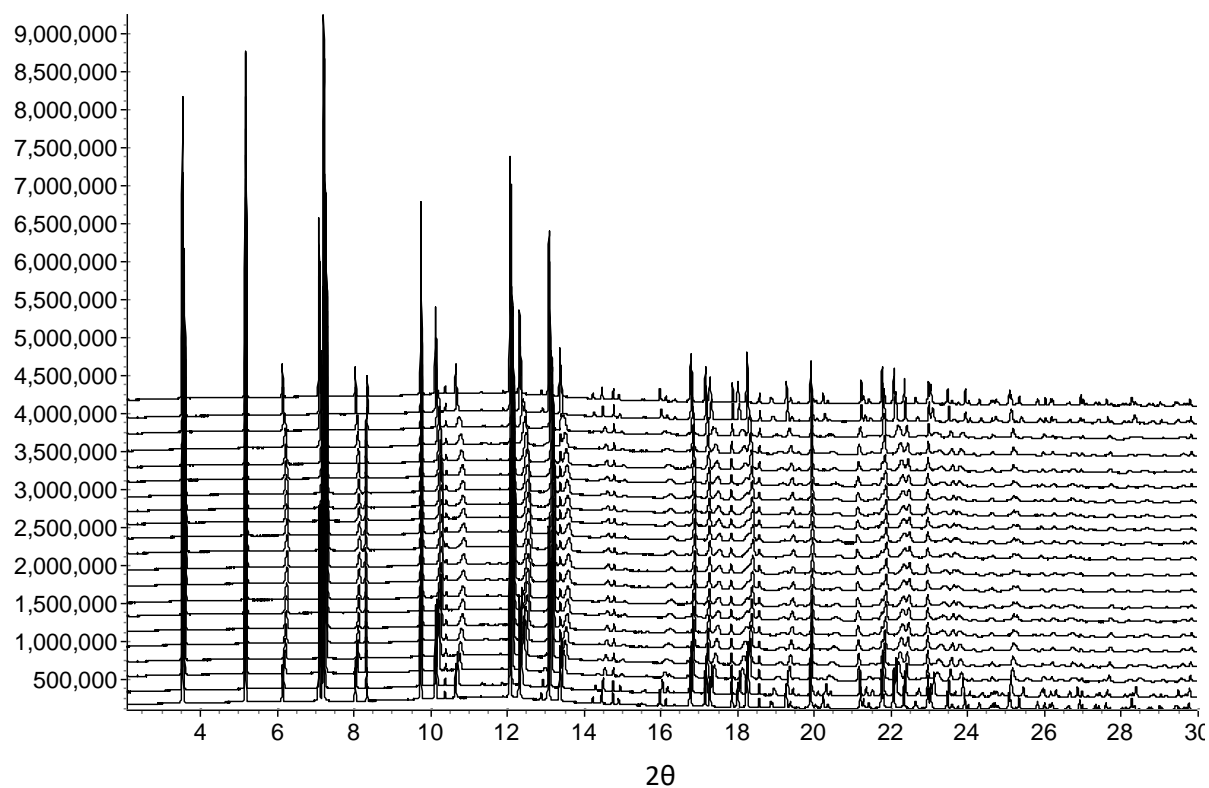


Figure 4.11. Powder patterns obtained in the *in situ* variable temperature study VT5, in ascending order; *i.e.* bottom pattern is the top row of Table 4.13, measurement at 300 K; top pattern is bottom row of Table 4.13, also at 300 K. Details of Pawley refinements are provided in Table 4.13.

Table 4.13. Details of Pawley refinements study VT5.*

Temperature / K	R_{wp}	R_{wp}'	Lattice Parameters		
			$a / \text{Å}$	$c / \text{Å}$	$V / \text{Å}^3$
300	0.0416	0.0955	15.35834(7)	12.50260(7)	2553.99(3)
250	0.0494	0.1138	15.29143(8)	12.53023(9)	2537.38(3)
200	0.0917	0.2234	15.2189(3)	12.5590(3)	2519.1(1)
180	0.0966	0.2412	15.1807(4)	12.5755(4)	2509.8(1)
160	0.0963	0.2441	15.1479(4)	12.5887(4)	2501.6(2)

140	0.0953	0.2441	15.1199(4)	12.5994(5)	2494.5(2)
130	0.0936	0.2413	15.1078(4)	12.6048(5)	2491.6(2)
120	0.0914	0.2386	15.0963(5)	12.6090(5)	2488.6(2)
110	0.0892	0.2345	15.0858(5)	12.6129(5)	2485.9(2)
100	0.0865	0.2291	15.0763(5)	12.6167(5)	2483.5(2)
90	0.0855	0.2255	15.0658(5)	12.6205(5)	2480.8(2)
100	0.0865	0.2314	15.0763(5)	12.6163(5)	2483.4(2)
110	0.0882	0.2348	15.0866(5)	12.6123(5)	2486.0(2)
120	0.0890	0.2364	15.0970(5)	12.6078(5)	2488.6(2)
130	0.0904	0.2404	15.1075(5)	12.6030(5)	2491.1(2)
140	0.0915	0.2444	15.1184(5)	12.5975(5)	2493.6(2)
160	0.0949	0.2509	15.1448(4)	12.5842(4)	2499.7(2)
180	0.1048	0.2740	15.1786(5)	12.5662(5)	2507.2(2)
200	0.1145	0.2989	15.2293(5)	12.5386(5)	2518.5(2)
250	0.0811	0.1968	15.3188(2)	12.4920(2)	2538.70(8)
300	0.0548	0.1323	15.3554(1)	12.4897(1)	2550.38(4)

* For all patterns: $\lambda = 0.82471$; *ca.* 150 reflections; 1 zero error; 5 profile parameters; trigonal/hexagonal lattice; 2 cell parameters refined.

4.4. Results & Discussion

4.4.1. Synthesis & Characterisation.

Wang *et al.* originally reported the preparation of $[\text{NMe}_2\text{H}_2]_2[\text{Cd}(\text{NO}_2\text{BDC})_2]$ in 2013;⁶ whereby they combined cadmium nitrate tetrahydrate and nitroterephthalic acid with DMF (*N,N*-dimethylformamide) in an autoclave, which was then heated under solvothermal conditions for 72 hours at 160 °C. They also reported analogous conditions for the preparation of the bromo-

functionalised, amino-functionalised, and non-functionalised isomeric materials. The bromo-functionalised analogue has the β -quartz topology and is isostructural to **QMOF-2**¹ and $[\text{NMe}_2\text{H}_2]_2[\text{Cd}(\text{NO}_2\text{BDC})_2]$, whereas the amino- and non-functionalised materials are three-fold-interpenetrated diamondoid networks and reside in the orthorhombic space group $Fdd2$.⁶ The authors rationalise the different topologies based on steric effects: the larger functional groups, nitro and bromo, require more space and “force” the adoption of the quartz topology. However, this argument does not explain why **QMOF-2**, which is non-functionalised, adopts the quartz topology,¹ nor does it explain the fact that the quartz-type analogue of $[\text{NMe}_2\text{H}_2]_2[\text{Cd}(\text{BDC})_2]$ (*i.e.* the non-functionalised material) was published two years later.⁵ Additionally, $[\text{NMe}_2\text{H}_2][\text{In}(\text{NH}_2\text{BDC})_2]$ exists as both the orthorhombic diamondoid form (**SHF-61**)² and as the hexagonal quartz form.⁷ Unfortunately, we were unable to successfully prepare any of the reported compounds, other than **QMOF-2**, to a phase-pure standard by following the published or modified procedures. Relatively early in the project, it became apparent that directing the synthesis of cadmium-based MOFs to a desired topology is a challenge, due to the lack of directional coordination preferences of a Cd^{II} centre (which was indeed listed as an advantage in Section 1.4.2). In our hands the synthesis conditions reported by Wang *et al.* in 2013⁶ proved far too harsh, and our initial attempts to synthesise $[\text{NMe}_2\text{H}_2]_2[\text{Cd}(\text{NO}_2\text{BDC})_2]$ resulted in the formation of an unidentifiable black sludge. By lowering the reaction temperature to 130 °C and shortening the reaction time to 24 hours (the conditions used for the preparation of **SHF-61**), we were able to prepare the desired material alongside many impurities. This was also the case for the bromo-functionalised analogue. Our attempts to prepare the non-functionalised and amino-functionalised analogues by using these conditions resulted in the formation of various “pinwheel” type framework structures, which consist of a discrete number (≥ 3) of metal ions connected in a line *via* either coordinating ligands, solvent molecules or both. These “pinwheels” of metal ions can either be capped at the ends with solvent molecules, or link to other pinwheels *via* linker species (terephthalates in this case). These pinwheel structures are particularly common for cadmium-based MOFs,²³⁻²⁸ but although interesting in their own right, they are not immediately relevant to this project. It is also worth mentioning that our attempts to produce indium-based analogues were also unsuccessful. An

interesting example was attempted synthesis of the compound $[\text{NMe}_2\text{H}_2][\text{In}(\text{NO}_2\text{BDC})_2]$ from indium nitrate hydrate and nitroterephthalic acid in DMF, which unexpectedly produced the mixed-ligand MOF $[\text{NMe}_2\text{H}_2][\text{In}(\text{BDC})_x(\text{NH}_2\text{BDC})_y(\text{NO}_2\text{BDC})_z]$ (where $x > y > z$) alongside various by-products. This observation was later confirmed by Kruger *et al.*, who published very similar results in 2017,²⁹ although the mechanism for the spontaneous ligand reduction is seemingly unknown.

Ultimately, we were able to consistently produce phase-pure $[\text{NMe}_2\text{H}_2]_2[\text{Cd}(\text{NO}_2\text{BDC})_2]$ by adding 0.1 equivalents of dimethylammonium chloride to the reaction mixture (which has been reported in the synthesis of orthorhombic $[\text{NMe}_2\text{H}_2]_2[\text{Cd}(\text{BDC})_2]$ ²⁶), and heating at 130 °C for 24 hours (*c.f.* synthesis of **SHF-61**²). Phase purity was confirmed by powder X-ray diffraction (Figure 4.5, Section 4.3.2). Despite the relatively small amount of template salt used, the reaction has a 74 % yield, showing that the vast majority of the dimethylammonium ions present in the material are generated from the hydrolysis of DMF during the solvothermal reaction.³⁰ This suggests that the template salt either: a) is involved in initiating the reaction, but not necessarily propagating it; b) primarily has a role of *preventing* the formation of by-products; or c) encourages the conversion of kinetic by-products into the desired material. These proposals are, of course, speculative. As work on the other isostructural materials listed above did not reach a stage of obtaining phase-pure materials, they will not be discussed further (other than in reference to $[\text{NMe}_2\text{H}_2]_2[\text{Cd}(\text{NO}_2\text{BDC})_2]$).

As mentioned in Section 4.2, $[\text{NMe}_2\text{H}_2]_2[\text{Cd}(\text{NO}_2\text{BDC})_2]$ is isostructural to **QMOF-2**. It therefore consists of eight-coordinate cadmium ions surrounded by four nitroterephthalate linkers, in a pseudo-tetrahedral arrangement (Figure 4.12a). It is two-fold interpenetrated and adopts the quartz network topology. Channels run through the structure parallel to the *c*-axis (Figure 4.12b), which are lined with the nitro functional groups, and are host to guest solvent molecules (DMF and water- see later) and the dimethylammonium counter-ions, which we were able to locate crystallographically, and are held in place *via* hydrogen-bonding interactions with the framework carboxylate groups (Figure 4.13). As cadmium is in the +2 oxidation state (rather than +3 as is the case for indium in **SHF-61** and **QMOF-2**), two dimethylammonium counter-ions per cadmium centre are required to balance the charge of the framework.

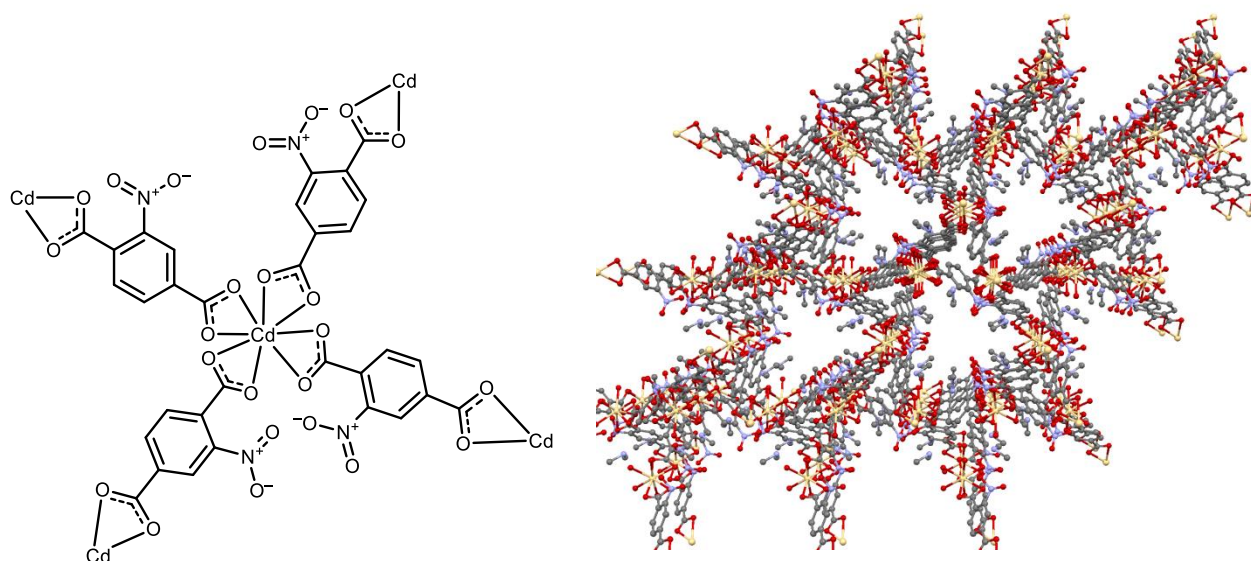


Figure 4.14. Left: a) Four nitroterephthalate linkers surrounding the eight-coordinate cadmium in a pseudo-tetrahedral arrangement. Right: b) Crystal structure of $[\text{NMe}_2\text{H}_2][\text{Cd}(\text{NO}_2\text{BDC})_2]$ viewed along the c -axis, showing the channels. Cadmium = beige; oxygen = red; nitrogen = blue; carbon = grey. Hydrogen atoms omitted for clarity.

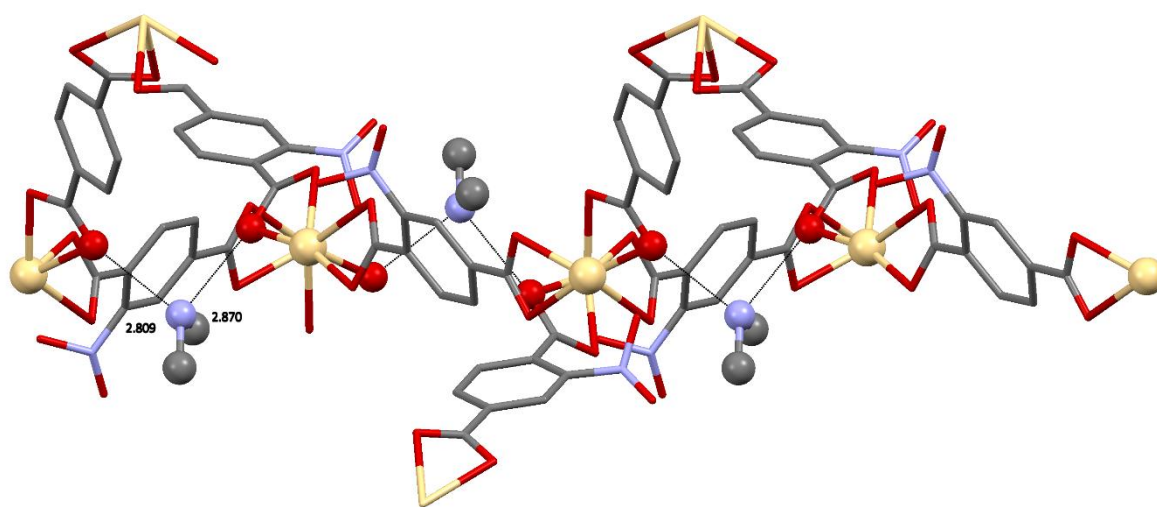


Figure 4.15. Hydrogen-bonding interactions between the dimethylammonium counter-ions and the framework carboxylates of $[\text{NMe}_2\text{H}_2][\text{Cd}(\text{NO}_2\text{BDC})_2]$, viewed along the a -axis (c -axis horizontal). Cadmium = beige; oxygen = red; nitrogen = blue; carbon = grey. Hydrogen atoms omitted for clarity. The counter-ions are crystallographically identical, so bond distances are shown only for one example.

In the original report by Wang *et al.*,⁶ $[\text{NMe}_2\text{H}_2][\text{Cd}(\text{NO}_2\text{BDC})_2]$ is described as residing in the hexagonal space group $P6_222$, with two-fold positional disorder of the nitro groups (Figure 4.14), and no counter-ion located in the crystal structure. We found, however, that the material is better described in the trigonal space group $P3_221$, with no local disorder of the ligands.

$[\text{NMe}_2\text{H}_2][\text{Cd}(\text{NO}_2\text{BDC})_2]$ is pseudo-merohedrally twinned, with two distinct crystallographic

domains which are identical to each other but oriented differently. The relation between the domains is a two-fold rotation about the *c*-axis (Figure 4.15); the twin law $[-1,0,0,0,-1,0,0,0,1]$. In the solvated structure, the cadmium ions happen to reside very close to special positions in the unit cell, and the structure can be solved and refined in the hexagonal space group without any apparent problem. In this case, the twinning phenomenon is simply being modelled incorrectly as disorder (Figure 4.16). Crystal data in Tables 4.12a and 4.12b in Section 4.3.2 describe, respectively, refinement of a trigonal model and hexagonal model for the same data set. Although the two models are very similar, a slightly better R1 (%) factor is obtained with the trigonal solution, albeit with a lower data:parameter ratio, and the counter-ion was not able to be located in the hexagonal solution. Additionally, as will be discussed in Section 4.4.2, desolvating the material leads to the cadmium ions moving away from the special crystallographic positions, and the hexagonal solution is no longer a viable approximation to the correct model; the desolvated MOF can only be modelled in the trigonal space group $P3_221$, despite crystallinity clearly being retained during the desolvation process.

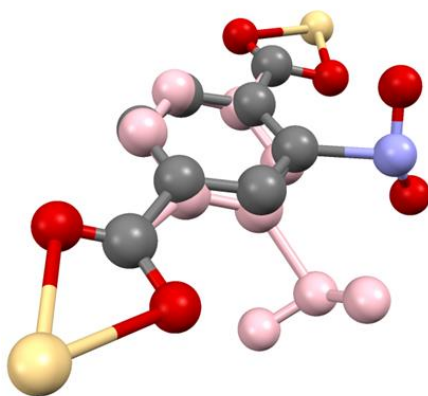


Figure 4.16. Two-fold positional disorder of the nitro groups observed in our hexagonal model (space group $P6_422$) of the crystal structure of $[\text{NMe}_2\text{H}_2]_2[\text{Cd}(\text{NO}_2\text{BDC})_2]$. Cadmium = beige; oxygen = red; nitrogen = blue; carbon = grey. Hydrogen atoms omitted for clarity.

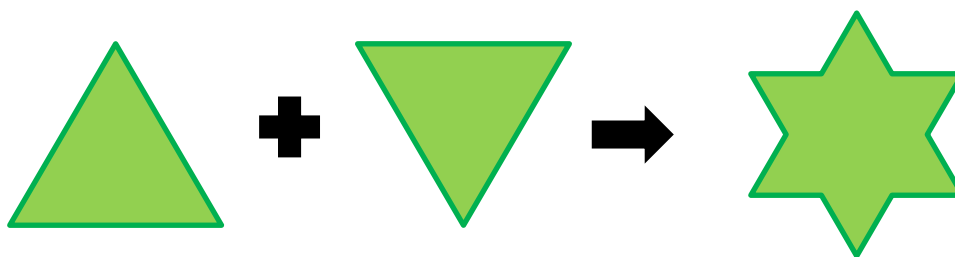


Figure 4.17. Two identical trigonal systems related by a two-fold rotation about the principal (3-fold) axis appear to have hexagonal symmetry when superimposed.

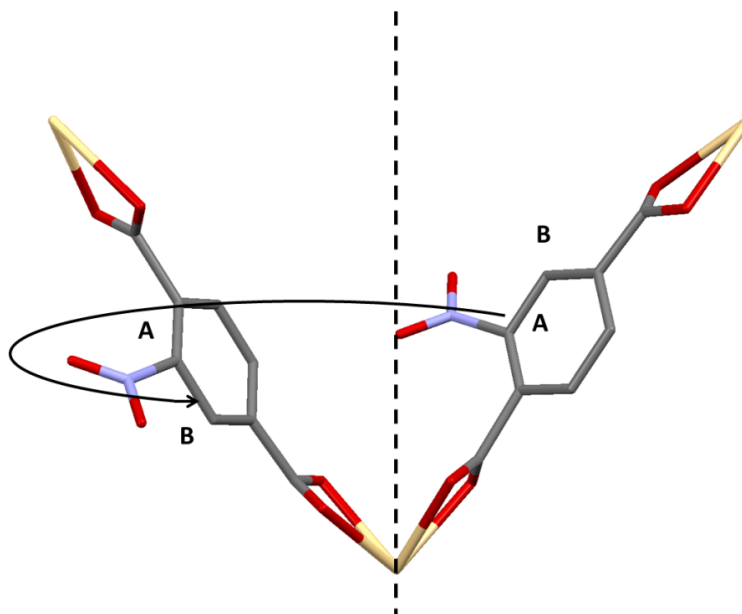


Figure 4.18. A two-fold rotation of the structure of $[\text{NMe}_2\text{H}_2]_2[\text{Cd}(\text{NO}_2\text{BDC})_2]$ about the c -axis (dotted line) superimposes the nitro group to position B (when in fact it resides on position A), so positional disorder of the nitro group is observed if crystal structure is modelled according to the symmetry of the hexagonal space group. Cadmium = beige; oxygen = red; nitrogen = blue; carbon = grey. Hydrogen atoms omitted for clarity.

The nature of the solvent guest inside $[\text{NMe}_2\text{H}_2]_2[\text{Cd}(\text{NO}_2\text{BDC})_2]$ was elucidated using a combination of ^1H NMR spectroscopy and elemental analysis. A batch of the material was removed from the mother liquor, vacuum filtered and ground into a fine powder. Some of this powder was used to carry out elemental analysis immediately in order to minimise the risk of atmospheric water uptake (which is known to occur in **SHF-61**).² The rest was acid-digested using 35% deuterium chloride, and used for ^1H NMR spectroscopy. From integration of the signals in the ^1H NMR spectrum (Figure 4.17), the DMF content of the material was calculated as approximately 1.8 molar equivalents, based on the ratio of the DMF formyl proton and the aromatic protons of nitroterephthalate. Additionally, the best fit to the elemental analysis results is achieved with 1.8 equivalents of DMF and 0.4

equivalents of water (Table 4.14), which strongly suggests that the true formula of this batch of solvated material can be represented as $[\text{NMe}_2\text{H}_2]_2[\text{Cd}(\text{NO}_2\text{BDC})_2] \cdot 1.8\text{DMF} \cdot 0.4\text{H}_2\text{O}$. Interestingly, the SQUEEZE function in the PLATON software package¹⁷ estimated a residual electron count of 147 per formula unit in the crystal structure, which is almost twice as large as expected ($1.8\text{DMF} + 0.4\text{H}_2\text{O} = 76$ electrons). This could indicate that the material loses solvent as it is ground into a powder (which would not be unexpected due to the increase in surface area caused by the procedure).

The exact quantity of each solvent guest likely varies somewhat from batch to batch, and will depend on a number of factors including temperature, atmospheric humidity, exposure to air, and the age of the solvent (and hence, its water content). Due to this uncertainty, for the rest of this chapter, $[\text{NMe}_2\text{H}_2]_2[\text{Cd}(\text{NO}_2\text{BDC})_2] \cdot 1.8\text{DMF} \cdot 0.4\text{H}_2\text{O}$ will be referred to simply as “solvated $[\text{NMe}_2\text{H}_2]_2[\text{Cd}(\text{NO}_2\text{BDC})_2]$ ”.

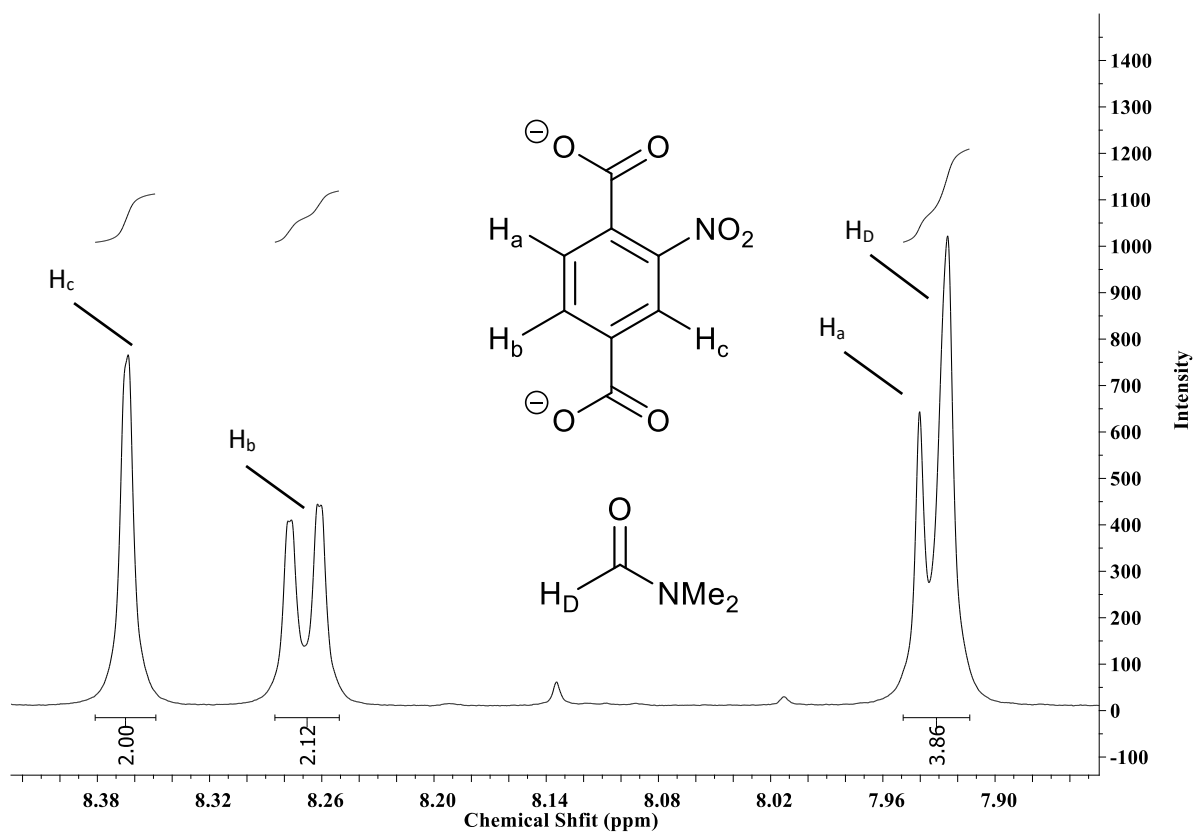


Figure 4.17. Expanded range of the aromatic region of the ¹H NMR spectrum of solvated $[\text{NMe}_2\text{H}_2]_2[\text{Cd}(\text{NO}_2\text{BDC})_2]$.

Table 4.14. Fitted elemental analysis results for $[\text{NMe}_2\text{H}_2]_2[\text{Cd}(\text{NO}_2\text{BDC})_2] \cdot 1.8\text{DMF} \cdot 0.4\text{H}_2\text{O}$.

Element	Expected % (exp)	Observed % (obs)	exp-obs
C	40.16	40.16	0.00
H	4.73	4.74	0.01
N	10.75	10.74	0.01
		Total:	0.02

4.4.2. Solvent Removal

The solvent guest in bulk-phase $[\text{NMe}_2\text{H}_2]_2[\text{Cd}(\text{NO}_2\text{BDC})_2]$ was removed by heating the material (as a ground powder) at 80 °C in a Schlenk tube under dynamic vacuum for 16 hours. ^1H NMR confirmed that the solvent guest had been removed and powder X-ray diffraction showed that the material was still phase pure (Section 4.3.3, Figures 4.6 and 4.7). A single crystal of $[\text{NMe}_2\text{H}_2]_2[\text{Cd}(\text{NO}_2\text{BDC})_2]$ was desolvated by heating at 100 °C for 1 hour, in a temperature-controlled oven and its crystal structure determined by single-crystal X-ray diffraction at 100 K. The local structure of the MOF does not change much upon desolvation, *i.e.* the metal ions and linkers still have the same connectivity, and the counter-ion is still present. However, the material is expanded by 0.46 Å in the *c*-axis and contracted by 1.28 Å in the *a*- and *b*-axes, which results in a narrowing of the channels. Many flexible terephthalate-based MOFs, including **SHF-61**, employ the “kneecap hinge” mechanism (rotation about the O···O vector of the ligand carboxylate – see Section 1.3.3) as a basis for their dynamic behaviour.^{2,11,31,32} However, $[\text{NMe}_2\text{H}_2]_2[\text{Cd}(\text{NO}_2\text{BDC})_2]$ is different, in the sense that its dynamic behaviour seems to arise from a distortion of the pseudo-hexagonal double helix which defines the channels (Figure 4.18, Table 4.15), which in turn arises from a shift of the cadmium position in the unit cell and hence a distortion of the cadmium coordination sphere (Figure 4.19). It is this movement of the cadmium ions that prevents a hexagonal solution for the desolvated material, and confirms that the crystal structure of the MOF is of trigonal symmetry, with two domains related

by the twin law $[-1,0,0,0,-1,0,0,0,1]$, rather than hexagonal, with local positional disorder of the nitro substituents.

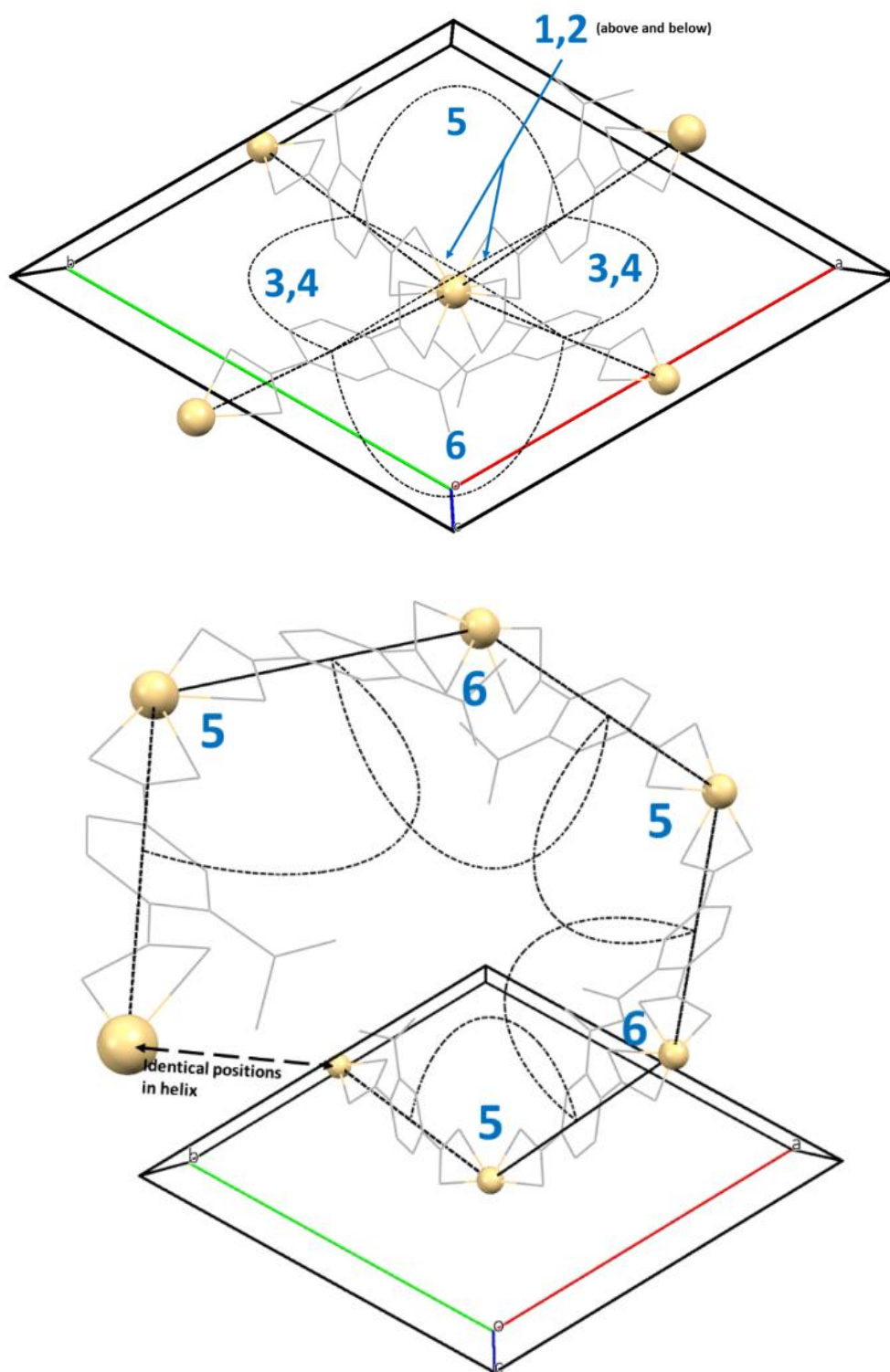


Figure 4.18. Labelling of $\text{Cd}\dots\text{Cd}\dots\text{Cd}$ angles within the structure of $[\text{NMe}_2\text{H}_2]_2[\text{Cd}(\text{NO}_2\text{BDC})_2]$, and a depiction of one half of the pseudo-hexagonal double-helix. Angles 1 and 2 are identical by symmetry, as are angles 3 and 4. Viewed along the c -axis.

Table 4.15. Summary of relevant structural angles which define the pseudo-hexagonal double-helix. The angles are defined in Figure 4.18.

State	Cd...Cd...Cd Angles (pseudo-hexagonal helix) (°)			
	1,2	3,4	5	6
Solvated	82.36	110.47	141.48	141.63
Desolvated	75.14	115.85	137.60	151.27

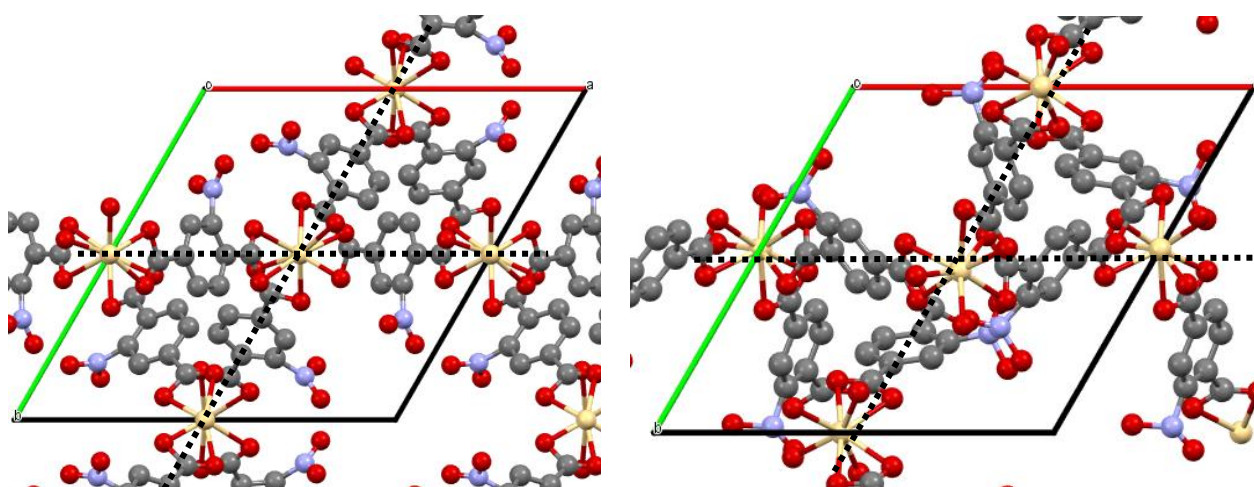


Figure 4.19. Left: Solvated $[\text{NMe}_2\text{H}_2]_2[\text{Cd}(\text{NO}_2\text{BDC})_2]$. Dotted lines divide the cell into 4 equal quadrants, with the central cadmium ion lying at the cell centre (when viewed as a 2D plane), and the others lying halfway along the *a*- and *b*-axes. Right: desolvated $[\text{NMe}_2\text{H}_2]_2[\text{Cd}(\text{NO}_2\text{BDC})_2]$. Here the cadmium ions have clearly shifted from their original locations and no longer lie on special crystallographic positions. Cadmium = beige; oxygen = red; nitrogen = blue; carbon = grey. Hydrogen atoms omitted for clarity.

Interestingly, the channels of $[\text{NMe}_2\text{H}_2]_2[\text{Cd}(\text{NO}_2\text{BDC})_2]$ are not completely closed after solvent removal; a small opening (diameter $\approx 1.7 \text{ \AA}$) can be seen in the crystal structure (Figure 4.20) and has implications for the gas uptake properties of the material (discussed further in Section 4.4.3). It is thought that this arises from the aromatic rings of the linker “locking” together in an end-to-face-type arrangement (Figure 4.21). With a distance of 5.711 \AA between the centres of the rings, this is unlikely to be a van der Waals interaction, but could nevertheless play a steric role in stabilising the desolvated form of the material. It should also be noted that the shift in position of the cadmium ions allows the nitro-groups to take up more space within the channels which was previously occupied by solvent guest, and this may play an additional role in stabilising the desolvated form of the MOF.

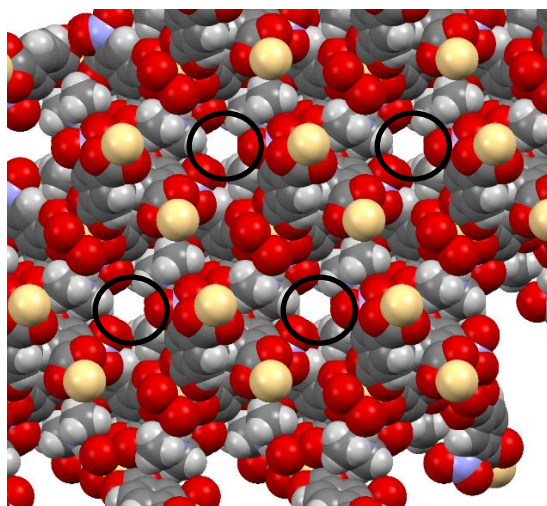


Figure 4.20. Structure of desolvated $[\text{NMe}_2\text{H}_2]_2[\text{Cd}(\text{NO}_2\text{BDC})_2]$, viewed along the c -axis, showing the narrow channels which are still present (encircled in black). Cadmium = beige; oxygen = red; nitrogen = blue; carbon = grey.

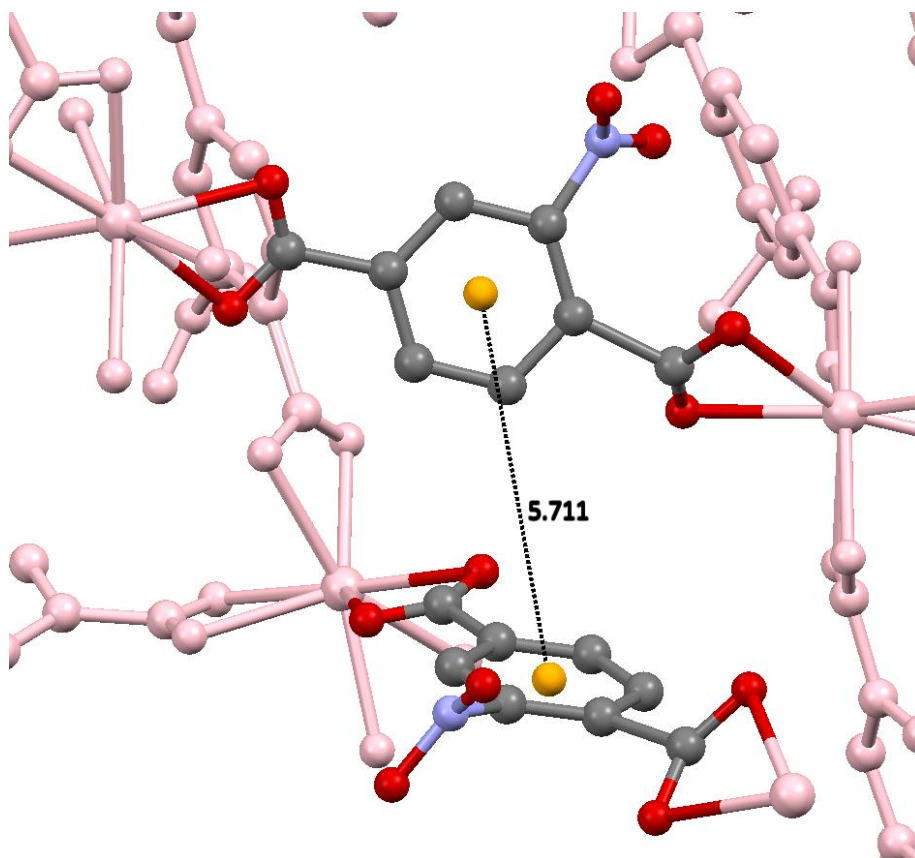


Figure 4.21. “Locked” aromatic rings of the two interpenetrated networks which may play a role in stabilising the desolvated structure. Distance is shown between the two ring centres (orange). The background framework is shown in pink for clarity. Cadmium = beige; oxygen = red; nitrogen = blue; carbon = grey. Hydrogen atoms omitted for clarity.

The extent of flexibility upon desolvation in $[\text{NMe}_2\text{H}_2]_2[\text{Cd}(\text{NO}_2\text{BDC})_2]$ is moderate; there is a *ca.* 13.4 % reduction in the unit cell volume, compared to *ca.* 15 % in **SHF-61**,² and *ca.* 25 % in **MIL-**

88A(Fe).³³ Table 4.16 compares the unit cell parameters of the solvated and desolvated material determined by single-crystal X-ray diffraction at 100 K and 195 K, and by powder X-ray diffraction at room temperature.

Table 4.16. Unit cell parameters obtained for solvated and desolvated $[\text{NMe}_2\text{H}_2]_2[\text{Cd}(\text{NO}_2\text{BDC})_2]$ by *ex situ* X-ray diffraction experiments. *These structures have been described/compared in the above discussion. **PXRD performed at room temperature – temperature was neither controlled nor measured.

Technique	Temperature / K	State	$a / \text{\AA}$	$c / \text{\AA}$	$V / \text{\AA}^3$
Single-crystal X-Ray Diffraction	100 K	Solv.*	14.8922(7)	12.7663(6)	2452.0(3)
		Desolv.*	13.6137(13)	13.2281(13)	2123.1(4)
	195 K	Solv.	15.0467(5)	12.6619(4)	2482.63(18)
		Desolv.	13.7699(3)	13.2048(3)	2168.32(11)
Powder X-Ray Diffraction	<i>ca.</i> 298 K**	Solv.	15.2736(2)	12.5538(3)	2536.23(10)
		Desolv.	13.931(2)	13.148(3)	2209.6(9)

X-ray diffraction studies on both a single-crystal and a powder sample were also performed with *in situ* desolvation. In these experiments, the samples were heated to a set temperature for a fixed period of time, and then cooled to 298 K. After a pause for equilibration, a data set was recorded, and the cycle repeated for successively higher temperatures. Details of the heating and equilibration times can be found in Section 4.3.3. In the single-crystal diffraction experiment, only enough data were recorded to determine the unit cell of the material, not the full crystal structure. Tables 4.17 and 4.18, and Figure 4.22 illustrate the results of these two experiments.

Table 4.17. Unit cell parameters obtained from *in situ* desolvation study with single-crystal X-ray diffraction. *‘‘Temperature’’ refers to the temperature the sample was heated to prior to data collection – all data were collected at 298 K.

Temperature* / °C	<i>a</i> / Å	<i>c</i> / Å	<i>V</i> / Å ³
25	15.144(3)	12.638(3)	2510.0(6)
40	15.069(3)	12.682(3)	2494.0(6)
60	14.932(17)	12.762(12)	2464(4)
80	14.232(18)	13.051(15)	2289(4)
100	14.202(10)	13.076(7)	2284(2)
120	14.122(6)	13.105(4)	2264(1)
140	14.058(8)	13.102(6)	2242(2)
160	14.152(5)	13.051(4)	2264(1)

Table 4.18. Unit cell parameters from Pawley refinement to fit the data from *in situ* powder diffraction desolvation experiment. *As with Table 4.17, all data were collected at 298 K – the ‘‘Temperature’’ column refers to the temperature the material was heated to prior to data collection. Phase 1 = open-pore phase; phase 2 = narrow-pore phase.

Temperature* / °C	<i>R</i> _{wp}	<i>R</i> _{wp} '		<i>a</i> / Å	<i>c</i> / Å	<i>V</i> / Å ³
25	0.0650	0.1632		15.1241(8)	12.6216(8)	2500.3(3)
40	0.0566	0.1401		15.0963(7)	12.6371(7)	2494.1(3)
60	0.0539	0.1351		15.0606(5)	12.6589(6)	2486.6(2)
80	0.0438	0.1009	Phase 1	15.0235(6)	12.6846(6)	2479.4(2)
			Phase 2	14.511(6)	12.996(7)	2370(2)
100	0.0459	0.1045	Phase 1	14.9980(7)	12.7000(6)	2474.0(3)
			Phase 2	14.429(3)	12.997(6)	2343(1)
			Phase 1	14.9890(8)	12.7046(7)	2471.9(3)

120	0.0458	0.0767	Phase 2	14.327(2)	13.039(4)	2318(1)
			Phase 1	14.978(1)	12.692(1)	2465.9(5)
140	0.0593	0.1232	Phase 2	14.279(2)	13.031(2)	2300.9(7)
160	0.0717	0.1703		14.279(1)	13.012(2)	2297.6(5)

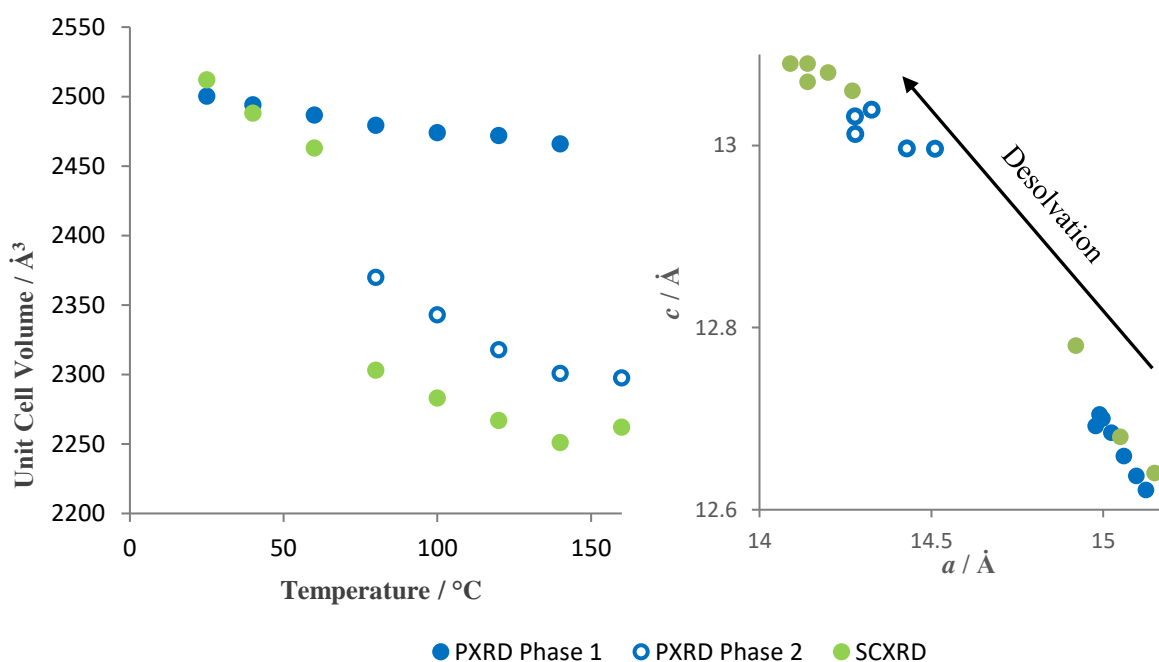


Figure 4.22. Graphical representation of the data from Tables 4.17 and 4.18. Left: Cell volumes against temperature. Right: c -axis plotted against a -axis, to represent the opposite motion of the axes – similar to the “ c -axis vs b -axis” plots used for studies of dynamic behaviour of the MOF SHF-61 (Chapters 1 and 2).²

Inspection of the powder patterns during *in situ* desolvation shows that crystallinity of the sample is preserved throughout the process, despite the successive cycles of heating/cooling and flexibility of the material. Additionally, the powder patterns do not indicate the formation of any new crystalline phases, showing that desolvation does not decompose or degrade the material. The only changes observed in the powder diffraction patterns are peak shifts consistent with changes in the unit cell dimensions of the MOF (Figure 4.23). Interestingly, the desolvated material first appears as a minor phase after heating to 80 °C, and grows in intensity as the experiment progresses, gradually replacing the solvated phase of the material. After the final step only a trace of the first phase remains, and its

peaks are too small for a reasonable Pawley refinement. A similar effect is observed in the single-crystal diffraction experiment – although the crystal does not split into different phases (or domains with different levels of desolvation), the errors associated with the unit cell dimensions are larger after the 60 and 80 °C steps than the others, implying that the lattice symmetry is being slightly deformed throughout the crystal at the stage where most of the solvent is removed.

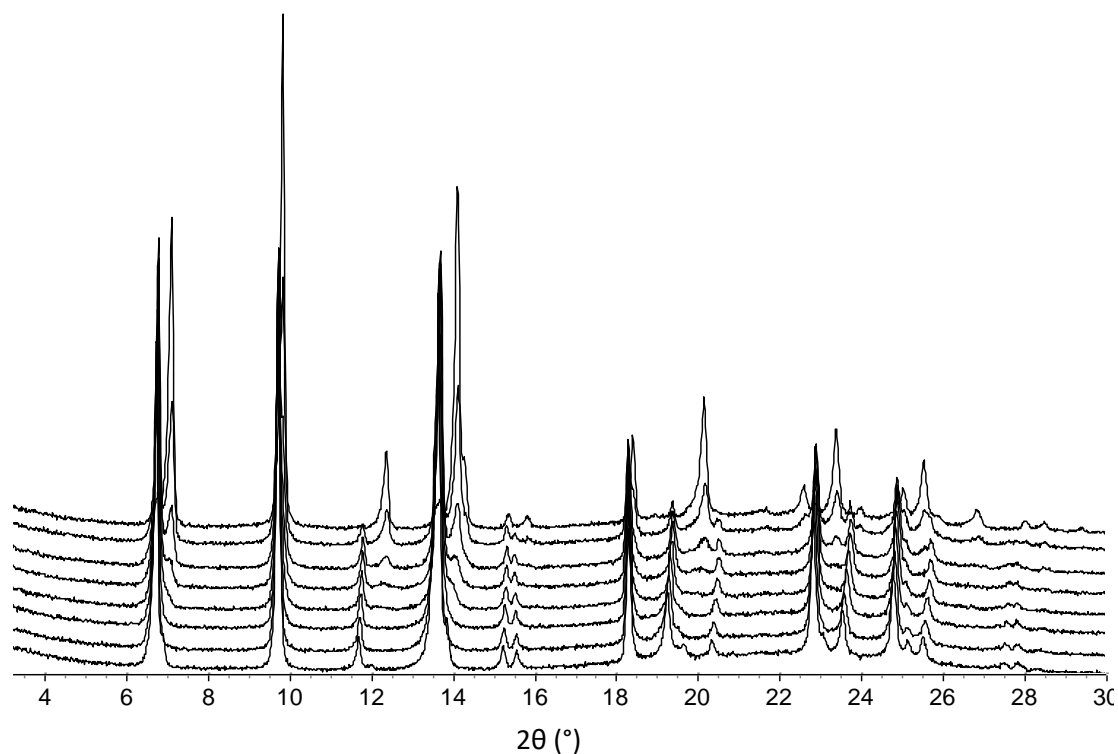


Figure 4.23. Powder X-ray diffraction patterns for the *in situ* desolvation of $[\text{NMe}_2\text{H}_2]_2[\text{Cd}(\text{NO}_2\text{BDC})_2]$. The full scan range can be found in Section 4.3.3, Figure 4.8.

In both the single-crystal and the powder *in situ* diffraction experiments, the largest structural change is observed after heating the material to 80 °C, implying that this temperature is sufficient to remove most of the solvent at atmospheric pressure. It should be noted, however, that whilst this dynamic transition is of a discrete nature (*i.e.* there are no intermediates), a moderate degree of continuous flexibility does occur before and afterwards, implying the framework can host variable amounts of solvent guest. The degree of dynamic range is slightly smaller in the powder diffraction experiment, which is not unexpected, since diffusion of evacuated guest species will be slower in a quartz capillary (powder experiment) than with the crystal directly exposed to a nitrogen stream

(single-crystal experiment). Furthermore, both *in situ* studies show a smaller dynamic range than the *ex situ* studies presented earlier (*c.f.* Table 4.16), which is expected, since the desolvation conditions were harsher in the *ex situ* experiments and likely removed more solvent.

4.4.3. Gas Uptake

The nitrogen uptake capacity for $[\text{NMe}_2\text{H}_2]_2[\text{Cd}(\text{NO}_2\text{BDC})_2]$ at 77 K was determined by volumetric gas adsorption (Figure 4.24). The amount of nitrogen adsorbed is very low – essentially nothing. This is similar to **SHF-61**, which also displays essentially zero nitrogen uptake at 77 K after DMF removal.²

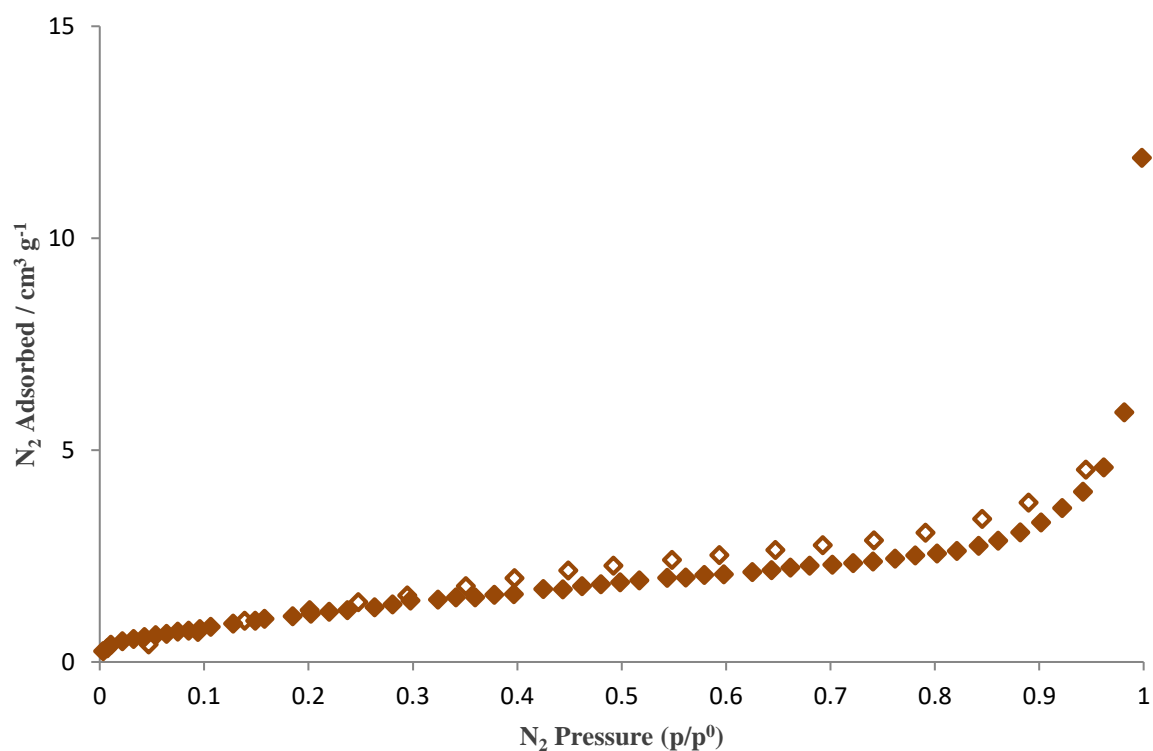


Figure 4.24. Volumetric N₂ adsorption (filled markers) and desorption (hollow markers) isotherms for $[\text{NMe}_2\text{H}_2]_2[\text{Cd}(\text{NO}_2\text{BDC})_2]$ at 77 K.

In the first publication of **QMOF-2** by Sun *et al.*, the authors reported a nitrogen adsorption capacity of around $50 \text{ cm}^3 \text{ g}^{-1}$,¹ although they do not mention the temperature at which these data were recorded. In a follow-up paper by Ji *et al.*, a nitrogen adsorption capacity of $70 \text{ cm}^3 \text{ g}^{-1}$ was reported for **QMOF-2** at 78 K, although importantly, the sample was solvent-exchanged with dichloromethane prior to activation.⁹ Unfortunately, Sun *et al.* do not report their activation procedure, instead stating

that the gas uptake experiments were “performed according to the normal method for microporous zeolite materials”. Clearly this could refer to a variety of temperatures, heating times, atmospheres (or lack of) and pre-treatments. Solvent-exchange treatments are reasonably common for MOFs, especially prior to activation, as less polar solvents such as chloroform and dichloromethane are significantly easier to expel than more polar solvents such as DMF. The publication by Collings *et al.* (Section 4.2) shows that **QMOF-2** flexes in the same fashion as $[\text{NMe}_2\text{H}_2]_2[\text{Cd}(\text{NO}_2\text{BDC})_2]$ upon desolvation, yet two papers have been reported showing reasonable nitrogen uptake, and in (at least) one of them a solvent-exchange for dichloromethane was performed beforehand. A plausible explanation for this seemingly contradictory set of information *could* be (speculatively) that **QMOF-2** is capable of the same solvent-switchable flexibility that is observed in **SHF-61**. This is something that would have been tested, both in **QMOF-2** and $[\text{NMe}_2\text{H}_2]_2[\text{Cd}(\text{NO}_2\text{BDC})_2]$, if time had allowed during the project.

The CO₂ uptake capacity for $[\text{NMe}_2\text{H}_2]_2[\text{Cd}(\text{NO}_2\text{BDC})_2]$ at 195 K was determined using volumetric adsorption to be *ca.* 105 cm³ g⁻¹, or 4.6 mmol g⁻¹; significantly larger than nitrogen uptake at 77 K. This suggests that the material is selective for CO₂ over nitrogen, although isotherms would need to be recorded at the same temperature for certainty. This result would be expected, however, as Ji *et al* showed that **QMOF-2** is selective for carbon dioxide over nitrogen at both 273 K and 293 K.⁹ Additionally, this is a greater volume of CO₂ than activated **SHF-61-DMF** adsorbs at 195 K (Section 2.4.2 – volumetric studies) or 298 K, or partially desolvated **SHF-61-DMF** at 298 K. However, it is a smaller amount than taken up by **MIL-53**, **MIL-53(AI)** and **MIL-47** at 304 K (*ca.* 10 – 12 mmol g⁻¹),³⁵ and by the framework **In(TCPBDA)**⁻ at 195 K (*ca.* 180 cm³ g⁻¹).³⁶

The interesting aspect of CO₂ uptake in $[\text{NMe}_2\text{H}_2]_2[\text{Cd}(\text{NO}_2\text{BDC})_2]$, however, is not the quantity adsorbed, but how the framework responds to the stimulus. To aid this discussion, the isotherm is plotted in the unusual units of CO₂ molecules per unit cell (Figure 4.25), using the equation below:

$$\begin{aligned} \text{mol g}^{-1} (\text{measurement units}) \times M(\text{MOF molar mass}) \times Z(\text{formula units per unit cell}) \\ = \text{CO}_2 \text{ molecules adsorbed per unit cell} \end{aligned}$$

Additionally, an analysis of available void space has been performed on the crystal structure of the desolvated material at 195 K using the program Mercury. A CO₂ molecule can be approximated as a cylinder with length 5.4 Å and radius 1.7 Å, so a spherical probe of 1.7 Å was used in the analysis. Finally, CO₂ uptake at 195 K was performed and the crystal structure monitored *in situ* by powder X-ray diffraction at beamline I11, Diamond Light Source. The unit cell parameters obtained from Pawley refinement are tabulated in Section 4.3.4 (Table 4.16) and shown graphically in Figure 4.26.

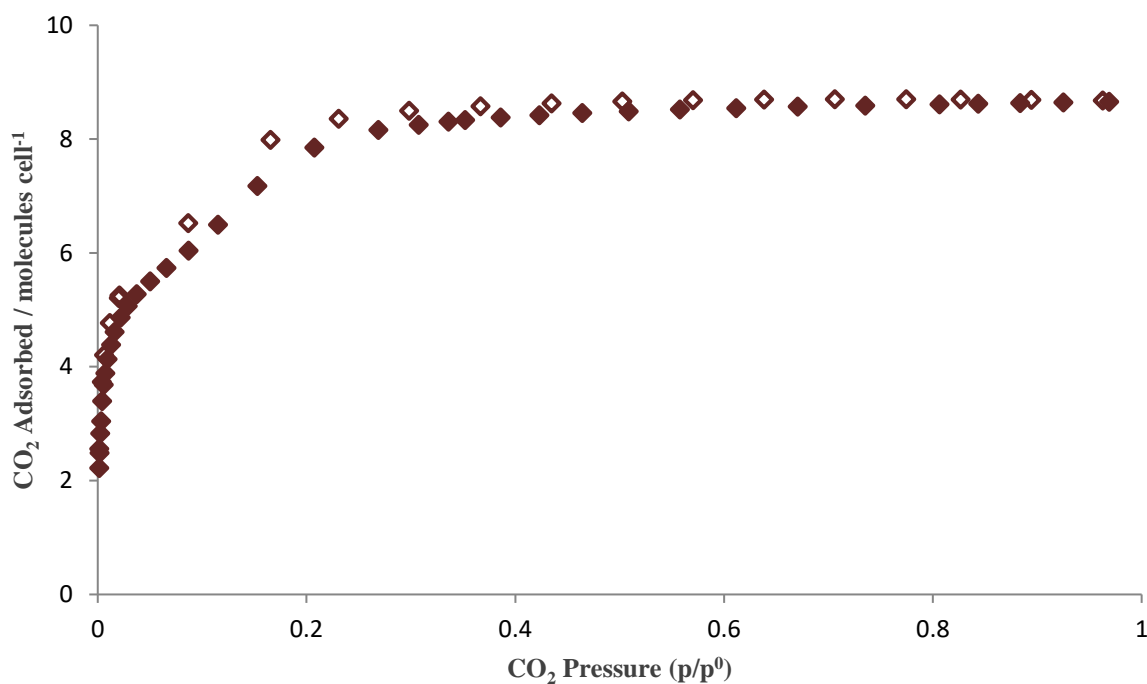


Figure 4.25. Volumetric CO₂ adsorption (filled markers) and desorption (hollow markers) profile for [NMe₂H₂][Cd(NO₂BDC)₂] at 195 K.

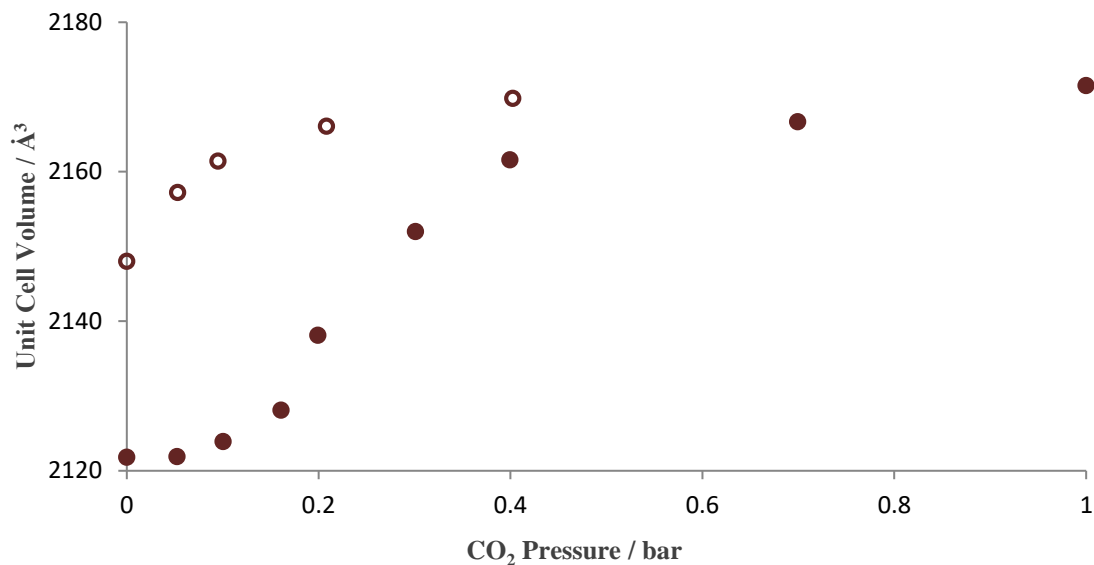
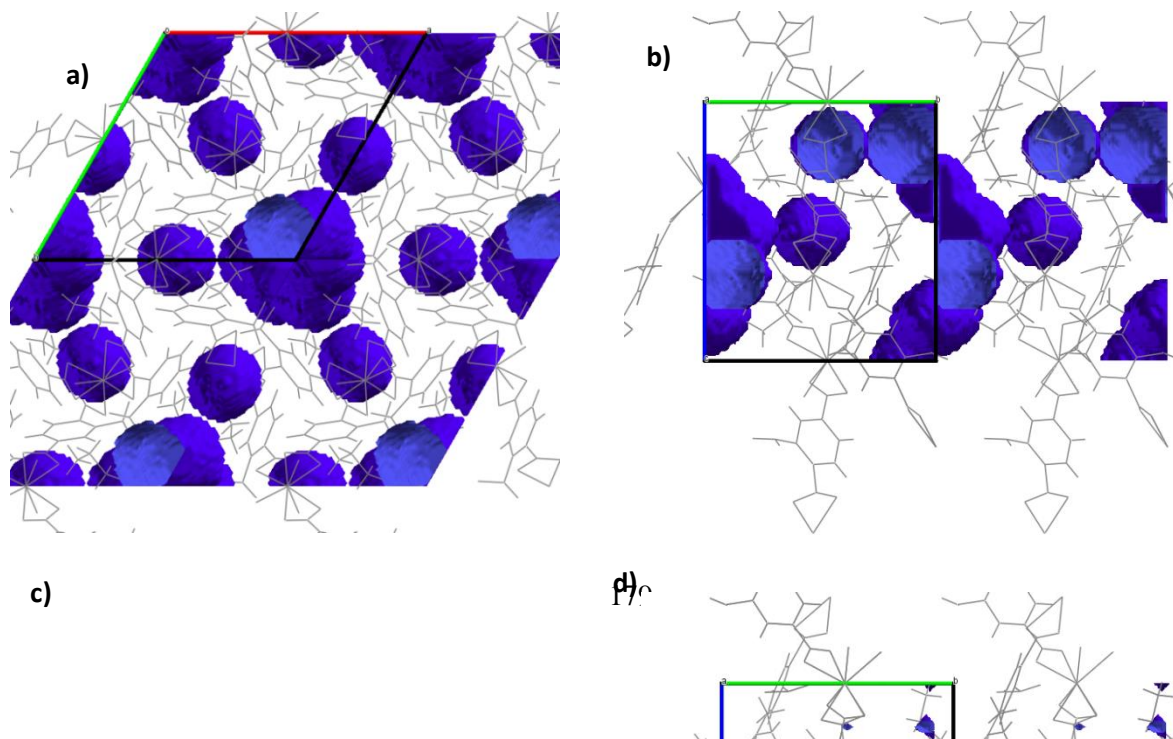


Figure 4.26. Unit cell volume of $[\text{NMe}_2\text{H}_2]_2[\text{Cd}(\text{NO}_2\text{BDC})_2]$ as a function of CO_2 pressure during the *in situ* powder diffraction study at 195 K. Filled circles are adsorption, hollow are desorption. Pressure of 0 bar corresponds to dynamic vacuum (10^{-7} bar).

The void space analysis of desolvated $[\text{NMe}_2\text{H}_2]_2[\text{Cd}(\text{NO}_2\text{BDC})_2]$ reveals a total accessible void space of 251.27 \AA^3 . However, from visual inspection, the only sites in the closed structure that can accommodate carbon dioxide as a guest species are the channels that run parallel to the *c*-axis (Figures 4.27a, 4.27c). Whilst there are other sites which could fit a sphere of radius 1.7 \AA , these are not long enough to host the length of a CO_2 molecule (5.4 \AA), without some structural rearrangement occurring. Each unit cell contains one channel, and within that channel, there are six possible locations for the centre of the spherical probe (Figure 4.27b, 4.27d), and hence six potential sites that a CO_2 molecule could occupy.



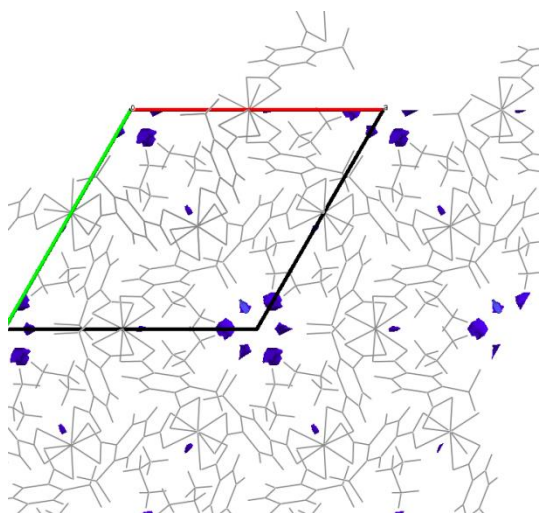


Figure 4.27. **a, b)** Total volume accessible by the spherical probe. **c, d)** Sites accessible by the *centre* of the spherical probe. **a, c)** Viewed along the *c*-axis. **b, d)** Viewed along the *a*-axis.

The relationship between the lengths of the *c*-axis and a CO₂ molecule can be expressed as:

$$2 \times \text{CO}_2 \text{ length} < c < 3 \times \text{CO}_2 \text{ length.}$$

Therefore, two CO₂ molecules per unit cell should be able to fit in the channels of the MOF, without any structural rearrangement occurring. This is shown exactly in the volumetric adsorption isotherm: the first point measured corresponds to an immediate uptake of two molecules per unit cell, implying that the framework can host these guests without any barrier to adsorption.

The total accessible volume of a unit cell, however, is large enough to accommodate five CO₂ molecules:

$$\begin{aligned} 251.27 \text{ \AA}^3 &> 5 \times \left\{ \pi (1.7 \text{ \AA})^2 \times 5.4 \text{ \AA} \right\} \\ &> 5 \times 49.0 \text{ \AA}^3 \\ &> 5 \times V(\text{CO}_2) \end{aligned}$$

Therefore, with a small degree of structural perturbation in order to allow the remaining void space to become accessible, a total of five CO₂ molecules per unit cell could theoretically be adsorbed.

Again, this is shown in the volumetric adsorption profile, at a low relative pressure of 0.02. In the powder diffraction experiment, very little expansion is observed in this region, supporting the notion that this process occurs without significant structural rearrangement. The volumetric adsorption isotherm then shows a subtle gate between the pressures of 0.03 and 0.2 bar, with the number of adsorbed CO₂ molecules reaching a plateau at *ca.* 8.6 per unit cell. In the diffraction experiment, this gate is observed between 0.05 and 0.4 bar. The reason for the shift in gate pressure is unknown, but is likely due to the degree of pore-closure in the material, which varies batch to batch. The sample used for the crystallographic experiment is amongst the most closed of all the samples observed in our studies of this material (the unit cell dimensions of the sample used for volumetric adsorption are unknown). It should also be mentioned that the volumetric adsorption isotherm is significantly more detailed than the *in situ* crystallographic experiment, as a much larger number of pressure steps are recorded.

To summarise, CO₂ uptake in desolvated [NMe₂H₂]₂[Cd(NO₂BDC)₂] occurs in three stages. First, two CO₂ molecules are adsorbed readily, without any apparent barrier. Secondly, a further three molecules are adsorbed at low pressure, possibly aided by small structural perturbations, but without large-scale flexibility of the lattice. Thirdly, a gated opening of the MOF occurs, allowing (or caused by) the adsorption of another 3.6 molecules per unit cell. In the volumetric *desorption* profile, a negligible hysteresis occurs, showing that CO₂ is not retained in the structure, and therefore implying that the guest is not strongly bound to the pore surface. A much larger hysteresis is present in the powder diffraction experiment, showing that the loss of CO₂ doesn't fully close the framework, with a final unit cell volume of 2148 Å³, compared to 2122 Å³ desolvated, and 2172 Å³ after CO₂ uptake.

The sample used for the 195 K *in situ* powder X-ray diffraction study had previously been used for an analogous experiment at 298 K, which allows for a direct comparison of the effect of temperature on CO₂ uptake without the variation in solvent content which often occurs in the studies of these materials. Due to the higher absolute pressures required at higher temperatures, the highest possible measurement was at 50 bar, which corresponds to $p/p_0 = 0.78$. Additionally, only one desorption

measurement was performed, under vacuum. Figure 4.28 displays the unit cell volume as a function of relative pressure.

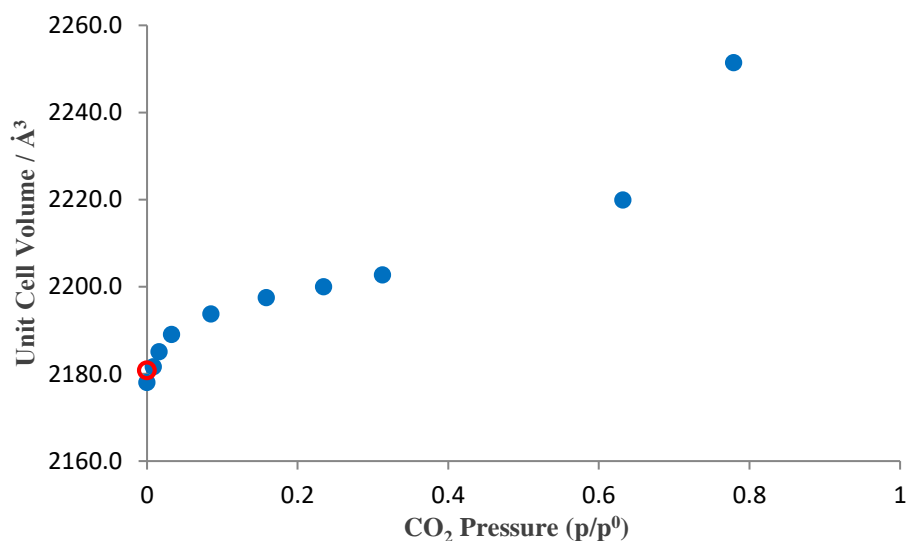


Figure 4.28. Unit cell volume as a function of CO₂ pressure at 298 K. Filled circles are adsorption measurements. The single desorption measurement is depicted larger, and in red, for clarity.

Interestingly, at 298 K, a continuous increase in the unit cell volume occurs immediately in the initial stage of the experiment. In the analogous 195 K experiment, very little expansion occurred at this stage and it was deduced that around five molecules of CO₂ per unit cell had been adsorbed. It is proposed that at the higher temperature of 298 K, these molecules have greater thermal motion, and their incorporation would therefore require some expansion of the framework. As in the 195 K experiment, a gated expansion is then observed. Whereas at 195 K this occurred between relative pressures of 0.05 and 0.4, at 298 K it takes place at a relative pressure of around 0.6, and is not completed within the pressure range of the experiment. Whilst the reason for this shift of the gate to a higher pressure is unknown, it is possible that it simply results from the 298 K structure having a higher unit cell volume (*ca.* 2200 Å³ at p/p_0 0.02, compared to 2138 Å³ at 195 K), and therefore a higher potential CO₂ capacity.

[NMe₂H₂]₂[Cd(NO₂BDC)₂] displays gated expansion in both *in situ* powder X-ray diffraction studies. However, in the single-crystal *in situ* diffraction experiment, no gate is observed. Instead, a

continuous expansion of the structure occurs, such that the first five points, up to a relative pressure of *ca.* 0.3, follow an apparent type I isotherm shape (Figure 4.29).

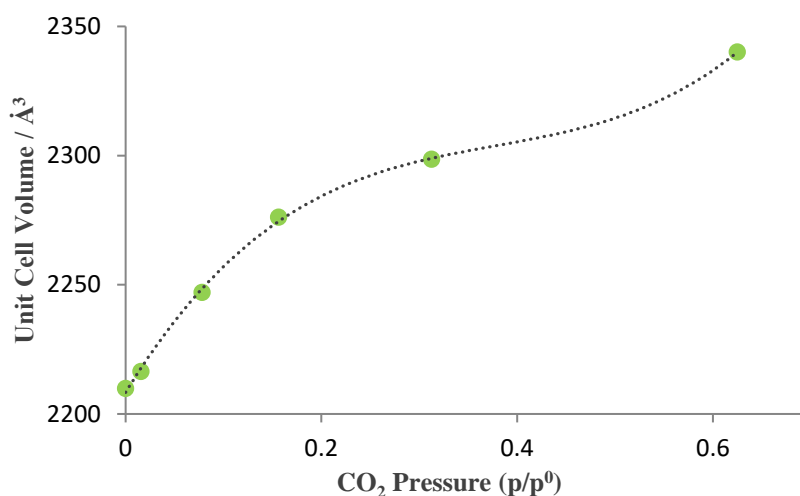


Figure 4.29. Unit cell volume as a function of CO₂ pressure during the *in situ* single-crystal X-ray diffraction study at 298 K. The dotted line illustrates that the final data point does not follow the same curve as the previous five.

The crystal used for this experiment has a unit cell volume of 2210 Å³, which is moderately larger than the sample used for the *in situ* powder diffraction study at the same temperature, implying that the single-crystal sample is not as desolvated. A void space analysis on the structure of this crystal at 0 bar (*i.e.* before exposure to CO₂) shows that the available sites for a CO₂ molecule are stretched continuously through the channels of the material (Figure 4.30), rather than the discrete locations that were found in the 195 K structure. It is therefore entirely logical that CO₂ uptake causes continuous flexibility, where the degree of pore-opening observed is proportional to the amount of CO₂ being adsorbed into the channels, which is in turn dependent on the CO₂ pressure applied. It is not obvious upon visual inspection, but it should be noted that the cell volume at a relative pressure of *ca.* 0.62 is larger than expected based on extrapolation of the curve approximated by the previous measurements. It is possible that this is actually the start of a gated opening, but one data point is not enough to be confident of this conclusion.

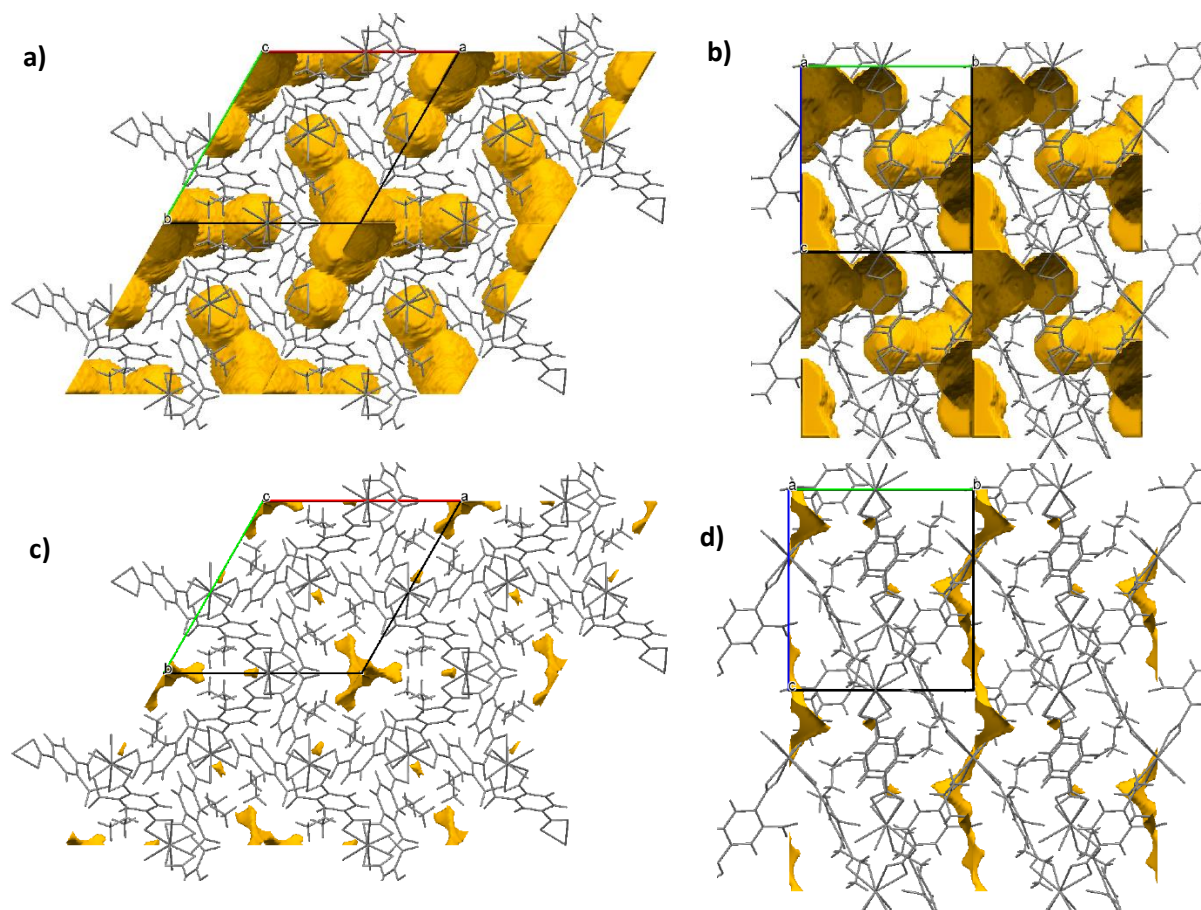


Figure 4.30. **a, b)** Total volume accessible by a spherical probe of radius 1.7 Å in the crystal structure of partially desolvated $[\text{NMe}_2\text{H}_2]_2[\text{Cd}(\text{NO}_2\text{BDC})_2]$ at the start of the 298 K *in situ* CO_2 uptake study. **c, d)** Accessible sites for the *centre* of the spherical probe. **a, c)** Viewed along the *c*-axis. **b, d)** Viewed along the *a*-axis.

Analysing the crystal structures in more detail provides more information on how the framework flexes on a molecular level. Whereas the so-called “knee-cap hinge” is a common mechanism in most flexible terephthalate-based MOFs,^{2,11,31} in $[\text{NMe}_2\text{H}_2]_2[\text{Cd}(\text{NO}_2\text{BDC})_2]$ the flexibility arises from out-of-plane distortion of the carboxylate groups on the ligands (Figure 4.31, Table 4.19). At the start of the study, the torsion angles between each of the carboxylates and the aromatic ring, as well as with each other, are reasonably large, particularly in the case of the carboxylate *ortho* to the nitro group. As CO_2 is adsorbed, these torsion angles decrease, causing the ligands to become more planar. This trend is not perfect – beam damage accumulated over the course of the study caused the quality of structure refinements to diminish somewhat. Nevertheless, a qualitative trend can be seen. The largest torsions are observed for the carboxylate *ortho* to the nitro group, likely due to steric effects. It therefore follows that the nitro groups could play a crucial role in the dynamic behaviour of the material.

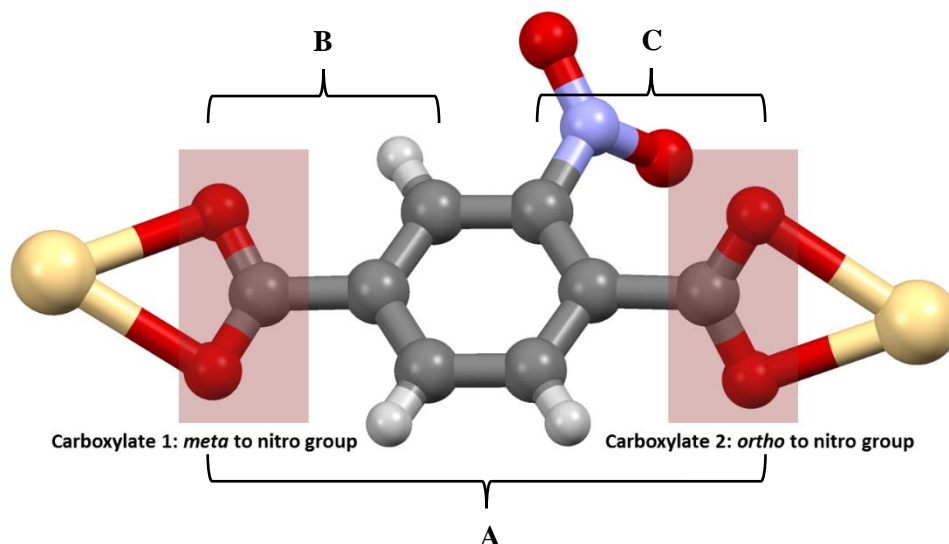


Figure 4.31. Numbering system for the carboxylates in $[\text{NMe}_2\text{H}_2][\text{Cd}(\text{NO}_2\text{BDC})_2]$, and torsion angle definitions.

Table 4.19. Carboxylate torsion angles during the *in situ* single-crystal diffraction study. Torsion angles **A**, **B** and **C** are defined in Figure 4.31.

Pressure / bar	Torsion Between Carboxylates, A (°)	Carboxylate 1 with Aromatic Ring, B (°)	Carboxylate 2 with Aromatic Ring, C (°)
0	27.68	19.06	45.27
1	25.92	18.46	43.45
5	26.00	17.51	40.62
10	28.39	20.37	39.81
20	21.67	14.86	36.46
40	16.87	12.24	23.99

The other key component to the flexibility is the $\text{Cd}\cdots\text{Cd}\cdots\text{Cd}$ angles first introduced in Section 4.4.2 (Figure 4.18), and the pseudo-hexagonal double-helix which they define. Angles 1 and 2 (which are identical) increase in value, and angles 3 and 4 (identical also) decrease. These four angles essentially return their values in the solvated structure (Section 4.4.2), and their contrary motion is the reason for the negative linear expansion observed in the *c*-axis and positive area expansion observed

in the *ab*-plane. Angles 5 and 6 are slightly more interesting. To recap: in the solvated structure, they are almost identical (*ca.* 141.5 °), but upon desolvation, angle 5 decreases and angle 6 increases, causing the channels of the material to narrow. Their change in magnitude is partially reversed upon CO₂ uptake, but they do not converge, meaning that the structure at relative pressure of 0.62 has a narrower channel than would be expected based on angles 1-4. This information is summarised in Table 4.20.

Table 4.20. Cd...Cd...Cd angles during the *in situ* single-crystal diffraction study.

Pressure / bar	Cd...Cd...Cd Angles (pseudo-hexagonal helix) (°)			
	1,2	3,4	5	6
0	76.97	114.40	137.07	150.29
1	77.14	114.23	136.66	150.55
5	77.83	113.72	136.79	149.86
10	78.56	113.19	137.06	149.02
20	79.81	112.31	137.84	147.25
40	80.58	111.75	138.25	146.24

To summarise the gas uptake studies with *in situ* diffraction, the unit cell parameters of the MOF have been plotted together in Figure 4.32 showing the full range of dynamic motion accessed by CO₂ adsorption.

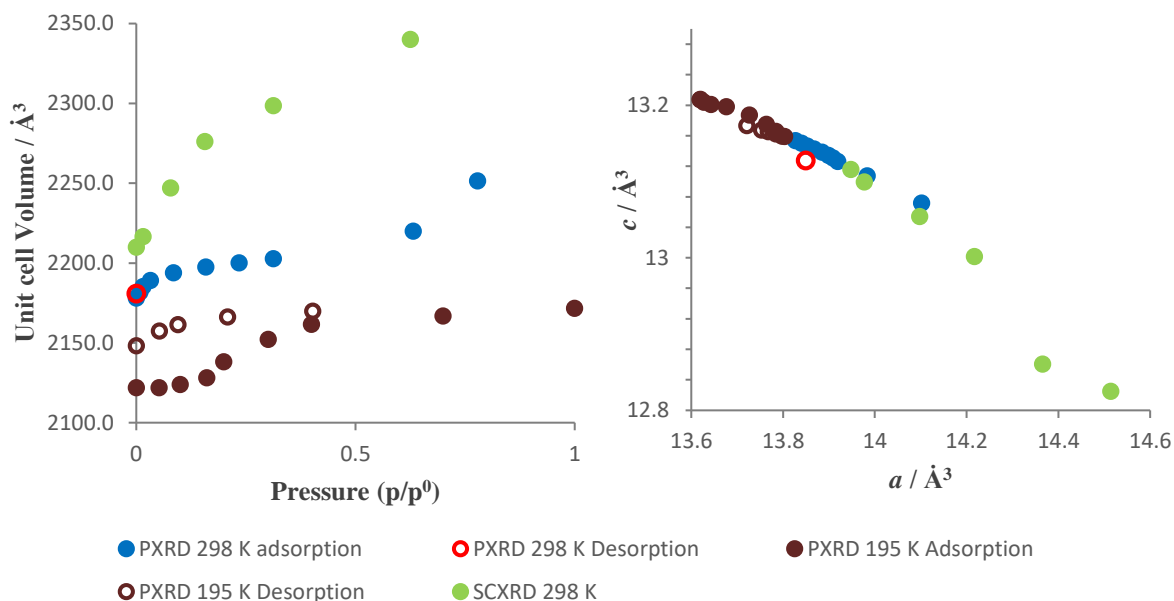


Figure 4.32. Left: Unit cell volume as a function of pressure for all gas uptake studies with *in situ* X-ray diffraction. Right: Comparison of the *c*- and *a*-axis changes for the same data sets.

The results presented here show that $[\text{NMe}_2\text{H}_2]_2[\text{Cd}(\text{NO}_2\text{BDC})_2]$ has unique CO_2 adsorption properties, whilst sharing notable similarities with published materials. Like **MIL-53**,³¹ $[\text{NMe}_2\text{H}_2]_2[\text{Cd}(\text{NO}_2\text{BDC})_2]$ rapidly and readily adsorbs an amount of CO_2 upon initial exposure. However, where **MIL-53** adopts a closed-pore structure as a result of this, $[\text{NMe}_2\text{H}_2]_2[\text{Cd}(\text{NO}_2\text{BDC})_2]$ is already in a narrow-pore form, and either remains structurally unchanged at 195 K, or displays a small opening at 298 K. Like **SHF-61**,² $[\text{NMe}_2\text{H}_2]_2[\text{Cd}(\text{NO}_2\text{BDC})_2]$ displays both discrete and continuous flexibility. In **SHF-61**, this is either a particle-size effect, or is determined by the level of desolvation – full desolvation leading to continuous opening upon CO_2 uptake, and partial desolvation introducing a gate. However, in $[\text{NMe}_2\text{H}_2]_2[\text{Cd}(\text{NO}_2\text{BDC})_2]$ it is the other way around – CO_2 uptake is gated, unless the material is solvated enough that its pore space is connected in a continuous fashion, in which case continuous flexibility is observed.

4.4.4. Temperature-Dependent Flexibility

The introduction to this chapter discussed briefly the temperature-dependent dynamic behaviour of **QMOF-2**, which was reported by Collings *et al.* in 2014.¹⁰ Since $[\text{NMe}_2\text{H}_2]_2[\text{Cd}(\text{NO}_2\text{BDC})_2]$ is

isostructural to **QMOF-2**, we conducted similar experiments, using *in situ* single-crystal and powder X-ray diffraction. In total, four *in situ* single-crystal diffraction studies were performed using our in-house diffractometers (**VT1** – **3** solvated, **VT4** desolvated; **VT** = Variable Temperature), and one *in situ* powder diffraction study was performed at Diamond Light Source on the solvated material (**VT5**). The data are summarised in Section 4.3.5, and studies **VT3** – **5** are presented graphically in Figure 4.33. In studies **VT2** – **4**, only sufficient data were collected to determine the unit cells of the material, not the full crystal structure.

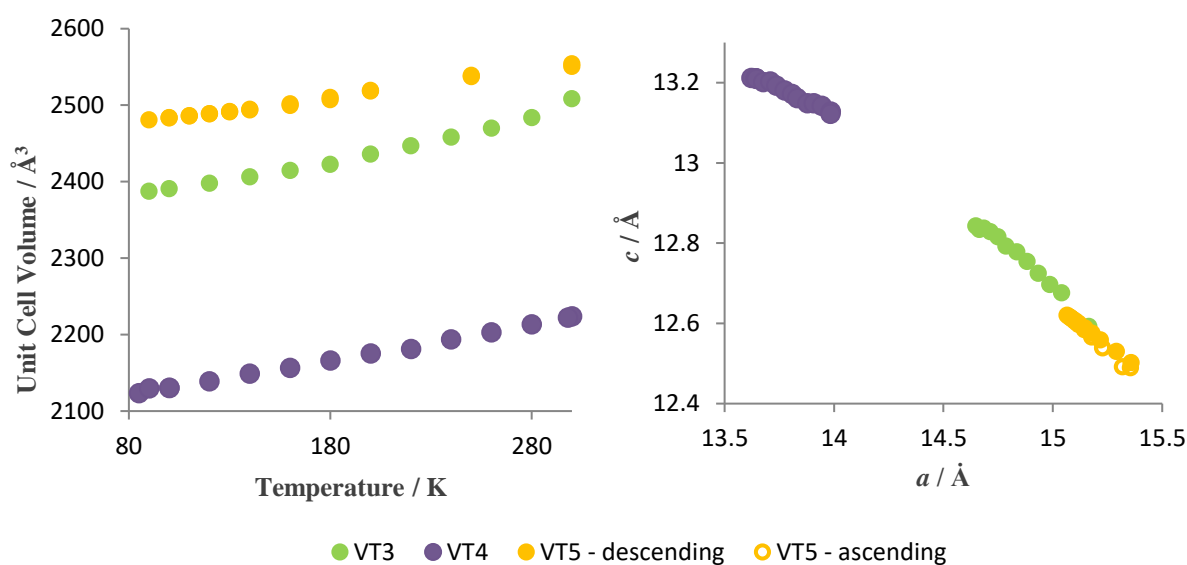


Figure 4.33. Left: Cell volume as a function of temperature in studies **VT3** – **5**. Right: Comparison of cell parameters obtained in studies **VT3** – **5**.

It is clear from the data that the material displays temperature-dependent dynamic behaviour. Additionally, study **VT5** shows that this flexibility is reversible. This is directly comparable to **QMOF-2**, and supports the notion by Collings *et al.* that this behaviour is caused by the frameworks having the **qtz** topology.¹⁰ Since the ρ value of $[\text{NMe}_2\text{H}_2]_2[\text{Cd}(\text{NO}_2\text{BDC})_2]$ is above 0.53 (*ca.* 0.85 solvated; *ca.* 0.97 desolvated), it flexes in the same manner as **QMOF-2** – NTE in the *c*-axis and PTE in the *ab*-plane. This is fundamentally different to the negative thermal expansion which can occur in a two-dimensional wine-rack system such as $[\text{Zn}_2(\text{BDC})_2(\text{DACBO})]$,¹¹ as in these quartz-type frameworks, all three spatial dimensions are involved.

The range of motion displayed by **QMOF-2** is plotted alongside all studies **VT1 – 5** in Figure 4.34 to allow for a direct comparison. Included in this plot also is the data from Table 4.16, Section 4.4.2, as these desolvation studies provide further evidence of temperature dependent flexibility, and provide more desolvated samples to compare to **VT4**.

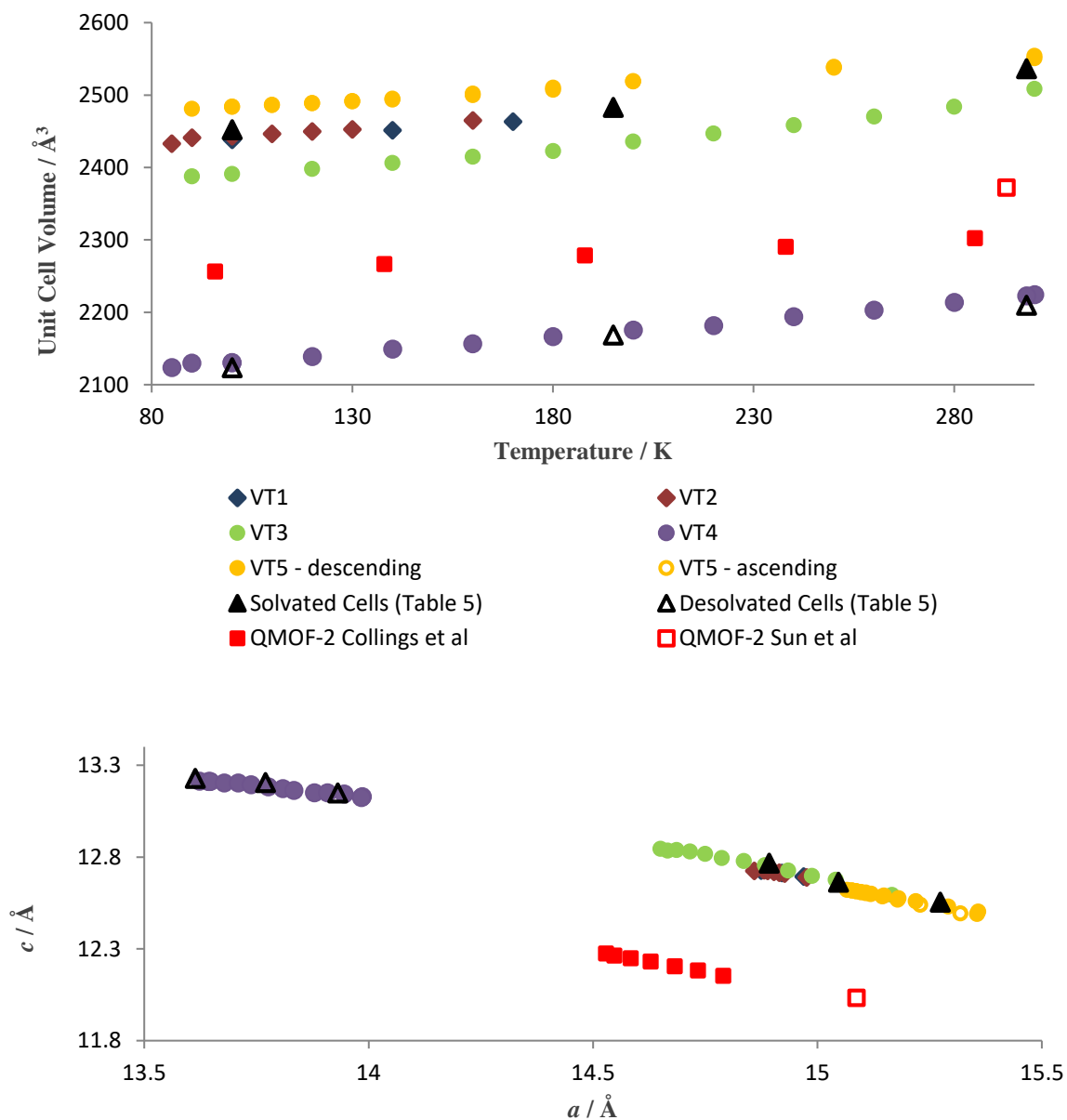


Figure 4.34. Top: Unit Cell Volume as a function of temperature in $[\text{NMe}_2\text{H}_2]_2[\text{Cd}(\text{NO}_2\text{BDC})_2]$ and **QMOF-2**. The 12 K and 42 K measurements by Collins *et al.* have been removed, to allow easier reading of the rest of the data sets. **Bottom:** Comparison of lattice parameters for the two materials (the 12 K and 42 K measurements by Collins *et al.* are included).

Considering both solvated and desolvated states, $[\text{NMe}_2\text{H}_2]_2[\text{Cd}(\text{NO}_2\text{BDC})_2]$ displays a greater range of dynamic motion than **QMOF-2** as a response to temperature. The reason for this is not

known. The nitro groups appear to play an important steric role in the distortion of the ligand (and by extension the whole framework) upon desolvation and gas uptake, and they could be having a similar effect here, albeit over a smaller range of motion.

In order to try to understand this in more detail, the crystal structures obtained in study **VT1** were analysed in more detail. Tables 4.21 and 4.22 list the carboxylate torsion angles and Cd...Cd...Cd angles, respectively, of the three structures.

Table 4.21. Carboxylate torsion angles in the structures obtained in study **VT1**. Carboxylate 1 is *meta* to the nitro group, carboxylate 2 is *ortho* to the nitro group (*c.f.* Figure 4.31, Section 4.4.3).

Temperature / K	Torsion Between Carboxylates (°)	Carboxylate 1 with Aromatic Ring (°)	Carboxylate 2 with Aromatic Ring (°)
170	22.29	20.56	6.18
140	22.43	21.19	6.87
100	22.86	20.20	7.12

Table 4.22. Cd...Cd...Cd angles in the structures of study **VT1**. The numbering system is defined in Figure 4.18, Section 4.4.2.

Pressure / bar	Cd...Cd...Cd Angles (pseudo-hexagonal helix) (°)			
	1,2	3,4	5	6
170	82.98	109.98	141.24	141.38
140	82.72	110.19	141.37	141.46
100	82.48	110.37	141.49	141.53

The Cd...Cd...Cd angles 1, 2, 3 and 4 essentially behave the same way with temperature increase as they do upon CO₂ uptake, but on a smaller scale. Interestingly, angles 5 and 6 move in opposite directions upon gas uptake (5 expands; 6 contracts), but decreasing temperature causes them both to

expand together. Although the structural changes induced by temperature are smaller than those caused by CO₂ uptake, it seems the mechanism is subtly different in each case. It is difficult to deduce an exact mechanism from the carboxylate torsion angles, as carboxylate 1 does not follow a clear trend. However, given that the changes are relatively small in each (compared to the changes observed upon CO₂ uptake), it *is* possible to deduce that carboxylate torsion caused by proximity to the nitro group is *not* having a large effect in the variable temperature experiment(s). Therefore, the reason for [NMe₂H₂]₂[Cd(NO₂BDC)₂] having a larger range of temperature-induced flexibility remains unknown.

To summarise this results section, the full range of dynamic motion achieved in [NMe₂H₂]₂[Cd(NO₂BDC)₂] is plotted in Figure 4.35. We have successfully demonstrated that the quartz-type metal-organic framework exhibits moderate dynamic flexibility, which can occur in a discrete or continuous fashion, as a response to solvent-content, CO₂ pressure, and temperature.

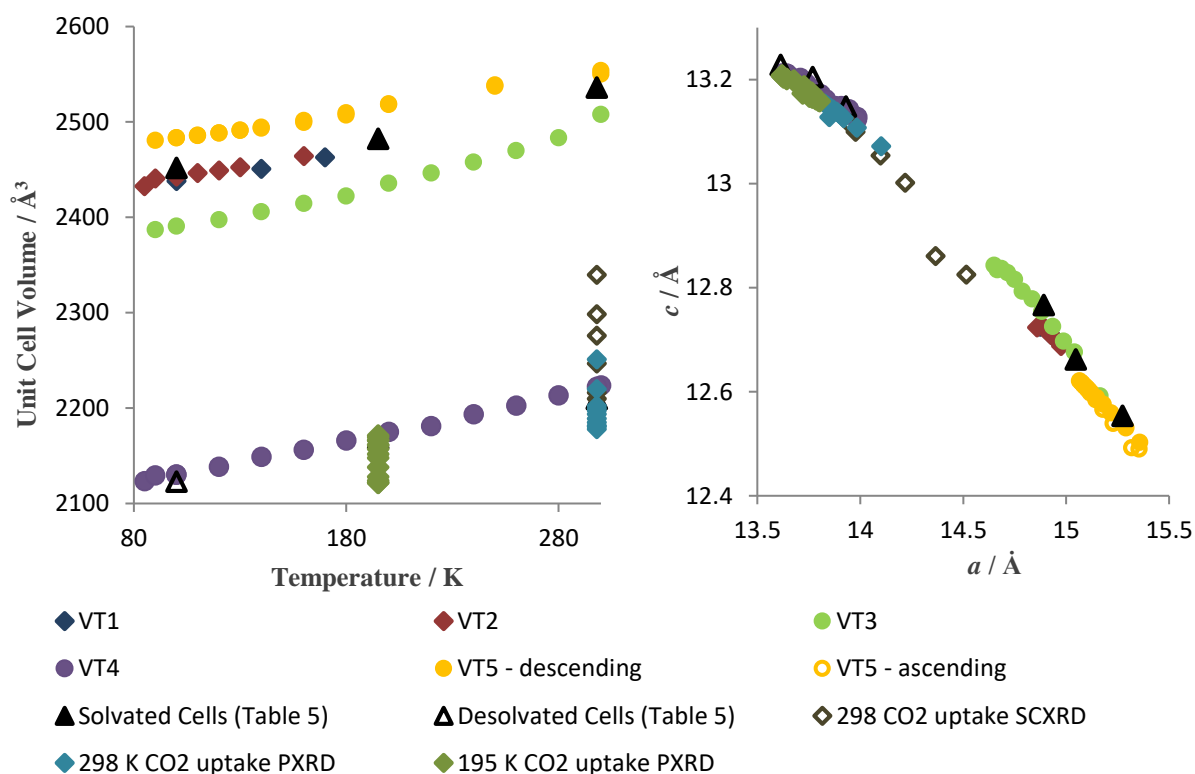


Figure 4.35. The full dynamic range of [NMe₂H₂]₂[Cd(NO₂BDC)₂]. **Left:** As a function of temperature (gas uptake studies are isothermal). **Right:** Comparison of unit cell parameters, showing the NLE displayed by the *c*-axis.

4.5. Conclusion

4.5.1. Summary

We have demonstrated that the synthesis of the quartz-type framework $[\text{NMe}_2\text{H}_2]_2[\text{Cd}(\text{NO}_2\text{BDC})_2]$ can be carried out reliably with the use of a template species, and different solvothermal conditions to the original reported synthesis. The solvent guest is mainly DMF, with a small amount of water. The removal of solvent causes a moderate structural change in the material, which comprises a contraction of the *ab*-plane and an extension of the *c*-axis, and is accompanied by a narrowing of the channels within the material. A combination of volumetric gas adsorption and the change in framework structure during gas uptake, studied *in situ* by X-ray diffraction, were used to show that the desolvated material can be re-opened to some extent by carbon dioxide adsorption at both 195 K and 298 K, with a temperature dependent gate-pressure. Gas uptake with *in situ* single-crystal diffraction showed that partially desolvated $[\text{NMe}_2\text{H}_2]_2[\text{Cd}(\text{NO}_2\text{BDC})_2]$ can also open in a continuous fashion, likely due to the extent of desolvation of the sample. This differs from the diamondoid **SHF-61-DMF** system, where continuous uptake is observed in the fully desolvated material, and gated uptake in the partially desolvated material. $[\text{NMe}_2\text{H}_2]_2[\text{Cd}(\text{NO}_2\text{BDC})_2]$ was also shown by variable-temperature single-crystal and powder X-ray diffraction to exhibit positive thermal expansion in the *ab*-plane and negative thermal expansion in the *c*-axis, consistent with reported studies on an analogous framework, **QMOF-2**. The range of temperature-driven dynamic behaviour is greater in $[\text{NMe}_2\text{H}_2]_2[\text{Cd}(\text{NO}_2\text{BDC})_2]$ than **QMOF-2**, which (speculatively) may arise from the former having nitro groups, which may cause greater distortion of the organic linker components as a result of steric effects.

4.5.2. Next Steps

Activation of **SHF-61-DMF** results in a closed-pore structure, whereas activation of **SHF-61-CHCl₃** results in an open-pore material. The published gas uptake behaviour for **QMOF-2**, after activation from dichloromethane, could be the result of a similar effect, as activation of the DMF-containing MOF results in a closed-pore structure which would be expected to be non-porous with respect to nitrogen. This is reflected in $[\text{NMe}_2\text{H}_2]_2[\text{Cd}(\text{NO}_2\text{BDC})_2]$, which is non-porous to nitrogen

but expands to accommodate carbon dioxide. This could be tested by preparing both DMF and chloroform-containing versions of **QMOF-2** and $[\text{NMe}_2\text{H}_2]_2[\text{Cd}(\text{NO}_2\text{BDC})_2]$, and performing bulk-phase desolvation, with powder X-ray diffraction and volumetric adsorption.

It would be interesting also to determine whether the degree of pore-closure in **QMOF-2** and $[\text{NMe}_2\text{H}_2]_2[\text{Cd}(\text{NO}_2\text{BDC})_2]$ could be altered by adjusting the size of the counter ion. Exchanges with solutions of NR_2H_2^+ , where R = H, Et, Pr, Bu, could be performed, the resultant products characterised and the extent of closure upon desolvation determined using the methods outlined in this thesis (and indeed the theses of previous students in the group). Similar procedures have been performed by previous students on the **SHF-61** system, pending publication, so results could be compared directly.

Another possibility is the preparation of various analogues, using different ligands, such as BrBDC^{2-} or $\text{NH}_2\text{BDC}^{2-}$, and a combination of either indium or cadmium centres. Whilst replication of the published examples via solvothermal methods has proved difficult, it is possible that they could be accessed by other routes, such as: solvent-assisted-ligand-exchange (SALE) or solvent-assisted-metal-exchange (SAME), starting with either **QMOF-2** or $[\text{NMe}_2\text{H}_2]_2[\text{Cd}(\text{NO}_2\text{BDC})_2]$; crystallisation straight from a stoichiometric solution of the MOF components, (perhaps by slow evaporation or cooling a hot, saturated solution); templating with dimethylammonium chloride, or indeed other dialkylammonium salts; or seeding with a small quantity of **QMOF-2** or $[\text{NMe}_2\text{H}_2]_2[\text{Cd}(\text{NO}_2\text{BDC})_2]$, with the aim of purification by successive “dilutions”, *i.e.* after performing several successive seeding procedures, each time using a seed from the previous batch.

4.6. References

- 1 J. Sun, L. Weng, Y. Zhou, J. Chen, Z. Chen, Z. Liu & D. Zhao, *Angew. Chem. Int. Ed.*, 2002, **41**, 4471–4473.
- 2 E. J. Carrington, C. A. McAnally, A. J. Fletcher, S. P. Thompson, M. Warren & L. Brammer, *Nat. Chem.*, 2017, **9**, 882–889.

- 3 M. J. Ingleson, J. P. Barrio, J. Bacsá, C. Dickinson, H. Park & M. J. Rosseinsky, *Chem. Commun.*, 2008, 1287–1289.
- 4 S. M. Cohen, *Chem. Rev.*, 2012, **112**, 970–1000.
- 5 X. X. Wang, Q. G. Zhai, S. N. Li, Y. C. Jiang & M. C. Hu, *Inorg. Chem. Commun.*, 2015, **61**, 200–203.
- 6 X. F. Wang, Y. B. Zhang & Y. Y. Lin, *CrystEngComm*, 2013, **15**, 3470–3477.
- 7 L. Pan, G. Liu, H. Li, S. Meng, L. Han, J. Shang, B. Chen, A. E. Platero-Prats, W. Lu, X. Zou & R. W. Li, *J. Am. Chem. Soc.*, 2014, **136**, 17477–17483.
- 8 J. M. Gu, S. J. Kim, Y. Kim & S. Huh, *CrystEngComm*, 2012, **14**, 1819–1824.
- 9 W. Ji, H. Hu, W. Zhang, H. Huang, X. He, X. Han, F. Zhao, Y. Liu & Z. Kang, *Dalton Trans.*, 2013, **42**, 10690–10693.
- 10 I. E. Collings, M. G. Tucker, D. A. Keen & A. L. Goodwin, *CrystEngComm*, 2014, **16**, 3498–3506.
- 11 Y. Kim, R. Haldar, H. Kim, J. Koo & K. Kim, *Dalton Trans.*, 2016, **45**, 4187–4192.
- 12 K. Takenaka, *Sci. Technol. Adv. Mater.*, 2012, **13**, 013001.
- 13 R. H. Blessing, *Acta Cryst. A*, 1995, **51**, 33–38.
- 14 L. Krause, R. Herbst-Irmer, G. M. Sheldrick & D. Stalke, *J. Appl. Cryst.*, 2015, **48**, 3–10.
- 15 O. V. Dolomanov, L. J. Bourhis, R. J. Gildea, J. A. K. Howard & H. Puschmann, *J. Appl. Cryst.*, 2009, **42**, 339–341.
- 16 G. M. Sheldrick, *Acta Cryst. A*, 2008, **64**, 112–22.
- 17 A. L. Spek, *Acta Cryst. C*, 2015, **71**, 9–18.
- 18 A. L. Spek, *Acta Cryst. D*, 2009, **65**, 148–155.

- 19 S. P. Thompson, J. E. Parker, J. Potter, T. P. Hill, A. Birt, T. M. Cobb, F. Yuan & C. C. Tang, *Rev. Sci. Instrum.*, 2009, **80**, 075107.
- 20 S. P. Thompson, J. E. Parker, J. Marchal, J. Potter, A. Birt, F. Yuan, R. D. Fearn, A. R. Lennie, S. R. Street & C. C. Tang, *J. Synchrotron Radiat.*, 2011, **18**, 637–648.
- 21 G. S. Pawley, *J. Appl. Cryst.*, 1981, **14**, 357–361.
- 22 **a:** A. A. Coelho, TOPAS Academic. Version 4.1, 2007. See <http://www.topas-academic.net>;
b: A. A. Coelho, J. S. O. Evans, I. R. Evans, A. Kern and S. Parsons, *Powder Diffr.*, 2011, **26**, S22–S25.
- 23 C. Zhang, L. Sun, Y. Yan, J. Li, X. Song, Y. Liu & Z. Liang, *Dalton Trans.*, 2015, **44**, 230–236.
- 24 J. L. Du, X. Lu, T. L. Shen, C. P. Li, Y. J. Mu & L. J. Li, *Mater. Lett.*, 2015, **158**, 225–228.
- 25 X. Li, F. Jiang, L. Chen, M. Wu, S. Lu, J. Pang, K. Zhou, X. Chen & M. Hong, *CrystEngComm*, 2016, **18**, 2239–2243.
- 26 A. D. Burrows, K. Cassar, T. Düren, R. M. W. Friend, M. F. Mahon, S. P. Rigby & T. L. Savarese, *J. Chem. Soc., Dalton Trans.*, 2008, 2465–2474.
- 27 B. Fernández, G. Beobide, I. Sánchez, F. Carrasco-Marín, J. M. Seco, A. J. Calahorra, J. Cepeda & A. Rodríguez-Diéguez, *CrystEngComm*, 2016, **18**, 1282–1294.
- 28 X. F. Wang, Y. B. Zhang, X. N. Cheng & X. M. Chen, *CrystEngComm*, 2008, **10**, 753–758.
- 29 M. Krüger, M. Albat, A. K. Inge & N. Stock, *CrystEngComm*, 2017, **19**, 4622–4628.
- 30 A. D. Burrows, K. Cassar, R. M. W. Friend, M. F. Mahon, S. P. Rigby & J. E. Warren, *CrystEngComm*, 2005, **7**, 548–550.
- 31 C. Serre, F. Millange, C. Thouvenot, M. Noguès, G. Marsolier, D. Louër & G. Férey, *J. Am. Chem. Soc.*, 2002, **124**, 13519–13526.

- 32 G. Férey & C. Serre, *Chem. Soc. Rev.*, 2009, **38**, 1380–1399.
- 33 C. Mellot-Draznieks, C. Serre, S. Surblé, N. Audebrand & G. Férey, *J. Am. Chem. Soc.*, 2005, **127**, 16273–16278.
- 34 M. D. Donohue & G. L. Aranovich, *Adv. Colloid Interface Sci.*, 1998, **76–77**, 137–152.
- 35 S. Bourrelly, P. L. Llewellyn, C. Serre, F. Millange, T. Loiseau & G. Férey, *J. Am. Chem. Soc.*, 2005, **127**, 13519–13521.
- 36 X. Li, X. Chen, F. Jiang, L. Chen, S. Lu, Q. Chen, M. Wu, D. Yuan & M. Hong, *Chem. Commun.*, 2016, **52**, 2277–2280.

5. Conclusions

This thesis has added insight into the **SHF-61** framework, probing gas uptake with a combination of *in situ* X-ray diffraction at beamlines I11 and I19, Diamond Light Source. These experiments revealed the presence of a gate pressure, and *b*-axis threshold which must be reached before gated expansion can occur. Using SO₂ at 273 K rather than CO₂ at 195 K shifts this threshold down by *ca.* 0.6 Å, but does not seem to affect the gate pressure, which remains at approximately 0.2 bar. Monitoring CO₂ uptake with *in situ* infra-red spectroscopy at beamline B22, Diamond Light Source, reveals that the gas interacts weakly with the framework amine bands.

Solvent uptake was also investigated using *in situ* infra-red spectroscopy, with interesting results. DMF is found to interact strongly with the framework amine bands, and induces a gated opening in the closed-pore material. Cyclopentanone is found to interact weakly with the amine bands, and trace contaminants of DMF were able to successively compete with isopropanol and cyclopentanone, despite the latter solvents being in excess. Water is found to interact strongly with the framework amine bands also, and water uptake may induce a pore-closing effect in the open-pore material.

The reliable synthesis of a trigonal, cadmium-based metal-organic framework is described, and the compound found to exhibit pseudo-merohedral twinning. *In situ* and *ex situ* diffraction studies, both in-house and at beamlines I11 and I19, Diamond Light Source, reveal that the MOF undergoes a pore-narrowing upon desolvation from DMF at 80 °C. The activated material undergoes gated expansion upon CO₂ uptake, with a temperature-dependent gate pressure. In a less desolvated sample, continuous expansion is instead observed upon CO₂ uptake. The origin for this effect is revealed, using crystal structure pore space analysis and volumetric gas adsorption, to be that pore space is distributed in discrete pockets in the fully-desolvated material, but in continuous channels in the partially-desolvated material. Additionally, the solvated and desolvated material displays temperature dependent three-dimensional flexibility, involving uniaxial negative thermal expansion, monitored by a combination of *in situ* and *ex situ* single-crystal and powder X-ray diffraction.

SHF-61, $[\text{NMe}_2\text{H}_2]_2[\text{Cd}(\text{NO}_2\text{BDC})_2]$ and **QMOF-2** were first reported without the authors' knowledge of their dynamic properties. This statement is not intended to criticise, but to draw attention to the fact that if specific properties/behaviours are not being actively investigated in a material, they can easily go unnoticed. These materials are in fact very similar on a molecular level. They each consist of two identical networks constructed by eight-coordinate d^{10} metal centres bridged by terephthalate-based linkers. They are anionic structures with the same charge-balancing counter-ion (albeit in different stoichiometric quantities) and importantly, have network types which are made up of helical arrangements (**dia** and **qtz**). In fact, it could be argued that these helical arrangements ultimately govern the flexibility of the material, although this would be a simplification. There exist a handful of reported structures, some of which were mentioned in Section 4.2, which also share these similarities, and for which dynamic behaviour has yet to be investigated (or at least, reported). Given the large range of dynamic motion expressed by **SHF-61**, its solvent-switchable nature, and its gas sorption properties which appear to be desolvation-level-dependent, the few materials which are structurally analogous will be interesting by comparison. Similarly, $[\text{NMe}_2\text{H}_2]_2[\text{Cd}(\text{NO}_2\text{BDC})_2]$ has gas sorption properties which appear to depend on temperature, desolvation level or both, and additionally exhibits negative thermal expansion in one crystallographic dimension. Similar temperature-dependent behaviour has already been demonstrated in **QMOF-2**. As with **SHF-61**, any materials structurally analogous to **QMOF-2** and $[\text{NMe}_2\text{H}_2]_2[\text{Cd}(\text{NO}_2\text{BDC})_2]$ will likely be interesting in their own right, and will improve our understanding of these types of materials. If a novel material is presented which shares structural similarities with **MIL-53**, some of the first questions asked are "is it flexible?", and "does it behave like **MIL-53**". This should now be the case with MOFs built from **dia** or **qtz** networks containing d^{10} metal centres and ditopic dicarboxylate linkers, as the three which have been tested thus far have shown positive and interesting results, and have expanded the ever-growing field of flexible metal-organic frameworks.

"It's five past two in the afternoon – nothing's gonna get done soon"

-Kris Drever